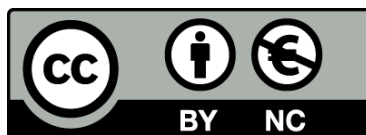




UNIVERSITAT_{DE}
BARCELONA

3D *in vitro* models for neural progenitor cell differentiation and network formation

Inês Sousa Pereira



Aquesta tesi doctoral està subjecta a la llicència **Reconeixement- NoComercial 4.0. Espanya de Creative Commons.**

Esta tesis doctoral está sujeta a la licencia **Reconocimiento - NoComercial 4.0. España de Creative Commons.**

This doctoral thesis is licensed under the **Creative Commons Attribution-NonCommercial 4.0. Spain License.**

Doctoral Thesis

3D *in vitro* models for neural progenitor cell
differentiation and network formation

Inês Sousa Pereira



UNIVERSITAT_{DE}
BARCELONA

2023

3D *in vitro* models for neural progenitor cell differentiation and network formation

Programa de doctorat en Biomedicina

Universitat de Barcelona

Autor:

Inês Sousa Pereira

Directors:

Josep Samitier Martí and
Maria José López
Martinez

Tutor:

Josep Samitier Martí

Tesis realizada en Instituto de Bioingeniería de Catalunya (IBEC)



UNIVERSITAT DE
BARCELONA

Table of Contents

List of Abbreviations	9
List of Figures	11
List of Tables	15
Abstract	17
Resumen.....	19
Chapter 1 – Introduction	21
1. The brain	21
1.1. Components and their functions	21
2. Neurodegenerative diseases	23
2.1. Impact of NDs on the society	24
3. Research models	24
3.1. <i>In vivo</i> models.....	26
3.2. <i>In vitro</i> models.....	27
3.2.1. Two-dimension (2D) in vitro models	27
3.2.2. 3D models	27
3.2.2.1. Spheroids and organoids.....	28
3.2.2.2. Scaffold-based models.....	29
3.2.3. Organ-on-a-chip models.....	30
3.3. Type of cells used in <i>in vitro</i> models.....	30
4. Focus on scaffold-based models	32
4.1. Important scaffold properties in 3D models	33
4.1.1. Biocompatibility.....	33
4.1.2. Biomimetic composition	34
4.1.3. Stiffness	34
4.1.4. Electrical conductivity.....	35
4.1.5. Porosity.....	35
4.1.6. Degradability	36
4.2. Biomaterials used in 3D brain models:.....	37
4.2.1. Hydrogels	37
4.2.1.1. Natural polymers	37
4.2.1.1.1. Collagen.....	37
4.2.1.1.2. Gelatin.....	40
4.2.1.1.3. Alginate	40

4.2.1.1.4. Hyaluronic Acid.....	41
4.2.1.1.5. Matrigel.....	41
4.2.1.1.6. Silk.....	42
4.2.1.2. Synthetic polymers	42
4.2.1.2.1. Polyethylene glycol (PEG)	42
4.2.1.2.2. Polycaprolactone.....	43
4.2.1.2.3. Self-assembling peptides	43
4.2.2. Combination of natural and synthetic polymers	43
4.2.3. Decellularized scaffolds	44
4.3. 3D bioprinting.....	45
4.4. Limitation of scaffold-based culture.....	50
5. Focus on organ-on-a-chip models for the brain.....	51
5.1. Axonal guidance and/or separation	52
5.2. Axon's directionality	54
5.3. Static versus dynamic models.....	55
5.4. 3D microfluidic devices.....	56
5.5. Limitations of microfluidic devices.....	58
6. Conclusions and Future Perspectives.....	59
Chapter 2 – Aims of the thesis.....	61
Chapter Three – Methodology	63
1. Formulation of the Polymer Precursors	63
2. Composite Hydrogel preparation.....	63
3. Physical characterization	64
3.1. Swelling analysis	64
3.2. Degradation assay.....	64
3.3. Measurement of compression modulus	65
3.4. Scanning electron microscopy (SEM).....	65
4. Cell cultures	65
4.1. Mouse neuroprogenitor C17.2 cells culture and differentiation.....	65
4.2. 2D C17.2 cell culture in coverslips	66
4.3. Dopaminergic neuron differentiation	66
5. Sample fabrication	68
5.1. Inclusion of the cells in the hydrogel as drops	68
5.2. Bioink preparation and extrusion bioprinting parameters	69
6. Biological assays characterization	70

6.1.	Live/Dead in 3D culture	70
6.2.	Immunolabelling.....	71
6.2.1.	C17.2 cells.....	71
6.2.2.	EPISPC cells	71
6.3.	Real-Time Quantitative Reverse Transcription (qRT-PCR).....	72
6.4.	Calcium imaging.....	73
7.	Microfabrication	74
7.1.	Designs	75
7.1.1.	3D Microfluidic devices – 3D device	75
7.1.2.	2D microfluidic design with microchannels and 2 cell chamber – 2D-2C device	75
7.1.3.	2D microfluidic device with microchannels and 3 cell channels – 2D-3C device	76
7.2.	SU-8 master fabrication.....	77
7.3.	Fabrication of the PDMS replicas	79
7.3.1.	Diffusion test.....	79
7.4.	Inclusion of the cells in the 3D microfluidic device.....	79
7.4.1.	C17.2 cells.....	79
7.4.2.	EPISPC cells	80
7.5.	Biological assays:.....	80
7.5.1.	Live/Dead.....	80
7.5.2.	Immunolabelling	80
8.	Differentiation of cortical and striatal neurons	80
8.1.	Cortical neurons differentiation.....	80
8.2.	Striatal neurons differentiation	82
8.3.	Dopaminergic neurons differentiation.....	83
9.	Inclusion of iPSC-derived cells into the microfluidic device	83
10.	Biological characterization for the cell in the 2D-3C microfluidic device	85
10.1.	Immunolabelling.....	85
10.2.	Calcium imaging.....	86
11.	Statistical analysis	86
Chapter 4 - RESULTS		87
PART I - Development of a compatible biomaterial for neuronal models.....		87
1.	Optimization of the composition	87
1.1.	Viability assessment of the encapsulated cells	88

1.2.	Protein expression assessment of encapsulated cells	89
2.	Physical characterization of the hydrogels	91
3.	Evaluation of GelMA + AlgMA + HA hydrogel for long-term culture of C17.2 cells	93
3.1.	Viability assays of C17.2 cells throughout 28 days in culture	93
3.2.	Differentiation of C17.2 cells up to 28 days in culture	96
3.3.	Validation of the differentiation process through gene expression	98
3.4.	Evaluation of the functional network of C17.2 cells	99
3.4.1.	Study of functional activity in 3D	100
4.	GelMA + AlgMA + HA: a bioink for extrusion bioprinting	103
4.1.	Viability assays for C17.2 cells after printing	104
4.2.	Differentiation of C17.2 cells after printing	105
4.3.	Evaluation of the functional network of the 3D bioprinted construct	106
5.	Incorporating the developed biomaterial in a microfluidic device	108
5.1.	3D culture in a microfluidic device	108
5.2.	Viability & Differentiation of C17.2	108
5.3.	Functional network in the 3D system with GelMA + AlgMA + HA	110
6.	Inclusion of human pluripotent stem cells in the 3D culture models	112
6.1.	Viability of EPIPSC cells	112
6.2.	Differentiation of EPISPC cells	114
6.3.	Viability and differentiation of EPISPC cells in the 3D microfluidic device ...	115
6.4.	The influence of the dissolution medium on the 3D culture	118
PART II - Development of micro-compartmentalized models for 2D models with iPSC-derived neuronal cells		121
1.	Design and fabrication of a platform for a neuron-on-a-chip model	122
1.2.	2D microfluidic device with microchannels and 3 cell channels – 2D-3C device	124
1.3.	Co-culture on neuron-on-a-chip - Cortico-striatal circuit model	126
1.3.1.	Differentiation of cortical and striatal neurons	126
1.3.2.	Assessment of unidirectional cortical-striatal connection	126
1.4.	Co-culture on neuron-on-a-chip - Striatal-dopaminergic circuit model	129
1.4.1.	Impact of the co-culture on the differentiation of mDA neurons	129
Chapter 5 - Discussion		131
1.	The development of a suitable hydrogel to support the culture and differentiation of neurons	131
2.	The composite hydrogel as bioink for extrusion bioprinting of neuronal cells	134

3. Combining microfluidic devices and the developed hydrogel to create a 3D culture model.....	136
4. Inclusion of human pluripotent stem cells into the 3D cultures	138
5. Neuron-on-a-chip for recreation of cortico-striatal and dopaminergic-striatal communication.....	140
Chapter 6 - Conclusions.....	143
Bibliography	145
Appendix 1 - ¹ H-NMR spectra of AlgMA and GelMA.....	197
Methodology	197
Results.....	197
Appendix 2 – GelMA + AlgMA + HA crosslinked at 395 nm.....	199
Introduction.....	199
Methodology	199
Results.....	200
Conclusions and Future Perspectives.....	202
Bibliography	203

List of Abbreviations

Abbreviation	Description
2D	Two dimensional
3D	Three dimensional
AD	Alzheimer's Disease
AlgMA	Methacrylated Alginate
AL-PVA	Alginate-polyvinyl Alcohol
ALS	Amyotrophic Lateral Disease
A β	β -amyloid
BBB	Blood-brain Barrier
CNS	Central Nervous System
DMEM	Dulbecco Modified Eagle Medium
EB	Embryonic Bodies
ECM	Extracellular Matrix
EDC	N-(3-Dimethylaminopropyl)-N-ethylcarbodiimide hydrochloride
GAGs	Glycosaminoglycans
GelMA	Methacrylated Gelatine
HA	Hyaluronic Acid
HA-PVA	Hyaluronan-polyvinyl Alcohol
HD	Huntington's Disease
iPSC	Induced Pluripotent Stem Cells
LAP	Lithium Phenyl-2,4,6-trimethylbenzoylphosphinate
MEA	Microelectrode Arrays
mDA	Midbrain Dopaminergic Neurons
MMP	Matrix Metalloproteinase
ND	Neurodegenerative Diseases
NFT	Neurofibrillary tangles
NPS	Neuronal Progenitor Cells
NSC	Neuronal Stem Cells
NVU	Neurovascular Unit
PD	Parkinson Disease
PDMS	Polydimethylsiloxane

PEG	Polyethylene Glycol
PEGDA	Poly(ethylene glycol) Diacrylate
PEGMA	Poly(ethylene glycol) Methacrylate
PLC	Polycaprolactone
PHPV	Polyhydroxyphenylvalerate
qRT-PCR	Real-Time Quantitative Reverse Transcription
RGD	Arginine-glycine-aspartic Acid
ROI	Region of Interest
RT	Room Temperature
SAP	Self-assembling Peptides
SEM	Scanning Electron Microscopy
VGCC	Voltage-gated Calcium Channel

List of Figures

Figure 1 Main components of the brain.....	22
Figure 2 Schematic of the important properties in scaffolds for 3D neural models.....	34
Figure 3 Examples of scaffolds produced of natural polymers for 3D neural culture.....	39
Figure 4 Bioprinting techniques.....	46
Figure 5 Different types of typical gelation status.....	47
Figure 6 Examples of extrusion bioprinting using iPSC-derived cells.....	49
Figure 7 Microfluidic devices for axon separation and/or guidance.	53
Figure 8 Blood-brain barrier-on-a-chip models.....	56
Figure 9 3D microfluidic models.....	57
Figure 10 Schematic of C17.2 cells differentiation..	66
Figure 11 Schematic of the ESC-derived striatal neurons differentiation	67
Figure 12 Inclusion of C17.2 in the hydrogel in drop-shape samples.	68
Figure 13 Timeline of the experiments performed with EPISPC cells embedded in the hydrogel..	69
Figure 14 Schematic of the extrusion bioprinting of the gelatin-based biomaterials embedded with C17.2 cells.	70
Figure 15 Process of recording and analysis of cell activity through calcium imaging.	74
Figure 16 AutoCAD images of the 3D device.....	75
Figure 17 AutoCAD images of the compartmentalized device of the 2D-2C design.	76
Figure 18 AutoCAD images of the 2D-3C device.....	77
Figure 19 Step-by-step representation of the process to produce a microfluidic device.	78
Figure 20 Schematic of the inclusion of the C17.2 cells embedded in the biomaterial inside the 3D microfluidic device.	80
Figure 21 Schematic of the ESC-derived cortical neurons differentiation.....	82
Figure 22 Schematic of the ESC-derived striatal neurons differentiation.	83
Figure 23 Timeline of the experiments with PSC-derived neurons in the 2D-3C device.	84
Figure 24 Viability assays performed on drop-shaped samples of C17.2 cells embedded in different polymer concentrations.	89
Figure 25 Differentiation of C17.2 cells embedded in different polymer concentrations.	90
Figure 26 Biomaterial drops with C17.2 cells encapsulated on days 1 and 7 of culture.	91

Figure 27 Physical characterization of the study formulation GelMA + AlgMA + HA compared with the control formulation of GelMA + AlgMA	92
Figure 28 Scanning electron microscopy (SEM) of the hydrogels.....	93
Figure 29 Long-term viability assay on C17.2 cells embedded in GelMA + AlgMA (control) or GelMA + AlgMA + HA hydrogels for up to 28 days.	95
Figure 30 Evaluation of the differentiation of C17.2 cells embedded in GelMA + AlgMA (control) or GelMA + AlgMA + HA hydrogels for 28 days.	97
Figure 31 Quantitative gene expression of C17.2 cells in GelMA + AlgMA (control) or GelMA + AlgMA + HA hydrogels on day 1, 15 and 28 of culture.	98
Figure 32 Functional assessment of C17.2 cells in 2D.....	100
Figure 33 Functional assessment of the C17.2 cells through calcium imaging with Fluo4AM on day 15.....	101
Figure 34 Functional assessment of the C17.2 on GelMA + AlgMA + HA cells through calcium imaging with Fluo4AM on days 15 and 28.	102
Figure 35 Optimization of the printing parameters.....	103
Figure 36 Bioprinting studies of C17.2 cells embedded in the two different bioprinted hydrogels for 15 days.....	104
Figure 37 Evaluation of the differentiation of C17.2 cells embedded in the hydrogel after printing for up to 15 days.....	106
Figure 38 Functional assessment of the cells embedded in the bioprinted biomaterials through calcium imaging with Fluo4AM.....	107
Figure 39 3D microfluidic device setup.....	108
Figure 40 Viability assays of C17.2 cells embedded in GelMA + AlgMA (control) or GelMA + AlgMA + HA hydrogels inside the microfluidic device for 28 days.	109
Figure 41 Evaluation of the differentiation of C17.2 cells embedded in GelMA + AlgMA (control) or GelMA + AlgMA + HA hydrogels inside the microfluidic device for 28 days.	110
Figure 42 Functional assessment of C17.2 cells embedded in the biomaterial and cultured in the 3D microfluidic device.....	111
Figure 43 Viability assays of EPIPSC cells cultured in 2D and embedded in the GelMA + AlgMA (control) or GelMA + AlgMA + HA hydrogels.	113
Figure 44 Differentiation of EPIPSC cells embedded in GelMA + AlgMA (control) or GelMA + AlgMA + HA hydrogels.	114
Figure 45 Viability assays on EPIPSC cells cultured in the 3D microfluidic device.	115
Figure 46 Differentiation of EPIPSC cells in the 3D microfluidic device..	117

Figure 47 Images of the GelMA + AlgMA + HA hydrogels on day 11 of culture (day of EPIPSC inclusion in the biomaterial) and on day 21 of culture.	118
Figure 48 Viability assays of EPIPSC cells cultured in the GelMA + AlgMA (control) or GelMA + AlgMA + HA hydrogels and with two different cell media.....	119
Figure 49 Design and fabrication of microfluidic device 2D-2C.	123
Figure 50 Design and fabrication of microfluidic device 2D-3C.	125
Figure 51 Biological assays performed on microfluidic device 2D-3C for the cortico-striatal neuronal model.....	128
Figure 52 Co-cultures with mDA or striatal neurons on the microfluidic device 2D-3C.....	129

List of Tables

Table 1 Representation of the different pre-clinical models to study the brain.....	25
Table 2 Different polymer concentration tested in the optimization process.	64
Table 3 Conditions of optimization of printing process.	70
Table 4 List of antibodies used for immunolabelling of C17.2 cells.....	71
Table 5 List of antibodies used for immunolabelling of EPISPC cells.	72
Table 6 Genes used in the qRT-PCR experiments.....	73
Table 7 List of antibodies used for immunolabelling of cortical and striatal neurons.	85

Abstract

Conventional 2D *in vitro* and animal models have been found inadequate to fully uncover the intricate mechanisms happening in the brain and its diseases. Engineering-based models emerge as promising alternatives to the development of more complex and dependable brain models. Scaffold-based culture is one example of this type of models where cells are cultured in a biomaterial that simulates more closely the organ environment and function. Another example is microfluidic devices as they combine micropatterned platforms with cell culture to create models with a tuneable framework using small amounts of resources.

In this work, we used methacrylated gelatine, methacrylated alginate and hyaluronic acid to develop a biomaterial with adjustable mechanical properties and biocompatibility that resembles the extracellular matrix for neural culture. This composite biomaterial presented suitable physical properties with high water intake, low stiffness, and slow degradation. Through the evaluation of cell viability and the expression of differentiation markers, we could observe that our formulation was compatible with the culture, differentiation, and network formation of murine neuroprogenitor cells into early neurons. Calcium imaging also validated the activity of the cells in the system. This biomaterial was assessed as bioink for the extrusion bioprinting of the same cell line, presenting good definition, high cell viability, the expression of differentiation markers, and functional activity. The combination of our biomaterial with a 3D microfluidic device of three parallel channels separated by triangular-shaped pillars was also possible, with viable cultures up to 21 days. We complemented these results with the evaluation of the compatibility of our hydrogel with human induced pluripotent stem cells and observed good viability results and the start of differentiation into dopaminergic neurons.

In parallel to the development of our biomaterial, we designed a microfluidic device capable of being used for the culture of different neuronal subtypes. The design consisted of three parallel channels connected through oblique microchannels with dimensions below 5 μm to isolate and direct axons from the lateral channels to the central channel. This model was used to recreate the cortico-striatal circuit with successful differentiation of cortical and striatal cells and the influence of the co-culture was validated through calcium imaging. The dopaminergic-striatal circuit was also modelled using our device with results pointing to the influence of the striatal neurons in the differentiation of dopaminergic neurons.

Resumen

Los modelos *in vitro* convencionales y los ensayos con animales han resultado inadecuados para descubrir por completo los mecanismos complejos que tienen lugar en el cerebro y en sus enfermedades. Los modelos basados en ingeniería surgen como alternativas prometedoras al desarrollo de modelos cerebrales más complejos y fiables. Los cultivos *scaffold-based* son un ejemplo de este tipo de modelos, donde las células son cultivadas en un biomaterial que simula mejor el ambiente del órgano y su función. Otro ejemplo son los dispositivos de microfluídica que combinan plataformas micropatrónicas con cultivos celulares para crear modelos personalizados usando pequeñas cantidades de recursos.

En este trabajo, usamos gelatina metacrilada, alginato metacrilado y ácido hialurónico para desarrollar un biomaterial con propiedades mecánicas ajustables y biocompatible que se parece a la matriz extracelular para cultivos neuronales. Este material compuesto presentaba las propiedades físicas adecuadas, con una absorción de agua elevada, dureza baja y degradación lenta. A través de la evaluación de la viabilidad celular y la expresión de marcadores de diferenciación, pudimos observar que nuestra formulación era compatible con el cultivo, con la diferenciación y con la formación de una red de células neuroprogenitoras de ratón en neuronas inmaduras. El análisis del calcio también validó la actividad de las células en el sistema. Este biomaterial fue evaluado como biotinta para la biopimpresión por extrusión de la misma línea celular, presentando buena definición, alta viabilidad celular, expresión de marcadores de diferenciación y actividad funcional. La combinación de nuestro biomaterial con un dispositivo 3D de microfluídica, que consistía en tres canales paralelos separados por pilares triangulares también fue posible, con cultivos viables hasta 21 días. Complementamos estos resultados con la evaluación de la compatibilidad de nuestro hidrogel con el cultivo de células humanas pluripotentes inducidas de células madre y observamos buena viabilidad celular y el inicio de la diferenciación en neuronas dopaminérgicas.

En paralelo al desarrollo de nuestro biomaterial, desarrollamos un dispositivo de microfluídica capaz de ser utilizado para el cultivo de distintos subtipos neuronales. El diseño consistía en tres canales paralelos conectados por microcanales oblicuos con dimensiones inferiores a 5 μm para aislar y dirigir los axones desde los canales laterales hacia el canal central. Este modelo fue usado para recrear el circuito córtico-estriatal donde la diferenciación de células corticales y estriatales fue exitosa y la influencia del co-cultivo fue validada a través de análisis de calcio. El circuito dopaminérgico-estriatal también fue modelado usando nuestro dispositivo, con

resultados que apuntaban a la influencia de las neuronas estriatales en la diferenciación de las neuronas dopaminérgicas.

Chapter 1 – Introduction

This chapter includes an overview of the state of the art on engineering-based models for neurobiology. The majority of this chapter is present in the paper: “Pereira I., Lopez-Martinez M. J., Samitier J., *Advances in current in vitro models on neurodegenerative diseases.*, Frontiers in Bioengineering and Biotechnology (in preparation).

1. The brain

1.1. Components and their functions

The brain is a complex organ with the responsibility of controlling the whole body. Functions such as perception, thought, movement and emotion impact the survival and well-being of every person. The brain has a dynamic organization that changes in temporal and spatial scales, resulting in refined molecular, cellular, and neuronal inputs¹. The cerebral cortex is responsible for language, problem-solving, reasoning and other high-level cognitive functions as well as four of the five senses (touch, vision, taste, and hearing)². The limbic system is in control of emotional responses and motivation. It has two important structures: the amygdala, in charge of processing fear and negative emotions, and the hippocampus, responsible for memory formation. The cellular composition of this organ is heterogeneous³. Brainstem is the region responsible for automatic functions such as breathing, of which thalamus is a part of and is involved in sensory information processing⁴.

Neurons are the major cellular components of the brain, followed by glial cells, which include astrocytes, oligodendrocytes, and microglia⁵. Neurons are responsible for processing, storing, and transmitting information through chemical and electrical synapses, being in this way the major players in the brain function. They are supported energetically by astrocytes through the astrocyte-neuron lactate shuttle. Astrocytes also regulate the calcium concentration, essential for neuronal activation⁶. They also play an important role in neurogenesis, synaptogenesis, and extracellular homeostasis⁷. Oligodendrocytes are involved in the myelination of neuronal cells while supporting axon metabolism and promoting neuroplasticity⁸. The primary immune cells of the central nervous system (CNS) are the microglia. They are crucial to the immune response, development, and function of the neuronal system, which includes apoptosis, neurogenesis, and myelinogenesis⁹. They are responsible for the CNS surveillance and clearance of pathogens, damaged tissue, and synapses. Lastly, pericytes and endothelial cells

are part of the neurovascular unit (NVU) that interact with neurons and astrocytes to form the blood-brain barrier (BBB)¹⁰. This barrier is highly selective for the entrance of cells, macromolecules, and pathogens from blood to the CNS and when its integrity is disrupted by genetic anomalies on the neurovascular unit cells or other extrinsic factors associated with neurodegenerative diseases, this unit is damaged¹¹.

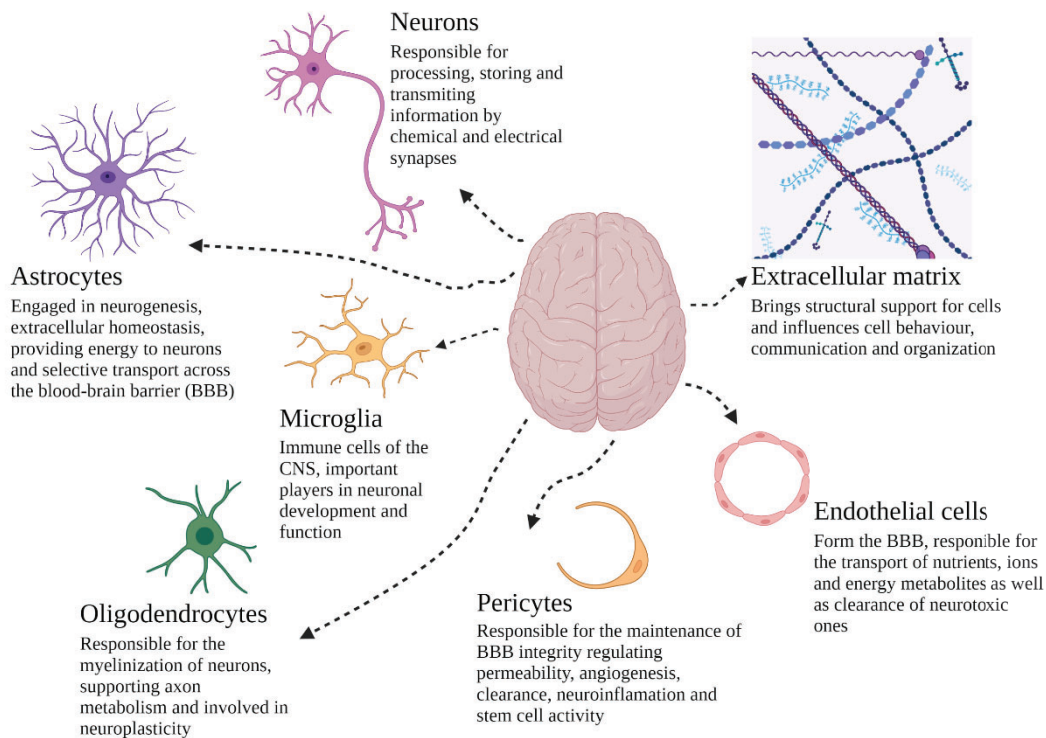


Figure 1 Main components of the brain. Neurons, astrocytes, microglia, oligodendrocytes, pericytes, and endothelial cells are represented as cellular components. The extracellular matrix is also represented. Created with Biorender.com.

Extracellular matrix (ECM) is a key component of brain tissue. Its mechanical and chemical cues influence the development and physiology of the brain, and it has a major role in homeostasis and pathology¹². ECM allows for the structural support for the cells of the CNS, permitting their anchoring and communication, regulating their activity. It takes around 20% of the brain's space and it consists of glycoproteins, lecticans, proteoglycans, glycosaminoglycans (GAGs), and tenascin family proteins¹³. Fibronectin and collagen type I, which are abundant in ECM of other tissues, are almost absent in the brain. Because GAGs, (e.g. hyaluronic acid (HA)) and proteoglycans are the major components of the ECM, this matrix is characterized by a high degree of hydration and low elastic modulus (from 0.1 to 1 kPa)¹⁴⁻¹⁶. The mechanical properties of ECM directly influence the fate of cell differentiation

and the organization of the brain regions. The grey matter region has a low elastic modulus (around 1.4 kPa) and it is composed of neuronal cell bodies. The white matter region is characterized by being the stiffer region, with an elastic modulus around 1.9 kPa, and comprised mostly by glia and neurons' axons¹⁷.

2. Neurodegenerative diseases

Environmental or genetic factors can lead to damage in the cellular or matrix components of the brain, leading to dysfunction and degeneration. Neurodegenerative diseases (ND) are a broad group of conditions characterized by the irreversible decline of one or more structures in the central or peripheral nervous system, leading to gradual disability and grave interference with daily activities¹⁸.

Neurodegeneration is mainly due to the accumulation of proteins such as β -amyloid ($A\beta$) peptide, tau, or alpha-synuclein which originates progressive loss of neuronal cells and the synapses formed between them¹⁹. Of the different neurological disorders, Alzheimer's disease (AD) is the most common form of ND. It is characterized by the extracellular accumulation of $A\beta$ in amyloid plaques as well as the formation of intracellular neurofibrillary tangles (NFT) of the hyperphosphorylated microtubule-associated protein tau. Both $A\beta$ plaques and NFTs lead to neuronal toxicity and degeneration. The disease mostly affects neurons located in the hippocampus and cerebral cortex, which are crucial for memory and cognitive functions. The causes of the accumulation of $A\beta$ and increasing inflammation observed in AD are still an open issue but some of the hypotheses points to the active inflammatory state of astrocytes and microglia as possible contributors^{20,21}. Besides AD, there are other important diseases associated with progressive loss of neurons.

Parkinson's disease (PD) is the second most common ND with several genomic predispositions and risk factors identified as possible causes of the disease²². Here, midbrain dopaminergic neurons are selectively lost in the *substantia nigra pars compacta*²³. These cells are connected to the striatum and help regulate movement. When the dopamine they produce is reduced in the striatum, the motor symptoms of PD, such as tremors, stiffness and difficulty in controlling movement, arise. Huntington's disease (HD) is caused by a mutation of the HTT gene. The most affected area of the brain is the striatal cortical of the basal ganglia, where middle spiny and cortical neurons are damaged²⁴. As the striatum is the brain region responsible for movement control, the degeneration of these neurons leads to movement impairment coupled with cognitive and psychiatric problems²⁵.

Apart from neurons, other neural cell types are affected in NDs. In AD and PD, for example, oligodendrocytes are compromised and rise to the demyelination of the neurons causing their further degeneration. Changes in ECM composition caused by NDs also contribute to the deregulation of the remyelination process²⁶⁻²⁸. The disruption of myelination hampers the conduction of electric impulses by neurons, which causes muscle weakness, numbness, loss of muscle coordination and fatigue. Microglia is also affected in brain pathologies that can result in chronic neuroinflammation. In AD, for example, the protein aggregates lead to the release of proinflammatory molecules from microglia, which causes neuronal damage²⁹. Besides knowing the cellular consequences of brain-related diseases, it is also important to understand their burden on society.

2.1. Impact of NDs on the society




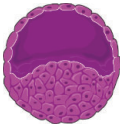

One percent of worldwide deaths are attributed to neurodegenerative diseases and predictions render higher numbers for each passing year³⁰. The number of people with dementia at present is 55 million³¹. From these patients, two-thirds are attributed to AD while PD, epilepsy, HD, and motor neuron diseases like amyotrophic lateral disease are the other third³². As neurodegenerative diseases do not cause immediate death, patients' care treatment tends to last a long period, in which their quality of life decreases with a great economic and social burden. The estimated worldwide cost for dementia is 1 trillion US dollars^{32,33}. Both incidence and economic burden are expected to increase due to the aging of the population and the overall increase in lifespan. The incidence rate is predicted to triple by 2050 and dementia costs double by 2030³². Better solutions to study and treat NDs are needed.

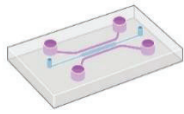
3. Research models

Even though the discovery of neurodegenerative diseases dates back 100 years, they remain difficult to diagnose and treat³⁴. The exact molecular mechanisms behind NDs are still mostly unknown because of the difficulty of access to patient brain samples or availability of suitable disease models²³. This difficulty is also reflected in the drug development for the treatment. Drug discovery and validation are lengthy and costly processes, mainly due to the strict control necessary to avoid side effects, reducing the number of efficient trials. A lot of new drugs fail to translate into new therapies in clinical trials, despite their success in preclinical trials. The main reason for this is that many preclinical models are not physiologically relevant, failing frequently in the prediction of drug effectiveness in humans³⁵. This issue is particularly relevant in neural conditions, as limited complex brain models are available. Better models of the brain

in health and disease are therefore necessary to fill the gaps in our knowledge, thereby improving drug development.

Table 1 Representation of the different pre-clinical models to study the brain. Figures were created with Biorender.com.

Preclinical brain models		Advantages	Disadvantages
<p><i>In vivo</i></p> 		<ul style="list-style-type: none"> • Complex system • Allows the evaluation of the systemic effect 	<ul style="list-style-type: none"> • Ethical concerns • Expensive and time consuming • Interspecies differences
<p><i>Ex vivo</i></p> 		<ul style="list-style-type: none"> • The complex brain structure is preserved 	<ul style="list-style-type: none"> • Brain functions are not reproduced • Reduced availability • Short-term experiments
<i>In vitro</i>	<p>2D</p> 	<ul style="list-style-type: none"> • Simple • Inexpensive • Reproducible 	<ul style="list-style-type: none"> • Lack of complexity • Most cultures only use one or two cell types
	<p>3D</p> <p>Spheroids and Organoids</p> 	<ul style="list-style-type: none"> • High throughput screening • Long-term culture • Similar organization as brain tissue • Mimic brain function and features 	<ul style="list-style-type: none"> • Necrotic core • High variability
	<p>Scaffold-based</p> 	<ul style="list-style-type: none"> • Mimics 3D cellular environment 	<ul style="list-style-type: none"> • High costs associated with increased reagents

			<ul style="list-style-type: none"> Controlled deposition of cells and material 	<ul style="list-style-type: none"> and necessary equipment Bigger size of samples Difficult to standardize
		<p>Organ-on-a-chip</p> 	<ul style="list-style-type: none"> High throughput screening Low amount of reagents Possible to be perfused 	<ul style="list-style-type: none"> Time-consuming for reproducibility and standardization Needs specialized equipment

3.1. *In vivo* models

Animal models have been the gold standard in drug development as they allow the testing of drug efficiency and selectivity in a complex organism. From the non-mammalian models, *Danio rerio* (zebrafish), *Caenorhabditis elegans* (nematode), and *Drosophila melanogaster* (fruit fly) are the most common³⁶. These organisms are small and transparent, making them suitable for the study of developmental mechanisms and molecular processes in adulthood. Genetic modification is also relatively easy, and the embryos grow rapidly, which translates into a high number of mutant individuals and experimental replicates. However, these models cannot fully replicate all the biochemical mechanisms present in humans. Zebrafish share 75% of genes with humans while rodents share 85%. With this common genetic background, mice are the most used animal model³⁷. Even though their fecundity rate is lower than non-mammalian models, their small body size, short lifespan, short gestation, complex immune systems, and relatively easy genetic manipulation make these animals perfect candidates for *in vivo* models in comparison to bigger mammals. Animal models are a crucial step before clinical trials, as they are the most complex and predictable models. In brain research, these models have been used to study processes such as brain ischemia, primary brain tumors, brain metastasis and NDS³⁸⁻⁴¹. Nonetheless, they can fail to predict the clinical behavior of the drugs due to the physiological differences between humans and the animals used⁴². Moreover, disease animal model may not portray all the hallmarks of the disease, representing a short-coming to predict effectiveness in clinical settings. The use of animal models can be expensive, time-consuming, and raise ethical questions. To reduce costs and the animal lives used during the

drug development, ineffective or toxic drugs should be identified in the earlier stages of the process, preferably before the *in vivo* studies⁴³. Additionally, there is a European incentive to replace the use of animal models for the validation of drug efficacy and safety. First, the EU banned the use of animal models in cosmetic product testing in 2013 (EU Regulation 1223/2009), and recently, on the 16th of September 2021, the EU Parliament decided to support the total replacement of animal experimentation, using instead other effective testing platforms⁴⁴. Altogether, it highlights the need to develop robust and versatile disease models for drug screening.

3.2. *In vitro* models

In vitro models are described as the culture of isolated cells, tissue, or organs in a controlled reproducible environment. These models offer important insights into the mechanisms underlying biological events, making them useful for tissue modelling, drug screening, and toxicology studies.

3.2.1. *Two-dimension (2D) in vitro models*

2D models have been used in science for more than 100 years and most breakthroughs in science were only possible because of them⁴⁵. In these *in vitro* models, the cell type of interest is cultured usually in a culture flask or Petri dish and a monolayer is grown. Several biological processes can be studied using 2D cultures, such as cell growth, differentiation, migration, metabolism and drug effect. The substrate can be coated with several types of coatings to mimic the ECM and influence cellular behavior. 2D cell models are reproducible and allow for the easy analysis of well-established techniques on the cells and their visualization through microscopy.

Even though these models are easily produced and inexpensive, they lack several clues in the architecture of a tissue that modulates the cell-cell interaction as well as the relation between the environment and the cells^{43,46}. The morphology of the cells in 2D culture is usually flatter and smaller, more similar to fetal cells than adult cells.⁴⁷ Moreover, the viability, gene expression and protein synthesis in 2D culture can be lower than in Three-dimensional culture⁴⁸. It has become clear the importance of the development of more complex *in vitro* models, such as three-dimensional (3D) models.

3.2.2. *3D models*

3D models were introduced to better mimic the tissue environment and function. The presence of a 3D frame in a cellular model is extremely valuable for cell-cell and cell-matrix

interactions⁴⁹⁻⁵². In 3D models, cells show a behavior closely to *in vivo* processes. Their morphology is different from flat cell cultures, and it resembles more closely the tissue morphology. Additionally, other processes like differentiation, proliferation, or migration mimic better the physiological conditions than on 2D cell cultures.⁵³⁻⁵⁵ Some examples of 3D models are: spheroids and organoids, scaffold-based models and microcompartmentalized devices.

3.2.2.1. Spheroids and organoids

In neuronal cell culture, it is common to use cell aggregates, tissue strands, or cell sheets that grow and become complex structures during culture⁵⁶. Spheroids for neuronal models are characterized by an agglomeration of a single type of neural cells, formed spontaneously or by force when neuronal cells are prevented from adhering to the substrate material. This agglomeration process resembles embryonic development where cells self-assemble to form more complex tissues⁵⁷. One of the most interesting features of spheroids is that cells can produce their own ECM as they are forced to interact with each other⁵⁸. Besides producing ECM, spheroids recapitulate cell-cell interactions and features of natural tissue such as mechanical stiffness and electrophysiology⁵⁷. These characteristics make spheroids good candidates to model the brain, either for performing drug screening or modeling a disease when compared to 2D cultures⁵⁹⁻⁶¹. Spheroids with specific neural cell types can be combined with each other or with scaffolds to recreate a more complex structure for brain disease modelling⁶²⁻⁶⁴.

Organoids are similarly formed as spheroids but with a higher degree of complexity. As for cell origin, spheroids are based on a single cell type while organoids are built using stem cells or tissue progenitor cells. Stem cells within organoids can self-organize and differentiate within the aggregate, creating a complex organ-like structure with different cell types. The spatial organization of the cells in organoids resembles the tissue more closely than spheroids or 2D models, better mimicking some of the organ's functions. They are also more stable and survive longer periods than spheroids⁶⁵. Compared with 2D cultures, metabolic function, gene and protein expression and microscale tissue architecture is closer to the native tissue in organoids⁶⁶. Organoids are used in several types of studies, such as fetal development, disease modelling, and/or drug screening⁶⁷⁻⁷¹. Raja *et al.* generated brain organoids derived from early onset familial AD patients. The results showed these organoids were able to replicate important features of AD, such as A β aggregates, hyperphosphorylated tau proteins and abnormal endosomes⁷². Wulansari *et al.* developed midbrain-like organoids using hESC with DNAJC6

mutation (identified in early-onset PD patients). The model was capable of replicating midbrain-type dopamine neuron degeneration, aggregation of pathologic α -synuclein, mitochondrial and lysosomal dysfunctions and increase of intrinsic neuronal firing frequency⁷³.

One of the disadvantages of these aggregates is that the “vasculature” networks formed are insufficient. Consequently, the center of the organoid experience low oxygen and lack in nutrients, limiting their culture time and growth^{74,75}. The same issue is present in spheroids. This inability to culture organoids for long periods is also a problem for the development of neurodegenerative disease models. As these diseases are characterized by late onset, the culture time of these organoids might not be sufficient to grow mature neurons and glial cells to display the characteristics of diseased cells⁷⁶. To overcome this difficulty, there is a need to find a way to perfuse the cells with a culture medium. Currently, bioreactors with agitation have been used to ensure oxygenation, allowing longer culture periods⁷⁷. To induce the vascularization of brain organoids, Pham *et al.* used endothelial cells from patients on 34-day old organoids embedded with Matrigel®. These organoids showed robust vascularization either during the 3-5 weeks of *in vitro* culture and 2 weeks after transplantation on mice⁷⁸.

Another disadvantage of organoids is the lack of control of the shape and size of the forming structures, translating into high variability. Moreover, as these structures are more complex, real-time optical monitoring becomes difficult. Live or time-lapsing imaging is challenging and to assess the center of the aggregate, researchers might use other imaging techniques, such as histological and immunohistochemical analysis⁶⁹. The sectioning the organoid and staining them to obtain images of the center will destroy the whole agglomerate, precluding further analysis⁷⁹.

3.2.2.2. Scaffold-based models

Scaffold-based culture is one of the most used methods to create 3D models. In this approach, a biomaterial is used to create a structure where the cells will be cultured on top or within the material. Biomaterials are defined as a formulation of biocompatible materials, pure or mixed, that act as a supportive ECM that contribute to the proliferation, migration, and differentiation of the cells⁸⁰. These scaffolds are usually customized in dimension, shape, biochemical and physical properties to better mimic the desired tissue⁴².

Modelling NDs, such as AD, in 3D scaffolds bring an interesting advantage. Usually, in 2D culture, the A β plaques and NFT are not present in the model since they are released by the cells and removed when the medium is changed. In 3D, these hallmarks are not eliminated and

can be observed during culture. Choi *et al.* also found that isoforms of 4RTau were expressed in 3D cultures using Matrigel, a feature that was not seen in 2D cultures⁸¹.

Scaffold-based models are limited by their size since larger structures can lead to a difficult diffusion of nutrients and oxygen. Additionally, these cultures are more expensive and time-consuming than 2D cultures⁸². Other engineering-based models, such organ-on-a-chip models might offer other advantages to neuronal cultures.

3.2.3. *Organ-on-a-chip models*

In parallel with biomaterial-based models, microfluidic devices arise as a promising way to study neuronal cell interaction. In these devices, micropatterned platforms are combined with 2D cell culture to create models with a tunable framework and mechanical forces using a small amount of resources⁸³. The small size of these models is an advantage that contributes to their compatibility with high throughput screening with benefits of drug efficacy and safety assessment⁸⁴. Commonly, microfluidic devices used in neuronal culture present separated cell chambers connected by microchannels to isolate axons from the cell body and study the interaction of the axonal growth with different cell types and/or drugs^{85,86}. Even though organ-on-a-chip focuses on recreating a small section or function of the brain, there is a possibility of interconnecting devices that simulate different organs, which allows for the evaluation of the effect of a drug in several different tissues besides the target one.

Nonetheless, these models have some disadvantages besides not being able to mimic the whole brain. One of those is the difficulty of accessing the cells for assays that require cell lysis such as RNA extraction when compared with 2D. Another disadvantage is the variability between replicates which can increase the time needed to ensure the reproducibility of the model⁴⁴.

3.3. Type of cells used in *in vitro* models

Choosing the appropriate cell type is crucial for the accurate information that we can gather from a model. The origin of these cells, human or animal, is also important and needs to be taken into consideration relative to what the model is for. Animal cells are the most used source of cells for their availability and extended knowledge of their phenotypes, but they do not fully predict the complexity of human cells in healthy and in disease tissues. Instead of using animal cells, human cell lines arise as a more reliable option, especially when ND models are being planned⁸⁷.

Primary cells are one option to use for *in vitro* brain models. Although there are some primary cell lines commercially available, this type of cell is usually harvested from human or animal tissue and has proven to provide higher functional output, reflecting better what happens *in vivo*⁸⁸. However, these cells are difficult to purify and while growing at a slower rate, can lose their phenotype in culture⁸⁹. Immortalized cell lines are one of the most used types of cells in scientific research. These cells are derived from tissue and undergo significant mutations to avoid cell death and are able to proliferate indefinitely. Immortalized cell lines are widely used for their ability to grow fast, allowing high passages while maintaining their robustness, and for their low cost in acquisition and maintenance compared to other cell choices. Even though this type of cells is very useful when a new model is being optimized, the results obtained from these cells can be misleading and not a fair replica of what happens *in vivo*, especially in what concerns transporters, tight junctions, and barrier function⁹⁰.

Besides primary cultures or immortalized cell lines, stem cell culture is widely used in research. Stem cells are characterized by their ability to self-renew while being able to differentiate into all cell types. This cell type can be classified into three different stem cells according to its source: embryonic stem cells, which are obtained from the inner cell mass of the blastocyst; adult stem cells from adult organs or induced pluripotent stem cells from somatic cells. Embryonic stem cells have a great potential for their ability to differentiate into all differentiated cell types, but the use of these cells is often coupled with ethical problems⁹¹. Adult stem cells are multipotent, meaning that they can divide into different cell types, but all are related to the same lineage. They are present in adult organs in few quantities and their extraction is difficult or even not feasible⁹². Within stem cell culture, human induced pluripotent stem cells (iPSC) arise as a promising cell type in brain models since they represent the closest to the human brain without the need to be harvested from the organ itself. These cells are obtained from somatic cells, from healthy humans or patients, that go through a reprogramming process when exposed to a specific cocktail of factors, Oct3/4, SOX2, c-Myc, and Klf4⁹³. Besides their use as a therapeutic approach to neurodegenerative diseases, iPSCs have been used for disease modeling and drug screening, allowing personalized medicine as they contain the genetic information of the patient^{94,95}.

4. Focus on scaffold-based models

Tissue engineering and regenerative medicine are research fields highly interested in the biomaterial-based culture for the development of more accurate *in vitro* brain models and new therapies for NDs or injuries in the nervous system^{82,96,97}.

3D brain tissue models are designed to allow a more complex interaction between cells and their environment, mimicking the communication and electrophysiology network characteristics of the brain tissue that are possible with 2D models⁴⁶. By combining biology and engineering, these models are built with materials capable of simulating the biochemical and biophysical properties of the brain, allowing control over cell culture in processes such as cell adhesion, morphology, migration, proliferation, and differentiation^{98,99}. One of the main characteristics of a scaffold is durability. Scaffolds should be fabricated to allow the long-term culture that certain cell types need while being slowly replaced by the ECM the cells themselves secrete¹⁰⁰.

Several works compared neuronal cell culture in 2D versus 3D and reported better outcomes in 3D culture. Zhang *et al.* compared a 2D and a 3D culture to study AD, using a PuraMatrix hydrogel supplemented with laminin to culture human iPSC-derived neuroepithelial stem cells. The results proved that the 3D model was more capable of mimicking the redistribution of P21-activated kinases, seen in this pathology, originated by A β oligomers¹⁰¹. Adil *et al.* differentiated hPSC to striatal progenitors in a 2D Matrigel-coated surface for 90 days or in PNIPAAm-PED hydrogels for 26 days and then harvested and cultured in a laminin-coated surface. The results showed a 7-fold increase of DARPP32⁺ cells and a 13-fold increase of CTIP2⁺ cells for the 3D cultures at day 28 compared with 2D cultures at day 25. At day 60, the cells differentiated in 2D cultures were not active while 69% of cells cultured 26 days in 3D were spontaneously firing action potentials. The 2D culture was 73% active only on day 90¹⁰². The cells differentiated in 3D culture were then transplanted into a HD mouse model which slowed the progression of the disease and improved the motor coordination and survival of the animals.

Several scaffolds possess fibers, pores, or channels to stimulate communication within the model. Conventional methods for scaffold fabrication are phase separation¹⁰³, self-assembly¹⁰⁴, freeze-drying¹⁰⁵, and solvent casting¹⁰⁶. Other techniques coming from microsystem technology such as photolithography, soft lithography, or laser texturing involve another type of expensive machinery, but they can pattern structures with detail for cell culture.

Electrospinning¹⁰⁷ or electrospraying are also techniques available to produce solid scaffolds¹⁰⁸. There is however a recent technique, called bioprinting, that has been gaining popularity for its control over the architecture produced¹⁰⁹.

4.1. Important scaffold properties in 3D models

To build a suitable scaffold, the materials must comply with several requirements to act as scaffolds such as biocompatibility, easy manipulation, fit for chemical or physical modification; permeability to oxygen, nutrients, and electrical conductance; reproducible and affordable¹¹⁰.

4.1.1. *Biocompatibility*

One of the most important features of a scaffold is its biocompatibility with the cell culture. It is one of the first steps when characterizing biomaterial suitability to test if the cells remain viable during culture, avoiding the overactivation of apoptotic pathways and rejection.

The scaffold should also elicit a response from the cells instead of being inert since the native ECM interacts with the cells to stimulate tissue formation. Incorporating various modes of interaction, such as adhesion sites, allows dynamic biological processes, such as cell migration and communication, to take place⁹⁶.

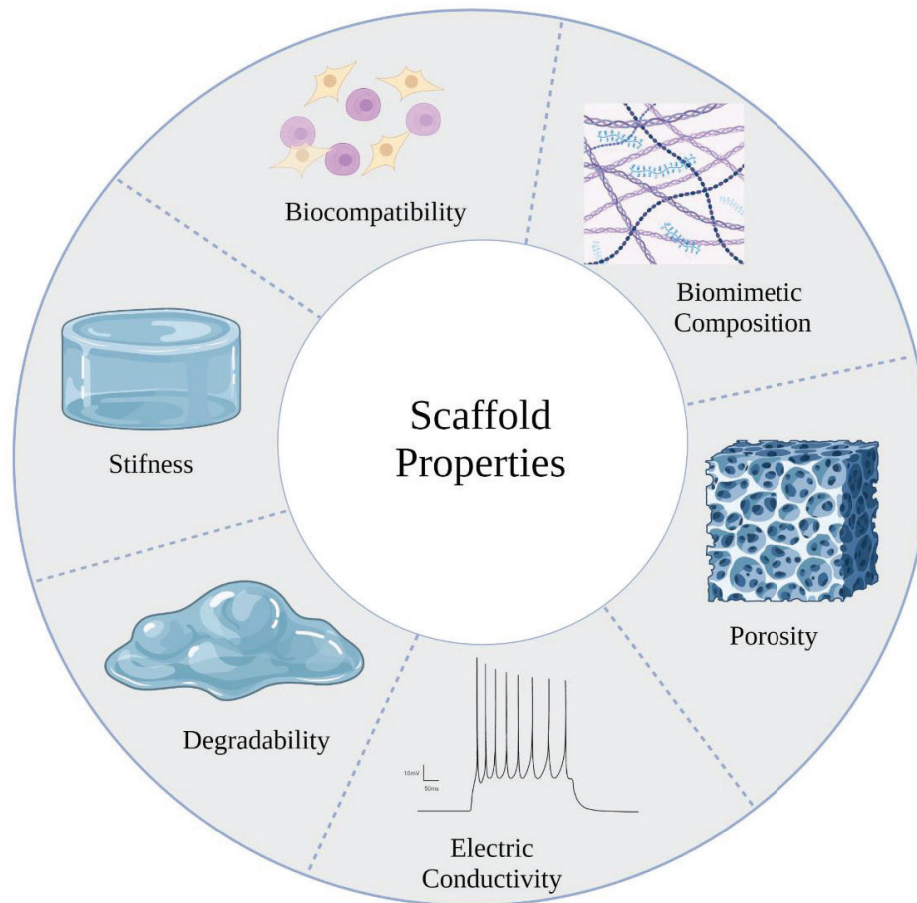


Figure 2 Schematic of the important properties in scaffolds for 3D neural models. Biocompatibility, biomimetic composition, stiffness, electric conductivity, porosity and degradability. Created with Biorender.com.

4.1.2. Biomimetic composition

In addition to the requirements mentioned above, it is relevant to choose biomimetic materials in the composition of the scaffold, such as proteins or small molecules that are present in the native brain ECM. By having a biomimetic composition, the cells can recreate the structure and function of the tissue more accurately, allowing the generation of a more realistic model capable of simulating brain function and the mechanisms of brain disorders¹¹¹. Laminin¹¹², hyaluronic acid¹¹³, arginine-glycine-aspartic acid (RGD) peptides¹¹⁴, poly(lysine)¹¹⁵, and poly(ornithine)¹¹⁶ are examples of molecules that can be included in the scaffold composition that favor the survival and differentiation of neuronal cells.

4.1.3. Stiffness

The stiffness of the substrate influences the fate of the differentiation of neuronal cells. Since the brain is the softest tissue of the body, the scaffold should have a low mechanical stiffness, with values around 0.1-1 kPa¹¹⁷. The sensibility to the stiffness of the substrate was shown *in*

vitro with neuronal stem cells (NSC) differentiating into neurons on softer gels (100-500 Pa), with increased cell migration while in stiffer substrates, the cells differentiated glial cells (>1 kPa)¹¹⁸. Mesenchymal stem cells were also sensitive to the stiffness of the matrices, differentiating into glial cells on stiffer substrates (10 kPa) or neuronal cells in softer ones (1kPa)¹¹⁹.

However, it is challenging for the scaffold to keep its shape and durability for long-term culture when the values are so low. As a compromise, stiffness from 0.1 to 10 kPa is considered the suitable range for a neuronal model¹²⁰.

4.1.4. Electrical conductivity

Electroconductivity is essential for the communication and survival of neuronal cells. Neural cells communicate through electrical signaling and the monitorization of electroconductivity is a measure of the formation and maturation of neural networks. The electrophysiological behavior of the cells can be measured by patch clamp recordings, optogenetics, calcium imaging, or microelectrode arrays (MEA)¹²¹. In 3D culture, calcium imaging is used to monitor the voltage-gated calcium channel (VGCC) functionality by detecting the changes in intracellular calcium levels. The VGCC functionality can differ from 2D to 3D. Lai *et al.* assessed this difference, comparing 2D cultures of primary neuronal cells from mice with superior cervical ganglion to 3D cultures and freshly dissected superior cervical ganglion tissue. The results showed that 3D cultures and freshly dissected ones had a similar calcium increase while 2D cultures demonstrated an exaggerated increase, making 3D culture more physiologically relevant¹²². In other studies, electrically conductive polymers such as polyaniline or carbon and nanotubes can be added to the scaffold to promote conductivity and/or neural regeneration¹²³⁻¹²⁶.

4.1.5. Porosity

The porosity degree and pore size affect the mechanical properties of the scaffold, such as the degradation rate, and biological processes like cell infiltration. The porosity should be appropriate for the size of the adult stem cell (around 20 μm). Pores with a small size support stem cell adhesion and the formation of the local niche but can reduce the velocity of penetration of morphogenetic factors that influence cell culture and differentiation. Bigger pores allow a faster nutrient and oxygen diffusion but can result in a lower mechanical integrity^{96,127}.

The porosity of the biomaterial also relates to the swelling rate. The swelling rate is a measurement of the increasing weight of the sample when in contact with water, indirectly measuring the water intake⁹⁶. This measurement is of big importance to assess if the material would allow a sufficient medium intake, necessary for the nutrition and differentiation of neuronal cells. However, when the pores of the material are composed of thick walls, the increase in swelling could lead to an increase in the thickness of these walls, which in consequence would lead to a decreased size of the pores¹²⁸. It is then important to ensure the scaffold has a porosity appropriate for cell migration without compromising its mechanical integrity¹²⁹.

4.1.6. Degradability

As mentioned before, a scaffold should keep its integrity long enough for cells to reorganize and start producing their own ECM to replace it¹⁰⁰. The degradation of biomaterials is usually defined as the breakdown of the material into smaller when in contact with a biological environment. During degradation, the scaffold loses its mechanical strength and is usually accompanied by a decrease in the pH of the medium caused by the by-products of the degradation which compromise cell viability¹³⁰. This factor explains why the frequency of culture medium replacement influences the degradation, with cultures with fluid flow presenting lower rates of degradation¹³¹. The porosity, swelling rate, and chemical composition also influence the degradation. Higher porosity decreases the rate of degradation but pores with thicker walls have a higher rate due to the autocatalysis related to hydrolysis¹³¹.

The influence of stiffnesses and degradability of hydrogels on neuronal progenitor cells (NPC) stemness was accessed by Madl *et al.* They produced hydrogels composed of elastin-like proteins with RGD bioactive domains with different stiffnesses and degradability. Surprisingly, the maintenance of stemness was dependent on the degradability and not the stiffness of the substrate¹³². Later, Madl also reported that proteolytically degradable hydrogels culture with NPC induced the differentiation to lineage-specific cells expressing neuronal and astrocytic markers allowing the maturation to neurotransmitter-responsive neurons when the matrix degradation occurred before differentiation in opposite with stiffer matrixes or degradation occurring later on¹³³.

4.2. Biomaterials used in 3D brain models:

4.2.1. Hydrogels

Hydrogels are the most used biomaterial type used in neuronal scaffold culture¹³⁴. They are described as polymeric networks created through chemical and physical crosslinking with high water content and permeability¹³⁵. Hydrogels are biocompatible and flexible in their physical characteristics and composition which allows them to be used in several applications such as cell culture, cell therapy, and drug delivery^{136,137}. They can be tuned to encompass biochemical and biophysical cues to promote dynamic interaction between cells and their environment¹³⁸. In neuronal culture, hydrogels have been developed to incorporate the mechanical, architectural, and biochemical cues present in the brain, and different mechanisms are used to create the appropriate soft scaffolds needed¹³⁴. Hydrogels can be classified as natural, synthetic, or hybrid based on the origin of the material.

4.2.1.1. Natural polymers

Natural polymers are obtained from plants or animals and incorporate in their composition molecules present in native ECM, as well as the products of its degradation. Usually, the most used natural polymers are polysaccharides that when in an aqueous solution, can reversibly transition from solid to gel through external stimuli such as chemical crosslinking or temperature, forming hydrogels⁸². Gelatin¹³⁹, alginate¹⁴⁰, collagen^{141,142}, hyaluronic acid^{16,143}, Matrigel⁸¹, silk¹⁴⁴, or cellulose¹⁴⁵ are some examples of naturally sourced polymers. Since these materials englobe ECM molecules, they are generally biocompatible, biodegradable, and bioactive, with binding sites that allow the interaction between cells and their environment¹⁴⁶.

However, these materials are difficult to purify and sterilize, processes which can even denaturant the proteins present in this material¹⁴⁷. In consequence, there is less control over their physical and chemical properties as well as their degradation rates, when compared with synthetic biomaterials, presenting differences from batch to batch. Nevertheless, a combination of different materials can be helpful to achieve the desired scaffold¹⁴⁸.

4.2.1.1.1. Collagen

Collagen is one of the most commonly found proteins in the mammalian tissue ECM, comprising an overall 25% of the protein content, with desirable properties like biocompatibility, biodegradability, and cell adhesion¹³⁷. Contrary to other tissues, the most common variable form of collagen in the brain is collagen IV¹⁴⁹.

In vitro, collagen scaffolds triggered neurotrophic factors such as BDNF and GDNF when implemented after brain trauma. Huang *et al.* also reported a functional recovery after the implementation of the scaffold¹⁵⁰. Cairns *et al.* developed a 3D brain model using a doughnut-shaped silk protein sponge infused with collagen to mimic the white and grey areas of the brain (Figure 3A). Within it, they cultured human-induced neural stem cells, differentiated by direct reprogramming. They used a herpes simplex virus type 1 and could replicate several hallmarks of Alzheimer's disease, such as A β plaque formation, neuroinflammation and neuronal loss in the model.¹⁵¹ Führmann *et al.* used collagen type-I for a nerve regeneration model where 2D and 3D architecture were tested for the axon growth-promoting the effects of human neural progenitor-derived astrocytes found in dorsal root ganglion axon regeneration. The results showed greater axon regeneration on 3D culture when compared to laminin-coated substrate that acted as a positive control. The 3D scaffolds where hNP-astrocytes were seeded with dorsal root ganglion explants showed greater axon regeneration than those without astrocytes. The porosity and topography of the scaffold also contributed to better communication with the astrocytes and the Schwann cells/fibroblast that migrated from the explant¹⁵².

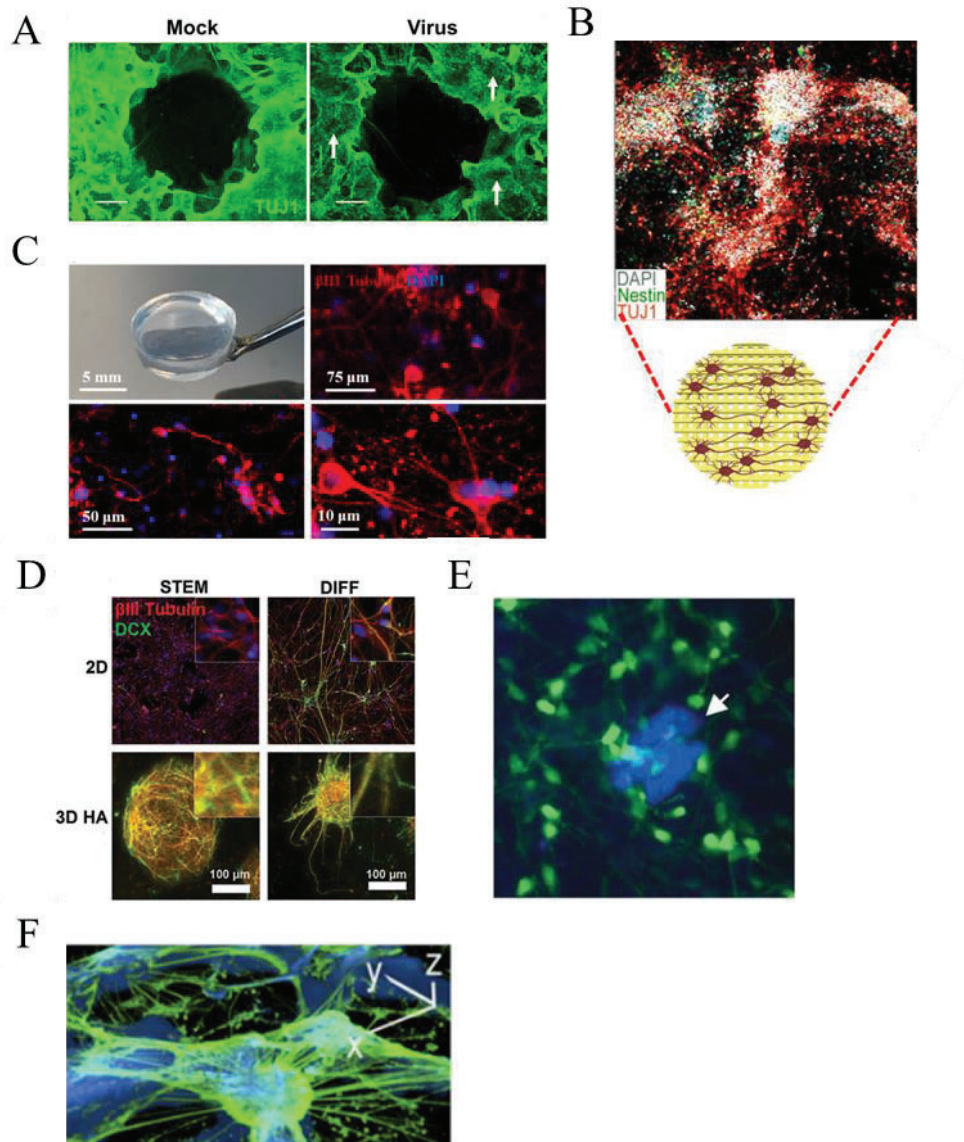


Figure 3 Examples of scaffolds produced of natural polymers (collagen, gelatin, alginate, hyaluronic acid, Matrigel and silk) for 3D neural culture. (A) Immunostaining of doughnut-shaped silk protein sponge infused with collagen where seeded cells were infected with mock or herpes simplex virus type 1. The arrows point to the areas where the neuronal loss is visible by the decrease in TUJ-1 (green) expression. Adapted from ¹⁵¹. (B) Scaffold comprised of gelatin methacrylate functionalized with dopamine where the neural differentiation, assessed through immunocytochemical stain, demonstrated the differentiation of neural cells by the expression of TUJ-1 (red) at day 12 of culture. Adapted with permission from ¹⁵³. (C) Immunofluorescence images of β -III tubulin (red) expression at day 10 in neurons encapsulated in blended alginate/collagen hydrogel. Adapted with permission from ¹⁵⁴. (D) Immunofluorescence images of the expression of β -III tubulin (red) and doublecortin (DCX, green) of NP cells cultured in 2D and HA-based hydrogels. DCX expression is apparently higher after the differentiation protocol (DIFF) and in 3D culture. Adapted with permission from ¹⁵⁵. (E) Immunofluorescence image of amyloid- β deposits (blue) in familial AD ReN cells (GFP stained in green) cultured in 3D Matrigel scaffolds. Arrow points to extracellular amyloid- β deposits. Adapted with permission from ⁸¹. (F) Fluorescent image of neurons (green) cultured in silk scaffold infused with collagen (blue). Adapted from ¹⁵⁶.

4.2.1.1.2. Gelatin

Gelatin is a hydrolysate of collagen with lower immunogenicity, which is biocompatible, biodegradable, and with natural RGD sequences that aid cell attachment^{157,158}. In addition, it has matrix metalloproteinase (MMP) sequences which allow cell mobility and remodelling¹⁵⁹. Gelatin is thermosensitive and can degrade relatively fast. To gain control over the polymer, gelatin is usually crosslinked chemically (using glutaraldehyde, carbodiimide, dextran dialdehyde, or formaldehyde for example) or physically with methacrylic groups that interact with a photoinitiator activated by UV light¹⁶⁰⁻¹⁶³. Gelatin is widely used in scaffold-based models because of its variable mechanical properties, such as pore size and stiffness, that can be adapted to encapsulate neuronal cells^{62,137}. Zhou *et al.* developed a scaffold for the differentiation of injured nerves using gelatin methacryloyl in combination with dopamine (GelMA-DA) with mouse-derived NPC (Figure 3B). The results showed a porous and interconnected scaffold, helpful for the growth of NPCs. The differentiation of the cells was validated by the increase in TUJ1 and MAP2 expression while Nestin was downregulated. When compared with single stem cell transplants, NPCs showed a significant improvement in their differentiation¹⁵³.

4.2.1.1.3. Alginate

Alginate is a polysaccharide found in seaweed, biocompatible and non-immunogenic. However, alginate is bioinert and has low bioadhesivity, and can be difficult to purify¹⁶⁴. Alginate is an interesting polymer to use for hydrogel production for its capacity to retain water. The mechanical properties of alginate, such as stiffness or porosity, are tunable by changing its concentration or conjugation with different ligands or materials. This can be beneficial to adapt the hydrogel according to the properties of the extracellular matrix needed^{165,166}.

Alginate is widely used in neural tissue engineering models^{167,168}. Wen *et al.* used a functionalized alginate hydrogel to encapsulate and differentiate NPCs to oligodendrocytes. The system was able to replicate the difference between human and mouse NPCs on the timeline of oligodendrocyte development⁶². Moxon *et al.* also used alginate in combination with collagen to create a tuneable biomaterial for 3D neuronal culture (Figure 3C). The results showed successful incorporation of the fibrils on the scaffold structure as well as adherent human iPSC-derived neurons capable of creating complex neural networks. The gene expression of the cells was also influenced by the mechanical tuning of the hydrogel stiffness¹⁵⁴.

4.2.1.1.4. Hyaluronic Acid

HA is one of the most present polysaccharides in the brain capable of regulating cell adhesion, migration, and differentiation¹¹³. It is non-immunogenic with good biocompatibility and biodegradability. HA has a high molecular weight and high ability to absorb water, which contributes to the maintenance of the mechanical integrity, viscoelasticity, homeostasis, and lubrication of the tissues¹⁶⁹. By itself, hyaluronic acid has poor mechanical strength, but it can be functionalized or mixed with other materials to be used as scaffolds^{134,169–171}.

Hong *et al.* developed hyaluronic acid catechol biopolymers with both adhesive and cohesive properties depending on pH that also proved to be stable and compatible with neural stem cell culture. These properties make this biopolymer interesting for cell culture of these cells and the incorporation of those within gels¹⁷². Zhang *et al.* created a model to compare the maturation and differentiation of human iPSC-derived neuron progenitors from both healthy donors and Rett syndrome patients. In this case, the scaffolds were composed of methacrylate-modified hyaluronic acid. This combination accelerated the maturation and differentiation of the healthy cells while MeCP2-mutant cells were defective on migration, having a slower differentiation rate with defective neurite outgrowth and synaptogenesis¹⁷³. Seidlits *et al.* studied the effect of laminin-derived adhesion peptides added to HA-based hydrogels on the survival, proliferation and differentiation of neural stem and pluripotent cells (Figure 3D). Results showed that cells increased their differentiation towards neurons and oligodendrocytes over 3D cultures¹⁵⁵.

4.2.1.1.5. Matrigel

One of the natural materials most used in neuronal culture is Matrigel. Matrigel is a material extracted from a mouse sarcoma and it is filled with extracellular matrix proteins such as laminin, collagen, and growth factors. It also contains binding molecules (such as entactin) that allow the formation of a gel with this material¹⁷⁴.

Matrigel is used as a coating where human neural progenitor cells had a higher survival rate when differentiating into neurons¹⁷⁴. Cells cultured in a Matrigel substrate show complex cellular behavior that was not easily observed in 2D cultures. Kim *et al.* utilized Matrigel as a 3D scaffold for the culture of human-derived neurons expressing familial AD mutations. This model could reproduce not only the aggregation of amyloid- β but also the accumulation of hyperphosphorylated tau characteristic of the disease (Figure 3E)⁸¹. Miguel *et al.* also used Matrigel in the form of capsules coated with alginate for modeling tauopathies. The results

identified the switch in Tau splicing along the differentiation of iPSC-derived neurons as well as proved the iPSC-induced neurons able to differentiate into cortical neurons within the capsules¹⁷⁵.

Nevertheless, Matrigel presents drawbacks in batch-to-batch variability and low mechanical strength that limit its application in scaffold-based models⁸².

4.2.1.1.6. Silk

Silk is an interesting polymer to use in scaffold-based models, especially for long-term cultures. Silk protein scaffolds are biocompatible with robust mechanical properties and malleable porosity. The structure and pores of silk scaffolds can be maintained for several months because of the slow proteolytic degradation of the silk¹⁷⁶. Tang-Schomer *et al.* cultured primary rat cortical neurons with a silk-collagen scaffold that showed to produce a functional brain-like cortical tissue. This composite material created a compartmentalized scaffold capable of spatial separation between neuronal cell bodies and their projections, similar to the cerebral cortex structure (Figure 3F)¹⁵⁶.

4.2.1.2. Synthetic polymers

Synthetic materials are more easily tunable when it comes to their physical and chemical properties since their exact composition is known and can be adjusted. The mechanical properties and degradation rate, for example, can be controlled by changing parameters such as molecular weight or crosslinking level. This ability makes these materials much more reproducible when compared to natural polymers⁹². However, synthetic materials do not possess biomolecules such as adhesion ligands limiting the interaction between cells and scaffolds. An easy solution for this downside is to undergo biochemical modifications in the materials to insert biomolecules such as growth factors or adhesion molecules to create a scaffold more similar to the ECM. An important aspect to take into account is that synthetic materials are to make sure the products of their degradation do not become toxic for the cells⁹². Some examples of synthetic polymers are polyethylene glycol¹⁷⁷, poly 2-hydroxyethyl methacrylate¹⁷⁸, or RADA-16¹⁰¹.

4.2.1.2.1. Polyethylene glycol (PEG)

PEG is a polymer used in the fabrication of scaffold models and medical and pharmaceutical products. It is non-toxic and adheres poorly to proteins and cells. PEG is water soluble and usually mixed with poly(ethylene glycol) diacrylate (PEGDA) or methacrylate (PEGMA)¹⁷⁹. Crowe *et al.* used polyethylene glycol diacrylate with Irgacure 2959 (PEG2959) and Dental LT

Clear (DClear) as suitable biomaterials using a two-photon polymerization technique to create a scaffold for neural culture. This scaffold was biocompatible with the network development of these cells, facilitating observation using imaging techniques. The results showed a scaffold that supported the growth, differentiation, and alignment of the cells while being capable of optical access to the individual cells¹⁸⁰.

4.2.1.2.2. Polycaprolactone

Polycaprolactone (PLC) is one of the most used synthetic polymers in tissue engineering. It is a linear aliphatic thermoplastic polymer synthesized from caprolactone with biocompatibility and mechanical properties suitable to be used as a scaffold for cell culture¹⁸¹. However, for neuronal culture, PLC alone has a low biocompatibility. The combination of PLC with other materials can overcome this drawback¹⁸². Cerrone *et al.* used electrospinning to create polyhydroxyphenylvalerate (PHPV) with PCL nanofibers to assess their influence on neurite outgrowth of human iPSC. The results showed that this conjugation of synthetic materials increased the cells' lifespan up to 2.3-fold and the neurite elongation by 3.8-fold. The migration of the cells was also increased when compared to PCL alone¹⁸³.

4.2.1.2.3. Self-assembling peptides

Self-assembling peptides (SAP) are biosynthetic materials with increasing interest in 3D cell culture as scaffolds to recreate the internal organization of the ECM¹⁸⁴. RADA 16-like SAPs are formed by natural amino acids capable of spontaneously self-assemble in physiologic conditions into antiparallel β -sheets that mimic the architecture of the ECM. In neuronal cultures, RADA 16-I have shown to induce neurite outgrowth and synapse formation, and favor the proliferation and differentiation of NSC¹⁸⁵. Cunha *et al.* RADA 16-I based self-assembly peptides combined with RGD and laminin-derived motifs, BMHP1 and BMHP2, to create a 3D scaffold for the culture of neuro stem cells. The cells were found to be viable, and proliferative and they differentiated on this scaffold¹⁸⁶.

4.2.2. *Combination of natural and synthetic polymers*

Combining natural and synthetic materials is also a possibility¹⁸⁷. Natural polymers such as gelatin can be methacrylated to become more tunable and form hydrogels with biological properties suitable for cell culture¹⁵⁹. Additionally, this process can also help the conjugation of gelatin with other polymers, natural or synthetic. Hybrid scaffolds combine the best properties of natural and synthetic polymers, being reproducible, easy manipulation of their physical and chemical properties, and with high affinity to the cells.

Cantley *et al.* showed the combination of different materials to create a 3D architecture. This structure was able to support the long-time cultures required to differentiate neurons and glia cells from human iPSC. The scaffold was a sponge of fibroin coated with polyornithine and laminin to which collagen was added to support the cell culture. After 5 days of iPSC culture, this model permitted the culture of healthy and patient-derived iPSC in a functional network of interconnected neurons and astrocytes. Stem cells derived from Alzheimer's and Parkinson's disease expressed the growth and gene similar to the native disease tissue, proving that this scaffold was useful for neurodegenerative disease modelling¹⁸⁸. Karvinen *et al.* created a scaffold adequate for neural cell culture composed of hyaluronan-polyvinyl alcohol and alginate-polyvinyl alcohol. The results proved that this scaffold was tunable, with a similar stiffness to brain tissue. This enhanced the neuronal growth of iPSC-derived neurons¹⁸⁹.

4.2.3. Decellularized scaffolds

Another type of material to be used for scaffold in cell culture is decellularized ECM. It is characterized by the intact native ECM of a tissue where cells have been removed as a way to avoid immune and inflammatory responses from the antigens present¹⁹⁰. These scaffolds maintain the ECM proteins and growth factors, creating an ideal environment for 3D cell culture¹⁹¹. DeQuach *et al.* developed a process to decellularize the porcine brain using detergents capable of keeping several isoforms of collagen, glycosaminoglycans, perlecan, and laminin to be used in neural cell culture. This material was proven to be suitable as coating of iPSC-derived neurons which expressed normal neuronal markers as well as morphology¹⁹². Sood *et al.* studied the difference between using fetal and adult decellularized brains on the differentiation and functional maturation of hiPSC. Fetal ECM brain showed the best results for the maintenance of differentiated neurons in long-term culture and with better activity. Astrocytes were also present during the second month of differentiation, proving to be less toxic for the culture. The biochemical cues of both fetal and adult decellularized brains were accessed, showing properties similar to native tissue¹⁹³.

The decellularization process can most of the time damage the mechanical properties of the ECM, which can be a disadvantage. To overcome this change, the decellularized matrix can be crosslinked or combined with other polymers¹⁹⁴.

From the several fabrication techniques such as electrospinning, freeze-drying, self-assembly, solvent casting, and 3D printing, the latest has been gaining popularity due to the advantages it brings when producing scaffolds for 3D *in vitro* models.

4.3.3D bioprinting

3D printing arises as an innovative and useful tool to produce scaffolds. It can be described as a process where thin layers are deposited in a substrate to be cured later, producing a 3D structure. Bioprinting is a type of 3D printing where cells and materials are printed together. One of the most interesting features of this approach is that it provides precise control of the deposition site of materials and cells, allowing the control of the architecture model¹⁹⁵.

There are several parameters to consider when bioprinting. Some of the most influential ones are the ink rheological properties, nozzle diameter, working temperature, and radiation^{196,197}. The shear stress applied to the cells while printing can decrease cell viability, especially if the material is rigid. Shear-thinning bioinks are preferable since they confer more protection to the cells but also allow a high-resolution printing¹⁹⁸. The nozzle diameter is important since small diameters allow a better resolution but might suffer clogging¹⁹⁹⁻²⁰¹. Temperature and radiation also have to be sufficient to allow the printing of a defined scaffold while being adequate to not harm the cells during the process^{202,203}.

Several techniques can be used in bioprinting²⁰⁴. Extrusion-based bioprinting is the most used technique since it is the one which applies less pressure, making it safer for the cells and avoiding the dispersion of them into the edge of the construct that can lead to a non-homogeneous distribution of cells (Figure 4A)¹⁹¹. Micro-extrusion-based deposition techniques are used when the material is extruded in a controlled manner, usually by pneumatic or mechanical extrusion systems, and deposited in a substrate as continuous fibers¹⁹⁵. The microfluidic extrusion is a similar technique where the bioink and the crosslinking agent meet in a microfluidic chamber before extrusion, polymerizing before the deposition which allows an easy flow when passing through the nozzle and the print of more defined structures²⁰⁵. These techniques are suitable for more viscous bioinks as well as cell densities when compared to inkjet techniques, however, they can have lower cell viability and lower resolution²⁰⁶.

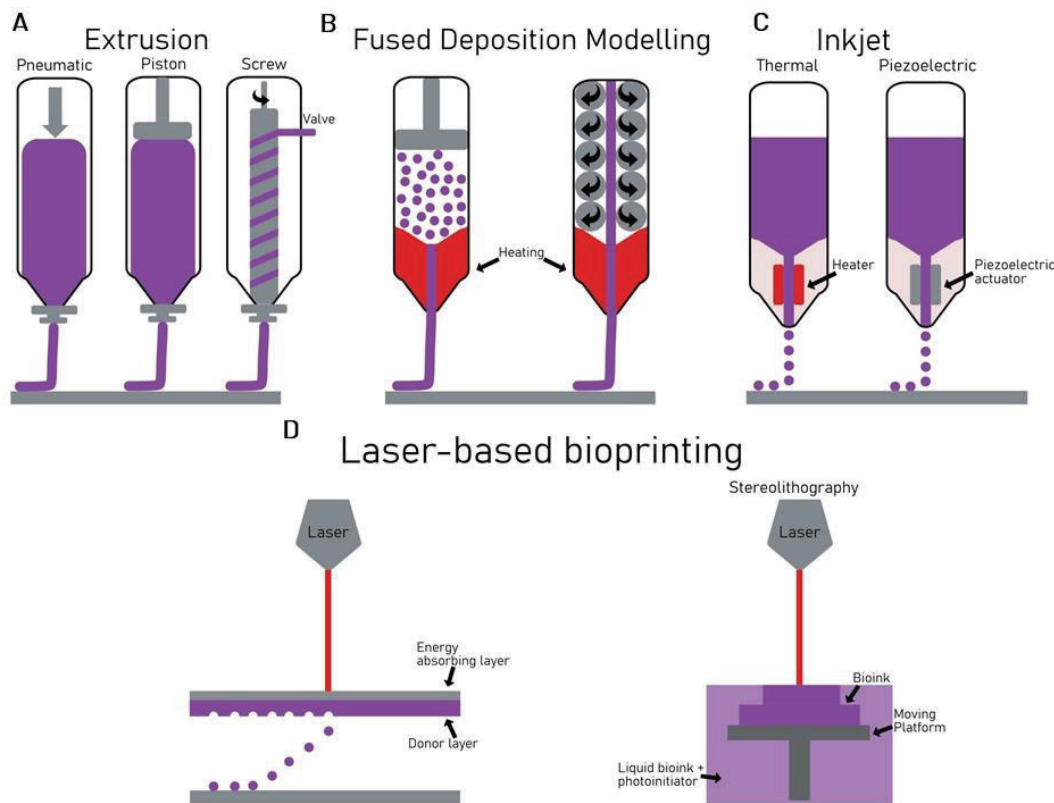


Figure 4 Bioprinting techniques. (A) Extrusion by pneumatic forces, piston, or a screw; (B) Fused deposition modeling; (C) Inkjet can be thermal or piezoelectric and (D) Laser-based bioprinting which includes stereolithography.

Fused-Deposition modeling is a technique included in the extrusion-based techniques that deposits a melted thermoplastic layer-by-layer on a substrate to build the scaffold. It is the most inexpensive technique but also the least accurate and with lower resolution (Figure 4B). Cell survival using this technique is very low since the cells do not resist the high temperatures used in the bioprinting process. Selective laser sintering is similar to fused deposition but with higher resolution. This technique uses a low-wavelength laser to fuse the beads of the premade material²⁰⁷. Inkjet bioprinting is a technique known to use forces such as thermal, acoustic, piezoelectric, or electro to eject the drops of the bioink into the substrate²⁰⁸ (Figure 4C). Its main advantages are the lower cost when compared with other techniques, high printing speeds and high spatial resolution. However, it is limited to the fact that can only print low viscosity bioinks and low cell density as the clogging of the nozzle is common. It is a technique suited for low thermal bioinks as well¹⁹⁷. Laser-based bioprinting is another technique where a laser beam is focused in an absorbing layer that propels the bioink toward the collector (Figure 4D). It is a technique able to maintain a high resolution with a medium/high speed of printing,

however, is expensive when compared to other bioprinting techniques. In addition, the laser as well as the force in which the drop is placed on the collector can cause cell death²⁰⁹. Stereolithographic bioprinting is a type of laser-based bioprinting where a scanning laser beam is used to solidify liquid photosensitive bioinks through photopolymerization. Compared with laser bioprinting, stereolithography is faster, has a higher resolution, and has a lower cost¹⁹⁷.

The gelation status of the biomaterial is important to create a defined scaffold, especially in extrusion bioprinting (Figure 5). When the material is under-gelated, the ink leaves the nozzle in drops creating undefined filaments, wider than the nozzle size, that fuse. The holes between filaments are rounder and there is no clear separation of the layers, resulting in a poorly defined structure. When the polymer is over-gelated, the filament is irregular and even though there are still square holes between filaments, the structure is fractured. With proper gelation, the filament runs fluidly and creates a connected and uniform scaffold, with the width of the filaments the same or very similar to the nozzle size. The layers of the scaffold are also clear, with square holes with defined edges²¹⁰.

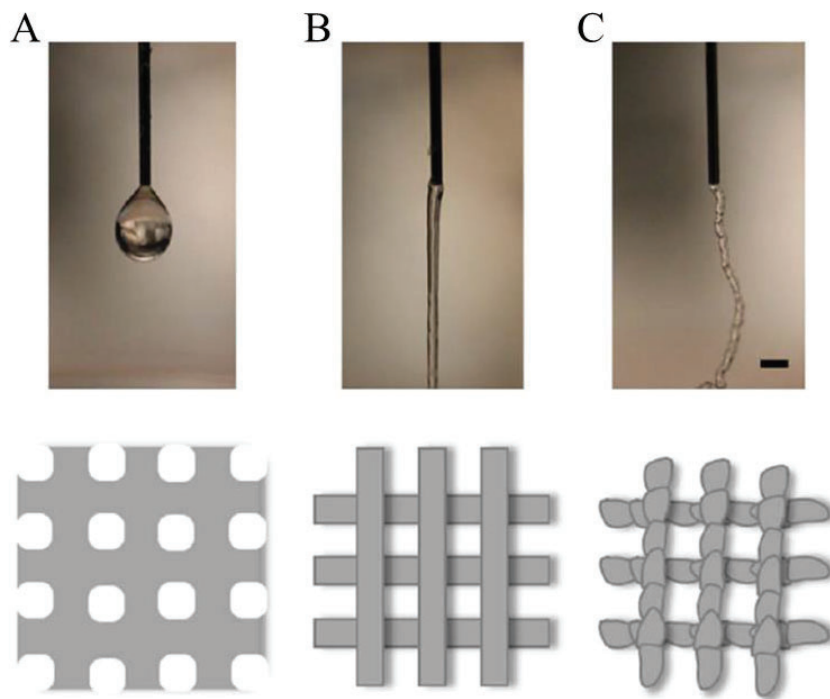


Figure 5 Different types of typical gelation status: (A) under-, (B) proper-, and (C) over-gelation. Scale bar 1mm. Adapted with permission from ²¹⁰.

It is important to notice that bioprinting is a procedure that allows printing multiple cell types as you can load different bioinks in independent print heads¹⁰⁰. Culturing multiple cell types is of big interest in brain models. Printing neurons together with glia cells (astrocytes and

pericytes) would produce a more accurate model. Joung *et al.* were able to create a 3D bioprinted platform that incorporates spinal neuronal progenitor cells and oligodendrocytes progenitor cells capable of a later differentiation to spinal neurons and oligodendrocytes (Figure 6A). Spinal neural progenitor cells and oligodendrocytes progenitor cell clusters were bioprinted through extrusion-based multi-material 3D bioprinting, allowing precise control over the position of these cell agglomerates and the use of different bioinks in different print heads. These oligodendrocytes were capable of myelinating the axons and providing a model for damaged central nervous system tissue²¹¹. One big advantage of printing different cell types is the possibility to print endothelial cells, thus promoting the growth of vascular networks in the model. The vasculature is essential for the tissues to get nutrients, so creating vasculature would not only be a better mimic of the *in vivo* situation but also would allow cell culturing for long-time periods²⁰⁴.

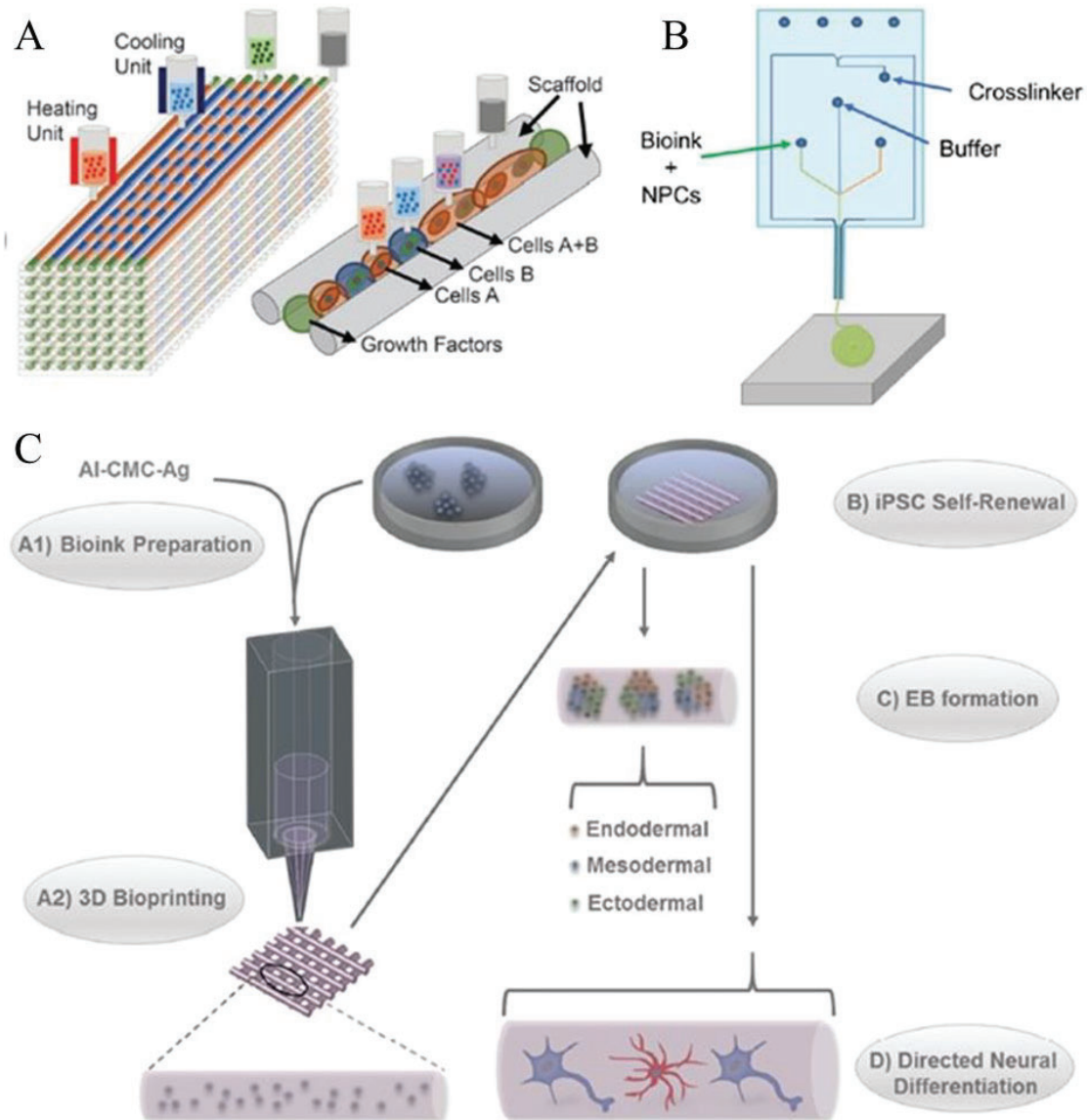


Figure 6 Examples of extrusion bioprinting using iPSC-derived cells. (A) Different cell types and hydrogels are used to replicate a spinal cord injury. Adapted with permission from ²¹¹. (B) Microfluidic extrusion technique used to quickly print iPSC-derived neuronal progenitors. Adapted with permission from ²¹². (C) Bioprinting of iPSC cells in agglomerated to form embryonic bodies and latter differentiated in several neural cell types. Adapted with permission from ²¹³.

Creating bioprinted scaffolds for neural cells is not an easy task as these cells prefer softer scaffolds. Printing materials with low elastic modulus can affect the integrity of the scaffold, not allowing the creation of a layered structure or obtaining high dimensions on 3D models¹¹⁹. Collapsing of the structures is a recurrent problem found when using this type of materials, increasing the difficulty of the construction of the scaffolds^{214,215}. De la Vega *et al.* used microfluidic extrusion to print hiPSC-derived neural progenitor cells in under 5 minutes while maintaining the viability and differentiation capacity of the cells to generate spinal cord motor

neurons (Figure 6B). This bioprinter can process the materials before printing, allowing the programming of the cell-laden bioinks patterns. Cells were cultured for a month and exposed to small molecules to evaluate their effect during the differentiation process²¹². Gu *et al.* successfully bioprinted human iPSCs with a polysaccharide-based bioink using an extrusion method. This system the proliferation and differentiation of the iPSCs into neuronal subtypes and supporting microglia (Figure 6C). This bioprinted scaffold proved to be a useful model to perform drug screening in addition to the disease models²¹³.

Although biomaterial-based models are in constant development and bring several advantages in 3D *in vitro* models, there are some limitations left to improve.

4.4. Limitation of scaffold-based culture

3D culture has certain limitations. Even though the deposition of the cells can be controlled, especially with 3D bioprinting, after the fabrication of the samples, the direction where the cells displace is uncontrollable⁸³. This unpredictability is coupled with the difficulty to monitor the culture through microscopy since the cells are not all in the same focus depth, which can cause difficulties for working with these cultures and interpreting their results^{43,216}.

The size of the culture is not as compatible with genetic and biochemical assays as 2D cultures²¹⁷. In processes such as neuronal differentiation, it is important to monitor if the differentiation process is taking place according to the protocol by assessing the expression of specific proteins and genes. In 3D cultures, there are diffusional limitations and immunostaining processes, which might need an extra amount of antibodies or incubation time to allow for the correct staining of the cells, making these protocols longer and more expensive than in 2D cultures. Another step that might be necessary to aid the visualization of 3D cultures is embedding the sample in paraffin and block sectioning followed by immunohistology staining and visualization²¹⁸. This not only adds more time to the protocol but also extra expenses. On protocols for a genetic profile evaluation, such as PCR, there is a need to lyse the cells to extract their DNA. In 2D samples, this process is also easier and quicker but in 3D, the dissociation of the sample can be difficult²¹⁹.

Cells secrete molecules throughout the culture to monitor the culture in health or response to external stimuli (such as drugs). In 2D culture, these secreted molecules can be collected during media exchanges and analyzed, without interrupting the culture. In 3D cultures, this collection might not be possible since the secreted molecules can be entrapped in the biomaterials. To access them, the sample needs to be dissociated, which requires different samples for different

timepoints²¹⁷. The main reason is that these techniques were developed taking into consideration 2D cultures. As cultures are shifting to other configurations, the evaluation techniques also need to evolve to match.

3D culture also presents more variability for the increase in factors which can contribute to different outcomes⁴⁹. Reproducibility is harder to obtain than in 2D but must be ensured to fully extract conclusions from the results. An improvement in the standardization of the protocols also needs to be made. Since this type of culture is considered recent, several groups develop their own protocol, adapted to specific type of cells. This can make the replication of protocols and comparison of results difficult, pointing the need for more standardization²¹⁹.

Another limitation of the scaffold culture is the co-culture of different cell types, such as neuronal cells and endothelial cells. Some efforts have been made using 3D bioprinting to deposit different cell types and recreate some vasculature in the model²²⁰. However, different cell types have different cell culture media to keep the typical phenotype of each type²²¹. When the cells are cultured in the same sample, the cell culture medium needs to be the same. This might entail a study to find a suitable medium that allows different cell types to survive but taking into consideration the complex composition of cell media during neuronal differentiation, it is improbable to find such conditions.

5. Focus on organ-on-a-chip models for the brain

Microfluidics can be defined as the study and manipulation of small quantities of fluid (10^{-9} to 10^{-18} L) through micro-sized channels. Microfluidic chips or devices are small platforms where channels and compartments can be fabricated with dimensions below 100 μm usually constructed with the aid of photolithography and soft lithography²²². When these devices are used as cell culture platforms to mimic organ microenvironment and function, it is called organ-on-a-chip. The small size, tunable framework, low volume requirement of reagents and cells, and control over fluid flow make these devices advantageous as *in vitro* models²²³. These devices are usually fabricated with transparent materials which make them compatible with techniques such as optical or high-resolution video microscopy allowing easier monitoring of the culture over time^{224,225}.

In neuronal cultures, microfluidic devices can have several applications. As cell sorting devices, microfluidic chips can help with the separation and sorting of neurons that later go through single-cell analysis. This contributes to the purification of the culture and identification of the genetic mechanisms that happen in the differentiation of the cells²²⁶. When using

microfluidic devices for the cell sorting process, fewer resources are used and different steps can be done simultaneously or in parallel, reducing the time of the overall process. Microfluidic devices can also be used to facilitate and automatize the differentiation process of stem cells into neural cells. Differentiation protocols follow complex steps of adding specific small molecules at specific timepoints. Microfluidic devices can allow the manipulation of different parameters simultaneously, such as the fluid flow to introduce the different cell media²²⁷.

One of the most explored applications of microfluidic models in neuronal cultures is the use of the same to create brain-on-a-chip cultures to replicate the network formation that happens in the tissue during brain development. Some of the important factors to simulate in the model are the proliferation, migration, differentiation, and functional activity of the specific types of neuronal cells.

In neuronal cultures, culturing different types of neural cells together can be challenging because the cell media is specific to the cell type. However, microfluidic devices can assist in this matter as cells can be cultured in interconnected chambers with a structure that allows the introduction of different fluids, independently or minimizing the mixing effect, and allowing each cell type receives its corresponding medium²²⁸. This allows the study of their interaction without risking the cell viability or changing the culture protocol.

5.1. Axonal guidance and/or separation

Microfluidic devices can be designed with structures as small as 1-2 μm . This small dimension is particularly helpful when culturing neural cells because it allows the separation of the cell body from its extensions (axons or dendrites). This separation is used to study axon biology and processes such the axonal growth, signal propagation, and cell-cell interaction^{229,230}. This type of study focused on the axonal response are very difficult to do in standard well-plates where the cells grow and differentiate in a bundle of cell bodies and their projections. With microfluidic devices, specific chambers are constructed and interconnected by microchannels which depending on the length, only axons can access⁸⁵. In a physically and chemically controlled environment such as this, it is possible to study the axonal response to biological cues or even the influence of other cell populations.

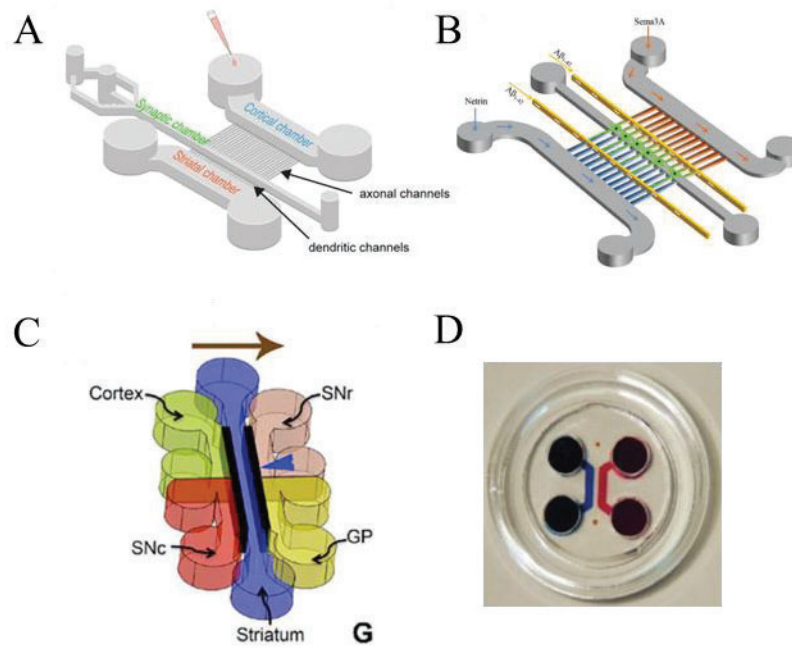


Figure 7 Microfluidic devices for axon separation and/or guidance. (A) a device with two cell chambers divided with microchannels with a synaptic chamber in between for Huntington's disease and (B) Alzheimer's disease. Adapted with permission from ^{231,232}. (C) Multichambered device for the culture of different types of neurons connected with microchannels. Adapted with permission from ⁸⁵. (D) Microfluidic-assisted axotomy device to study the regenerative ability of motor neurons after lesion. Adapted with permission from ²³³.

These devices are also used to study NDs that can affect axonal behavior. Virlogeux *et al.* used a three-compartment device connected by microchannels to recapitulate both the healthy and HD cortico-striatal network (Figure 7A). They use the chambers and channels to create a presynaptic, synaptic, and postsynaptic region. Results showed dysfunctions and hypersynchrony on the HD devices²³¹. Li *et al.* also used a three-compartment chip but this time to study the neurotoxicity of A β peptides, very characteristic of AD (Figure 7B). The authors integrated two microgrooves connected to the compartments to create a gradient of chemotactic factors. These devices allowed the demonstration of a localized mechanism on the neurotoxicity induced by A β peptides, useful for the development of Alzheimer's disease treatments²³². Kamudzandu *et al.* developed a microfluidic device to mimic the complex brain circuitry with 5 chambers connected by microchannels where different sub-types of neurons were cultured (Figure 7C). The chip proved to recapitulate the formation of an active neural network with normal cell morphology⁸⁵.

The design of the model can also help recreate the disease or injury. Sala-Jarque *et al.* developed a microfluidic device composed of two chambers separated by microchannels to mimic the neuromuscular junction on peripheral nerve injuries (Figure 7D). Motor neurons

were cultured on one side while muscle cells were on the other. A perpendicular channel between chambers and passing through all microchannels was used to vacuum-induce axotomy through air bubbles. The regenerative abilities of the neurons were accessed after optogenetic stimulation both on neurons and muscle cells. Results showed an increased axon regeneration after increasing neuronal activity as well as a release of paracrine factors by the muscle cells after stimulation, also triggering the regrowth of axons on the lesion area²³³.

Several brain-on-a-chip models use straight microchannels connecting the cell compartments. This architecture doesn't have control over the directionality of the axons and when two or more neural populations are seeded, the connectivity is bidirectional. These models are still useful for disease modeling and drug screening. However, in some brain regions, the connectivity of the cells is unidirectional, creating complex networks.

5.2. Axon's directionality

The versatility of the design of the device allows the incorporation of different techniques to achieve the unidirectional connection between cell populations. One of the techniques used is based on the cell-seeding protocol. By seeding cells with different densities, the densest population tends to occupy the microchannels first, creating a unidirectional connectivity²³⁴. Another option is to seed the cells on different days, allowing the first population to reach the microchannels first and then seeding the other population²³⁵.

Another commonly used technique to control the directionality of the connection is by using asymmetric geometries in the design of the device. By using microchannels with different width dimensions, one end smaller than the other, the direction of the connection is favored, from the wider to the narrow side. Peyrin *et al.* used a similar design and observed that the axonal growth was happening mostly unidirectionally (97% vs 3%)²³⁶. Besides the asymmetrical microchannels, other structures can be added to the small channels to facilitate unidirectionality. Gladkov *et al.* evaluated neurite growth in channels with different shapes ("spines", "triangles" and "zig-zag")²³⁷. Results showed that most axons grew in the promoted direction with a unidirectional spiking pattern on synaptic activity. The shape of the cell reservoir can also be designed to direct axonal growth. Forró *et al.* studied different geometries and reported that a stomach-shaped reservoir (one round and one sharp side) had 92% fidelity in directing axons²³⁸.

5.3. Static versus dynamic models

In microscales, the properties of fluids change when compared to the macroscale. In microfluidic devices, the flow is laminar, and the surface tension has an influence. This makes the inclusion of flow in cell culture models possible and beneficial, according to the organ and/or function, it is being modulated²²². With this possibility, the organ-on-chips have two different classifications, they can be static, when the cells and cell media are seeded and changed manually, or dynamic, where pumps are connected to the devices and the cell media can circulate automatically. Dynamic models can be used to make the culture more autonomous but also to expose the cells to shear stress that cells would be in contact with (endothelial cells in blood vessels for example), mimicking better the natural environment of the cells. It has been shown that in cell culture models, the use of dynamic cultures enhanced the expression of genes involved in cell growth, proliferation, and differentiation when compared to static cultures²³⁹.

Microfluidic devices with their architecture and perfusion can also help deliver specific molecules or drugs to study their effect in specific timepoints or a gradient manner. Gradients of chemical and mechanical cues are fundamental for cell polarization and axon direction growth. The disruption of the control over the cell processes can lead to unwanted connectivity and defective functionality, characteristic of neurological disorders²⁴⁰. Microfluidic devices can be used to generate gradients of attractant molecules to assess axon responsiveness or even guide the axonal cone growth^{241,242}. Ramamurthy *et al.* used an ultra-slow microfluidic device capable of generating continuous and overlapping chemical gradients to differentiate mouse embryonic stem cells into neuron-and Schwann cell-like cells with myelination events occurring²⁴³. Demers *et al.* developed a microfluidic platform with a gradient of chemical cues to recreate neural tube development. The study was able to mimic the neural tube patterning similar to what is observed *in vivo* with the opposing and/or orthogonal gradients recreated by the microfluidic device²⁴⁴. Uzel *et al.* designed two microfluidic devices capable of generating orthogonal gradients to study the ability of two different molecules the induction of cellular response with mouse embryonic stem cells²⁴⁵.

One of the most explored applications of dynamic models in neurobiology is blood-brain barrier models. The BBB, as mentioned before, is a crucial part of the brain vasculature defined by a tight unit that is built by not only endothelial cells but also neuronal cells such as astrocytes and pericytes²⁴⁶. Several models of BBB-on-a-chip take advantage of the architecture of the device to culture multi-cell types present in the neurovascular unit as well as include fluid flow

in the lateral channels^{228,247–251}. Sances *et al.* developed a spinal cord-chip system with iPSC-derived spinal neural progenitor cells cultured with brain microvascular endothelial cells (Figure 8A)²⁵². This co-culture model had increased neuronal activity in vascular-neural interaction genes, showing a developmental gene expression closer to what happens *in vivo*. Vatine *et al.* used a BBB-on-a-chip with co-culture of neural and endothelial cells, and perfusion which enhanced the performance of the barrier, exhibiting physiologically relevant TEER values (Figure 8B)²⁵³. The model was able to replicate the inflammatory response and transport of biomarkers. When using cells from patients, the model could detect functional differences when compared to healthy donors.

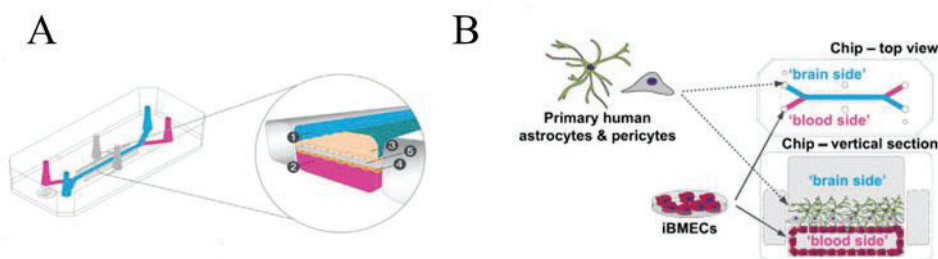


Figure 8 Blood-brain barrier-on-a-chip models. (A) and (B) combination of iPSC- derived neurons culture with endothelial cells in sandwich formation for BBB mimicking. Adapted with permission from^{252,253}.

There are a superior number of publications on static devices than on dynamic ones. This is mainly due to the difficulty in introducing fluid flow in neuronal culture and the physiology of the brain tissue itself. Cells in the brain are extremely sensitive, especially primary cultures or induced stem cells. A small movement in the seeding or maintenance of the culture can lead to a dragging and subsequent loss of the cells in the culture. In some cases, high shear stress can be used to model traumatic brain injury²⁵⁴.

5.4.3D microfluidic devices

Another common architecture of brain-on-a-chip is the parallel formation, where channels are aligned laterally to each other and separated by small pillars^{247,248,255}. This architecture is not only important for cell compartmentalization but also to include materials in the model, making it three-dimensional^{248,256–258}. Adding a biomaterial in the environment where neurons are cultured is valuable not only to better recreate the native tissue, but it is also helpful in the question of the high sensitivity of the cells to fluid flow. By adding the neural culture mixed in the middle channels, the lateral channels can be used to pass the cell culture media. The lateral channels can also be cultured with endothelial cells which are exposed to shear stress *in vivo*,

elevating the model to incorporate the BBB too. Osaki *et al.* used a 3D platform to study the interaction between microvascular and neuronal networks (Figure 9A). The design had triangular-shaped pillars separating the channels where endothelial cells were cultured from motor neuron spheroids. The co-culture showed improvement in neurite elongation and neuronal connectivity as well as an effect in the formation of the vascular network under perfusion²⁵⁵.

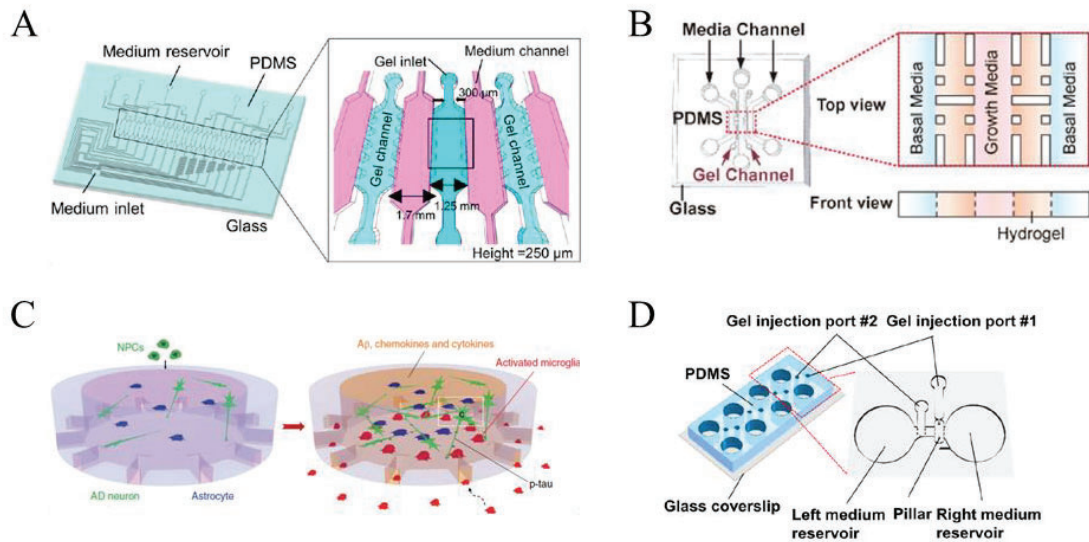


Figure 9 3D microfluidic models. (A) Multi-channel microfluidic device with channels separated by triangular-shaped pillars for the co-culture of human iPSC-derived endothelial cells and motor neuron spheroids. Adapted with permission from ²⁵⁵. (B) 3D BBB model with human endothelial cells embedded in Matrigel. Adapted with permission from ²⁵¹. (C) 3D Alzheimer model using a microfluidic platform for the tri-culture of neurons, astrocytes and microglia. Adapted with permission from ²⁵⁹. (D) Microfluidic platform for the study of amyotrophic lateral sclerosis (ALS) using i3D skeletal muscle bundles and iPSC-derived motor neurons spheroids. Adapted with permission from ²⁶⁰.

Chung *et al.* used 3 channels where brain endothelial cells were cultured on the middle one for blood-brain barrier modeling (Figure 9B). The receptor-mediated transcytosis, as well as brain endothelial-specific penetrating abilities of different peptides, were evaluated and the models were proven to use for drug development²⁵¹. Adriani *et al.* built a 3D neurovascular microfluidic model with 4 channels separated by pillars to mimic the neurovascular unit²⁴⁸. The channels were filled with medium, primary rat astrocytes embedded in the hydrogel, primary rat neurons embedded in the hydrogel, and human endothelial cells plus medium. The cells presented type-specific morphology and functional properties similar to other existing models. Lee *et al.* developed a microfluidic device of 3 channels separated with pillars where hiPSC-derived endothelial cells, primary brain pericytes, and astrocytes were cultured with a

fibrin hydrogel to quantify nanoparticle permeability. Surface-functionalized particles showed a higher permeability than non-functionalized ones. This model enabled rapid analysis of the permeability compared to Transwells models and with a more physiological relevance²⁶¹. Park *et al.* incorporated three different cell types in a 3D architecture for Alzheimer's disease modeling (Figure 9C)²⁵⁹. Neurons, astrocytes, and microglia cells derived from iPSC were chosen to recapitulate representative features of Alzheimer's disease such as beta-amyloid aggregation, neuroinflammatory activity, and phosphorylated tau accumulation.

3D culture in a microfluidic device can be achieved with the combination of biomaterials and spheroids/organoids²⁶². Neural cells in organoids present a higher resistance to shear stress and fluid flow can be easily incorporated at the embryonic body stage of differentiation, which would also be advantageous to the perfusion problem organoid culture faces^{256,263}. The combination of microfluidic devices in organoid culture is a possible solution to allow the continuous exchange of cell culture medium without the need for big reactors. The generation of organoids inside a microfluidic device also decreases the heterogeneity of organoids' size. Osaki *et al.* used a compartmentalized model to study amyotrophic lateral sclerosis by culturing iPSC-derived motor neurons from patients in the form of spheroids together with skeletal muscle bundles (Figure 9D). The results showed the neuromuscular junctions between the axons and the muscle fibers. It also demonstrated fewer muscle contractions, motor neuron degradation, and increased apoptosis of the muscle on the ALS-motor unit, compared to non-ALS device²⁶⁰. Wang *et al.* used a microfluidic platform for brain organoid culture to evaluate the effects of nicotine exposure on prenatal brain development. The device was composed of 5 channels, two here the iPSC-derived organoids were encapsulated on Matrigel and the other 3 channels for fluid flow²⁵⁶. The dimensionality of the organoids and fluid flow increased the cell viability and marker expression in comparison with the 2D culture.

5.5. Limitations of microfluidic devices

Even though brain-on-a-chip models have been explored as useful models for 2D and 3D neuronal network studies, including long-term and organoid culture, there are still some limitations to this type of culture. The complexity of the fabrication and handling of the devices in the initial stages of design and culture is important to stress. It is necessary to ensure the homogeneity of every manual replica, with special care for the small structures represented. During culture and/or perfusion, issues with bubbles, clogging of the channels, and debris can happen which influence the shear stress and culture conditions²²³. It is critical to have precise

evaluations and frequent quality checks to control the microenvironment and ensure reproducible results²⁶⁴.

Imaging during and after cell culture is an aspect that needs to be considered even before the design of the device. For example, 2D devices with microchannels are more suitable to monitor the axon's growth than 3D devices. The type of material used for the fabrication of the replicas is also important for imaging. Polydimethylsiloxane (PDMS) is often used for its biocompatibility properties and transparency, but it is known to absorb small molecules, which can influence, for example, the staining of the culture, changing the optical properties of the model²⁶⁵. Electrophysiological recordings of neural cell activity can also be challenging, depending on the design. Patch-clamp measurements, for example, need the culture to be accessible from the top, which most devices are not. Incorporating electrodes, such as MEAs, as done by Habibey et al²⁶⁶, is very useful to monitor if the network is functional and acting according to healthy or diseased circumstances. However, including MEA in 3D cultures is still challenging²⁶⁷.

6. Conclusions and Future Perspectives

The increase in the longevity of the population is accompanied with an increase of ND incidence. Traditional 2D *in vitro* and animal models are insufficient to give answers to questions about the origin of these diseases and how to better treat them. Engineering-based models arise as promising solutions for the development of more complex and reliable brain models. The inclusion of architecture clues and different cell types are some examples of the current goals in ND modelling. From the several types of 3D models, scaffold-based models and microfluidic devices are two of the most promising options. Scaffold-based models use materials such as hydrogels to culture neural cells in a 3D environment where the cells receive stimulus from all sides and can communicate between each other in a more complex network. Furthermore, 3D cultures can be constructed with techniques such as 3D bioprinting which control the deposition of the cells and the material into specific patterns or architectures. Microfabrication techniques are very useful in neural modelling since they allow the fabrication of small structure capable of separate and direct axon's growth. It also allows the co-culture of multiple cell types present in the native tissue and recreate the important circuits in health and disease scenarios.

There are still several aspects where these models can be improved in the future. 3D models need to be fitting for long-term protocols, especially since the culture and differentiation of

hiPSC can take several weeks. The compatibility of these models with imaging techniques is also a point to upgrade since most of the existent equipment was designed and optimized for 2D cultures. The perfect *in vitro* model for ND still needs to be found but we can combine the strengths of the new engineering-based models to overcome their weaknesses. One example is the inclusion of biomaterials in microfluidic devices, where we can culture cells in a 3D environment while including perfusion to facilitate the nutrient and oxygen diffusion through the system. Efforts such as this combination show we are going in the right direction to build more accurate neural models to better understand and treat NDs.

Chapter 2 – Aims of the thesis

The main objective of this thesis is to develop 3D models suitable for the culture and differentiation of neuronal cells to be used for the study of NDs. Then, we focus on the exploration of different engineered-based *in vitro* models to create functional neuronal models. Accordingly, the work is divided into two parts: the first is focused on developing a biomaterial with physical characteristics similar to the native brain ECM while being compatible with the culture, differentiation, and activity of neural cells. In addition, the biomaterial has to be used in 3D bioprinting and in 3D microfluidic devices. The second part explains the development of a microfluidic device capable to recreate the cortico-striatal and dopaminergic striatal connection. To achieve these goals, several key objectives were defined:

1. Development of a composite biomaterial with physical characteristics similar to the native brain ECM and compatible with neural culture.
2. Evaluation of the viability, differentiation, and function of the neural cells embedded in the biomaterial in long-term culture.
3. Application of the developed biomaterial as a bioink for extrusion bioprinting and the assessment of the viability, differentiation, and function of the culture after printing.
4. Evaluation of the use of the developed biomaterial in a 3D microfluidic device for neural culture.
5. Design and fabrication of a microfluidic device suitable for the culture of different types of neurons to recreate the cortico-striatal and dopaminergic-striatal circuits for HD's and PD's studies.

Chapter Three – Methodology

1. Formulation of the Polymer Precursors

Gelatin (G1890, Sigma-Aldrich, USA) was altered to achieve a theoretically methacrylation degree of 40% as previously described by Visser *et al.*²⁶⁸. Shortly, gelatin was dissolved at a concentration of 10% (w/v) in 10mM PBS (Phosphate buffered saline, P4417, Sigma-Aldrich, USA) and 1.25% (v/v) methacrylic anhydride (276685, Sigma-Aldrich, USA) was added dropwise under constant stirring. After one hour, 10 mM PBS was added to stop the reaction by diluting to 5x the solution. The solution was then dialyzed against Milli-Q water in 3.5kDa SnakeSkin membranes (ThermoFisher Scientific, USA) for three days at 40 °C. The final solution of gelatin methacryloyl was lyophilized and stored at – 20 °C. The methacrylation of sodium alginate was performed as described previously Kloxin *et al.*²⁶⁹. Briefly, sodium alginate (1% w/v) (W201502, Sigma-Aldrich, USA) was dissolved in 50 mM MES buffer at pH 6.5. Then, 20 mM EDC (N-(3-Dimethylaminopropyl)-N-ethylcarbodiimide hydrochloride) (39391, Sigma-Aldrich, USA) and 10mM N-hydroxysuccinimide (51655, Sigma-Aldrich, USA) were added to the solution. After ten minutes, 10 mM 2-Aminoethyl methacrylate hydrochloride (516155, Sigma-Aldrich, USA) was added. Succeeding an incubation of 24 h at 40 °C, acetone (131007, Panreac, Spain) was used to stop the reaction, and the solution was filtered with a vacuum flask. Milli-Q water was used to dissolve the precipitate which was then filtered. The final solution of methacrylated alginate (AlgMA) was dialyzed, lyophilized, and stored as described for gelatin methacrylation.

2. Composite Hydrogel preparation

Different formulations were produced to obtain a composition that better resemble the ECM (Table 2). GelMA was used in a range 3-5%; AlgMA in 0-1% and HA (600-01-02, 15-30 kDa, Contripo, Czech Republic) in 0-5%. A formulation with the same percentages of GelMA and AlgMA but without HA was used throughout all the work as control. The polymers were diluted in 10 mM PBS, for physical characterization, or in cell proliferation media for biological assays, overnight at 40 °C.

Table 2 Different polymer concentration tested in the optimization process.

GelMA	AlgMA	HA
3%	-	2.5%
3%	-	5%
3%	0.5%	2.5%
3%	0.5%	5%
5%	1%	-
5%	1%	1.5%
5%	1%	1.5%

Then, 0.05% of the photoinitiator lithium phenyl-2,4,6-trimethylbenzoylphosphinate (LAP) (L0290, TCI EUROPE N.V., Belgium) was added to the hydrogel. The hydrogels were then crosslinked for 5 s using a 3D bioprinter (3DDiscovery BioSafety, RegenHU; Switzerland, 365 nm, 3 W cm⁻²) with the UV light source.

3. Physical characterization

3.1. Swelling analysis

300 µl of the polymers solution was placed in a 48-well plate and exposed to UV light. The samples were then removed from the plate, weighed, and placed in a 24-well plate with 10 mM PBS. The weight was then measured at 15-min intervals for the first hour and then at 2, 4, 6, 8, 24, and 48 h. The wet weight increase ratio (ΔW) was calculated using the following equation.

$$\Delta W = \frac{W_s - W_i}{W_i} \cdot 100 \quad (1)$$

Here, W_s represents the weight after swelling, and W_i is the initial weight of the sample. The mass increase was normalized to the initial weight of the sample.

3.2. Degradation assay

For this analysis, the fabricated samples were placed in a 12-well plate with 10mM PBS for 24 h after removal from the 48-well plate. Collagenase type II (17101015, ThermoFisher, USA) was added (1.5 U mL⁻¹), and the samples were incubated at 37 °C under shaking conditions. The samples were weighed for 15 min in the first hour, and then at 2, 3, and 4 h. The percentage of the remaining sample (% W_r) was calculated using the following equation.

$$\Delta W_r = \frac{W_t}{W_i} \cdot 100 \quad (2)$$

Here, W_t represents the weight of the samples after incubation, and W_i is the initial weight.

3.3. Measurement of compression modulus

For the uniaxial compression test of the hydrogels, samples were prepared as before and transferred to a 12-well plate with 10 mM PBS. After 24 h in PBS, the samples were cut using a 10 mm diameter biopsy punch, and the diameter and height were measured with a vernier caliper (PR0192, Amidata, S.A, Spain). The samples were then tested with a Zwick Z0.5 TN instrument (Zwick-Roell, Germany) using a 5 N load cell at room temperature (RT) until 30% deformation was reached (0.1 mN of preload force and strain rate of 20% min⁻¹). The compressive modulus was determined by extracting the slope of the linear region in the interval of 10-20% deformation.

3.4. Scanning electron microscopy (SEM)

Samples were prepared as before and after 24 h in PBS, they were fixed with glutaraldehyde (2.5% diluted in 0.1 M PBS, pH 7.4, G6257, Sigma-Aldrich, USA) for 2 h. The samples were then dehydrated by immersion in graded ethanol solutions in Milli-Q water: 50% (once for 10 min); 70% (twice for 10 min); 90% (thrice for 10 min); 96% (thrice for 10 min) and 100% (trice for 10 min). The samples were then placed at the critical point dryer (Leica EM CPD300, Austria) and imaged using ultrahigh resolution scanning electron microscopy (Nova NanoSEM 230, FEI Company, Netherlands).

4. Cell cultures

4.1. Mouse neuroprogenitor C17.2 cells culture and differentiation

Mouse NPCs C17.2²⁷⁰ (kindly provided by Dr Evan Y. Snyder, Department of Neurology and Pediatrics, Harvard Medical School and Division of Neuroscience, Children's Hospital, Boston, MA) were expanded in proliferation medium [Dulbecco Modified Eagle Medium (DMEM) high glucose, L-glutamine (41965039, Gibco, ThermoFisher, USA) supplemented with 10% fetal bovine serum (10270106, ThermoFisher, USA), 5% horse serum (26050088, Gibco, ThermoFisher, USA), 1% antifungal-antimitotic solution (Gibco, ThermoFisher, USA) and 1% GlutaMAX (35050-061, Gibco, ThermoFisher, USA)].

For differentiation, medium was changed on day 1 to DMEM:F12 (11320074, Gibco, ThermoFisher, USA) supplemented with 1% N-2 supplement (17502048, Life Technologies,

ThermoFisher, USA), 1% antifungal-antimitotic solution (15240062, Gibco, ThermoFisher, USA), 10ng mL⁻¹ NGF (13290010, Life Technologies, ThermoFisher, USA) and 10ng mL⁻¹ BDNF (450-02, Peprotech Inc., USA) (Figure 10).

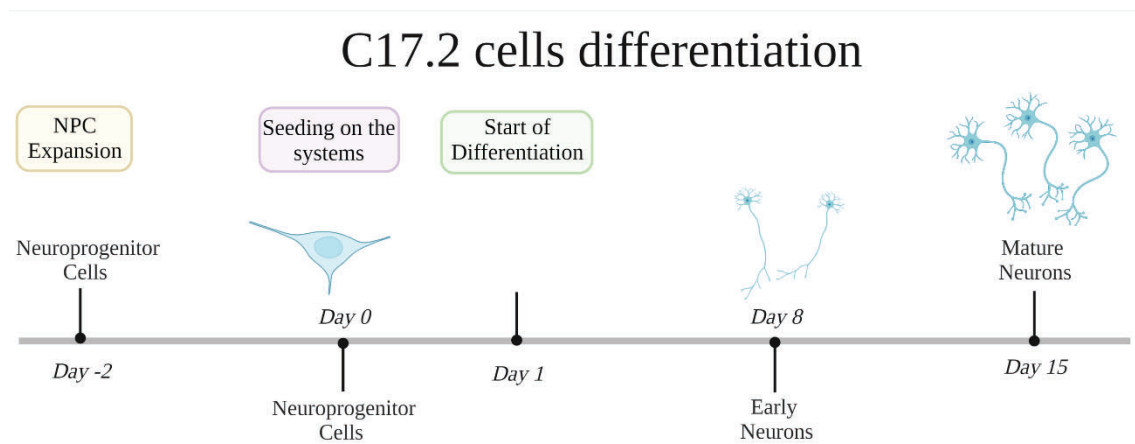


Figure 10 Schematic of C17.2 cells differentiation. Created with Biorender.com.

4.2.2D C17.2 cell culture in coverslips

For 2D culture of C17.2 cells, 12 mm coverslips placed in a 24-well plate were coated with poly-D-lysine (100 µg/ml, diluted in Milli-Q water, P6407, Sigma-Aldrich, USA) and incubated for 1 h at RT, followed by three washed with Milli-Q water. Matrigel (83.3 µg/ml, diluted in cell proliferation medium, 356237, Corning, Life Sciences, USA) was added for as a second layer of coating and left incubating for 1 h at 37 °C. C17.2 cells were then detached from the cell culture flask, counted and 80 µl drops containing 5000 cells each were placed on the coverslip and incubated for 30 min at 37 °C. Proliferation medium was then added to the wells. On the following day, the medium was replaced by differentiation medium and medium changes were performed every 2-3 days.

4.3. Dopaminergic neuron differentiation

The differentiation of dopaminergic neurons was performed in collaboration with Guochang Lyu from Ernest Arenas group, at Karolinska Institute.

iPSC cells were seeded in 6-well plates at day 1 at a density of 200,000 cells/cm² and differentiated until day 21-28 (Figure 11), following the protocol described by Nishimura *et al.*²⁷¹. Briefly, wells were coated with Geltrex (A1413201, Life Technologies, ThermoFisher, USA) and Laminin 511 (LN511, Biolamina, USA). From day 0 to day 3, cells were cultivated in Neurobasal A Medium (10888-022, Gibco, ThermoFisher, USA) supplemented with N2

(17502-048, Gibco, ThermoFisher, USA); B27 (17504-044, Gibco, ThermoFisher, USA); 2 mM L-glutamine (G8540, Sigma-Aldrich, USA), 250 nM LDN193189 (72102, Stemgent, USA), 10 μ M SB431542 (S4317, Sigma-Aldrich, USA), 2 μ M Purmorphamine (4551, Tocris Bioscience, UK) and 0.7 μ M CHIR99021(4423, Tocris Bioscience, UK). For the first 24 h, the media also contained 10 μ M Y27632 (1254, Tocris Bioscience, UK). CHIR99021 (7.5 μ M, 4423, Tocris Bioscience, UK) was administered from day 4-7. LDN, SB and Purmorphamine were withdrawn after day 7. From day 10 to day 28, cells were cultured on differentiation media: Neurobasal/B27/L-Glu media supplemented with 20 ng/mL hBDNF, 20 ng/ml hGDNF (212-GD-050/CF, R&D Systems, USA), 1 ng/ml hTGF β 3 (243-B3-010, R&D Systems, USA), 0.2 mM ascorbic acid (A4544-100G, Sigma-Aldrich, USA), 0.2 mM dibutyryl cAMP sodium salt (D0627-100MG, Sigma-Aldrich, USA), and 3 μ M CHIR99021. On days 11, cells were dissociated into single cells, re-plated at a density of 590,000 cells/cm² onto plates coated with poly-L-ornithine (P3655, Sigma-Aldrich, USA) and Laminin 511 or included in the biomaterial at a density of 5M cells/ml and treated with 10 μ M Y27632 for one day. The mDA differentiation media was supplemented with 10 mM DAPT (2634, Tocris Biosciences, UK) from day 12-28. The small molecule GW3965 (10 μ M, G6295, Sigma-Aldrich, USA) was administered from day 12 to day 15, followed by a cocktail of small molecules consisting of 1 μ M PD0325901 (PZ0162-5MG, Sigma-Aldrich, USA) and 5 μ M SU5402 (SML0443-5MG, Sigma-Aldrich, USA), from day 16 to day 21.

Dopaminergic neurons differentiation

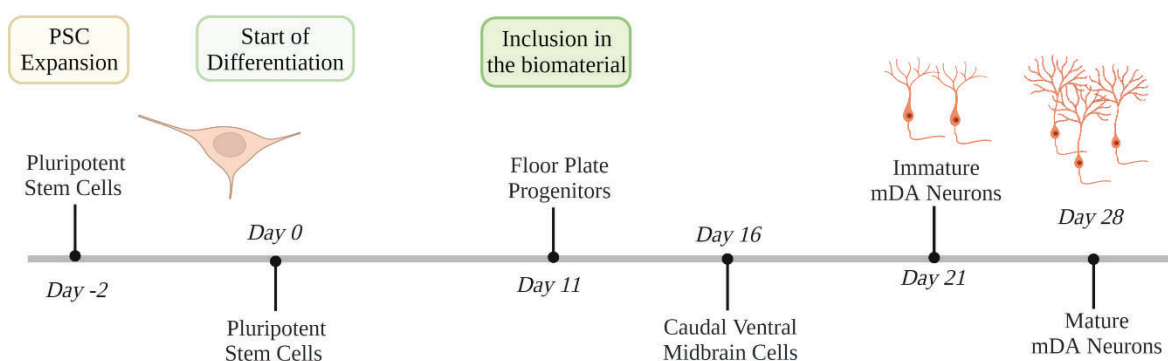


Figure 11 Schematic of the ESC-derived striatal neurons differentiation. Created with Biorender.com.

5. Sample fabrication

5.1. Inclusion of the cells in the hydrogel as drops

The polymer precursors were dissolved overnight in proliferation media and on the next day, C17.2 cells were mixed with the solution at a density of 1×10^6 cells/ml as well as the photoinitiator LAP. After, 30 μ l drops were plated in a 24-well plate, and each well was irradiated for 5 s using a 3D bioprinter (3DDiscovery BioSafety, RegenHU; Switzerland, 365 nm, 3 W cm^{-2}) with UV light source (Figure 12). Proliferation media was then added to the wells and replaced with differentiation media on the following day. Medium was changed every 2-3 days.

For the encapsulation of the cells in Matrigel as control, the same cell concentration was used, mixed with Matrigel cooled at $4 \text{ }^\circ\text{C}$ and plated in 30 μ l drops. The plate was then placed on the incubator for 15 min at $37 \text{ }^\circ\text{C}$. Cell proliferation media was added to each well and replaced to differentiation media on the next day (day 1). Medium was changed every 2-3 days.

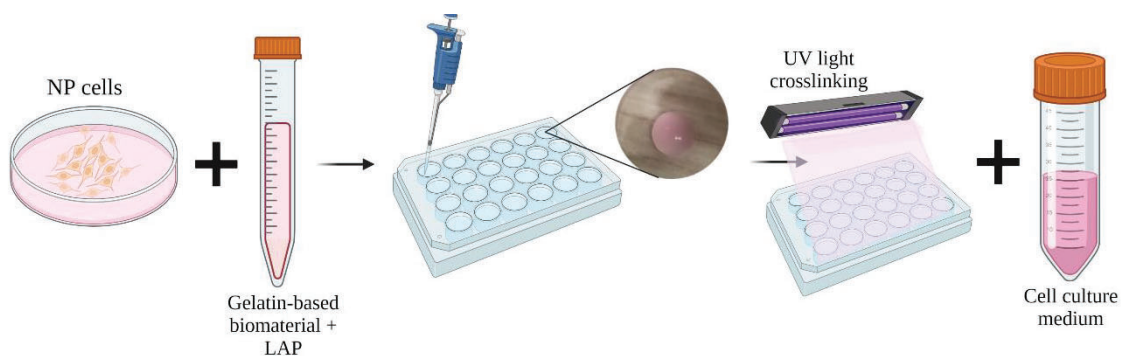


Figure 12 Inclusion of C17.2 in the hydrogel in drop-shape samples. Created with BioRender.com.

Consistent drop shaped samples were prepared using iPSC-derived cells for midbrain dopaminergic neuron differentiation (EIPSC cells) instead of C17.2 cells. In this case, the medium used to dissolve the polymers was the base medium (Neurobasal media supplemented with B27 and L-glutamine) or day 11 (D11) complete differentiation medium (Neurobasal media supplemented with B27, L-glutamine, hBDNF, hGDNF, hTGF β 3, ascorbic acid and dibutyl cAMP sodium salt). The cells were embedded in the hydrogel at day 11 of differentiation at a density of 5×10^6 cells/ml. The culture was kept until day 28 of differentiation, 17 days after inclusion in the hydrogel (Figure 13).

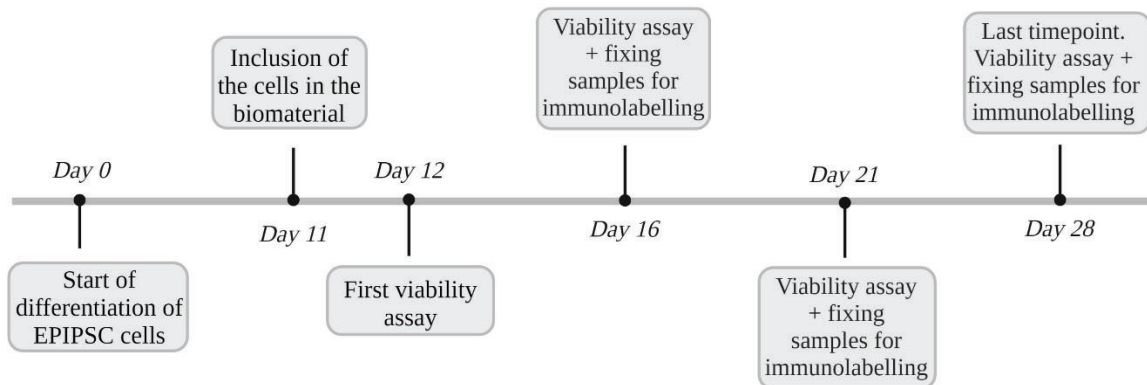


Figure 13 Timeline of the experiments performed with EPIPC cells embedded in the hydrogel. Cells were included in the 3D culture on day 11 of differentiation and evaluated at day 12, 16, 21 and 28. Created with BioRender.com.

5.2. Bioink preparation and extrusion bioprinting parameters

After overnight dissolution in cell proliferation media, the polymers were mixed with C17.2 cells at 1×10^6 cells mL⁻¹ and the photoinitiator LAP. The bioinks were then placed in a 3-cc printing syringe (Nordson Corporation, USA) and loaded into the direct dispensing head of the bioprinter (3DDiscovery BioSafety, RegenHU Ltd.; Switzerland, 365 nm, 3 W cm⁻²) with a cooling chamber at 12 °C or 18 °C. Grid squares (10 mm) were designed with BioCAD v1.0 software (RegenHU Ltd., Switzerland) and converted to computer-aided design (CAD) files, which were opened in the 3D DISCOVERY HMI software interface (regenHU Ltd.). The bioinks were printed in two layers via a 200 µm nozzle at a rate of 30 mm s⁻¹ with 2 Pa pressure. The printing parameters were optimized by testing three different conditions as presented in Table 3.

Table 3 Conditions of optimization of printing process.

	Pressure (Pa)	Printing speed (mm/s)	Temperature (°C)
Condition 1	2	3	12
Condition 2	2	3	18
Condition 3	2	30	18

After each layer was printed, the sample was irradiated with UV light for 5 s. Cell proliferation medium was then added to the wells (Figure 14). On the next day, the medium was replaced by differentiation medium and changed every 2-3 days until day 15 of culture.

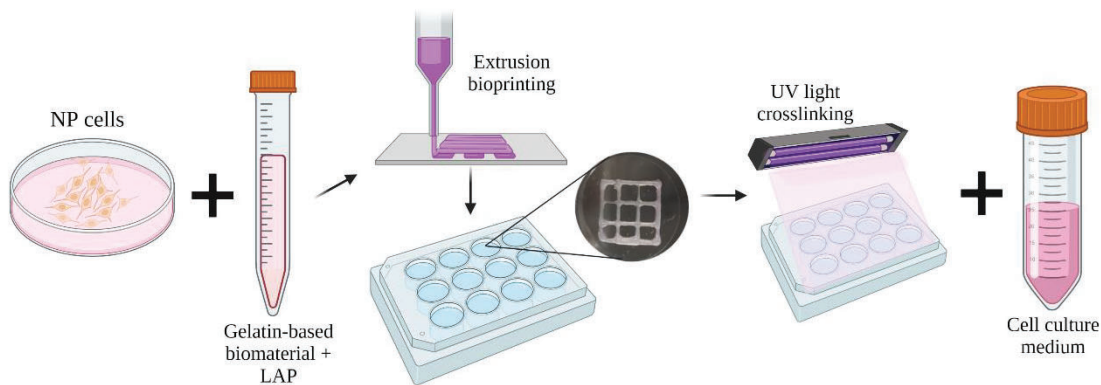


Figure 14 Schematic of the extrusion bioprinting of the gelatin-based biomaterials embedded with C17.2 cells. Created with BioRender.com.

6. Biological assays characterization

6.1. Live/Dead in 3D culture

Cell viability was assessed using a live/dead assay kit (L3324, ThermoFisher, USA) comprising of Calcein AM and Ethidium homodimer (EthD-1). After washing with 10 mM PBS, the samples were incubated with 1% v/v calcein, 1% v/v EthD-1, and 1% v/v Hoechst (H3570, Life Technologies, ThermoFisher, USA) for 20 min at 37 °C. Another three washes with PBS were then performed and the samples were examined under the confocal microscope (SP5 Leica, Austria) where fluorescence images were captured at 20×. The percentage of cell survival was calculated by counting the number of live cells using MATLAB® software.

6.2. Immunolabelling

6.2.1. C17.2 cells

The samples were fixed and stained to evaluate the expression of proteins involved in the differentiation process of C17.2 cells at different time points until day 28 of differentiation. Briefly, the samples were washed 2-3 times with PBS, fixed with 4% paraformaldehyde (P6148, Sigma-Aldrich, USA) for 15 min, and then washed an additional 2-3 times with PBS for 10 min. The samples were then permeabilized with 0.1% v/v Triton X-100 (T8787, Sigma-Aldrich, USA) and 5% v/v FBS for 2 h. Three washes with PBS containing 0.1% Triton were performed, and the samples were incubated overnight with the primary antibody solution the antibodies described in Table 4 at 4 °C under shaking conditions. The secondary antibody solution containing the fluorophore-conjugated antibodies described on Table 4 was added after three washes with PBS-Triton 0.1%. The samples were incubated overnight at 4 °C under shaking conditions protected from light. After, the samples were washed 3 times with PBS, and a 1% Hoechst (Life Technologies, ThermoFisher) was added for 15 min, followed by three washes with PBS. The samples were then observed under a confocal microscope.

Table 4 List of antibodies used for immunolabelling of C17.2 cells.

Primary Antibodies			
Target	Dilution	Reference	Supplier
Nestin	1:250	MBS500041	MyBioSource, USA
β -III tubulin (TUJ1)	1:1000	ab18207	Abcam, UK
Fluorophore-conjugated Secondary Antibodies			
Alexa Fluor 488	1:1000	10677	Invitrogen, USA
Alexa Fluor 568	1:1000	11011	Invitrogen, USA

6.2.2. EPISPC cells

In the experiments using EPISPC cells, the immunolabelling was performed 20 minutes at RT with 4% paraformaldehyde solution (P/0840/53, ThermoFisher, USA), washed three times with PBS and stored with 0.03% sodium azide (71289, Sigma- Aldrich, USA) at 4 °C. Samples were blocked and permeabilized for 45 min at RT with PBS with 0.3% Tipton X-100 (T8532, Sigma-Aldrich, USA), 0.03% sodium azide, 1% BSA (A9647- 1006, Sigma-Aldrich, USA),

5% normal goat serum (S-1000, Vector Laboratories, USA) and/or 5% donkey serum (017-000-121, Jackson Immuno Research Laboratories, USA). The samples were then incubated overnight at 4 °C with the primary antibodies described on Table 5. After an overnight incubation, the samples were washed and overnight with the secondary antibody solution described on Table 5.

Table 5 List of antibodies used for immunolabelling of EPISPC cells.

Primary Antibodies			
Target	Dilution	Reference	Supplier
MAP2	1:1000	ab92434	Abcam, UK
TH	1:1000	T292	Pel-Freeze, USA
Fluorophore-conjugated Secondary Antibodies			
AF488 Donkey α -R	1:500	711-545-152	Jackson Immuno Research Laboratories, USA
Cy5 Goat α -M	1:500	A21236	Invitrogen, USA

6.3. Real-Time Quantitative Reverse Transcription (qRT-PCR)

TRIzol™ Reagent (15596018, ThermoFisher, USA) was used to mechanically homogenize the samples at three different time points of culture (day 1, 15 and 28). RNA was extracted following the manufacturer's protocol. Briefly, chloroform (C2432, Sigma-Aldrich, USA) was used for phase separation followed by 2-propanol to precipitate RNA. The pellet was washed with ethanol and the pellet and dissolved in nuclease-free water (R0581, Sigma-Aldrich, USA). cDNA retrotranscription was performed using Ready-To-Go You-Prime First-Strand Beads (27926401, GE Healthcare, USA). Polymerase chain reaction (PCR) solutions were produced using PowerUp™ SYBR™ Green Master Mix (A25742, Applied Biosystems, USA). The genetic expression was evaluated with the StepOnePlus™ Real-Time System (Applied Biosystems, USA), and the expression was calculated with the following formula: $(\Delta C\tau \text{ GADPH} - \Delta C\tau \text{ Sample}) \times 10^4$. Mouse primer sequences used are described in Table 6 and, were extracted from the PrimerBank Database (<https://pga.mgh.harvard.edu/primerbank/>).

Table 6 Genes used in the qRT-PCR experiments.

Gene	PrimerBank ID
Nestin	15011851a1
β -III Tubulin	12963615a1
MAP2	68341934c3
GFAP	196115326c1
PAX6	346644711c1
DCX	46575787c1
S100b	6677839a1

6.4. Calcium imaging

Calcium imaging recordings were performed to assess neuronal activity in the cultures. On the day of recording, the cell medium was removed, and samples were washed with artificial cerebrospinal fluid solution (aCSF) [0.1 M HEPES (H4034, Life Technologies, ThermoFisher, USA), 128 mM NaCl (131659, Panreac, Spain), 4 mM KCl (601242, Sigma-Aldrich, USA), 10 mM glucose (G8769, Sigma-Aldrich, USA), 45 mM sucrose (107651, Merck, USA), 2 mM CaCl₂ (C3306, Sigma-Aldrich, USA) and 1 mM MgCl₂ (M8266, Sigma-Aldrich, USA) dissolved in Milli-Q water, pH7.4]. Then, the samples were placed in glass bottom chambers with a diameter of 35 mm (MatTek Corporation) and incubated with 2 ml of aCSF containing 2 μ M Fluo4-AM (F14201, Life Technologies, ThermoFisher, USA) for 15 min at 37 °C. The samples were washed again with aCSF to remove excess fluorescent dye and placed under the fluorescence microscope (Nikon Eclipse Ti2, Nikon Instruments Inc., USA). The samples were recorded for 10 min under a 20 \times objective with a frame rate of 2.2 frames per second (fps). Calcium recordings were analyzed using the custom-made software NETCAL²⁷² by which the activity traces were extracted. (Figure 15).

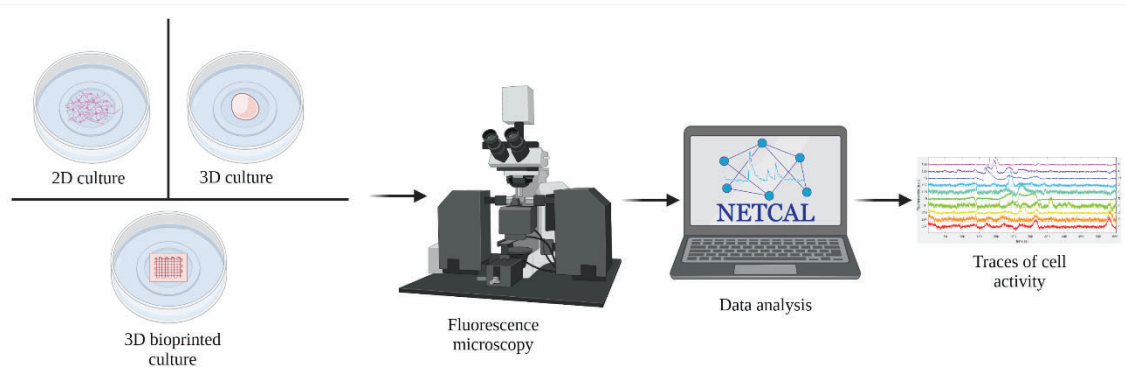


Figure 15 Process of recording and analysis of cell activity through calcium imaging. Created with BioRender.com.

For each recording, around 300 cells were either automatically or manually selected by the fluorescence signal detection. A region of interest (ROI) of a round section of 8 pixels wide was associated to each cell. For each ROI, a trace was obtained after corrected from global drifts and artifacts. After drift correction, a baseline fluorescence level (ΔF_0) and the neuronal firing was preserved, excluding the time-scale fluctuations. The fluorescence was then normalized as a function of time, $\Delta F_{(t)}$. The neurons were then divided into three groups (active, inactive or fluctuant) according to their fluorescence profiles through machine learning tools. Briefly, around 15% of the traces were manually selected, active cells presenting sharp increases in calcium oscillation (spikes); inactive cells demonstrating oscillations close to the baseline, and fluctuant cells presenting small oscillation or in both sides of the baseline. Then, the software automatically assigned the remaining traces to the three populations. The active traces were separated and exported as images. The frequency of spikes was manually counted from the exported images.

7. Microfabrication

Three different designs were created during this work using AutoCAD software. The first was done with the purpose of culturing NP cells in 3D. The designs were performed in collaboration with Ana Pascual, Dr Adrián Lopez, and Dr. Oscar Castaño of Biomaterials for Regenerative Therapies from IBEC.

The two other designs were created with the purpose of culturing human pluripotent stem cell-derived neurons while isolating the cell body from the axons. This work was performed in collaboration with Clelia Introna, Prof. Josep Canals and Dr. Daniel Tornero from Stem Cells and Regenerative Medicine Laboratory at the University of Barcelona and Guochang Lyu and Prof. Ernest Arenas from Ernest Arenas group at Karolinska Institute.

7.1.Designs

7.1.1. 3D Microfluidic devices – 3D device

For the assays performed in the 3D microfluidic device, the design chosen was similar to the previously published by Osaki *et al.*²⁵⁵. This design was composed of three channels separated by triangular-shaped pillars (Figure 16A). The central channel had a 1.2 mm inlet and outlet and measured 1.6 mm in width. The triangular-shaped pillars measured 300 μm on the base facing the lateral channel and 200 μm length while being separated from each other by 100 μm (Figure 16B). The lateral channels were in contact with the pillars for 8.1 mm length and presented 300 μm of width, with two 6 mm inlet and outlet each (Figure 16C).

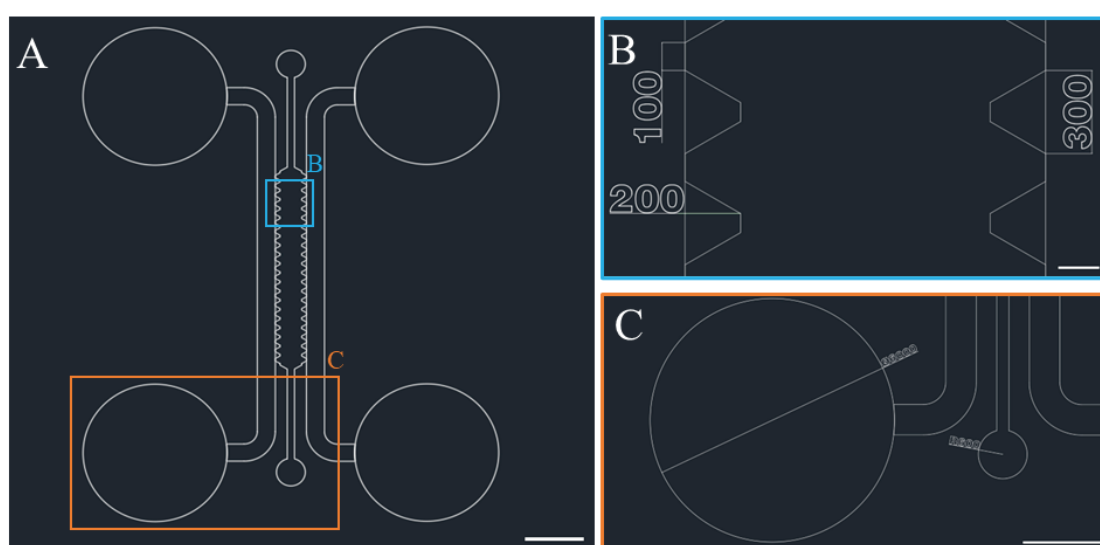


Figure 16 AutoCAD images of the 3D device. (A) Complete view of the design. Scale bar 2.5 mm. (B) Zoom section in blue of (A) where the measurement of the pillars is visible in μm . Scale bar 150 μm . (C) Zoom section in orange of (A) where the diameter of the inlets/outlets are visible (the lateral inlets/outlets measuring 6 mm of diameter and the radius of the smaller 600 μm). Scale bar 2mm.

7.1.2. 2D microfluidic design with microchannels and 2 cell chamber – 2D-2C device

This design was composed of 4 circular 12 mm chambers, two intended for cell seeding located in the center of the device and two lateral chambers as medium reservoirs, connected by 4.6 mm length channels (Figure 17A-C). The chambers and connected channels were designed to be 100 μm height but the chambers were to be manually opened later. The central chambers were connected by oblique microchannels of 1 mm length that went from 5 μm to 2 μm wide and 5 μm high, with squares placed throughout the length of the microchannel every 200 μm (Figure 17D).

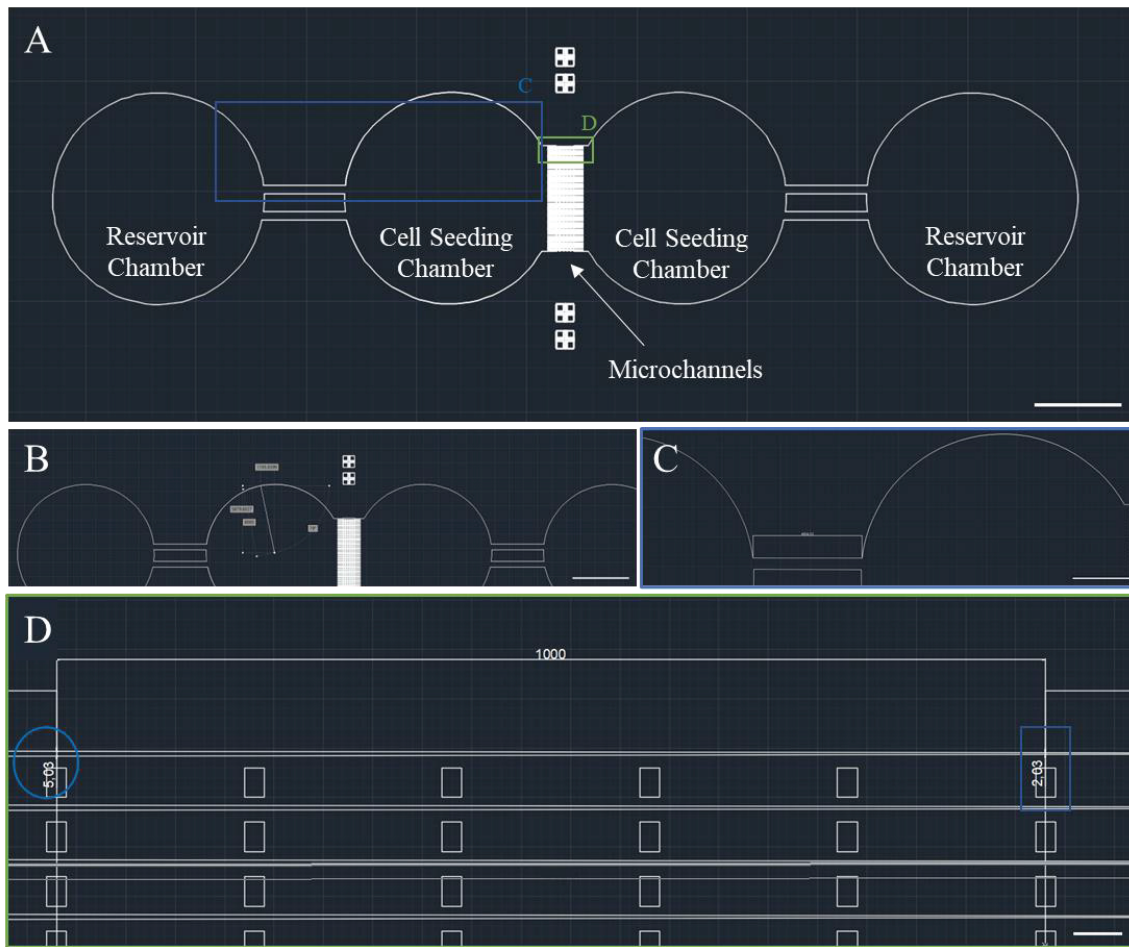


Figure 17 AutoCAD images of the compartmentalized device of the 2D-2C design. (A) The complete design. The two rectangles represent the zoomed sections C (blue) and D (green). Scale bar 5 mm. (B) A zoom of image A. The radius of the chambers is 6000 μm . Scale bar 5 mm. (C) The length of the channels between the reservoir chamber and the cell seeding chamber is around 4.6 mm. Scale bar 2.5mm. (D) the length of the microchannels from one cell seeding chamber to another is 1 mm, the width of one extremity of the channel – 5 μm (blue circle) and the other extremity – 2 μm (blue rectangle). Square marks are present with 200 μm distance along the length of the microchannels. Scale bar 50 μm .

7.1.3. 2D microfluidic device with microchannels and 3 cell channels – 2D-3C device

This design was composed of three channels, each with an inlet and outlet of 8 mm diameter (Figure 18A). The height of the channels was designed to be around 200 μm , while the inlets and outlets were to be opened manually. The channels were connected, through a length of 10 mm, by obliquous microchannels of the same dimensions as the previous design with the wider end (5 μm) on the lateral side and the narrow end (2 μm) on the central side (Figure 18B). The height of the microchannels was designed to be 5 μm .

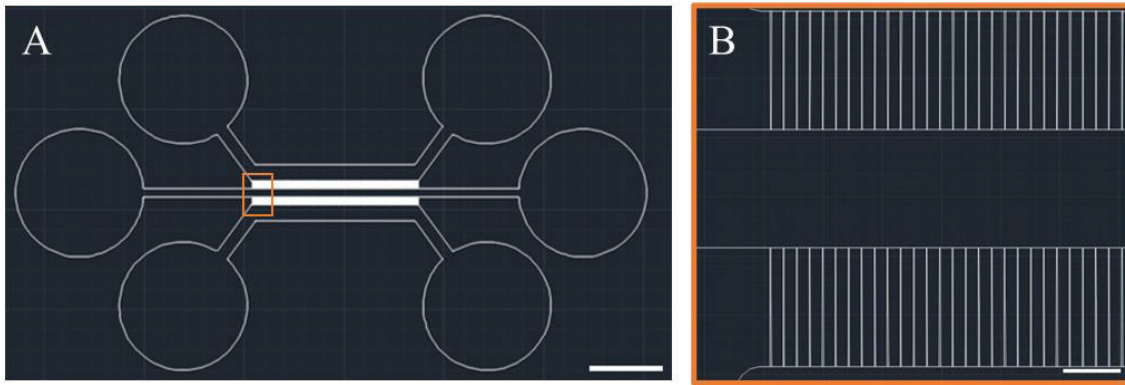


Figure 18 AutoCAD images of the 2D-3C device. (A) Three-Cell chambers device with six inlets/outlets. The side channels are 1mm in width and the middle channel 500 μm . Scale bar 5 mm. (B) Zoom image of the microchannel of image B (orange rectangle). The length of the microchannels– 500 μm , the width of one extremity of the channel – 5 μm and the other extremity – 2 μm (from side to central cell channels). Scale bar 250 μm .

7.2.SU-8 master fabrication

The master for the 3D chip was designed to have one height, around 150 μm . Since the structures were bigger than 100 μm , a high-quality acetate mask was used. For the 2D-2C master, two heights were designed, one with 5 μm for the microchannels and another for the chambers, around 100 μm . For the smaller height, a chrome mask was necessary and for the higher height, a high-quality acetate mask was used. For the 2D-3C master, the design encompasses two heights, 5 μm and 200 μm . For both heights, chrome masks were used. High-quality acetate masks were outsourced to JD Photo Data company, and chrome masks were ordered to MicroFabSpace and Microscopy Characterization Facility, Unit 7 of ICTS “NANBIOSIS” from CIBER-BBN at IBEC.

The SU-8 fabrication process (Figure 19) of all masters started with the desiccation of a 4” silicon wafer for 15 min at 200 $^{\circ}\text{C}$ followed by the activation of the surface in a PCD-002-CE Plasma Cleaner (Harrick Plasma) for 1 min at high potency.

For the 3D chip design: To fabricate a 150 μm layer, negative SU-8 3050 was poured twice. The first time, spin coated at 10 s at 500 rpm with 100 rpm of acceleration and 30 s at 1900 rpm with 300 rpm of acceleration. The wafer was soft baked for 40 min at 95 $^{\circ}\text{C}$. The second layer was poured, and spin coated at 10 s at 500 rpm with 100 rpm of acceleration and 30 s at 3000 rpm with 300 rpm of acceleration, followed by a soft bake of 40 min at 95 $^{\circ}\text{C}$.

For the 2D-2C and 2D-3C masters: An interlayer of around 10 μm was fabricated first. Negative SU-8 2010 photoresist was poured over the wafer and spin coated for 10 s at 500 rpm with 100rpm of acceleration and 120 s at 4000 rpm with 300 rpm of acceleration. The wafer

was exposed at 120 mJ/cm^2 and post-baked for 4 min at $95 \text{ }^\circ\text{C}$. For the layer of $5 \text{ }\mu\text{m}$ of height, negative SU-8 2005 photoresist was poured on the wafer and spin coated for 10 s at 500 rpm with 100 rpm of acceleration followed by 55 s at 8000 rpm with 300 rpm of acceleration. After a soft bake of 2 min at $95 \text{ }^\circ\text{C}$, the wafer was exposed at 125 mJ/cm^2 through a chrome mask with the pattern of the microchannels. Then a post bake of 2 min at $95 \text{ }^\circ\text{C}$ was performed. A layer of negative SU-8 2100 was spin coated on top of the wafer for 10 s at 500 rpm with 100 rpm of acceleration and 30 s at 3500 rpm with 300 rpm of acceleration. The wafer was soft baked for 5 min at $65 \text{ }^\circ\text{C}$ and 20 minutes at $95 \text{ }^\circ\text{C}$.

For the 2D-3C master: A second layer of SU-8 2100 was poured and spined-coated in the same conditions as before followed by a soft bake of 10 min at $65 \text{ }^\circ\text{C}$ and 40 min at $95 \text{ }^\circ\text{C}$.

The masters were exposed to 270 mJ/cm^2 through a high-quality acetate mask (in case of 3D chip and 2D-2C masters) or through a chrome mask (in case of 2D-3C master) with the motives of the channels and chambers. A post bake was then performed for 5 min at $65 \text{ }^\circ\text{C}$ and 10 min at $95 \text{ }^\circ\text{C}$, followed by a bath of 10 min in SU-8 developer to remove the excess of photoresist, and then washed with 2-propanol to stop the developer. The masters were then hard baked for 30 min at $95 \text{ }^\circ\text{C}$ and 10 min at $65 \text{ }^\circ\text{C}$. Lastly, the masters was exposed to trichloroperfluorosilane in a vacuum chamber for 1 h.

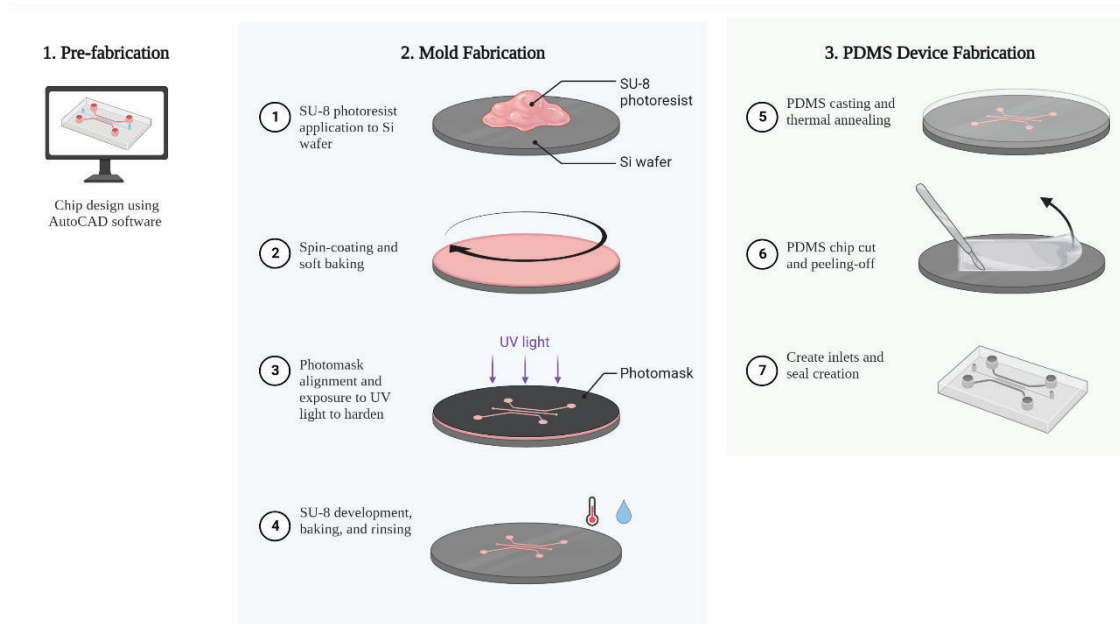


Figure 19 Step-by-step representation of the process to produce a microfluidic device. (A) Designing on AutoCAD software. (B) Fabrication of the mold in a silicon wafer through photolithography. (C) PDMS replica production of the final devices. Created by Biorender.com.

7.3. Fabrication of the PDMS replicas

Once the masters were fabricated, PDMS replicas were produced by pouring a mixture of 10:1 Sylgard 184 PDMS and curing agent onto the master (DCE-1673921, Dow Corning, USA). The PDMS was left curing at RT overnight and for 2 h at 95 °C on the following day. Then, the PDMS was cut and peeled from the master and divided into the individual devices.

Depending on the designs, different biopsy punches (Harris Uni-Core) were used to open the inlets and outlets. In the 3D devices, a 4 mm was used to open the inlet/outlet of the lateral channels and a punch of 1 mm, for the lateral channels. In the case of 2D-2C devices, a 12 mm punch was used; in 2D-3C devices, an 8 mm was used.

The PDMS replicas and thin cover glass slides (24 x 60 for the 3D devices and 26x76 for the 2D-2D and 2D-3C devices; #1.5; Menzel-Gläser) were washed with water and soap, followed by 15 min of sonication in ethanol. Then the PDMS and the slides were dried, and the surfaces were activated in the Plasma Cleaner for 30 s at 30 W with constant oxygen pressure of 80 bar. The PDMS replicas and the cover glass slides were then irreversibly bounded and placed on the hot plate at 65 °C for 15 min to guarantee the water produced in the activation is evaporated.

To change the surface charge of the 2D-2C and 2D-3C devices, each PDMS replica was activated in the Plasma Cleaner for 5 min at 11W to make the surface hydrophilic. Milli-Q water was then added to the inlets and outlets to help maintain the hydrophilicity until the devices were used in culture.

7.3.1. Diffusion test

In the 2D-3C device, a diffusion test was performed to ensure that the microchannels were opened and to evaluate if there would be diffusion of the media from the lateral channels to the central channel. After the devices were activated and kept with water, the water from the lateral channels was removed and replaced with fluorescein at 0.01 M (F6377, Sigma-Aldrich, USA; diluted in Milli-Q water). After 1 h, images were collected using a fluorescent microscope. Some samples were kept for 5 days at 4 °C, and images were collected at that timepoint.

7.4. Inclusion of the cells in the 3D microfluidic device

7.4.1. C17.2 cells

C17.2 cells (1×10^6 cells/ml) were mixed in the dissolved polymers together with LAP and 10 μ l of the mix were injected in the middle channel of the sterilized device. The device was then exposed to 5 s of UV light and proliferation media was added to the side channels (Figure 20).

On the next day the medium was changed to differentiation medium. Medium was replaced every day.

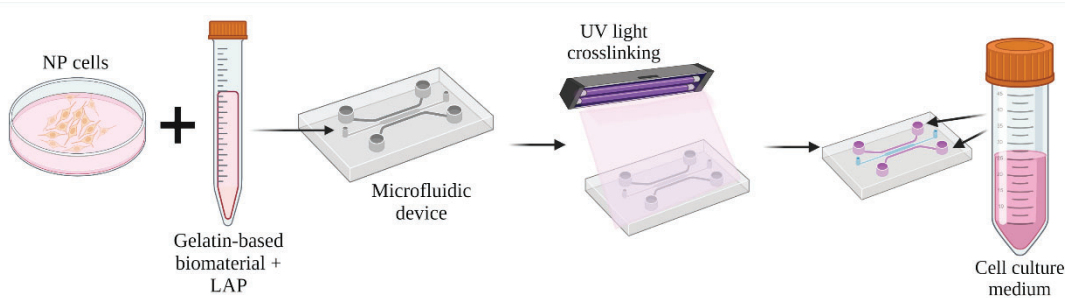


Figure 20 Schematic of the inclusion of the C17.2 cells embedded in the biomaterial inside the 3D microfluidic device. Created with BioRender.com

7.4.2. EPISPC cells

EPISPC cells were also included in the 3D device using a similar seeding protocol. Cells were harvest at day 11 of differentiation and mixed with the biomaterial and seeded at a density of 5 M cells/ml on the central channel. After UV-light exposure, cell differentiation media of day 11 was added to the lateral channels and changed every day to the corresponding differentiation media.

7.5. Biological assays:

7.5.1. Live/Dead

The viability assays were performed as described in section 6.1 with a modification in the incubation time, from 20 min to 40 min.

7.5.2. Immunolabelling

The immunofluorescence assays were performed as described in section 6.2.

8. Differentiation of cortical and striatal neurons

The differentiation of cortical and striatal neurons was performed in collaboration with Clelia Introna at Stem Cells and Regenerative Medicine Laboratory at the University of Barcelona.

8.1. Cortical neurons differentiation

Following the protocol described in Palma-Tortosa *et al.* 2020²⁷³ (Figure 21), at day 0 of differentiation, PSC-colonies were picked and planted in ultra-low attachment culture dishes to generate embryonic bodies (EBs) in presence of the EB medium [DMEM/F12 (05853,

STEMCELL Technologies, USA), 10% KnockOut Serum Replacement (10828-010, Gibco, USA), 0.1 mM 2-Mercaptoethanol (M6250, Sigma-Aldrich, USA), 0.1 Mm Non-essential amino acids (11140-050, Gibco, USA), 1 mM L-Glutamine (G8540, Sigma-Aldrich, USA)] with 10 μ M Rock inhibitor (Y-27632, Abcam, UK), 3 μ M dorsomorphin (P5499, Sigma-Aldrich, USA) and 10 μ M SB431542 (S4317, Sigma-Aldrich, USA). On day 5, EBs were collected and seeded on a 0.1 mg/ml poly-L-ornithine and 10 μ g/ml mouse laminin 111 (3400-010-02, R&D Systems, USA) coated surface for dual SMAD inhibition with 3 μ M dorsomorphin and 10 μ M SB431542. On day 6, the medium was changed to N2 medium [DMEM-F12 (without Hepses + Glutamine, 11320033, STEMCELL Technologies, USA), N-2 supplement (1:100), 1.6 g/l D-glucose (G7021, Sigma-Aldrich, USA)] supplemented with 1 μ M dorsomorphin and 10 ng/ml bFGF (F0291, Sigma-Aldrich, USA). On day 11, neuronal rosettes were carefully picked and grown in suspension in N2 medium with 20 ng/ml bFGF to generate spheroids that were collected, dissociated in small clumps with trypsin and grown in adhesion on 0.1 mg/ml poly-L-ornithine and 10 mg/ml laminin surfaces to generate the long-term neuroepithelial stem cells (It-NES). It-NES were routinely cultured in the presence of 10 ng/ml bFGF, 10 ng/ml EGF (PHG0314, Invitrogen, USA) and 1 μ g/ml B27 (17504-044, Invitrogen, USA). Cells were then passed at low density in the differentiation-defined medium in the presence of 10 ng/mL BMP4 (314-BP-010, R&D Systems, USA), 10 ng/mL Wnt3A (5036-WN-010, R&D Systems), and 1 μ M cyclopamine (C4116, Sigma-Aldrich, USA) for seven days to produce cortical progenitor cells that were harvested and seeded in the two lateral compartments of the 2D-3C microfluidic device. The cells were left in the device for an additional 28 days, with the final neural medium changed every 2-3 days. The final neural medium is composed of BrainPhys supplemented with B27 without vitamin A (1:50, 12587-010, Gibco, USA).

Cortical neurons differentiation

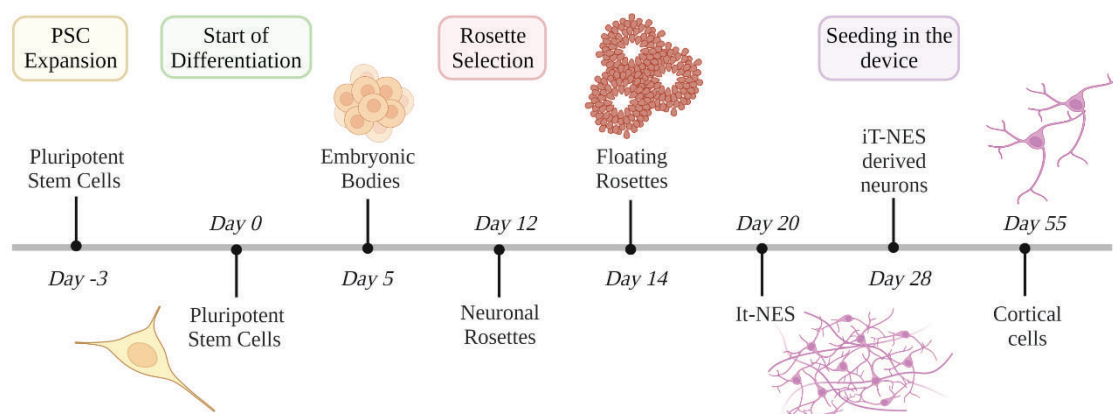


Figure 21 Schematic of the ESC-derived cortical neurons differentiation. Created with Biorender.com.

8.2. Striatal neurons differentiation

Following the published protocol described in Comella-Bolla *et al.* 2020²⁷⁴ (Figure 22), hESCs were treated with BMP/SMAD inhibitors, 1 μ M LDN 193189 (396388, EVOTEC Ltd. Milton, UK), 1.5 μ M IWR1 (476979, EVOTEC Ltd., Milton, UK) and 10 μ M SB431542 for 8 days until neuronal rosettes were obtained. At DIV8 cells were passed and plated in Matrigel-coated plates in presence of LDN and IWR1; SB was removed from the medium and the cells were left differentiating for 8 days. At day 16, telencephalic progenitors were dissociated and the resuspended in SCM1 medium and plated in the central compartment of the 2D-3C microfluidic device. SCM1 medium (At DIV 16, DIV 18 and DIV 21) contains: Advanced DMEM/F-12 (1X) (12634-010; Gibco, USA) with 2 mM of GlutaMax I 100x (35050-038, Gibco ThermoFisher, USA); 1 % penicillin-streptomycin (15140122; Life Technologies Europe BV, Netherlands); 2 % B-27 supplement (17504-044; Gibco, USA); 2 μ M PD 0332991 (482855; EVOTEC Ltd. Milton, UK); 10 μ M DAPT (396736; EVOTEC Ltd. Milton, UK); 0.6 mM CaCl₂ (to give 1.8mM final complete medium; Merck, USA), 200 μ M ascorbic acid (AA, A4544-100G, Sigma-Aldrich, USA), 10 ng/mL hBDNF; 10 μ M Forskolin (000087; EVOTEC Ltd. Milton, UK), 3 μ M CHIR 99021 (CH; 401952; EVOTEC Ltd. Milton, UK), and 300 μ M GABA (0.44; Tocris Cookson Inc., USA). On day 23, LGE neuroblast were switched to a final maturation medium SCM2 supplemented with a cocktail of differentiation factors, changed every 2-3 days, until the final day of differentiation 37. SCM2 medium (From DIV 23 to DIV 37; changed every two-three days) contains: (1:1) of Advanced D-MEM/F-12 (1X) with 2 mM of GlutaMax I 100x; Neurobasal A (10888-022; Life Technologies Europe BV, Netherlands);

1 % penicillin-streptomycin, 2% B-27 supplement; 2 μ M PD; 3 μ M CH; 0.3 mM CaCl₂; 200 μ M AA and 10 ng/mL hBDNF.

Striatal neurons differentiation

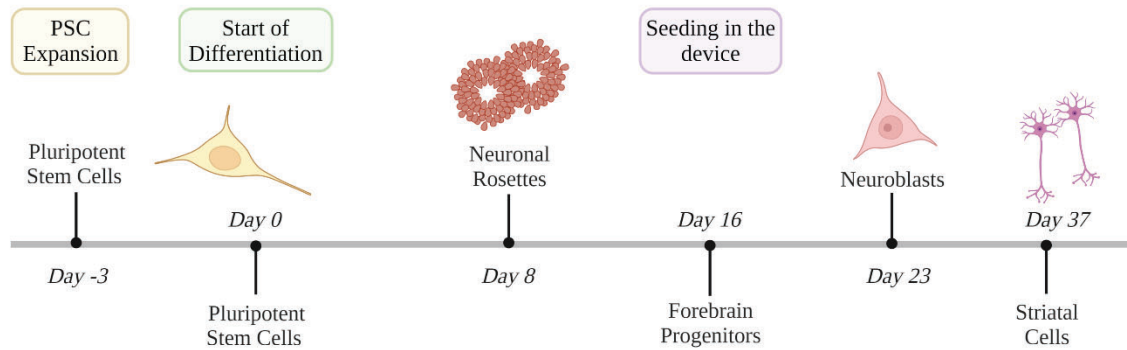


Figure 22 Schematic of the ESC-derived striatal neurons differentiation. Created with Biorender.com.

8.3. Dopaminergic neurons differentiation

In the experiments using the 2D-3C device, three iPSC lines for midbrain dopaminergic neurons were used: one derived from a healthy individual (EPISC), one from a PD patient with a GBAE326K mutation (5106) and the third was a control to the line 5106 with the corrected mutation (5108) in combination with the hESC differentiated to striatal neurons used above. The cells were differentiated as described on section 4.2 in collaboration with Ernest Arenas group.

9. Inclusion of iPSC-derived cells into the microfluidic device

After the 2D-3C microfluidic devices were produced and activated, sterilization was performed using 70% ethanol and 10-min UV light exposure on the laminar-flow hood. Then, each channel was rinsed thrice with Milli-Q water and left filled with PBS. Prior to use, the central chamber was coated with 100 μ g/ml poly-D-lysine in borate buffer, followed by three washes with PBS and coated with Matrigel. The lateral channels were coated with 0.5 μ g/ml poly-L-ornithine and maintained at RT overnight. On the next day, the lateral channels were washed three times with PBS and a solution of 10 μ g/ml of mouse laminin 111 in PBS (for cortical differentiation) or human laminin 511 in PBS (for dopaminergic differentiation) was added and incubated for at least 1 hour at 37 °C.

The NPCs were collected on day 16 for striatal and dopaminergic cells and at day 28 for the cortical cells. The cells were resuspended in 10 μ l of the differentiation media correspondent to each cell type at different cell densities and placed on the respective chambers of the device.

In the cortico-striatal 2D-3C device, cortical cells were seeded at 100.000 cells in 10 μ l in the lateral channels. The central channel of the device was coated with PDL/Matrigel supplemented with BDNF and kept empty for one week. Then, striatal cells were seeded at 100.000 cells in 10 μ l (Figure 23A). In the midbrain-striatal 2D-3C device, striatal cells were seeded at 100.000 cells in 10 μ l in the central channel while dopaminergic cells were seeded at 200.000 cells in 10 μ l in the lateral channels (Figure 23B).

In all samples, one hour after the seeding, the media of the cells was added to the left chambers (300 μ l) and then to the right ones (200 μ l). Media was changed every 2-3 days.

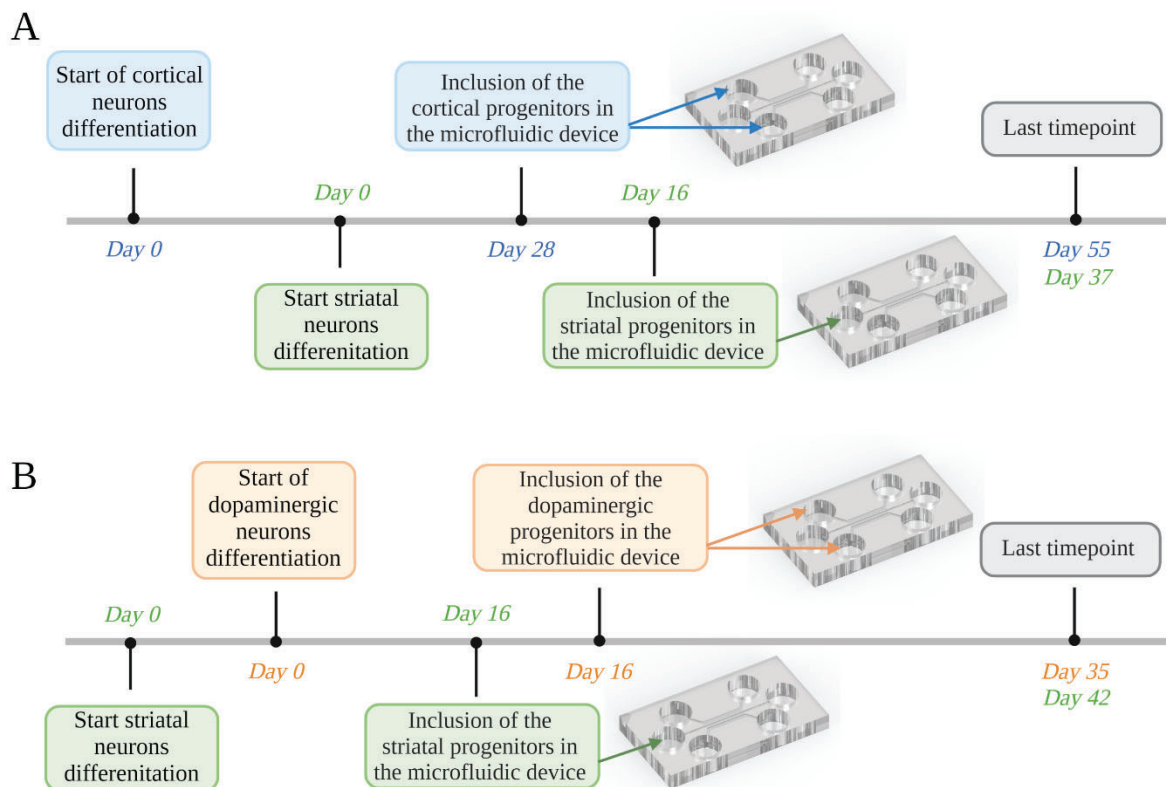


Figure 23 Timeline of the experiments with PSC-derived neurons in the 2D-3C device. (A) Co-culture of striatal and cortical neurons. Cortical progenitors were seeded at day 28 of differentiation on the lateral channels of the device. Striatal progenitors were seeded seven days later, at day 16 of differentiation, on the central channel of the device. (B) Co-culture of dopaminergic and striatal neurons. Striatal progenitors were seeded in the central channel at day 16 of their differentiation while dopaminergic progenitors were seeded seven days later, at day 16 of their differentiation on the lateral channels of the device. Created with BioRender.com.

10. Biological characterization for the cell in the 2D-3C microfluidic device

10.1. Immunolabelling

Human PSC-derived cells were fixed for 20 minutes at RT on the microfluidic device with 4% paraformaldehyde solution, washed three times with PBS and stored with 0.03% sodium azide at 4 °C. Samples were blocked and permeabilized for 45 min at RT with PBS with 0.3% Tipton X-100, 0.03% sodium azide, 1% BSA, 5% normal goat serum and/or 5% donkey serum. The samples were then incubated overnight at 4 °C with the primary antibodies described in Table 7.

Table 7 List of antibodies used for immunolabelling of cortical and striatal neurons.

Primary Antibodies			
Target	Dilution	Reference	Supplier
CTIP2 (25B6)	1:300	ab 18465	Abcam, UK
FOXP1	1:500	ab32010	Abcam, UK
GABA	1:500	A2052	Sigma-Aldrich, USA
Glutaminase (KGA)	1:300	ab156876	Abcam, UK
MAP2	1:1000	ab92434	Abcam, UK
Nestin	1:200	MAB5326	Millipore, USA
TBR1	1:500	ab31940	Abcam, UK
β -III tubulin (TUJ1)	1:500	T220	Sigma-Aldrich, USA
Fluorophore-conjugated Secondary Antibodies			
AF488 Donkey α - M	1:500	715-545-150	Jackson Immuno Research Laboratories, USA
Cy2 Donkey α -G	1:500	705-225-003	Jackson Immuno Research Laboratories, USA

Cy3 Donkey α -R	1:500	711-165-152	Jackson Immuno Research Laboratories, USA
Cy3 α -Rat	1:500	712-165-150	Jackson Immuno Research Laboratories, USA
Cy5 Goat α -M	1:500	A21236	Invitrogen, USA
FITC- α -Chicken	1:500	F10-05	Aveslab, USA
NL557- α -Chicken	1:500	NL016	R&D System, USA

After, the samples were washed three times for 10 min each with PBS. The cells were then incubated for 1-2 h at RT in darkness with the secondary antibodies described in Table 7, followed by three washes of 10 min with PBS.

10.2. Calcium imaging

The spontaneous activity of the hIPS cells was recorded on the last timepoint of differentiation (day 37 for striatal neurons and day 55 for cortical neurons). The samples were processed as described with the difference of adding 200 μ l of aCSF solution containing 2 μ M of Fluo4-AM into the chamber and washed twice for 15 min before recording the central part of the channels. Extracellular potassium chloride (KCl) was added to the lateral compartment only previous to the recording. The device was mounted on Olympus IX71 (Olympus America Inc., NY, USA) inverted microscope monitored with the Orca Flash 4.0 camera (C11440-22CU, Hamamatsu Photonics). The fluorescence source was provided by the Dual OptoLED power supply (Cairn Research Ltd., Faversham). Image sequences of neuronal activity were acquired for 10 min at RT, with a 10 \times objective with a 0.3 \times optical zoom, and a speed of 20 fps.

11. Statistical analysis

All graphs are presented with the mean and standard deviation values. Statistics analysis was performed with GraphPad using an unpaired t-test statistical analysis on the analysis of pore diameter and using a two-way variance analysis (ANOVA) with Turkey's and Sídák's post-hoc multiple comparisons test on all other analyses but only Sídák's post-hoc multiple comparisons test results were represented to simplify the visualization. P-values lower than 0.05 were considered statistically significant.

Chapter 4 - RESULTS

This chapter shows the results obtained during the experiments performed for this thesis. It is divided into two parts: the first focuses on developing a biomaterial suitable for 3D neural cultures; the second part is focused on designing a microfluidic platform for modeling Huntington's and Parkinson's disease.

The majority of the results presented in PART I are included on the published paper: "Pereira I., Lopez-Martinez M.J., Villasante A., Introna C., Tornero D., Canals J.M. and Samitier J. (2023), *Hyaluronic acid-based bioink improves the differentiation and network formation of neural progenitor cells*. *Frontiers in Bioengineering and Biotechnology* 11:1110547. doi: 10.3389/fbioe.2023.1110547"

PART I - Development of a compatible biomaterial for neuronal models

We wanted to explore the possibility of creating a biomaterial with a controllable composition that would be suitable for the culture of neuronal cells, their differentiation, and functionality. Matrigel is one of the currently commercially available materials used in 3D neuronal cultures. Even though the cells can survive and differentiate, the composition of Matrigel suffers variability from batch to batch, which impedes the standardization of differentiation protocols⁸².

From the wide range of polymers being explored in 3D modeling, we chose to work with three: gelatin, alginate, and hyaluronic acid. Gelatin is one of the most used biomaterials for its natural origin, biocompatibility and biodegradability. Alginate, also of natural origin, was included to bring support and durability to the composite material. Hyaluronic acid is one of the most common polysaccharides in the brain extracellular matrix and was chosen to bring the biomaterial a step closer to the original ECM composition of this organ.

1. Optimization of the composition

To ensure a homogenous and robust bond of gelatin with alginate, both polymers were chemically modified with methacrylic groups to allow photocrosslinking of the polymers. The formulation we wanted to evaluate would then be composed of GelMA, AlgMA and HA. However, their proportions on the final hydrogels needed to be optimized considering the

viability and behavior of the cells in the culture. We started with a range of 3 to 5% of GelMA, AlgMA from 0 to 1% and HA from 0% to 5%.

1.1. Viability assessment of the encapsulated cells

We evaluated the viability of culturing cells for all formulations described in Table 2 of Chapter Three – Methodology. The assay was performed with the C17.2 cells encapsulated and kept in culture until day 8, a time point used for the differentiation of C17.2 cells in 2D²⁷⁵. Matrigel was used as a control. Results showed the cells were able to proliferate in all conditions, increasing the cell number and spreading across the material, as seen in Figure 24. We observed that most cells were alive, for the majority of Calcein AM signal in green, surviving the inclusion in the hydrogels and 5 s UV irradiation needed for the crosslink, assuring that the fabrication process of the 3D culture was safe for the cells.

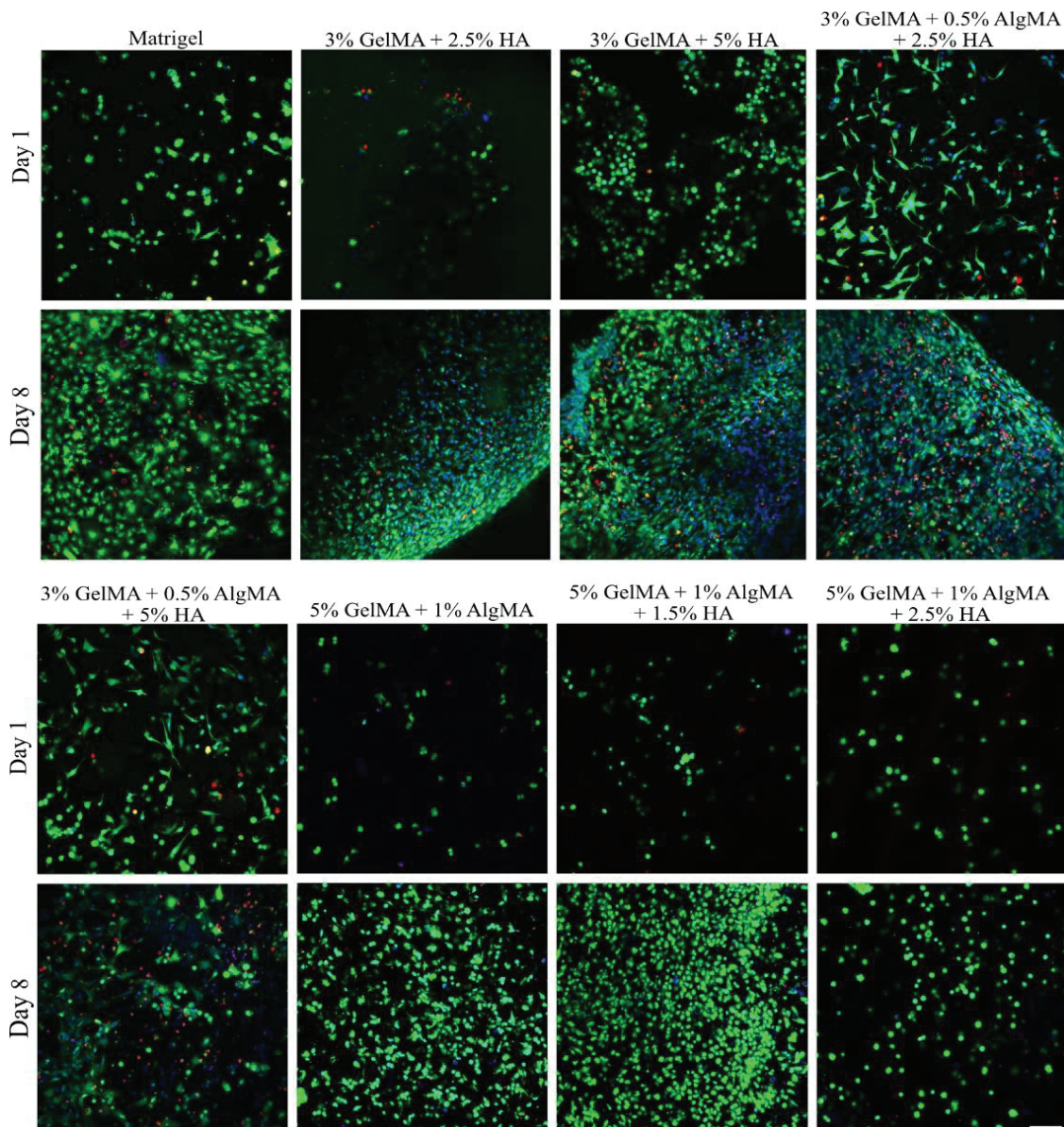


Figure 24 Viability assays performed on drop-shaped samples of C17.2 cells embedded in different polymer concentrations. Representative confocal images of biocompatibility results of C17.2 cells encapsulated in different concentrations of hydrogels for the optimization of the formulation at day 1 and day 8 of culture. Nuclei are stained blue, live cells in green and dead cells in red. Scale bar 100 μ m.

The morphology of the cells also changed over the 8 days of culture, going from most round cells on day 1 to cells with small projections by day 8. The formulations with 3% GelMA, 0.5% AlgMA and 2.5 or 5% of HA already showed some projections on day 1.

1.2. Protein expression assessment of encapsulated cells

Apart from the viability assessment, immunofluorescence assays were performed to assess protein expression and decide the final formulation. 2D culture and Matrigel were used as control. The samples were kept in a differentiation medium from day 1 to day 8. On day 1 and day 8, we evaluated the expression of nestin, a neuroprogenitor cell marker, and β -III tubulin, an early neuron marker (Figure 25). We observed in all formulations that the expression of both markers already on day 1 but on day 8, the expression of β -III tubulin increased.

We observed that on day 8, 3% GelMA + 2.5% HA and 3% GelMA + 0.5% AlgMA + 2.5% HA had a higher signal of β -III tubulin expression, similar to the controls. These formulations also showed increased cell projections. The formulations with 3% GelMA + 5% of HA and 3% GelMA + 0.5% AlgMA + 5% HA had less expression of this marker, and we noticed fewer projections of the cells, which can indicate that the percentage of HA is too high at 5%. The formulations with 5% GelMA showed an increase in β -III tubulin expression but with shorter cell projections, especially in 5% GelMA + 1% AlgMA + 2.5% HA. Nevertheless, as seen before, the viability of the cells was not affected by this increase.

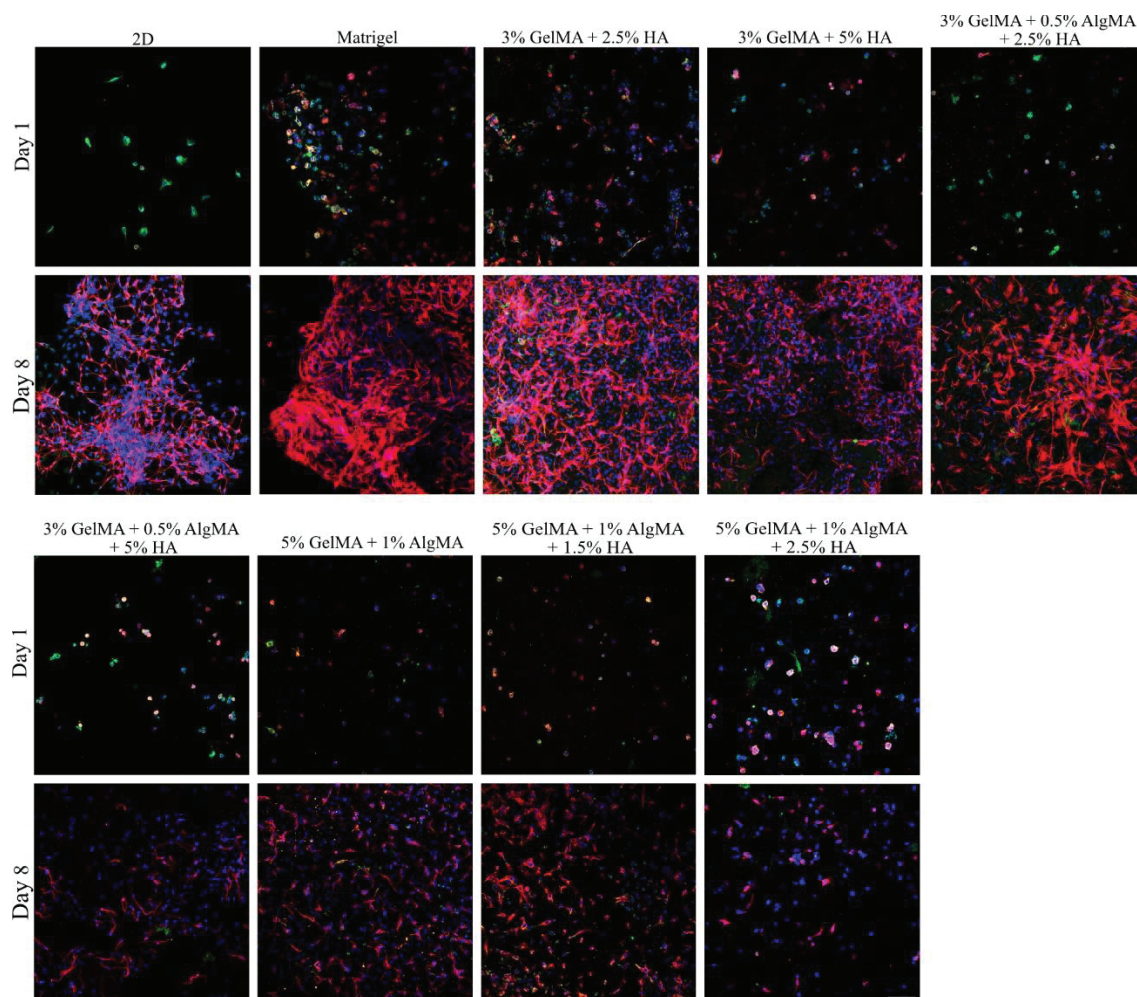


Figure 25 Differentiation of C17.2 cells embedded in different polymer concentrations. Representative confocal images of immunofluorescence images of C17.2 cells encapsulated in different hydrogels for 8 days of the differentiation process. Progenitor marker nestin is stained in green, early neuron marker β -III tubulin is stained in red, and nuclei in blue. Scale bar 100 μ m.

We had promising formulations with good viability and support of differentiation, namely the 3% GelMA + 2.5% HA and 3% GelMA + 0.5% AlgMA + 2.5% HA. However, the samples degraded fast (Figure 26). Samples with 5% HA had the most noticeable degradation by day 7, with 2.5% HA also showing a decrease in size after only one week of culture.

For long-term cultures, such as human pluripotent stem cell differentiation protocols, formulations with 3% GelMA without AlgMA or with only 0.5% were not sufficient as they degraded quickly. Between the HA percentages, 2.5% and 5% also showed the faster degradation of the samples, indicating that 1.5% HA was the most adequate percentage.

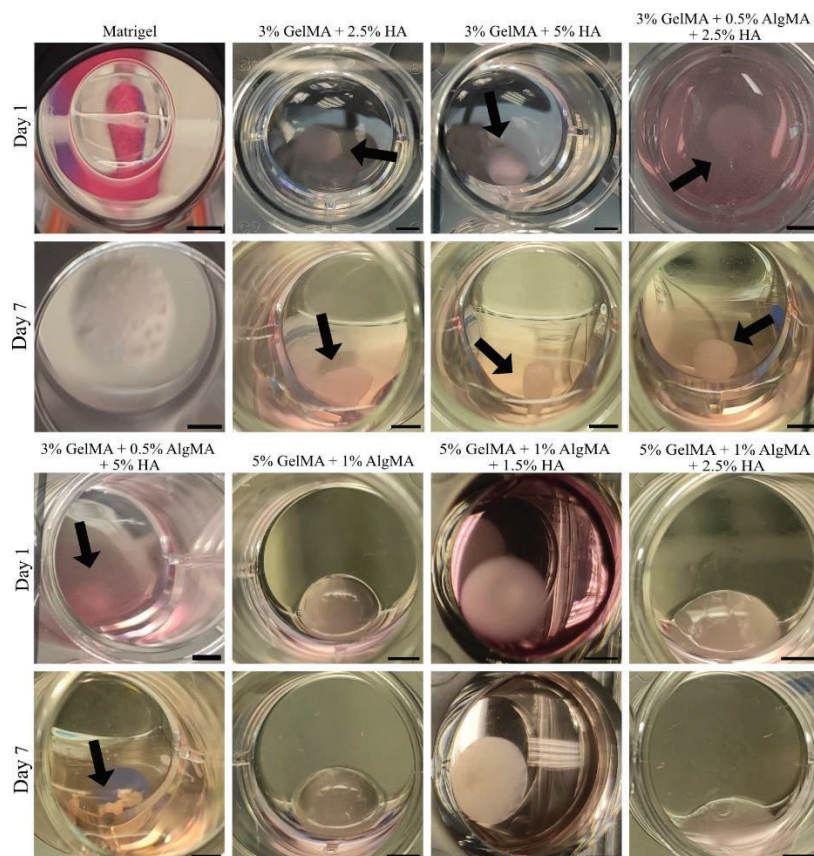


Figure 26 Biomaterial drops with C17.2 cells encapsulated on days 1 and 7 of culture. Black arrows point to the less visible drops. Scale 2.5 mm.

Finally, we settled with 5% GelMA + 1% AlgMA + 1.5% HA as our final formulation. During the following results, we used 5% GelMA + 1% AlgMA as a control formulation, assessing if the presence of the HA would jeopardize or enhance the culture and differentiation of the cells.

2. Physical characterization of the hydrogels

Besides the biocompatibility of the formulation, it is important to assess the physical characteristics of the formulation to ensure that parameters such as stiffness and porosity are adequate for a brain ECM-like material. We then complemented the characterization of the chosen formulation (5% GelMA + 1% AlgMA + 1.5% HA) and control (5% GelMA + 1% AlgMA) with physical assays: swelling, compression modulus, and degradation assays (Figure 27). In the swelling test, the maximum volume increase was $59.2 \pm 14.9\%$ for GelMA + AlgMA hydrogel and $67.2 \pm 16.9\%$ for the GelMA + AlgMA + HA hydrogel (Figure 27A). On the compression modulus assay, the control formulation presented a value of 4.6 ± 1.1 kPa whereas the formulation with HA showed a slightly lower value, 4.2 ± 0.8 kPa (Figure 27B).

Collagenase type II was added to study the degradation rate of the hydrogels, with GelMA + AlgMA + HA degraded more slowly (Figure 27C).

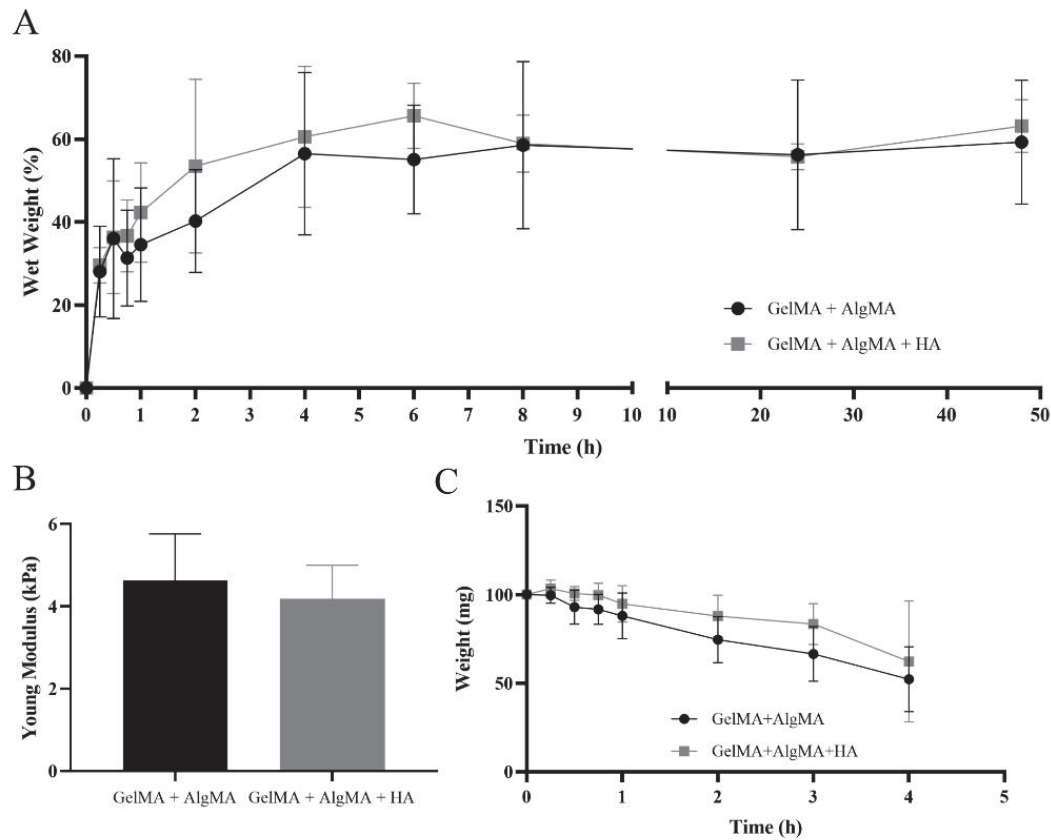


Figure 27 Physical characterization of the study formulation GelMA + AlgMA + HA compared with the control formulation of GelMA + AlgMA by (A) swelling, (B) compression, and (C) degradation assays.

SEM was performed on samples to evaluate the surface and porosity of our formulation and the control, as well as the cell morphology and attachment (Figure 28). GelMA + AlgMA hydrogel without cells is presented in Figure 28A, and GelMA + AlgMA + HA hydrogel in Figure 28C. When comparing these hydrogels, the formulation GelMA + AlgMA had a statistically significant higher pore diameter ($2.56 \pm 0.76 \mu\text{m}$) than GelMA + AlgMA + HA ($2.04 \pm 0.64 \mu\text{m}$); the quantification is represented in Figure 28G. On day 1 of culture GelMA + AlgMA showed dispersed cells both on the surface and underneath (Figure 28B). Similar results were observed with the GelMA + AlgMA + HA hydrogel embedded with C17.2 cells on day one (Figure 28E). On day 15, the cells embedded in GelMA + AlgMA hydrogel proliferated, and aggregates were formed (Figure 28C). An arrangement of the scaffold structure was also observed because of the ECM produced by the cells. For the GelMA + AlgMA + HA hydrogel embedded with C17.2 cells on day 15, the results were identical to

those of the control formulation, with increased cells, visible aggregates, and rearrangement of the scaffold (Figure 28F).

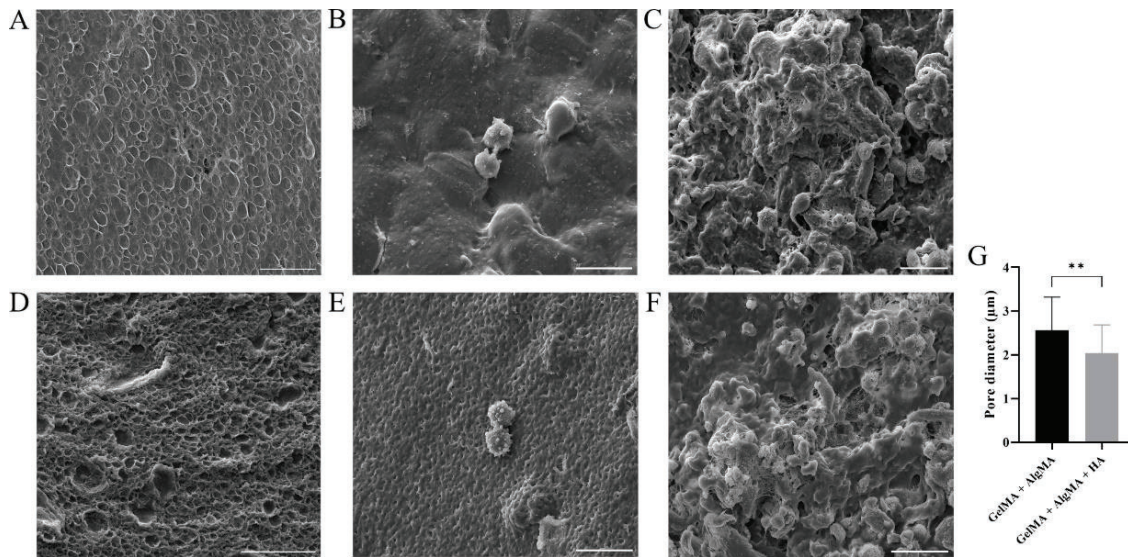


Figure 28 Scanning electron microscopy (SEM) of the hydrogels. GelMA + AlgMA without cells (A), on day 1 of culture (B) and day 15 (C); GelMA + AlgMA + HA without cells (D), on day 1 (E) and day 15 (F). Scale bar 20 µm; (F) Quantification of the pore diameter of both formulations. Data are presented as mean ± standard deviation. Unpaired *t*-test statistical analysis performed: **= $p < 0.05$.

3. Evaluation of GelMA + AlgMA + HA hydrogel for long-term culture of C17.2 cells

In order to assess the capability of GelMA + AlgMA + MA for long-term 3D cell cultures, we performed viability, differentiation and functional assays, using GelMA + AlgMA as a control formulation.

3.1. Viability assays of C17.2 cells throughout 28 days in culture

It was important to evaluate if the formulation that we selected was compatible with long-term culture protocols, common in neurobiology studies using stem cells. Accordingly, we studied for up to 28 days the durability and viability of the hydrogel for the formulation of choice with C17.2 cells cultured, using as control GelMA + AlgMA. Results in Figure 29A show a predominance of the rounder-shaped cells on the first two timepoints which changed after day 15, where cells became more elongated, with larger projections and increased cell connectivity. The viability rates of the formulation are above 65% at all time points and comparable to the control formulation (Figure 29B). The control formulation presented a significant decrease in viability throughout the time of culture whereas GelMA + AlgMA + HA hydrogel maintained

similar values of viability. We observed that the cells increased their proliferative rate in both formulations, particularly from day 1 to day 15, with our formulation presenting the highest number of cells than the formulation without HA, for day 15 and 21 of culture (Figure 29C). By day 28, samples from both formulations were able to last without much degradation, proving that the composition is suitable for the long-term culture of C17.2 cells (Figure 29D).

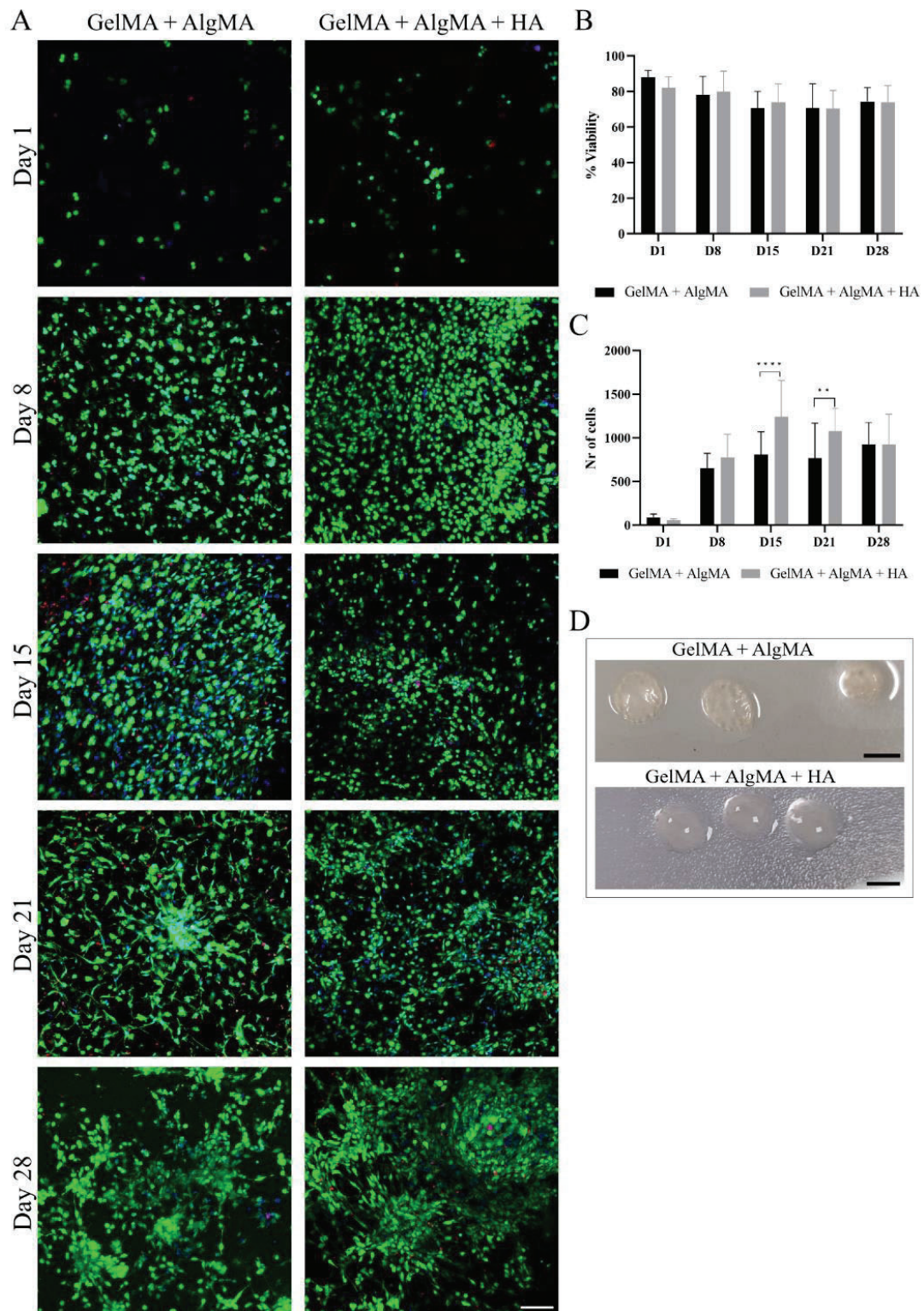


Figure 29 Long-term viability assay on C17.2 cells embedded in GelMA + AlgMA (control) or GelMA + AlgMA + HA hydrogels for up to 28 days. (A) Representative confocal images of biocompatibility studies. Nuclei are stained blue, Calcein AM in green representing the live cells and EthD-1 in red representing the dead cells. Scale bar 100 μ m. (B) Quantification of the viability of the cells. (C) Quantification of the number of cells throughout the 28 days in culture. (D) Photos of the samples on day 28 of culture. Data are presented as mean \pm standard

*deviation. Statistical significance was calculated using a two-way variance analysis (ANOVA) with Sidák's post-hoc multiple comparisons test considering ** $p < 0.01$; **** $p < 0.0001$.*

3.2. Differentiation of C17.2 cells up to 28 days in culture

For the formulations of GelMA + AlgMA and GelMA + AlgMA + HA, we performed the immunofluorescent assay with the differentiation markers, nestin, and β -III tubulin. As presented in Figure 30A, we observed changes in morphology, consistent with the viability results, where the increase in cell projections and connectivity is pronounced from day 15 to day 28. The quantification of the mean signal of the images showed a stable expression of nestin throughout the 28 days, with a significant difference between the two formulations only on day 21, HA formulation presenting a higher mean nestin signal (Figure 30B). The expression of β -III tubulin increased over time, particularly after day 15, with a significant difference at day 21, with GelMA + AlgMA + HA presenting a higher mean β -III tubulin signal (Figure 30C).

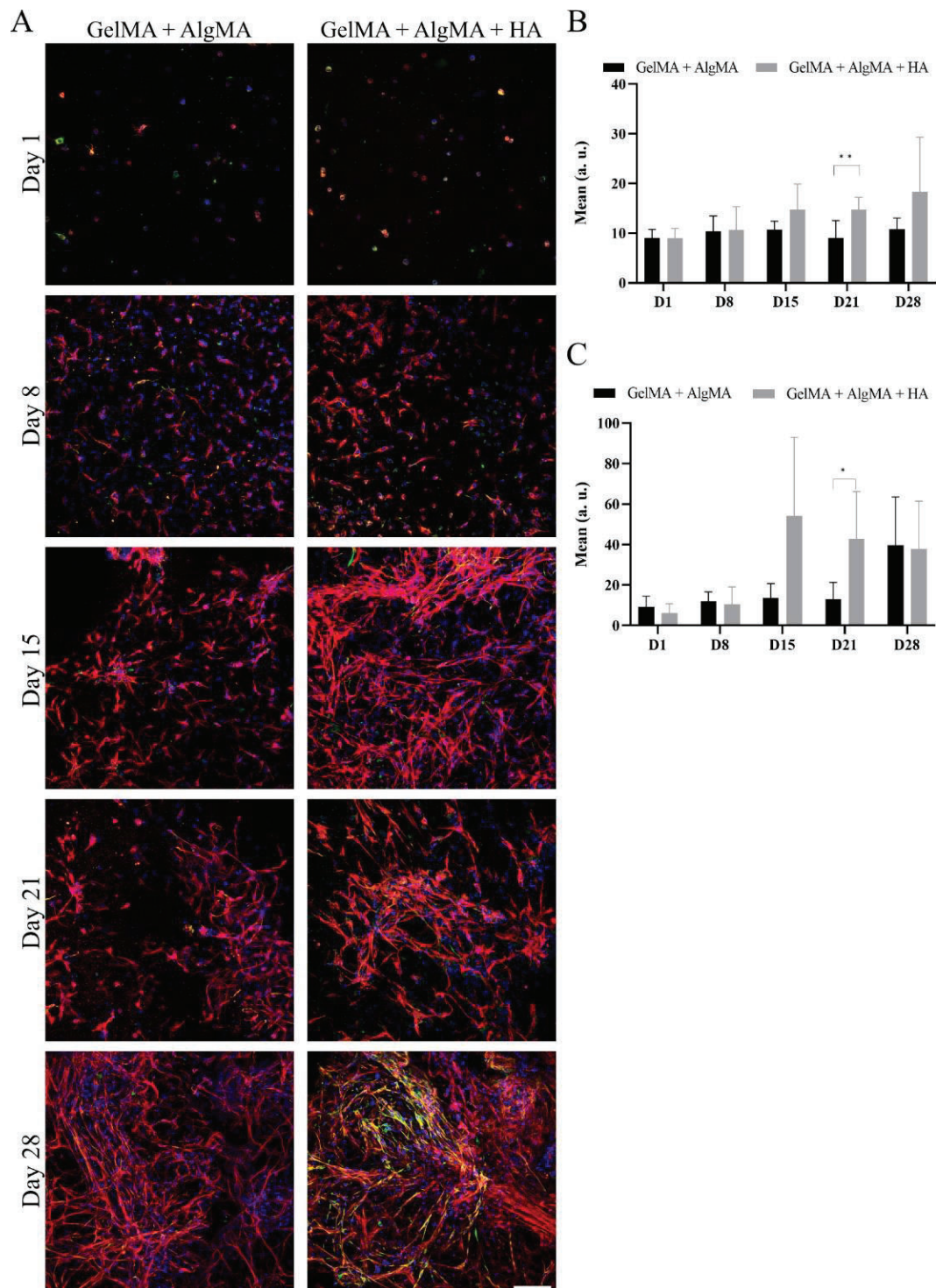


Figure 30 Evaluation of the differentiation of C17.2 cells embedded in GelMA + AlgMA (control) or GelMA + AlgMA + HA hydrogels for 28 days. (A) Representative confocal images of immunofluorescence assay. Progenitor marker nestin is stained in green, neuron marker β -III tubulin is stained in red and nuclei in blue. Scale bar 100 μ m. Quantification of the mean expression of nestin (B) and β -III tubulin (C) up to 28 days for both hydrogel formulations. Data are presented as mean \pm standard deviation. Statistical significance was calculated using a two-way variance analysis (ANOVA) with Sidák's post-hoc multiple comparisons test considering * $p < 0.05$; ** $p < 0.01$.

3.3. Validation of the differentiation process through gene expression

To further study the differentiation process occurring on the 3D culture, we performed qRT-PCR on GelMA + AlgMA and GelMA + AlgMA + HA samples on three different time points: day 1, day 15 and day 28 (Figure 31). Gene expression was normalized to glyceraldehyde 3-phosphate dehydrogenase (GAPDH).

Two progenitor cell markers, nestin and PAX6, were evaluated. Nestin was expressed evenly throughout the 28 days of culture. PAX6 expression increased from day 1 to day 15 in both formulations but decreased significantly by day 28. For early neuronal differentiation, the expression of β -III tubulin and DCX genes was assessed. β -III tubulin expression increased significantly from day 1 to day 15 on both biomaterials, whereas on day 28 decreased significantly, even though GelMA + AlgMA + HA maintained a higher expression at that time point. DCX levels remained similar on days 1 and 15 and, decreased on day 28. To assess the maturity of differentiation, the expression of mature neuron gene MAP2 was evaluated. MAP2 expression, similar to β -III tubulin levels, increased until day 15, especially in the HA formulation, but decreased significantly on day 28 on both hydrogels. As for astrocyte genes, GFAP was expressed mostly on day 15 in both formulations, while S100b was expressed significantly more in GelMA + AlgMA on day 15.

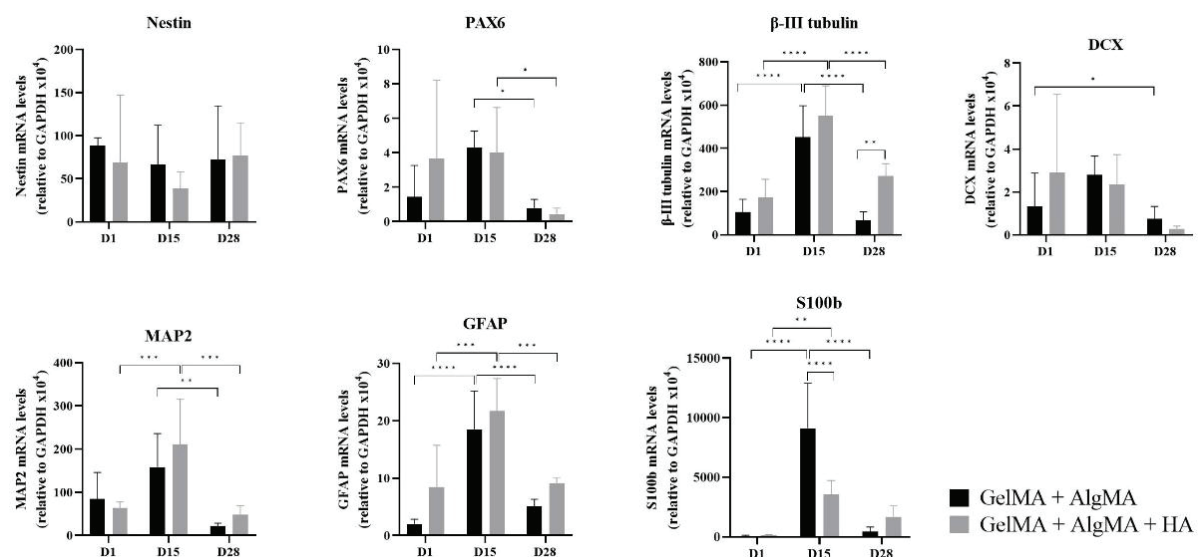


Figure 31 Quantitative gene expression of C17.2 cells in GelMA + AlgMA (control) or GelMA + AlgMA + HA hydrogels on day 1, 15 and 28 of culture. Nestin, PAX6, β -III tubulin, MAP2, GFAP, S100b and DCX genes relative to GAPDH are represented. Data are presented as mean \pm standard deviation. Statistical significance was calculated using a two-way variance analysis (ANOVA) with Turkey's and Sidák's post-hoc multiple comparisons test considering * $p < 0.05$; ** $p < 0.01$; *** $p < 0.001$; **** $p < 0.0001$.

3.4. Evaluation of the functional network of C17.2 cells

The functionality of neuronal cells is fundamental for their survival and differentiation. We started by assessing the spontaneous activity of the cells in 2D, as a control, before characterizing the activity in 3D. Cells were recorded through calcium imaging on four different time points, day 8, day 10, day 13 and day 15, to study the evolution of the spontaneous activity throughout the culture.

On day 8 we acquired a confluent monolayer of cells (Figure 32A) with traces of activity with multiple spikes (Figure 32B). On day 10 (Figure 32C-D) we could see a less confluent monolayer with spontaneous activity including cells with multiple spikes. On day 13 (Figure 32E) the monolayer changed, encompassing holes between the cells which is a hallmark of differentiation but made the manipulation of the culture difficult because the cells were easily detached. However, we could still successfully record their activity (Figure 32F). On the final day of culture, day 15, the monolayer presented increased spaces between cells, but we were where still able to obtain spikes of spontaneous activity. When comparing the traces of activity between time points, day 8 had traces with less noise and frequent spikes. This could be attributed to the good conditions of the monolayer that allowed an easy recording of the cell's activity.

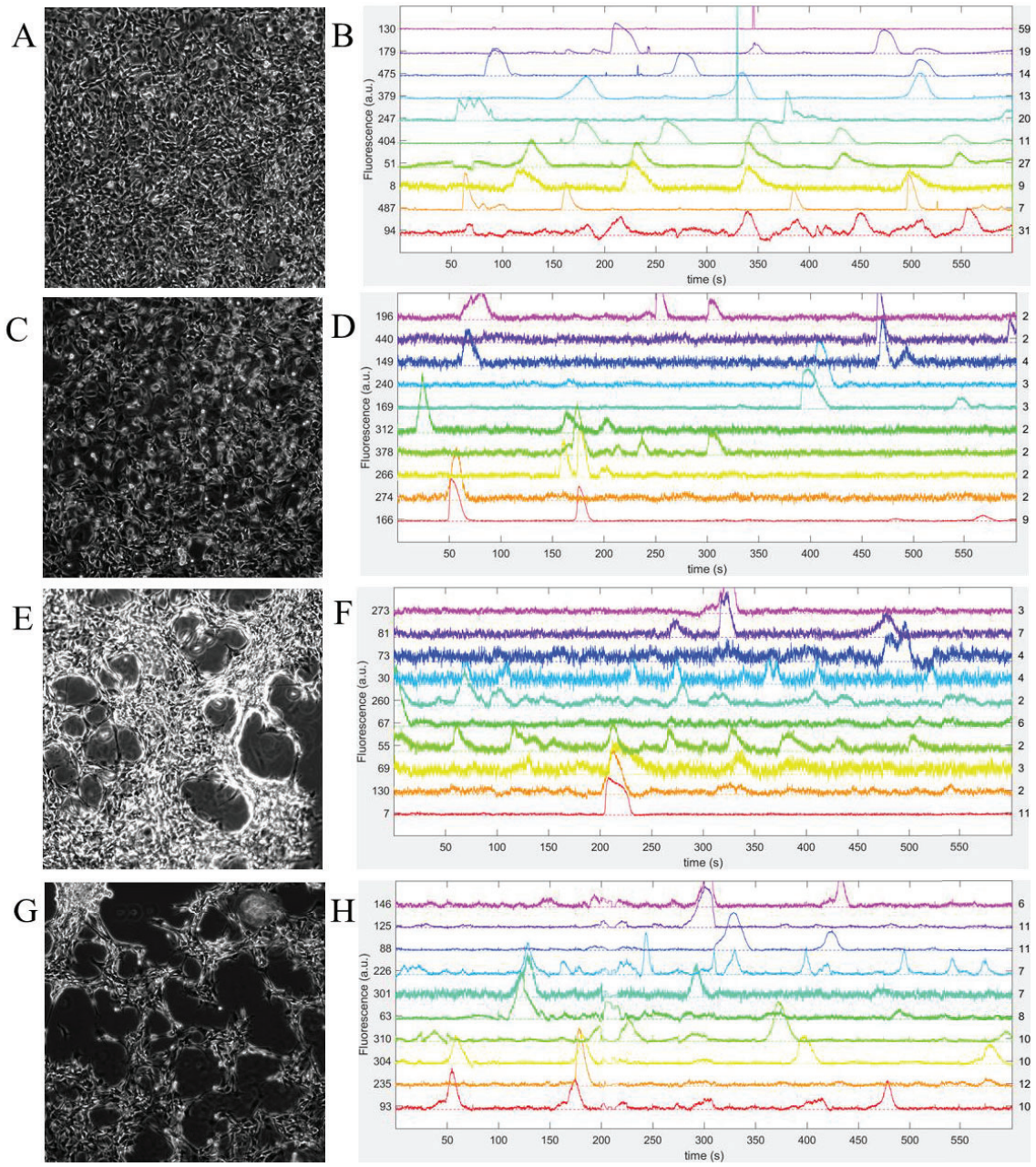


Figure 32 Functional assessment of C17.2 cells in 2D. (A, C, E, G) Brightfield photos of the recorded samples. (B, D, F, H) Traces of the spontaneous activity of the cells of the samples presented. (A, B) day 8 of culture; (C, D) day 10 of culture; (E, F) day 13 of culture and (G, H) day 15 of culture.

3.4.1. Study of functional activity in 3D

To evaluate of the spontaneous activity of the cells within the 3D material, we performed calcium imaging assays on the hydrogel on day 15 of culture since it was the time point where neuronal markers started to increase their expression (Figure 33).

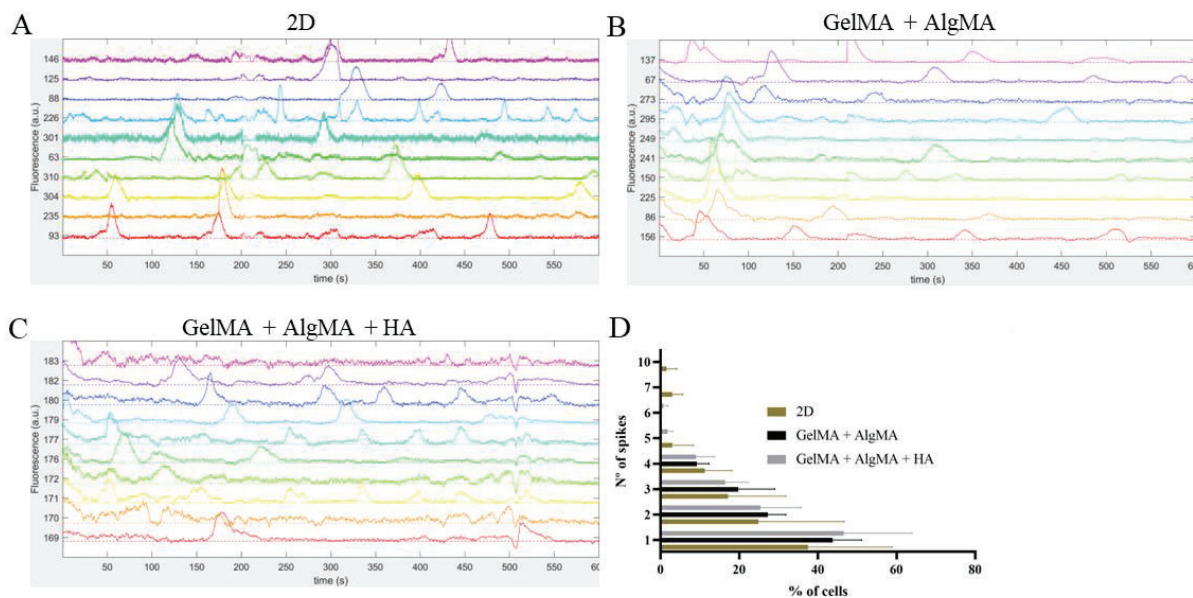
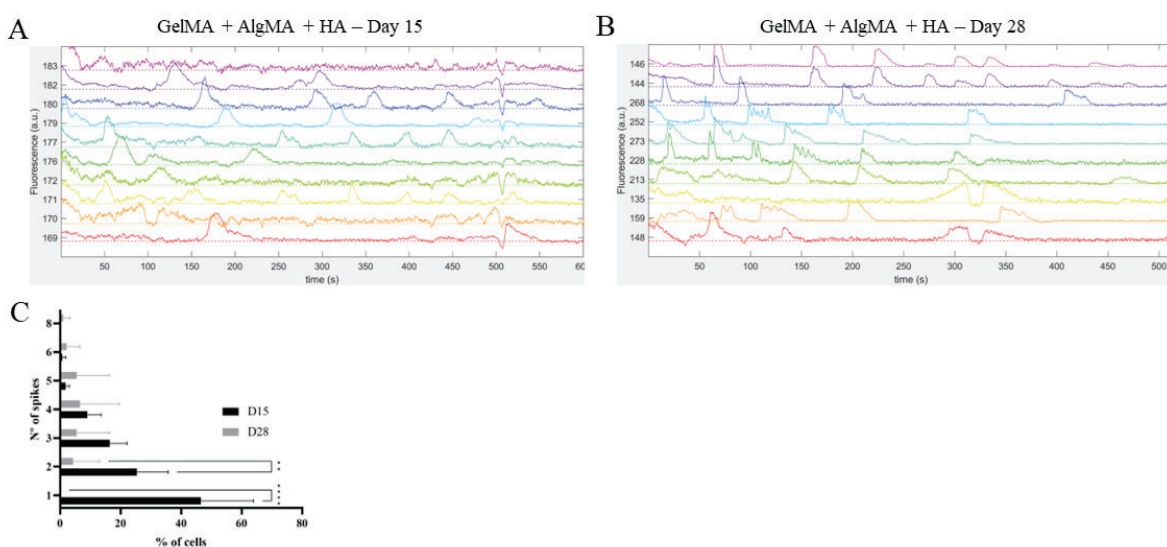


Figure 33 Functional assessment of the C17.2 cells through calcium imaging with Fluo4AM on day 15. Traces of spontaneous cell activity of C17.2 cells cultured in 2D on coated glass slides (A) or embedded in the hydrogels, (B) GelMA + AlgMA or (C) GelMA + AlgMA + HA. (D) Quantification of the percentage of cells with a determined number of spontaneous spikes (1, 2, 3, 4, 5, 6, 7 or 10) during the 10 minutes of recording. Data are presented as mean \pm standard deviation.

We could observe that the cells were active in both GelMA + AlgMA (Figure 33B) and GelMA + AlgMA + HA (Figure 33C), proving that the culture in 3D did not impair the functionality of the cells. When quantifying the frequency of spikes between the formulations, GelMA + AlgMA + HA presented a higher frequency of spikes than GelMA + AlgMA, reaching 6 spikes per active cell, a number closer to the 10 spikes per active cell obtained in 2D. The control hydrogel only reached a maximum of 4 spikes (Figure 33D).



*Figure 34 Functional assessment of the C17.2 on GelMA + AlgMA + HA cells through calcium imaging with Fluo4AM on days 15 and 28. (A) Traces of spontaneous activity of C17.2 cells on day 15 and on day 28 (B). (C) Quantification of the frequency of spikes in active cells. Data are presented as mean \pm standard deviation. Statistical significance was calculated using a two-way variance analysis (ANOVA) with Sidák's post-hoc multiple comparisons test considering ** $p < 0.01$; **** $p < 0.00001$.*

Then, we compared the frequency of spikes in active cells embedded in GelMA + AlgMA + HA hydrogel on day 15 (Figure 34A) and day 28 (Figure 34B) to evaluate if we can observe a mature network with a higher number of spikes. The cells on day 28 of differentiation increased their spontaneous spike frequency, reaching a maximum of 8 spikes per active cell, as shown by Figure 34C.

4. GelMA + AlgMA + HA: a bioink for extrusion bioprinting

Once we found the composition of the hydrogel that allows cell survival and differentiation, we wanted to assess its versatility as a bioink for extrusion bioprinting. This technique brings a solution to the lack of organization some 3D culture models have¹²⁰. Several parameters can influence the printing process, which needs to be taken into consideration when starting to use this technique. The printing pressure, temperature, nozzle size and speed influence cell viability, and for each type of culture, those must be adjusted²⁰⁶. GelMA and AlgMA have been widely used as bioinks¹⁶⁶ but the incorporation of HA modifies the properties of the hydrogel because HA is considered a shear-thinning fluid, which would render the bioink less viscous, and the structures could lose their definition¹⁷¹.

Taking this information into account, we optimized the printing temperature, speed and pressure to be able to print the final formulation, using GelMA + AlgMA as control.

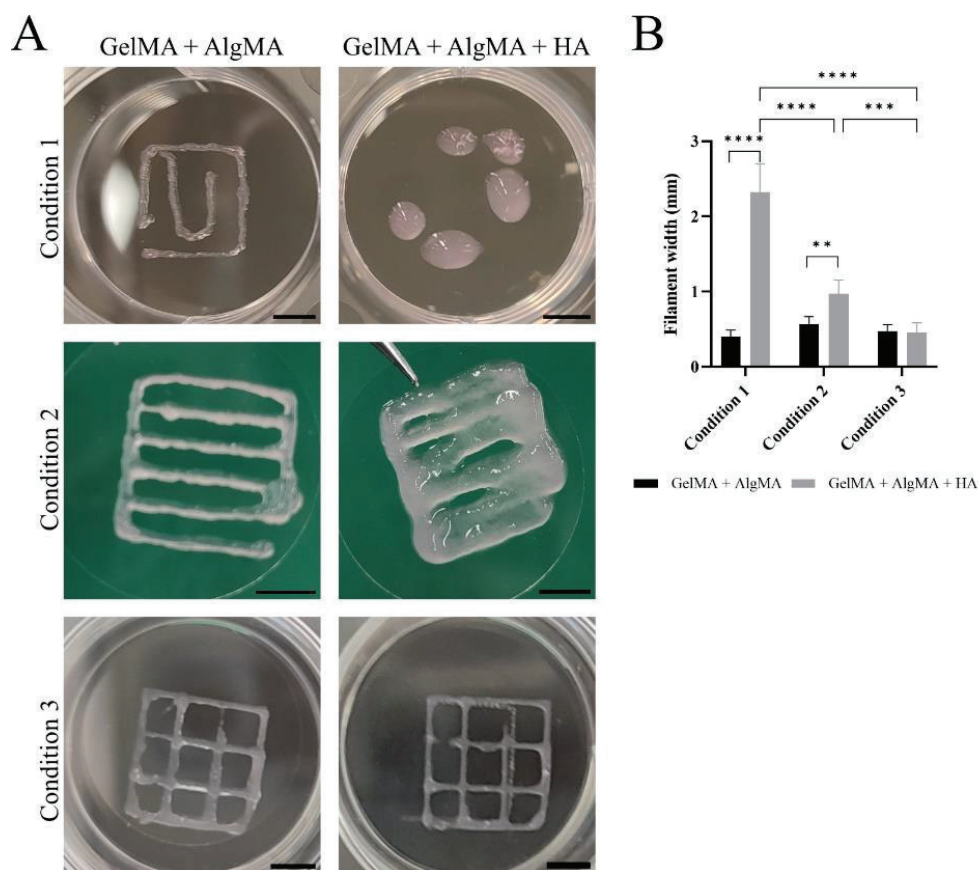


Figure 35 Optimization of the printing parameters. (A) Images of the printing scaffolds for the three conditions and both hydrogel formulations. Scale bar 2.5 mm. (B) Measurement of the filament width of the structures printed with the three optimization conditions. Data are presented as mean \pm standard deviation. Statistical significance was calculated using a two-way variance analysis (ANOVA) with Turkey's and Sidák's post-hoc multiple comparisons test considering ** $p < 0.01$; *** $p < 0.001$; **** $p < 0.0001$.

When printing at 12°C, GelMA + AlgMA had a poor definition where the filament was not able to form the continuous grid shape (Figure 35A). In GelMA + AlgMA + HA bioink, the filament was not achieved, and the ink was dispensed in drop shapes. When changing the temperature to 18 °C (Condition 2), we obtained continuous filaments, and a scaffold with two layers was produced. However, when comparing the thickness of the filaments, there was a significant difference between formulations, with higher values in HA formulation (Figure 35B). In the third condition, the speed of printing was increased. This permitted the deposition of the ink in a manner that the grid was formed with two layers while maintaining with no significant differences between the width of the filaments in the different formulations.

We proceed with condition 3 as it presented the better results for printing both formulations, managing to print a two-layer 10x10 mm grid square with a good definition (Figure 36A).

4.1. Viability assays for C17.2 cells after printing

We bioprinted both biomaterials (out formulation and control) to assess cell viability on three different time points (days 1, 8, and 15) (Figure 36B). Results showed rates of above 80% for all time points and for both biomaterials (Figure 36C). Specifically, on day 1, the viability rates were $90.5 \pm 4.2\%$ for GelMA+ AlgMA and $86.3 \pm 4.1\%$ for the GelMA + AlgMA + HA formulation. On day 8, the viability rates were $87 \pm 7.4\%$ for GelMA+ AlgMA and $81 \pm 9.1 \%$ for the GelMA + AlgMA + HA formulation. On day 15, the viability rates were $82.7 \pm 8.0\%$ for GelMA+ AlgMA and $84 \pm 6.9\%$ for the GelMA + AlgMA + HA formulation. As seen in the drop assays, the cells maintained a proliferative capacity after bioprinting, increasing cell density overtime.

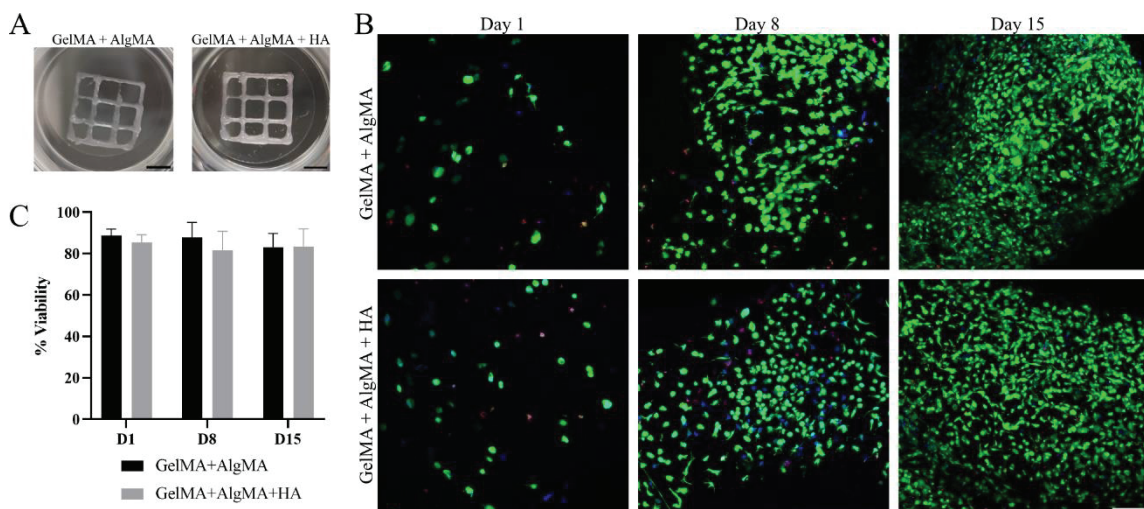


Figure 36 Bioprinting studies of C17.2 cells embedded in the two different bioprinted hydrogels for 15 days. (A) Photos of the bioprinted samples of both formulations. Scale bar 5mm. (B) Representative confocal images of

viability assay. Nuclei are stained blue, Calcein AM in green representing the live cells and EthD-1 in red representing the dead cells. Scale bar 100 μ m. (C) Quantification of the viability of the cells. Data are presented as mean \pm standard deviation.

4.2. Differentiation of C17.2 cells after printing

After, we assessed the differentiation process occurred after printing with immunofluorescence assays for nestin and β -III tubulin on days 1, 8 and 15 (Figure 37). Similar to previous results, we observed the increase in cell numbers and the difference in the morphology of the cells throughout the culture (Figure 37A). The expression of nestin was present in all time points, increasing significantly up to day 15 for GelMA + AlgMA + HA, one week more than with control (Figure 37B). Between GelMA + AlgMA + HA and the control, the latest had a significant increase of nestin expression over the formulation with HA on day 1 only. The expression of β -III tubulin was steady on the first two time points and on day 15 was significantly increased in both formulations (Figure 37C). As observed in the previous studies, the density of cells increased overtime and the morphology changed from a round shape on day to spread cells with increased projections and connectivity.

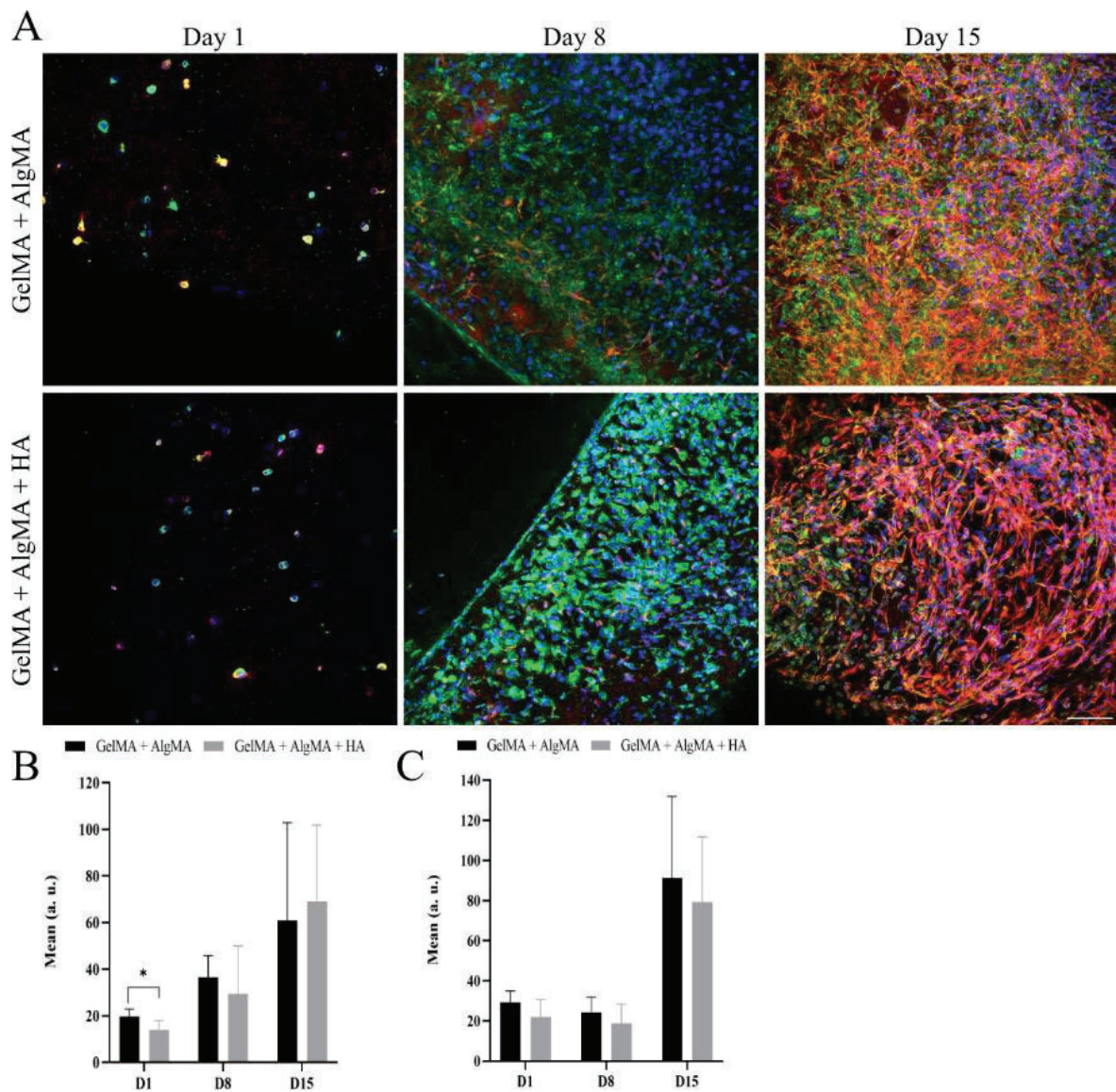


Figure 37 Evaluation of the differentiation of C17.2 cells embedded in the hydrogel after printing for up to 15 days. (A) Representative confocal images of immunofluorescence assay Progenitor marker nestin is stained in green, neuron marker β -III tubulin is stained in red and nuclei in blue. Scale bar 100 μ m. Quantification of the mean expression of nestin (B) and β -III tubulin (C). Data are presented as mean \pm standard deviation. Statistical significance was calculated using a two-way variance analysis (ANOVA) with Sidák's post-hoc multiple comparisons test considering $*p < 0.05$.

4.3. Evaluation of the functional network of the 3D bioprinted construct

We evaluated the activity of the cells on day 15 after printing (Figure 38). Our hydrogel and control demonstrated spontaneous cell activity, but our formulation showed a higher frequency of spontaneous spikes during the recording (Figure 38A-B). After classifying the percentage of cells with the number of spontaneous spikes (from 1 to 7 per cell), it was visible that the GelMA + AlgMA + HA formulation had a percentage of cells with 5 and 7 spikes per active

cell, not observed on the formulation without HA (Figure 38C). A significant difference (p -value = 0,0262) in the percentage of cells with only one spike between formulations was observed, presenting a higher value the control formulation ($73.9 \pm 9.8\%$ vs $42.0 \pm 22.8\%$). A difference in the distribution of the number of spikes is also noticeable when comparing the percentage of cells that have 1, 2, or more than 2 spikes (p -value = 0,0037) confirming the increase in the number of spontaneous spikes on GelMA + AlgMA + HA (Figure 38D).

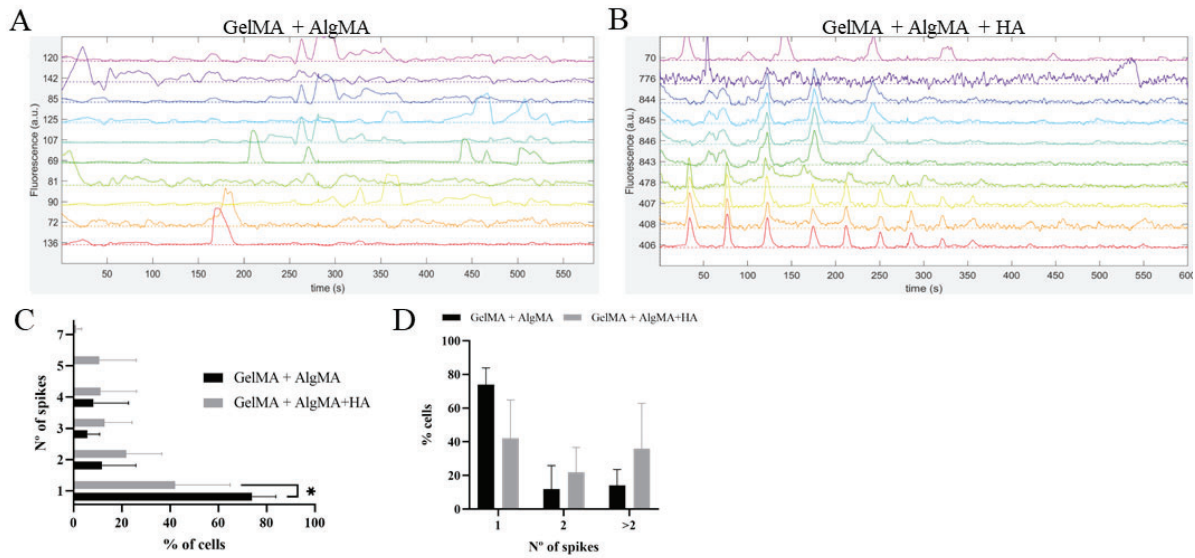


Figure 38 Functional assessment of the cells embedded in the bioprinted biomaterials through calcium imaging with Fluo4AM. Traces of spontaneous activity of the cells embedded in GelMA + AlgMA hydrogel (A) and GelMA + AlgMA + HA hydrogel (B) at day 15 of culture. (C) Quantification of the number of spontaneous spikes of active cells during the 10 minutes of recording in both hydrogels. (D) Representation of the quantification of the number of spikes separated by the percentage of cells that have 1, 2, or more than 2 spikes. Data are presented as mean \pm standard deviation. Statistical significance was calculated using a two-way variance analysis (ANOVA) with Sidák's post-hoc multiple comparisons test considering $*p < 0.05$.

5. Incorporating the developed biomaterial in a microfluidic device

After validating the compatibility of the cells in the hydrogels in a drop shape and bioprinted, we moved to the inclusion of this 3D culture in a microfluidic device. Combining 3D culture with the small compartments of a microfluidic device would be advantageous to bring a more defined architecture and decrease the number of cells and materials needed for the model⁸³. This is particularly important for future drug screening assays or modeling specific functions of the brain with cells that cannot be obtained easily in high concentrations, as sometimes is needed for 2D or 3D models.

5.1.3D culture in a microfluidic device

Inspired by the popular BBB-on-a-chip models²⁵⁵, we used a design with 3 parallel channels, separated by triangular-shaped pillars, where cells embedded in the biomaterial can be seeded in the central one while the others can be used to add the cell culture media (Figure 39). On the central channel, we included the cells embedded in the biomaterial while the cell culture medium was included on the lateral channels (Figure 39A).

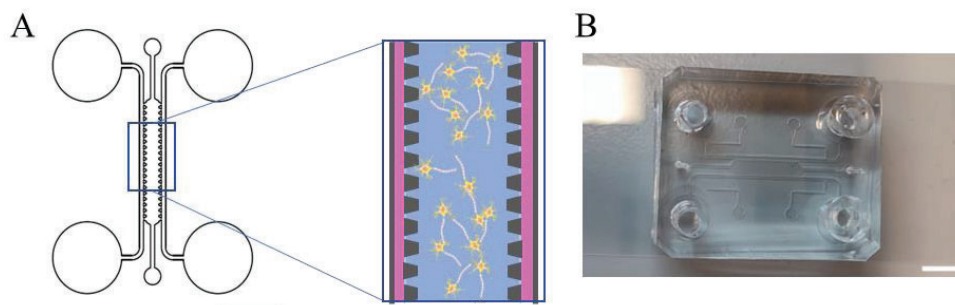


Figure 39 3D microfluidic device setup. (A) Scheme of the device with zoom on the central and lateral channels separated by triangular pillars. Scale bar 5mm. (B) PDMS replica of the device. Scale bar 5mm.

5.2. Viability & Differentiation of C17.2

We started with the viability evaluation of the cells (Figure 40A). Results for our formulation showed viability above 60% in all time points with no significant differences compared with control up to day 28 (Figure 40B). However, the viability decreases significantly throughout the time points on the GelMA + AlgMA formulation. We observed a tendency of the cells to move in the direction of the lateral channels.

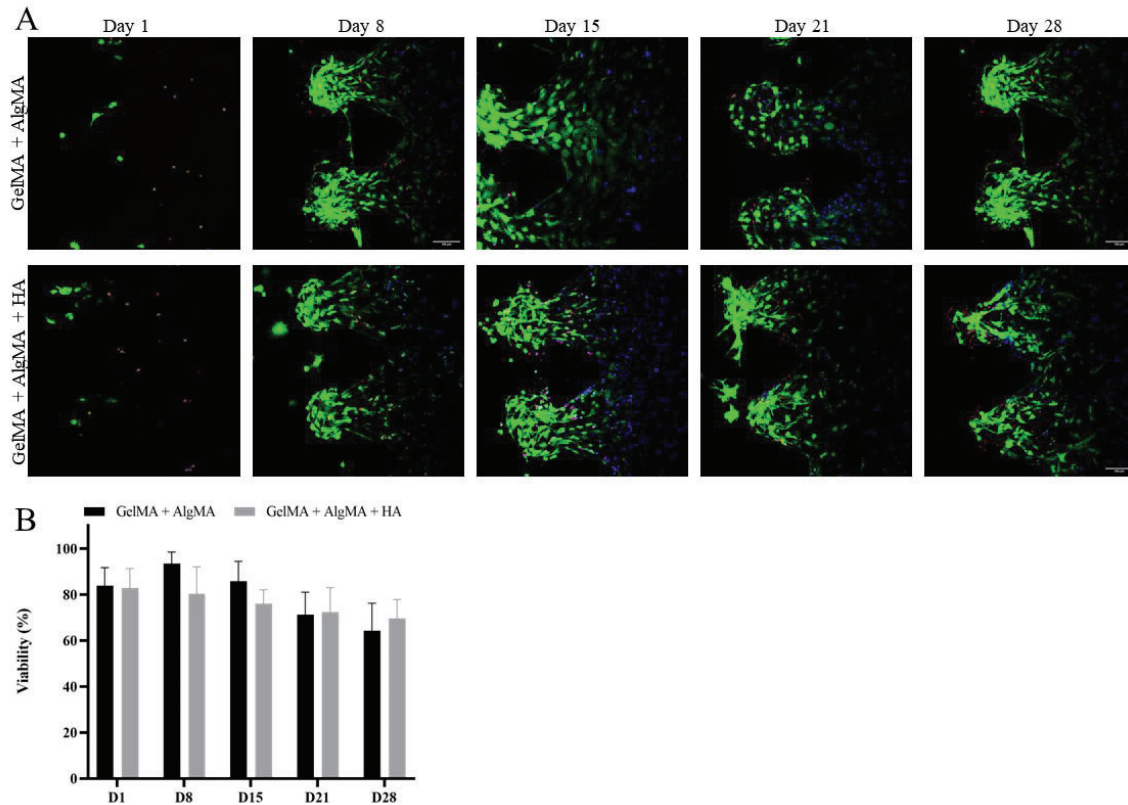


Figure 40 Viability assays of C17.2 cells embedded in GelMA + AlgMA (control) or GelMA + AlgMA + HA hydrogels inside the microfluidic device for 28 days. (A) Representative confocal images of biocompatibility studies. Nuclei are stained blue, Calcein AM in green representing the live cells and EthD-1 in red representing the dead cells. Scale bar 100 μ m. (B) Quantification of the viability rates. Data are presented as mean \pm standard deviation.

To assess the differentiation into early neurons, we performed an immunofluorescence assay on five different time points across 28 days of the differentiation process (Figure 41). The results showed a stable expression of nestin up until day 21 with a significant decrease on day 28 in GelMA + AlgMA + HA (Figure 41B). The expression of β -III tubulin increased overtime, with significantly higher values on day 1 for the GelMA + AlgMA + HA formulation, confirming the compatibility of the system with the differentiation of these cells. We observed a change in the cell morphology, going from a rounded shape to a more elongated one over time. Markers' expression and changes in morphology were similar to the ones obtained during the experiments performed in drop or bioprinted. We also saw that the biomaterials were more degraded on the last time point, shrinking into the middle of the central channel.

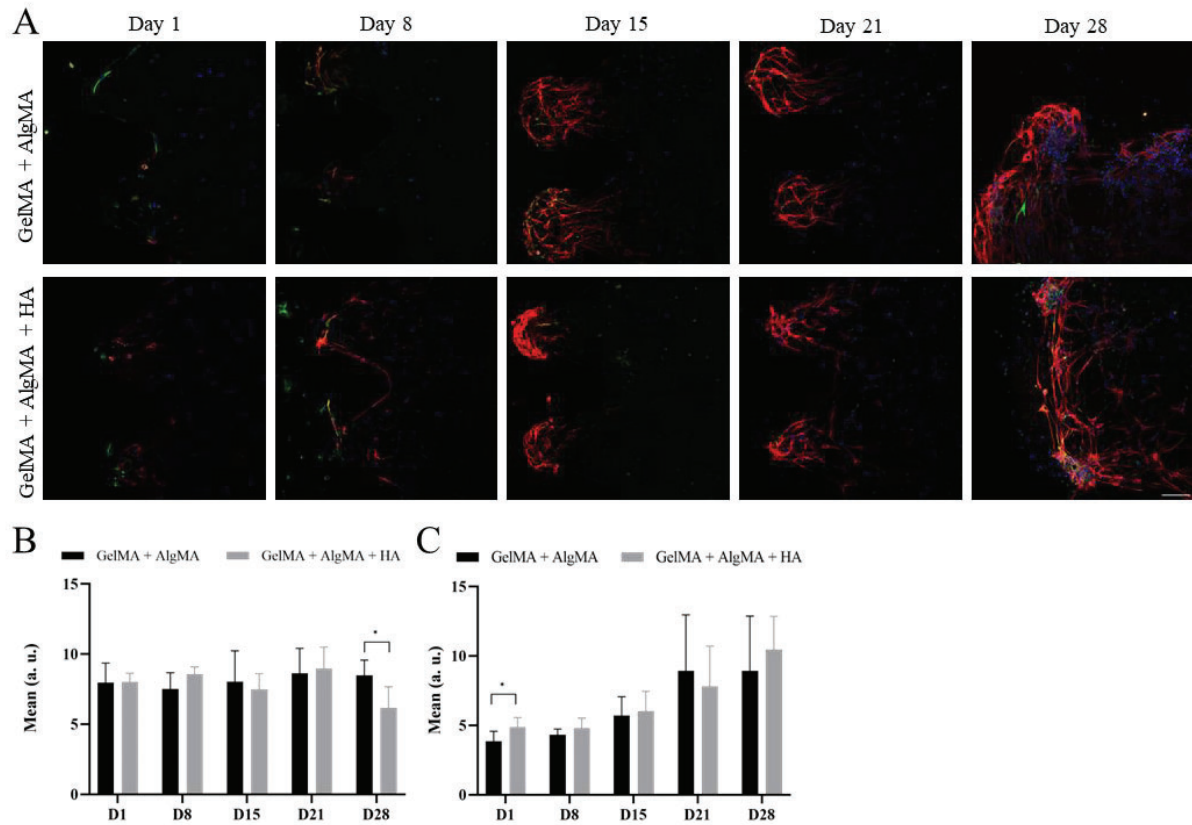


Figure 41 Evaluation of the differentiation of C17.2 cells embedded in GelMA + AlgMA (control) or GelMA + AlgMA + HA hydrogels inside the microfluidic device for 28 days. (A) Representative confocal images of immunofluorescence assay. Progenitor marker nestin is stained in green, neuron marker β -III tubulin is stained in red and nuclei in blue. Scale bar 100 μ m. (B) Quantification of the mean expression of nestin (B) and β -III tubulin (C). Data are presented as mean \pm standard deviation. Data are presented as mean \pm standard deviation. Statistical significance was calculated using a two-way variance analysis (ANOVA) with Sidák's post-hoc multiple comparisons test considering $*p < 0.05$.

5.3. Functional network in the 3D system with GelMA + AlgMA + HA

After assessing the expression of differentiation markers, we wanted to assess if the cells were also able to show spontaneous activity in this system. In this case we only tested the formulation we are developing, GelMA + AlgMA + HA, and we saw that the cells were spontaneously active on day 15 (Figure 42A), with the frequency of spikes going up to 4 spikes per active cell (Figure 42B).

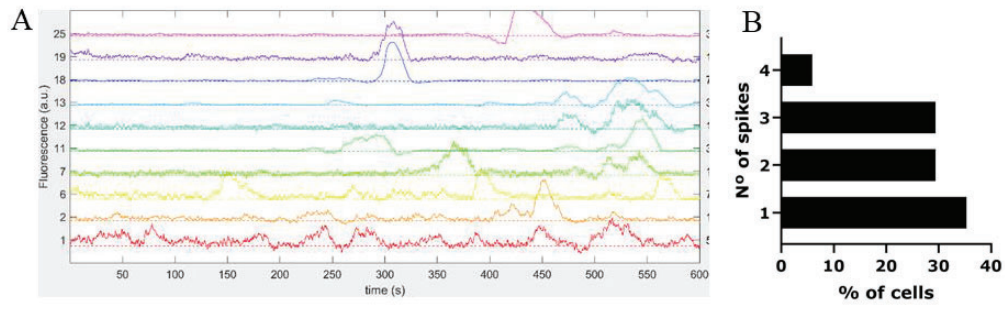


Figure 42 Functional assessment of C17.2 cells embedded in the biomaterial and cultured in the 3D microfluidic device. (A) Traces of spontaneous activity of C17.2 cells in GelMA + AlgMA + HA. (B) Quantification of the number of spontaneous spiker frequencies in the active cells.

6. Inclusion of human pluripotent stem cells in the 3D culture models

After confirming the suitability of GelMA + AlgMA + HA biomaterial with the culture and differentiation of the murine cell line C17.2, we wanted to evaluate the behaviour of human cells in this scaffold. The development of iPSC revolutionized brain modeling by the possibility of obtaining human neurons from somatic cells, with no ethical concerns, leading to the development of multiple differentiation protocols to achieve the different types of neurons and glia. Another big advantage is the possibility to collect cells from patients and better recreate cultures with the same genetic background²⁷⁶. Through a collaboration with Guochang Lyu from Ernest Arenas group at Karolinska Institute, we used an iPSC line derived from a healthy individual (EPIPSC) for midbrain dopaminergic (mDA) neuron differentiation in the 3D systems (drop or 3D microfluidic chip) using the GelMA + AlgMA + HA hydrogel and the control formulation (GelMA + AlgMA).

6.1. Viability of EPIPSC cells

Viability assays were performed at three time points of differentiation: day 12 which corresponded to the day after inclusion on the scaffold, day 16 (4 days after inclusion) and day 21 (10 days after inclusion). We used a 2D culture as a control throughout the time points. From the images in Figure 43 we observed that on the first timepoint, cells looked similar in all conditions (2D, GelMA + AlgMA and GelMA + AlgMA + HA), with a round shape and spread homogeneously across the culture area. It was also visible that most cells were alive (stained in green). Four days later, in the 2D culture we could see an increase in cell proliferation and a monolayer is accomplished with high viability. In 3D cultures, we observed cell agglomerates where cells were alive, in contrary to the cells that remained alone that were dead. This happened on both materials. On the last time point, we obtained a more advanced stage of differentiation in the 2D culture, with an increase in axon projections while keeping the viability high. In the 3D culture, the images showed a start on the axon projections outside the cell agglomerates.

Viability of the cells was above 60% at all time points which is a good value for 3D cultures of these cells. Although when quantifying the rates, we saw that 3D cultures presented a significantly lower value when compared to 2D culture. In case of our formulation, this difference was more significant on day16 while the control formulation had a significant lower value on day 16 and 21 (Figure 43B). However, we didn't have a difference in the values between the two formulations.

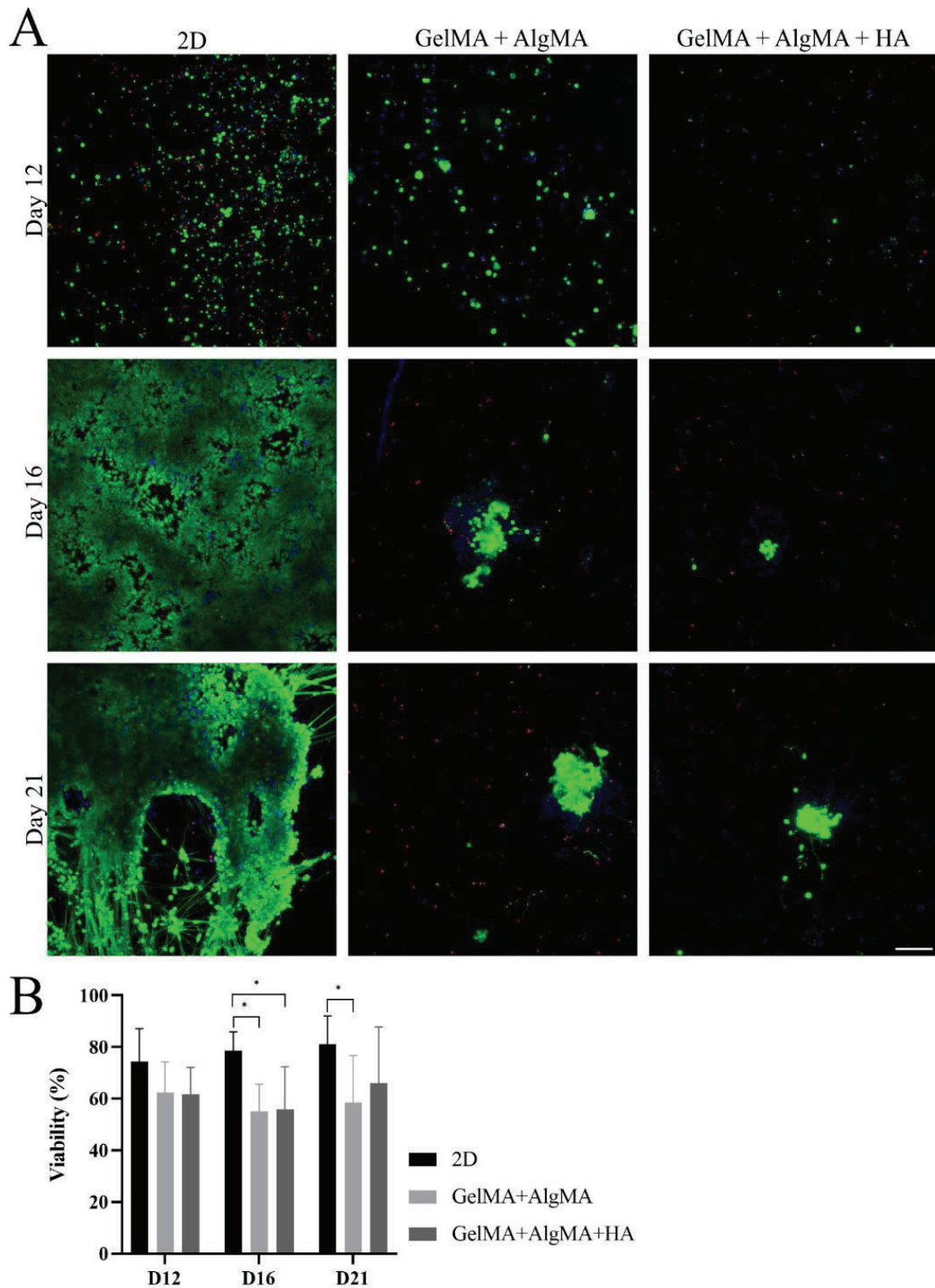


Figure 43 Viability assays of EPIPSC cells cultured in 2D and embedded in the GelMA + AlgMA (control) or GelMA + AlgMA + HA hydrogels. (A) Representative confocal images of the viability assays at day 12, 16 and 21 of differentiation. Nuclei are stained blue, Calcein AM in green representing the live cells and EthD-1 in red representing the dead cells. Scale bar 100 μ m. (B) Quantification of the viability rates of the cells in the three different conditions (2D, GelMA + AlgMA; GelMA + AlgMA + HA) and on three time points (day 12, 16 and 21

of differentiation). Data are presented as mean \pm standard deviation. Statistical significance was calculated using a two-way variance analysis (ANOVA) with Sidák's post-hoc multiple comparisons test considering $*p < 0.05$.

6.2. Differentiation of EPISPC cells

We also performed an immunofluorescence assay to check the expression of two markers, MAP2, as a characteristic of mature neurons and TH, a marker from mDA neurons on day 16 and 21 of differentiation (Figure 44). We could see on day 16 a lower expression of the markers in 3D compared to 2D, but there was an apparent increase of these expression on day 21, as well as the formation of some projection of the cells.

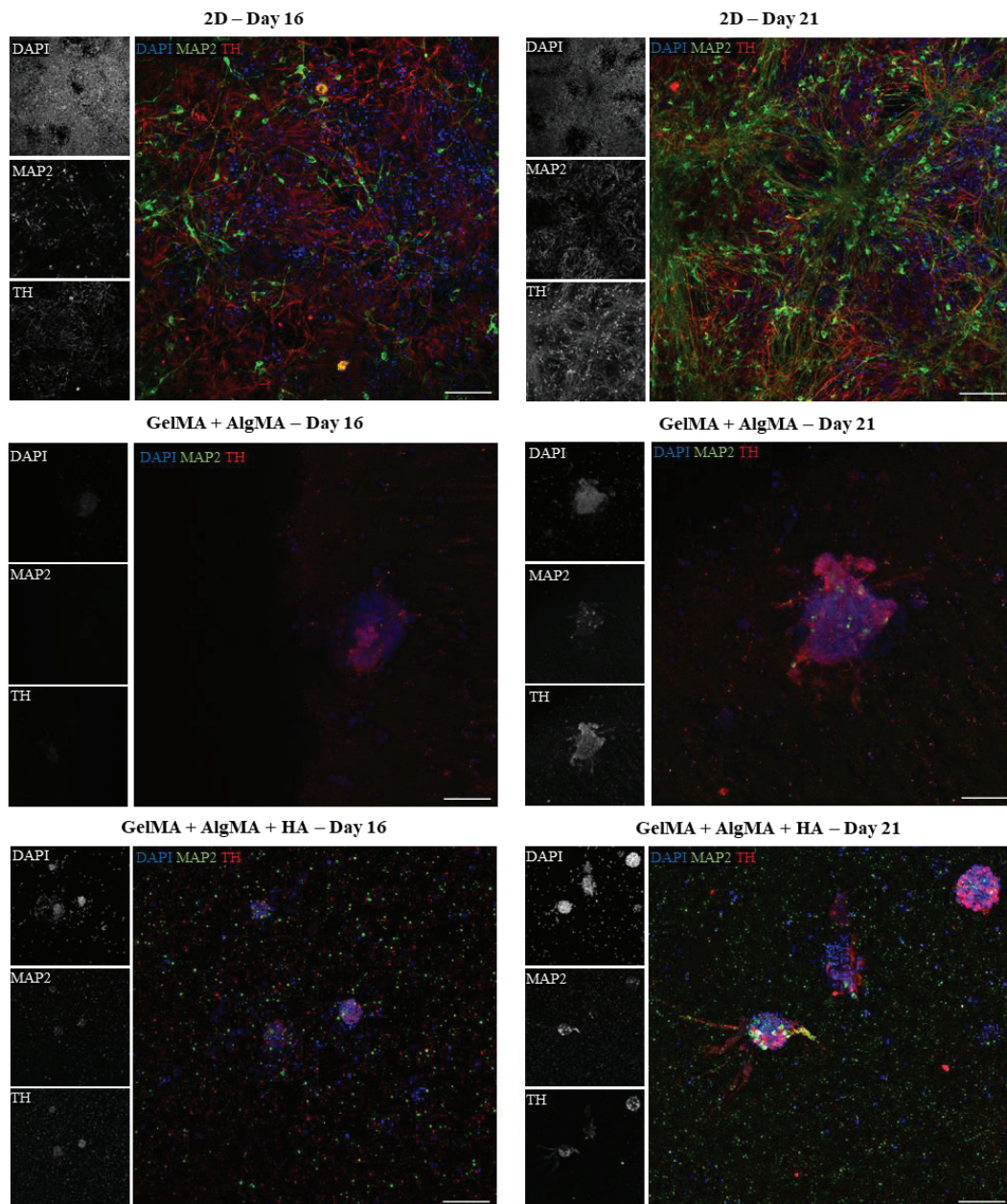


Figure 44 Differentiation of EPISPC cells embedded in GelMA + AlgMA (control) or GelMA + AlgMA + HA hydrogels. Representative confocal images of immunofluorescence assay performed on EPISPC cells in 2D and

embedded in the biomaterials on days 16 and 21 of differentiation. Nuclei are stained in blue, mature neuron marker MAP2 in green and mDA neuron marker TH in red. Scale bar 100 μ m.

6.3. Viability and differentiation of EPIPSC cells in the 3D microfluidic device

We also wanted to assess how the cells behavior and differentiation inside the 3D microfluidic device we used previously (Figure 39).

For this assay we used days 12, 21 and 28 of differentiation time points, for evaluation of the cells for a longer time, to see if they would reach a more mature state of differentiation (Figure 45A). We could see that similar to the other assay with EPIPSC, the viability values were above 60% in all time points without significant differences between formulations (Figure 45B). When looking at the morphology of the cells, the process of differentiation is noticeable with the increase of axon projections, similar to what we obtained in the 2D culture (Figure 43A).

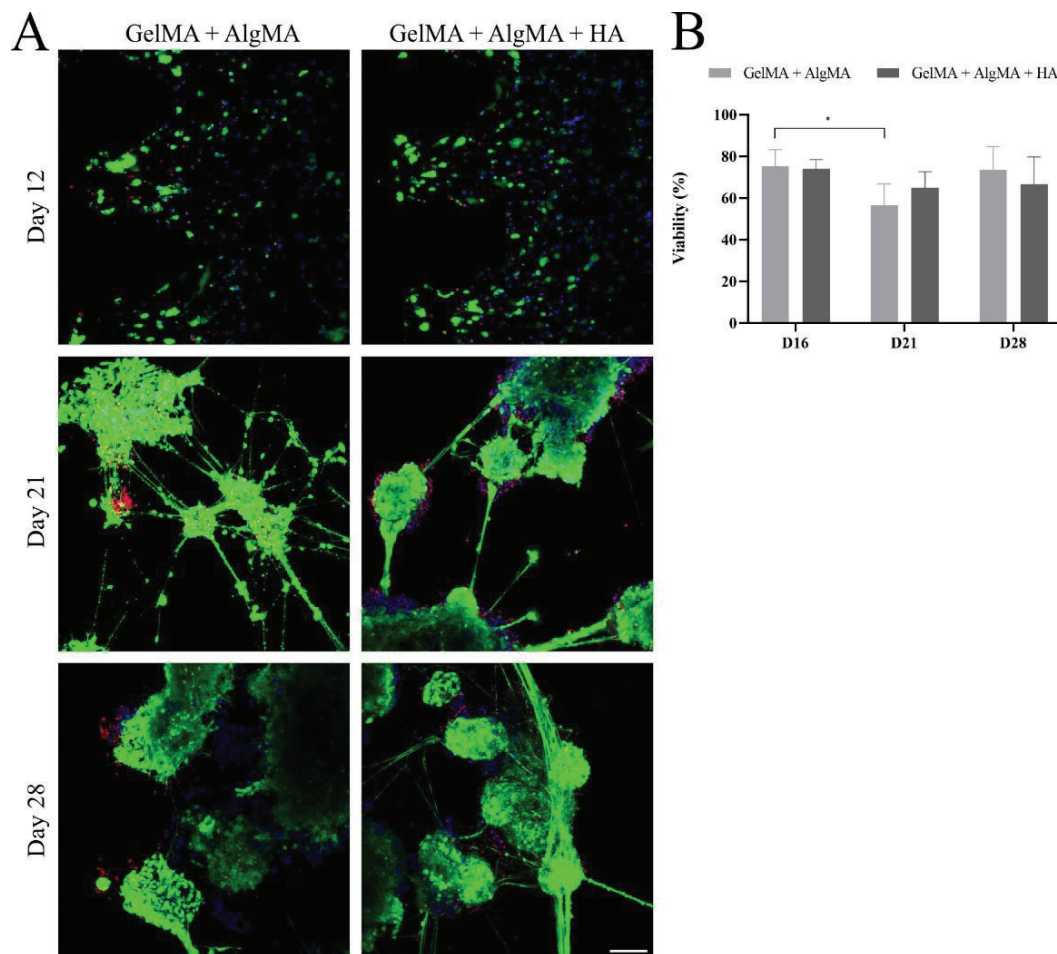


Figure 45 Viability assays on EPIPSC cells cultured in the 3D microfluidic device. (A) Representative confocal images of viability assay images of EPIPSC cells cultured in the device embedded in GelMA + AlgMA (control)

*or GelMA + AlgMA + HA hydrogels at day 12, 21 and 28 of differentiation. Nuclei are stained blue, Calcein AM in green representing the live cells and EthD-1 in red representing the dead cells. Scale bar 100 μ m. (B) quantification of the viability rates of the cells in the two biomaterials. Data are presented as mean \pm standard deviation. Statistical significance was calculated using a two-way variance analysis (ANOVA) with Sidák's post-hoc multiple comparisons test considering $*p < 0.05$.*

From the immunofluorescent assay (Figure 46), on day 16 we could see MAP2 expression on the control formulation but not in GelMA + AlgMA + HA while TH was not visible in either. By day 21, the expression of MAP2 seemed similar on the control hydrogel while starting to be visible on our formulation, especially closer to the lateral channels. We could also observe a morphological change on at day 21 of the control hydrogel that was not visible on the HA formulation. By day 28, both formulations presented MAP2 and TH expression as well as increased cell connectivity.

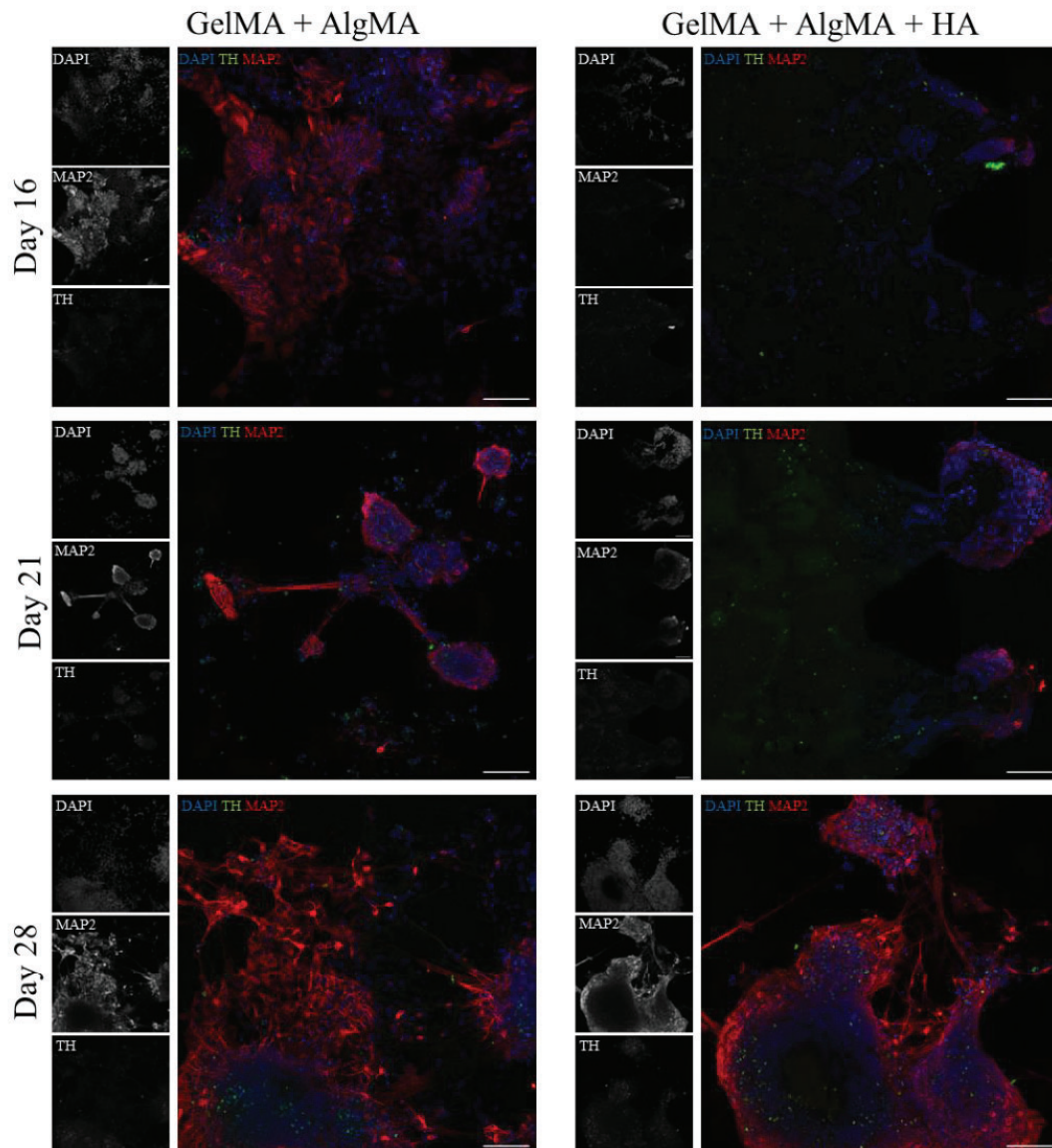


Figure 46 Differentiation of EIPSC cells in the 3D microfluidic device. Representative confocal images of immunofluorescence assay performed on EIPSC cells embedded in GelMA + AlgMA (control) or GelMA + AlgMA + HA hydrogels inside the 3D microfluidic device on days 16, 21 and 28 of differentiation. Nuclei are stained in blue, mature neuron marker MAP2 in green and mDA neuron marker TH in red. Scale bar 100 μ m.

However we observed along the experiments that the hydrogels were degrading faster than what happened on the assays with C17.2 cells. This faster degradation rate was also observed on the drop assays, making it difficult to keep three replicates until the last time points (Figure 47).

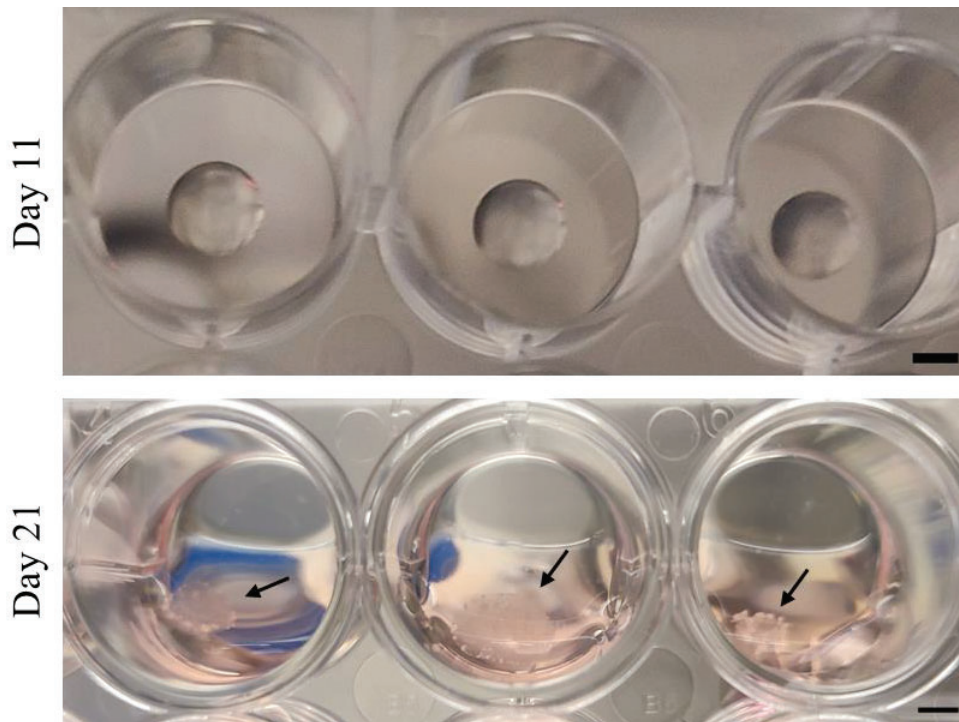


Figure 47 Images of the GelMA + AlgMA + HA hydrogels on day 11 of culture (day of EPIPSC inclusion in the biomaterial) and on day 21 of culture. Scale bar 2.5 mm.

6.4. The influence of the dissolution medium on the 3D culture

Since the cells presented a very round shape through the 3D culture and very few projections on the later timepoints, we wanted to evaluate if the medium where the hydrogels were solubilized would influence the cell culture and differentiation. Usually, when we prepare the biomaterial composite, we dissolve the GelMA, the AlgMA and HA in a cell culture medium overnight and on the next day we mix them with the photocrosslinker LAP and the cells. When we are preparing the samples for the mouse C17.2 cells, we dissolved them in complete proliferation medium since it is the medium where the cells are cultured on the day of seeding. In the case of the EPIPSC cells, on the previous assays we used the base medium (Neurobasal supplemented with B27 and L-glutamine), without specific growth factors to avoid the denaturation of the molecules during the overnight bath at 40°C. However, in this trial we wanted to see if we would see any difference in the cell culture by dissolving the polymers on the complete cell medium of day 11 (Neurobasal supplemented with B27, L-glutamine plus BDNF, GDNF, TGFb3, AA, dbcAMP, Y27632), since it is the day of differentiation the EPIPSC cells were included in the biomaterial.

We performed viability assays on days 12, 16, 21 and 28 of differentiation (Figure 48A). We observed that from day 16 on there was a clear difference in the morphology of the cells

between samples. On samples with D11 medium, the cells presented projections already at that time point, which increased in size and number by day 28. The viability was kept constant throughout the culture and in all conditions, at around 60% (Figure 48B).

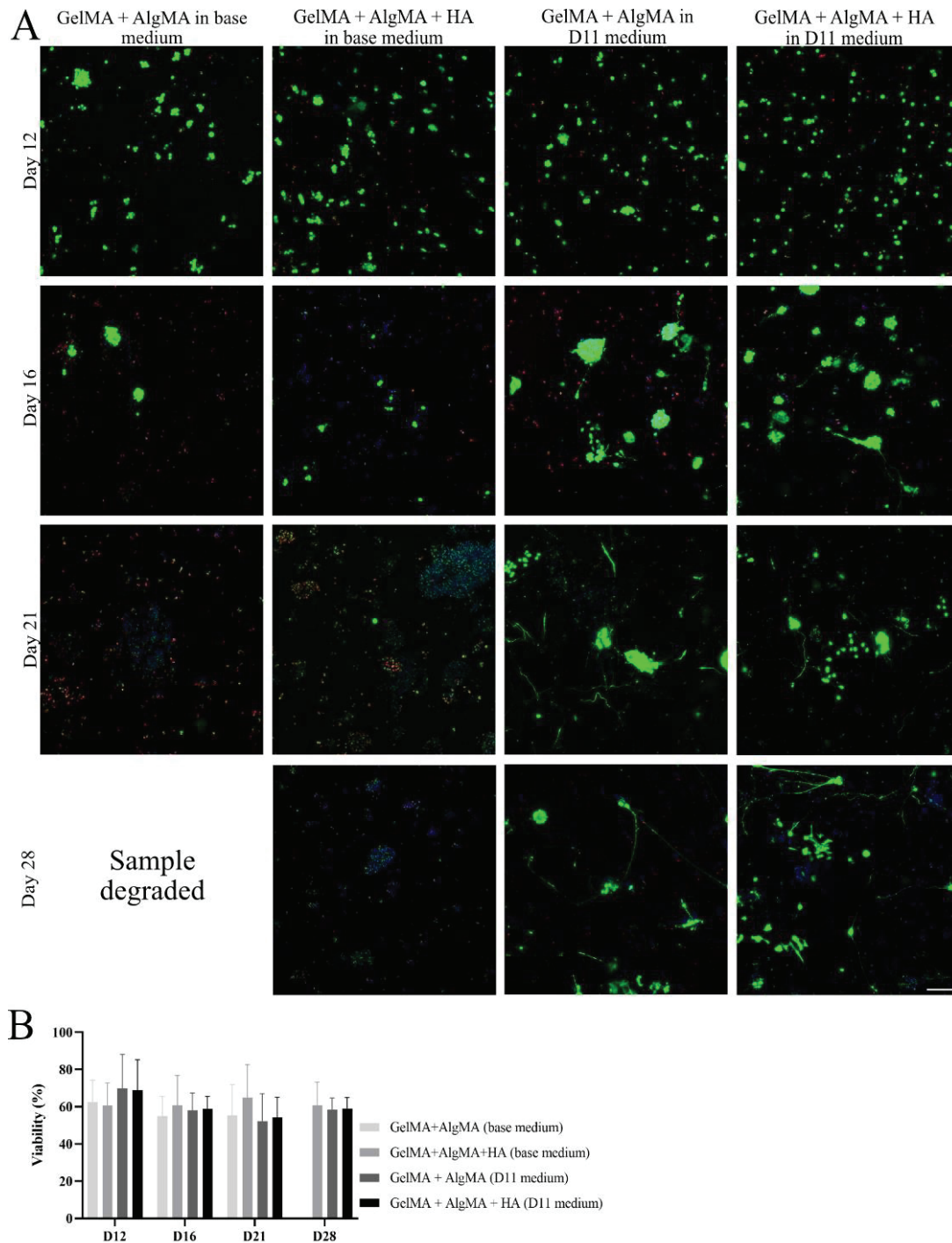


Figure 48 Viability assays of EPIPSC cells cultured in the GelMA + AlgMA (control) or GelMA + AlgMA + HA hydrogels and with two different cell media. (A) Representative confocal images of the viability assay performed on EPIPSC cells embedded in biomaterials where the polymers were dissolved using two different cell culture media (base medium or complete day 11 medium) at day 12, 16, 21 and 28 of differentiation. Nuclei is stained blue, Calcein AM in green representing the live cells and EthD-1 in red representing the dead cells. Scale bar

100 μm . (B) *Quantification of the viability rates of the cells in the four different conditions. Data are presented as mean \pm standard deviation.*

In summary, 5% GelMA + 1% AlgMA + 1.5% HA proven to be a formulation with high viability rates, slow degradation and compatible with the differentiation and functional activity of neuroprogenitor cells. This formulation was compatible with long-term studies, allowing the culture of cells for up to 28 days. When applied as a bioink for extrusion bioprinting, our biomaterial allowed the printing of defined structures while keeping high cell viability and allowing their differentiation. The biomaterial was included in a three-channel 3D microfluidic device and demonstrated high viability rates and differentiation markers for up to day 21 of culture. Human iPSC cells were included in the biomaterial in drop-shape and 3D microfluidic device and presented good viability rates. The differentiation into dopaminergic neurons was also visible but further optimization is required. When testing different cell culture medium for the solubilization of the polymers, the samples with polymers dissolved in complete cell culture medium presented better cell morphology with longer and more frequent projections.

PART II - Development of micro-compartmentalized models for 2D models with iPSC-derived neuronal cells

The study of synapse formation and maturation of neurons is essential to understanding brain development and the alterations that lead to brain pathologies. In the case of medium spiny neurons, their maturation and homeostasis are susceptible to the connections they establish during development. Standard 2D cultures have a heterogenous population during stem cell differentiation that even after purification processes still lacks spatial organization. This restricts the study of network formation between different neuronal populations and its influence on the maturation of one another, in brain development, and disease⁸³. Microfluidic devices offer a solution to this type of culture, with the possibility of culturing multiple neural cell types with axon isolation and directionality, which offers control over the culture conditions and network formation^{264,277}.

Within the Advanced Stem Cell Technologies in Neurobiology Training network we had the opportunity to collaborate with different institutions and contribute to the construction of novel neuronal models. One of the main goals of the project was recreating a cortico-striatal-dopaminergic neuronal model in an organ-on-a-chip platform. To assemble this model, combined efforts were made, with our collaborators at University of Barcelona, Clelia Introna, Prof. Josep Canals and Dr. Daniel Tornero at Stem Cells and Regenerative Medicine Laboratory, developing the protocol for the differentiation of hPS-derived striatal and cortical neurons while our collaborators at Karolinska Institute, Guochang Lyu and Prof. Ernest Arenas at Ernest Arenas group, developing the protocol for the differentiation of hiPSC-derived mDA neurons. We designed and fabricated a suitable microfluidic device compatible with the culture of these three cell types, while allowing the isolation of the axons and a unidirectionality found in the native circuit.

The majority of the results presented in PART II are included on the paper: “Introna C., Pereira I., Martin B. C.S., Estarellas M., Comella-Bolla A., Gómez F. P., Lopez-Martinez M.J., Tornero D., Samitier J. and Canals J.M., *Cortical stimulation enhances Medium Spiny Neurons maturation in a brain-on-a-chip model of human cortico-striatal synapse*. *Frontiers in Bioengineering and Biotechnology* (under review).

1. Design and fabrication of a platform for a neuron-on-a-chip model

1.1. 2D microfluidic design with microchannels and 2 cell chamber – 2D-2C device

To facilitate the axon's isolation and co-culture, we designed a microfluidic device with different cell compartments connected with microchannels. The compartmentalized microfluidic device 2D-2C was composed of two circular chambers with a diameter of 12 mm for cell seeding, connected with 1 mm long microchannels (Figure 49A). It integrated oblique microchannels going from 5 μm to 2 μm width to promote axon unidirectionality, going from the wider section (5 μm) to the narrowest (2 μm) (Figure 49B). Square marks were added at 200 μm of the distance between them along the length of the microchannels that separate the two cell chambers to measure how much the axon is growing. The 5 μm high was chosen to restrict the access to cells passing through the narrow channel. Two extra 12 mm diameter chambers were added as reservoirs to avoid evaporation and they were connected by 500 μm width x 4.6 mm length channels to the cell seeding chambers. They also allowed change of medium avoiding direct contact of pipette tip with cells. From the AutoCAD designs, acetate and chrome masks were obtained and used to produce the master (Figure 49C). From the master, we produced the PDMS replicas and irreversibly bonded them to thin glass slides (Figure 49G).

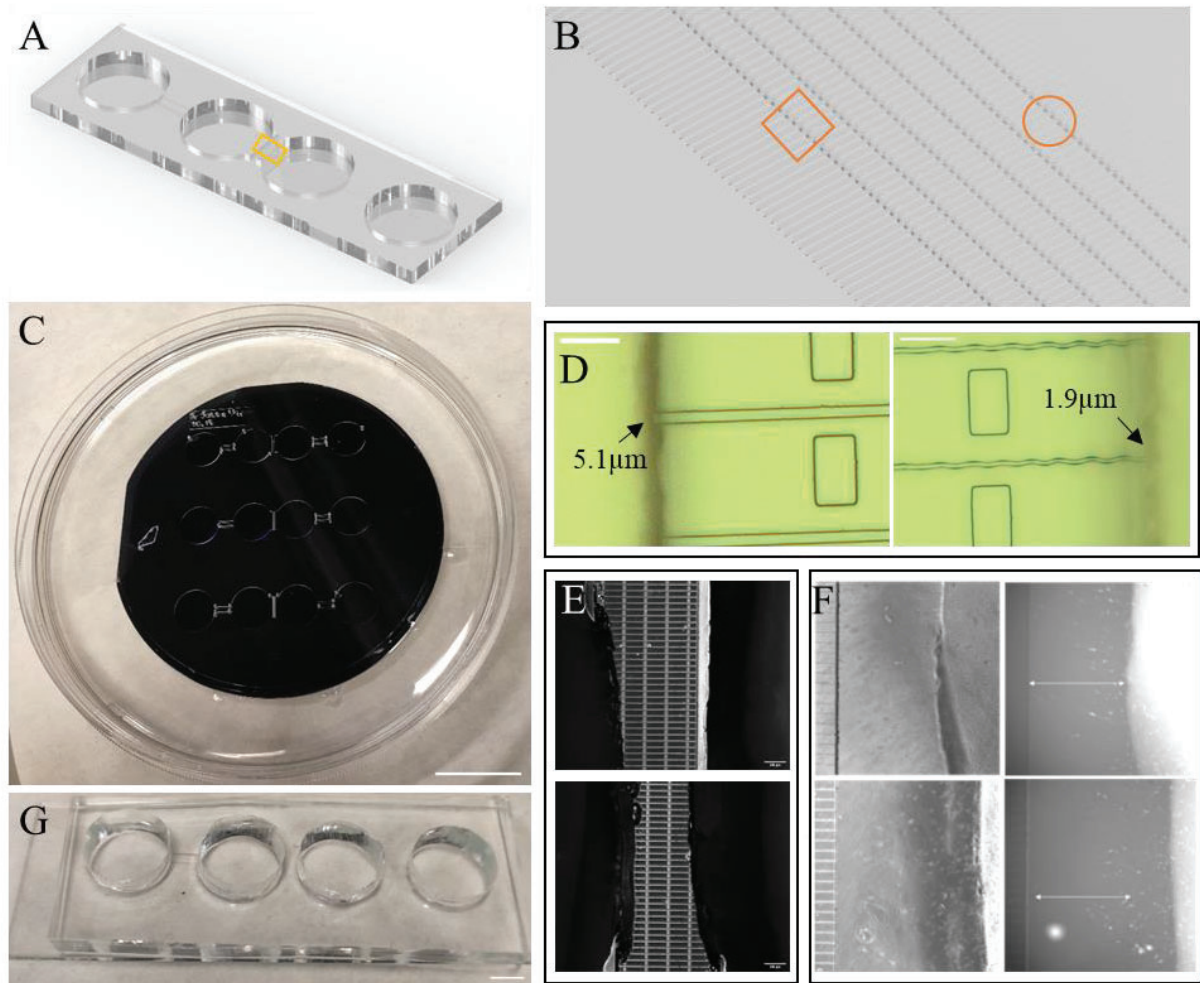


Figure 49 Design and fabrication of microfluidic device 2D-2C. (A) Render of the device. The yellow rectangle represents the zoomed section on (B). Scale bar 5 mm. (B) Zoom section of A presenting the oblique microchannels connecting the two cell chambers. The orange rectangle and circle represent the zoomed images presented in (D). Scale bar 50 μm . (C) Master produced through photolithography. Scale bar 25 mm. (D) Measurements of the width of the microchannels. In the first photo, an arrow is signaling the measure of the larger side of the microchannel, with 5,1 μm represented by the orange rectangle on (B). The arrow on the second photo is showing the measurement of the smaller side of the microchannel, 1.9 μm represented by the orange circle on (B). Scale bar 30 μm . (E) Examples of replicas where the opening of the central chambers cut through the microchannels. Scale bar 200 μm . (F) Culture of NPC on the device and different distances from the cell chamber opening to the microchannels in two different replicas. (G) Final PDMS replica bounded to the glass slide. Scale bar 5 mm.

The manual opening of the central chambers was performed with a punch of 12 mm. Some replicas were discarded because the opening was too close to the microchannels, damaging those (Figure 49E). To measure the growth of the axon, it was important to keep the same length for the cell chamber opening to the microchannels, but this was difficult to achieve by

performing the manual opening of the cell chambers (Figure 49F). To solve this problem another design was created.

1.2.2D microfluidic device with microchannels and 3 cell channels – 2D-3C device

This design had three cell channels with an 8mm diameter inlet and outlet each (Figure 50A). The side channels were 1mm in width and the central, 500 μm , all 220 μm in height. The channels were connected by microchannels also going from 5 to 2 μm wide, 500 μm long and 5 μm high (Figure 50B). The wider part of the microchannels was connected to the side channels and the smaller extremity was connected to the central channel (Figure 50C) and when measuring the microchannels we could observe the smaller end measured 1.85 μm while the other end measured 4.50 μm , which we considered inside the error design (Figure 50G).

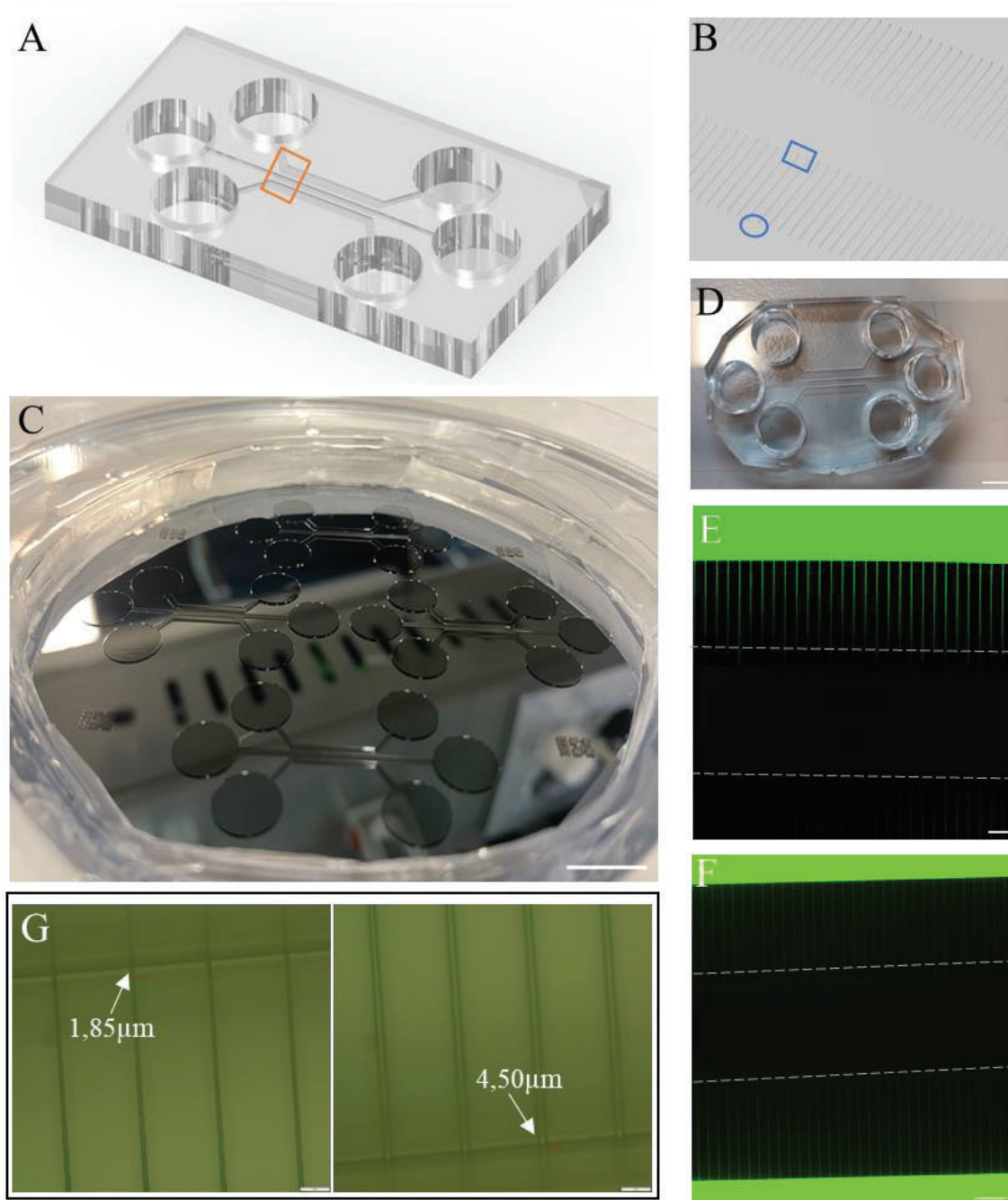


Figure 50 Design and fabrication of microfluidic device 2D-3C. (A) Render of the device. The orange rectangle represents the zoomed section on (B). Scale bar 5 mm. (B) Zoom section of A. The blue rectangle and circle represent the zoomed images presented in (G). Scale bar 250 μm . (C) Master produced through photolithography. Scale bar 25 mm. (D) Final PDMS replica bounded to the glass slide. Scale bar 5 mm. (E) Diffusion assay showing the microchannels stained with fluorescein for 1 hour of a section similar to (B). Dotted lines are placed in the interface between the microchannels and the central channel. Scale bar 100 μm . (F) Diffusion assay after 5 days showed only the lateral channel and the microchannels stained with fluorescein of a section similar to (B). Dotted lines are placed in the interface between the microchannels and the central channel. Scale bar 200 μm . (G) Measurements of the width of the microchannels. In the first photo, an arrow is signaling the measure of the smaller side of the microchannel, with 1.85 μm represented by the yellow rectangle in (B). The arrow on the

second photo is showing the measurement of the larger side of the microchannel, 4.50 μm represented by the yellow circle in (B). Scale bar 20 μm .

Then, we produced the PDMS replicas (Figure 50D) and performed a diffusion test with fluorescein to ensure the microchannels were opened. We could see that after 1 h of incubation, the microchannels were fluorescent, confirming that they were opened (Figure 50E). This information is also useful for the minimum incubation times for the coating of the channels that would need to be performed before cell culture. We also evaluated if there would be diffusion of the fluorescein after 5 days into the central channel, but we observe that that did not happen (Figure 50F) as central part remained without fluorescence. This can indicate that there is no major fluid interchange between the lateral and the central channels, which can permit the co-culture of cell types that need different cell media.

1.3. Co-culture on neuron-on-a-chip - Cortico-striatal circuit model

1.3.1. Differentiation of cortical and striatal neurons

Once the 2D-3C devices were produced, we started the differentiation process of the cells to obtain cortical and striatal neurons in collaboration with Stem Cell and Regenerative Medicine Laboratory at UB.

We evaluated through immunofluorescence the differentiation of the cells cultured inside the device at the last timepoint corresponding to day 55 of the cortical cells' differentiation and day 37 of the striatal cells' differentiation (Figure 51A). Results successfully confirmed the expression of mature neuronal markers (MAP2 and TUBB3) as well as cortical and glutaminergic markers (TBR1 and KGA) (Figure 51B). We could also validate the differentiation of the striatal neurons by the expression of striatal makers including GABA and MSNs markers CTIP2 and FOX1 (Figure 51C), as well as the good survival rate of the co-culture which can be observed by the good confluency of the cells and their morphology on Figure 51D.

1.3.2. Assessment of unidirectional cortical-striatal connection

A fundamental hallmark that we wanted to achieve was to have a synaptic connection that moves from cortical population toward striatal population and not vice versa. To ensure the unidirectionality of the corticostriatal connections happening from the cortical channels to the central striatal channel, the cortical progenitors were seeded 7 days before the other cell type. We could observe the GFP-labeled cortical axons projected to the central (striatal) chamber, validating the efficacy of the design and protocol for the co-culture of these two types of cells

together (Figure 51E). We also accessed the functionality of the cells through calcium imaging to evaluate the formation of functionally active circuits with monodirectional orientation. We could see that after KCl injection in the cortical compartment, asynchronous firing in the cortical cell population occurred, followed by an immediate and simultaneous depolarization in the striatal compartment (Figure 51F). This event was not observed without the addition of KCl.

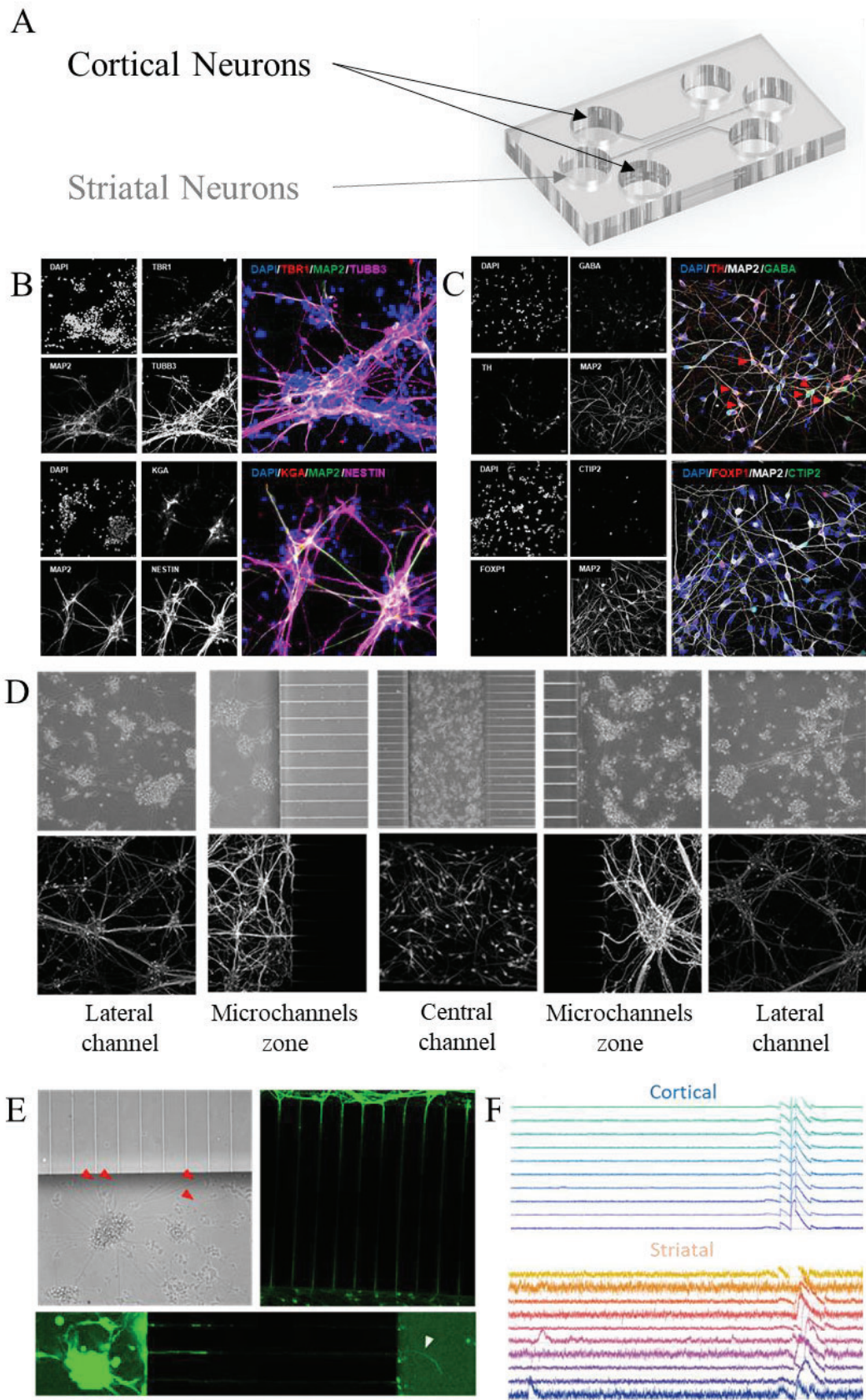


Figure 51 Biological assays performed on microfluidic device 2D-3C for the cortico-striatal neuronal model. (A) Schematic of the placement of the two different cell types, cortical and striatal neuron, in the microfluidic device.

Cortical neurons were seeded on the lateral channels and striatal neurons were seeded on the central channel. (B) Representative confocal images of iPSC-derived cortical neurons. (C) Representative confocal images of iPSC-derived striatal neurons. (D) Representative fluorescence images of co-culture of cortical and striatal neurons cultured in the microfluidic device. (E) Representative fluorescence images of cortical neurons cultured on the lateral chamber and their projections reaching the central chamber. Red arrows point to the projections entering the microchannels and white arrow points to the projection reaching the central channel. (F) Functional assay through calcium imaging of the co-culture.

1.4. Co-culture on neuron-on-a-chip - Striatal-dopaminergic circuit model

We then used the 2D-3C device to replicate the midbrain-striatal circuitry, affected in Parkinson's disease (PD) in collaboration with Ernest Arenas' group (Figure 52).

1.4.1. Impact of the co-culture on the differentiation of mDA neurons

We could observe differences in morphology of the two types of culture. In the control model with PD-mDA neurons cultured with EIPSC cells, the morphology of the cells on the lateral channels (dopaminergic neuron compartment) was more heterogeneous, with cells presenting a neuron-like morphology with elongated projections and epithelial-like cells attached to the bottom (Figure 52B). In the co-culture model where PD-mDA neurons were cultured with striatal neurons, the cells in the lateral channels had a homogeneous morphology with a better axon orientation towards the microchannels (Figure 52C).

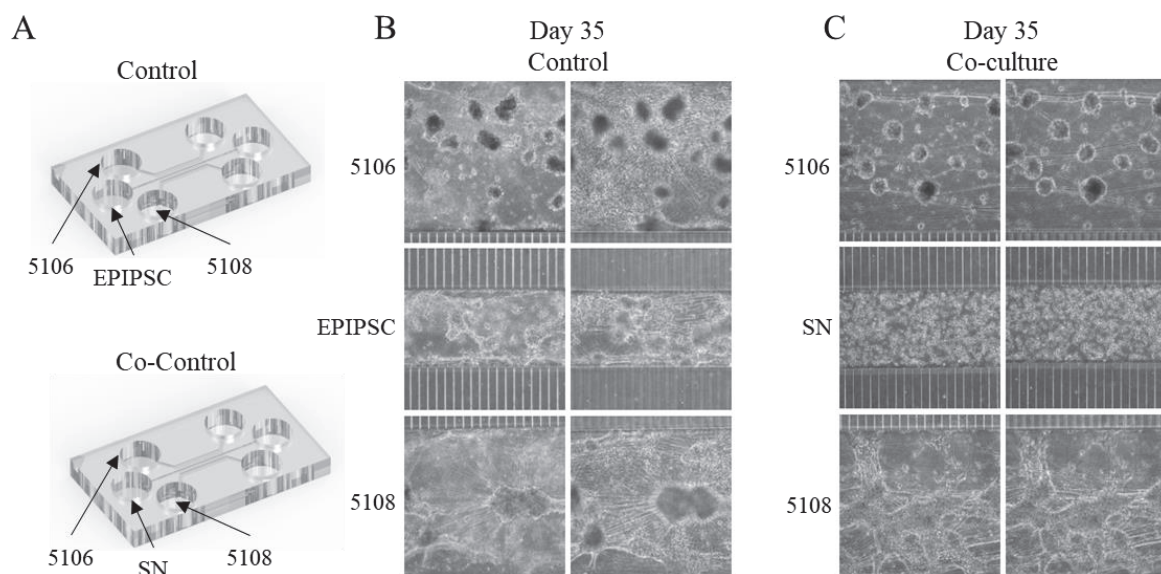


Figure 52 Co-cultures with mDA or striatal neurons on the microfluidic device 2D-3C. (A) The layout of the design of the microfluidic device with the indication of where the different cells were cultured. 10x magnification brightfield images of co-cultures with PD-iPSC mDA neurons (5106; 5108; DIV 35), and (B) control mDA

(EIPSC; DIV 35) or (C) striatal (DIV 42) neurons. Images were taken at different focal planes to demonstrate stratified layers of cells in controls.

In summary, two different designs were created to allow the co-culture of neural cells with axon's isolation and directionality. The second design designated 2D-3C with three channels connected with oblique microchannels was proven to have a more reproducible fabrication process. This design was also compatible with the culture and differentiation of cortical, striatal and dopaminergic neurons. The co-culture of cortical and striatal neurons was also achieved, validating the unidirectionality of the cells from the lateral channels to the central channel and the influence of cortical neurons in the activity of striatal neurons. 2D-3C device was also applied to the modelling of the dopaminergic-striatal circuit, where the co-culture model intended to a more homogeneous population of dopaminergic neurons than the control.

Chapter 5 - Discussion

1. The development of a suitable hydrogel to support the culture and differentiation of neurons

There is a considerable shift in cell culture to 3D models where new key players are introduced to bring complexity and better recreate the tissue in study²⁷⁸. One of these key players in the brain is the ECM. Due to the high sensitivity of neural cells, it is challenging to create an artificial matrix that ensures the support and mobility of the cells, while lasting the long-term culture protocols associated with the differentiation of these cells and allowing a correct diffusion of oxygen and nutrients²⁷⁹.

From the several explored materials used in 3D culture, hydrogels are used for their high-water content, biocompatibility, and elastic properties¹³⁷. Gelatin and Alginate are two popular natural-sourced materials, commonly chemically modified to create scaffolds alone or together^{159,280}. Both materials are biocompatible but have different degradability: gelatin is more degradable for its RGD binding sites which aid cell mobility while being exposed to MMP secreted by the cells degrades the matrix; alginate is less degradable by the cells but in return has less cell-binding sites. Together, these materials combine their advantages. The components present in the native brain ECM are materials desired to include artificial matrixes to incorporate the effect and architecture they have on the native tissue. HA is a polysaccharide highly present in the brain ECM^{119,281}. It is known to influence cell differentiation and is currently being explored for different types of 3D cultures.

To reach the final formulation, we evaluated several different polymer concentrations in the biocompatibility with cell culture and differentiation and durability in culture. Formulations containing 3% GelMA, 0.5% AlgMA and 0.5% or 5% HA presented small projections from the day one, increasing by day 8 as well as the β -III tubulin expression. However, these formulations would degrade quickly after one week of culture, especially the formulations with higher concentration of HA, demonstrating their unsuitability for long-term culture protocols. By increasing the GelMA and AlgMA concentration, we observed presented shorter cell projections at day 8 probably due to the higher concentration of the polymers which can create a stiffer environment that translates to a late start of cell mobility. However, 5% GelMA + 1% AlgMA + 1.5% HA supported the culture and differentiation while presenting minimal degradation after 8 days in culture, being selected as the working formulation.

We studied the physical characterization of this formulation coupled with the control formulation without HA. The diffusion of water, nutrients, and gases is essential for the survival of cells in 3D scaffolds as well as their mobility within the biomaterial. The swelling rate and porosity of the biomaterial are related to swelling rates increasing with an increase in porosity²⁸². The control formulation presented values of the swelling rate as previously reported by the group²⁸³ while our formulation with HA had slightly higher values of water intake. This result is consistent with previous works since HA formulations have previously been shown to increase the water uptake capability of scaffolds¹¹⁹. The stiffness is another important parameter of the 3D biomaterial since it can directly affect the differentiation and the activity of the cells^{119,284}. From the compression assay, our results showed that both formulations had values within the 1-10 kPa elastic modulus range, meaning that they are optimal for neuronal models¹²⁰, with GelMA + AlgMA + HA formulation reaching a slightly lower value compared with the control. This can be explained by the high-water intake of HA mentioned before. Also, the degradation rate is an important feature to be evaluated since the degradation can help neuronal cells to spread and move across the material or even control the differentiation of neuronal progenitor cells^{285,286}. Herein, results showed that both materials were degraded over time, with the biomaterial with HA having a slightly longer time of degradation which being beneficial for long-term assays, allowing more time for cells to adapt to the environment and start producing their own ECM.

From the SEM results, the porosity of the surface of our formulation and the control was visible, both having a high frequency of pores. A smaller pore size was measured in the formulation with HA which could be attributed to the complexity of the formulation. In other published works, the SEM images of biomaterials with similar compositions presented much bigger pores^{119,287,288}. This could be due to the methodology used for processing the samples for SEM analysis. Most works do freeze drying before the SEM analysis and this process can induce the production of bigger pores due to ice crystals^{282,287,289}. A high swelling rate in combination with a smaller pore size could also be an indicator that water was being absorbed by the pore walls¹²⁸. Another important point is that with the degradation of the biomaterial during the culture, the size of the pore is set to increase. With the increase in the pore size, cells tend to have higher extrusion of filopodia²⁹⁰. This is present in the results of these formulations in the immunostaining images, whereby on day 15 the cells presented bigger projections and connectivity as well as on the SEM images on day 15 the cell number and connectivity increased, which could be helped by the increase in pore size of the matrix.

Regarding the results for the evaluation of the compatibility with the neuronal cell culture and differentiation. The formulation with HA was demonstrated to be compatible with long-term culture (28 days), with viability rates similar of those of the control formulation. Cell proliferation was visible in the increased number of cells from day 1 to day 15 of culture. Mammalian cells usually proliferate until reaching that state of proximity where they stop division, cell growth, and motility²¹³. NPC, including C17.2 cells, are proliferative until they enter the post-mitotic phase during differentiation^{291,292}. Differentiation was also possible in the composite formulation with stable values of nestin expression and increasing β -III tubulin expression. These results can indicate that the C17.2-derived NPCs populations mature at different rates and one subpopulation keep an immature state while the other subpopulation of NPCs undergoes neural differentiation and maturation. However, the decrease in gene expression of Pax6 and DLX at the last timepoint is consistent with a large differentiation of NPCs, being more relevant for those NPCs cultured on GelMA + AlgMA + HA. The gene expression of nestin and β -III tubulin was coherent with the immunofluorescence assays by day 15. In addition, significant differences in the expression of the neuronal marker β -III tubulin were observed in the immunofluorescent assays at day 21, where GelMA + AlgMA + HA presented a significant increase in the expression of β -III tubulin compared to the control, meaning that cells were differentiating to neurons and validating our formulation suitable for neuronal culture and differentiation. The results were complemented by showing the expression of MAP2 and S100b, increased by day 15. These two markers indicated that part of the population was indeed differentiated into mature neurons but also there were astrocytes present. C17.2 cells are described to differentiate into a mixed population of neurons and astrocytes^{275,293}. However, in the formulation with HA, the expression of S100b was lower than the formulation without HA, suggesting a smaller population of astrocytes about neurons, which probably could be related to the better spontaneous activity observed. However, by day 28, the expression of most differentiation genes had decreased compared with day 15, which could be an indication of degeneration of differentiated C17.2 cells by that late timepoint, resembling the decrease in β -III tubulin and MAP2 reported in²⁹². Nevertheless, analyzing the β -III tubulin values at timepoint 28 it seems that GelMA + AlgMA + HA composition slows down this degeneration process compared with hydrogels without HA. The degeneration of differentiated neuronal cells may be produced by an unfavorable environment to maintain neuronal cells or a lack of enough cell networks that are necessary for long-term neuronal survival in vitro. The degradation of the hydrogels in both formulations is low until day 28, the interaction between neuronal cells seems that it's enhanced at day 28 with neuron clusters

formation, and the environmental conditions are not significantly modified suggesting that could be necessary between day 15 and 28 a modification of the media conditions to maintain the differentiation process.

The compatibility of a biomaterial with electroactive cultures is very important for the survival and maturation of the cells, especially from neural lineage¹²¹. Our formulation was proven to be electroconductive, with C17.2 being able to spontaneously fire. Our formulation outperformed the control formulation, presenting a higher number of spontaneous spikes. At day 28 the frequency of spikes increased, validating the maturation of the cell network formed in the system.

The increase in the spontaneous activity can indicate a more mature population which is contradictory to the PCR results that show a decrease in the general gene expression of neural markers by the same time point. Gene expression is precedent to protein expression²⁹⁴ and it can be an indicator that the protein expression of markers could decrease in the following days of culture if samples are in culture. Another explanation would be negative feedback, where the amount of markers would be sufficient for the full differentiation and no more gene expression would be needed²⁹⁵. We could also be measuring the activity and protein expression of only a part of the culture and not the entirety of it in Ca^{2+} imaging, whereas in PCR analysis, the quantification is for the entire sample. Then, the results obtained may indicate a mature population only referred to a subpopulation. It would be necessary more experiments to further validate these results and to understand which of these scenarios is the one taking place.

2. The composite hydrogel as bioink for extrusion bioprinting of neuronal cells

3D printing is a revolutionary technique that allows the controlled deposition of biomaterials and cells, solving the lack of control over the fabrication of 3D cultures. Extrusion bioprinting is one of the most used bioprinting methods, but the viability of the cells can be affected by the shear stress while printing²⁹⁶. The results obtained after bioprinting C17.2 cells in a defined square grid showed that the viability was higher than 80% after printing and this value was kept in the following two weeks, indicating that the formulations were able to be printed with a good definition without damaging the cells. Throughout the culture, cells proliferated until day 15, where they appear to reach confluency, identical to the increased proliferation observed in the previous results using hydrogel drops. A change in the morphology of the cells was distinguishable, going from having a round shape on the day after printing, to showing small

projections one week later and increasing those projections and cell connectivity by the last time point. A change in the size of the nuclei was noticed as well, from being characteristically big in the case of NP cells to decreasing over time, indicating the transition from NP to a neural phenotype, validating the process of differentiation²⁹⁷. The expression of nestin was constant throughout the two weeks while the expression of β -III tubulin increased over time, especially by day 15, coincident with the results obtained with the drop-shaped samples discussed in the previous section.

Despite the challenges in recording the activity of neuronal networks in 3D, spontaneous activity was detected on both hydrogels, with GelMA + AlgMA + HA outperforming the control formulation with a higher number of spontaneous spikes of activity. The increase in the number of spontaneous activity spikes is a characteristic of the maturation of neuronal culture²⁹⁸, which points to our formulation being capable of supporting the culture of a mature neuronal network.

3. Combining microfluidic devices and the developed hydrogel to create a 3D culture model

Microfluidic devices can be of assistance to 3D culture is the reduction in the size and quantity of materials used for culture and reagents for the monitoring assays²⁹⁹. To assess if the biomaterial we have developed would adapt to a 3D neuron-on-a-chip, we used a similar design, with three channels, where the biomaterial and C17.2 cells were cultured in the middle and the cell culture media were added to the lateral channels.

We kept the cells in culture for up to 28 days, measuring their viability rate and assessing if the differentiation was taking place by immunofluorescence assays. The results showed viability rates similar to the ones observed on the other assays with this HA formulation, although it slightly decreases over time. We could observe that the cells tend to concentrate in the contact area with the cell media channels. This could indicate that the cells are seeking a more nutritious space, pointing out that the dimensions of the device might not be ideal for a correct diffusion of cell culture media. The decrease in viability can also be linked to the time of culture. C17.2 cells are mouse cells that usually differentiate in 10 days. Time points further than that can lead to the degeneration of the fully differentiated cells. However, it was important to access if the system would last long-term culture and so we kept the culture up until day 28.

From the immunostaining, we can see a stable expression of nestin and increasing expression of β -III tubulin, in agreement with the previous 3D assays. However, in this case, the biomaterial seemed to be degrading and losing shape after day 21 in culture. We hypothesize that a smaller quantity of biomaterial (10 μ l) contributes to faster degradation. In comparison with the assays of viability, this degradation was not so visible. The type of assay also influences the final state of the culture when acquiring the images. In immunofluorescence assays, there are more steps in the protocol that include a fixation process and more washes. This can influence the degradation of the material, that at the end of long protocols such as this, can decrease its size.

We performed a functional assay on day 15 to see if, by that time point, there would be spontaneous activity. We were able to detect spontaneous activity, proving that the neuronal network was being formed in the model.

There are still some parameters to tune in this model. The size of the middle channel in proportion to the lateral channels might be too big to allow a correct diffusion of media. In the

future we would like to test the device under perfusion, to see if the diffusion of media would be improved and assess the influence of that in the culture. Another point to evaluate would be changing the dimensions of the design, ensuring that we can adapt the architecture to fit with the 3D culture more efficiently.

4. Inclusion of human pluripotent stem cells into the 3D cultures

After validating the suitability of the developed biomaterial for mouse neural culture and differentiation, we moved to the inclusion of hiPS-derived dopaminergic neurons in the model. It is unquestionable that to study the human brain and its pathologies, the *in vitro* model must include cells of human origin. The great advances in iPSC culture have allowed the development of differentiation protocols to achieve several types of neurons in healthy conditions or patient-derived, contributing to the modeling of several neurological disorders.

The viability studies performed showed a similar viability rate in 3D when compared to the 2D culture on the first time point but decreased in the following two, especially on the formulation without HA. The morphology of the cells was different between these conditions. In 3D, the cells presented a rounder shape, often dying when far from other cells, only starting to present some projections by day 21 of differentiation. This could indicate the material was not facilitating the movement of the cells, especially at the first time points. When checking for the expression of TH and MAP2, markers of mDA and mature neurons, we could see their expression by the latest time point as well, even though the staining was weak, pointing out that the cells were able to start their differentiation within the system. Another phenomenon we observed was a faster degradation of the samples, compared to the assays with C17.2 cells. Further studies are needed to confirm these results and assess if the composition of the biomaterial needs to be adjusted to further promote cell mobility.

In the study in the 3D microfluidic device, we could see better viability rates but after day 21, the biomaterial was mostly degraded. The cells also tended to cluster. However, several projections between the cell clusters were visible, which would indicate the cells were viable. We did not observe high levels of TH expression at any time point, but there was an increase in MAP2 expression. Between formulations, there is an apparent difference in the MAP2 expression on the first two time points, with GelMA + AlgMA showing higher protein expression, but the layout of the cells and biomaterial indicated that on the HA formulation, the biomaterial was less degraded and that could translate to a higher difficulty of the antibodies to penetrate. We could not conclude if our formulation GelMA + AlgMA + HA had a visible effect and differences on the culture of EIPSC in comparison with the control, but cells were viable, featuring a high capacity of metabolism and remodeling the environment within the material. Further assays are needed to optimize the culture conditions and immunofluorescence protocols.

The degradation of the samples in both models could be due to the composition of the cell culture media. The media of the differentiating cells is full of small molecules which vary in composition according to different time points in culture. Some of these small molecules, such as BDNF, GDNF and DAPT, stimulate cells to increase their metabolic activity in culture^{300–302}. This can translate to the production of enzymes by the cells that degrade the natural polymers present in the biomaterial.

Another study was performed where we changed the solution to where the polymers were dissolved before culture. In the other assays, GelMA, AlgMA, and HA were dissolved in the base medium of the cells. A medium without small molecules is added to differentiate the cells. Since these molecules can be degraded at temperatures close to 40 °C, we thought to spare their use for the solubilization process that happens at 40 °C, saving money as well. However, we tested if by solubilizing the polymers with the complete medium at day 11 there would be some difference in the viability of the cells. In terms of viability rates, we did not see significant differences between conditions but the same did not happen in the morphology. Surprisingly, as early as day 16 of differentiation, there was a clear difference between conditions. The samples with complete medium started showing projections from one cluster of cells to the other. On the following time points, these projections increased in number and length. Further studies are necessary to understand in depth if the physical structure of the material is changed or if the metabolic activity of the cells is increased.

These studies point to compatibility of the culture while also giving rise to new questions. In most published works there is no particular emphasis on the solution used to solubilize the polymers. Some studies use water³⁰³, others PBS³⁰⁴, or even complete medium²⁸³. These last results generated us more questions about the solubilization method and its influence on the culture. Further studies should be performed to validate these observations and evaluate the influence of the dissolution media in the physical characteristics of the biomaterials (stiffness and degradation for example) as well as the viability, morphology, motility and differentiation of the cells in culture.

5. Neuron-on-a-chip for recreation of cortico-striatal and dopaminergic-striatal communication

There are several areas of the brain where the connection between neural cells has a distinct direction that cannot be replicated in a well-plate³⁰⁵. In 2D cultures, the multi-culture of cells is difficult to achieve and when the cell population is heterogeneous, the orientation of the cells is unpredictable.

The cortico-striatal circuit connects the cerebral cortex responsible for cognitive functions to the striatum, responsible for motor control. This circuit is unidirectional, going from the cortex to the striatum and the disruption can lead to diseases such as HD³⁰⁶. It is important when modeling such a connection that unidirectionality is ensured.

Microcompartmentalized devices arise as a helpful solution to culture multiple cell types in communications in a controlled environment. The malleability of the design of microfluidic devices makes these models able to isolate the axons from the soma of the cells, allowing the study of axons' growth and cell-cell communications²⁶⁴.

In this work we developed first a device with separate cell compartments connected by oblique microchannels, to isolate the axons and promote unidirectionality. On the first design developed, we successfully produced a master with structures as small as 2 μm with the microchannels correctly aligned with the cell chambers. However, since the chambers were manually opened, it was not possible to guarantee reproducibility in the fabrication of the replicas. A second design was done, this time with three different cell channels, connected again with oblique microchannels.

This optimized design was used for the recreation of cortico-striatal and nigra-striatal circuits. We successfully differentiated cortical and striatal neurons as well as dopaminergic and striatal neurons until full maturation, without media contamination that could difficult the differentiation protocol. Apart from the differentiation, the cells of the cortico-striatal model were able to form active synapses and give rise to spontaneous action potentials. This event was not observed without the addition of KCl, which led us to conclude that the cortical neurons were able to induce the firing of the striatal MSN over the connections happening through the microchannels.

From the nigro-striatal model, we observed a difference in the morphology of the mDA cells when co-cultured with striatal neurons, suggesting an influence in the differentiation where in

the co-culture the morphology of the cells was more homogeneous, implying the culture could be purer.

Future steps involve combination of these two circuits, recreating the cortico-striatal-nigral connection. It would be important to have a model to study the influence of each cell type in brain development and use patient-derived cells, studying this connection in the case of HD and PD. The design of the device can also be adapted to include more cell channels and allow the culture of other cell types such as glia cells (astrocytes, oligodendrocytes, microglia, etc.) which play a critical role in brain development and pathologies.

Chapter 6 - Conclusions

1. Different concentrations of GelMA, AlgMA and HA were evaluated for the construction of a 3D neural model. 5% GelMA + 1% AlgMA + 1% HA was found to be the suitable formulation from all the other concentrations to explore as a scaffold to culture neuronal cells, with high water intake, low stiffness, and slow degradation rate.
2. This formulation was compatible with the long-term culture of C17.2 cells, lasting up to 28 days in culture while demonstrating good viability rates and increasing expression of neuronal markers.
3. GelMA + AlgMA + HA hydrogel was proven to be electrocompatible with neural culture with cells functionally active in the 3D culture, with increasing spike frequency over the 28 days in culture.
4. The developed formulation was fitting as bioink for extrusion bioprinting of C17.2 cells. The printed structure had a good definition and cells kept high viability rates after printing as well as in the following two weeks of culture.
5. The printed construct was also compatible with the differentiation of the NP cells, proved by the increased expression of β -III tubulin and functional activity of the cells. Significant differences in the activity of the cells were observed when compared with the control formulation, validating the positive effect of HA in the system.
6. GelMA + AlgMA + HA hydrogel was incorporated in the central channel of a 3D microfluidic device flanked by two cell culture media channels. C17.2 cells embedded in the biomaterial were able to survive, differentiate and be functionally active, proving the versatility of this hydrogel to be used in such 3D systems.
7. The first assays with hiPSC-derived dopaminergic neurons suggested that the material was compatible with the culture of these cells in both in drop shape and in the 3D microfluidic device systems by demonstrating good viability values and the start of differentiation. Further optimization of protocols, such as immunofluorescence staining, need to be performed.
8. The assays with hiPSC-derived dopaminergic neurons brought questions to the solubilization method of the hydrogel preparation, with formulations diluted in the complete cell media outperforming the samples prepared with base media in terms of number and length of cell projections.

9. Microfluidic devices were designed for the co-culture and tri-culture of neural cells, with axon's isolation and unidirectionality. SU-8 masters with two layers of distinct heights were successfully produced and PDMS devices fabricated to use for the culture of human derived progenitor cells.
10. The second design, 2D-3C, with three cell channels separated by obliquous channels was found to be the most suitable of the two designs for the culture and differentiation of hPSC.
11. Human cortical and striatal neurons were successfully cultured in this device and able to complete their differentiation. In addition, the connection between the two types of neurons was achieved unidirectionally, from the cortical to the striatal compartment, simulating the directionality this circuit presents *in vivo*.
12. The recreation of the cortico-striatal circuit was further demonstrated through the influence of cortical neurons in the activity of striatal neurons.
13. The device developed was also suitable for the culture of striatal and dopaminergic neurons, recreating the dopaminergic-striatal circuit, with the first trials pointing to an apparent improvement of the differentiation of the dopaminergic neurons when co-cultured, in comparison with the control.

Bibliography

1. Bassett, D. S. & Gazzaniga, M. S. Understanding complexity in the human brain. *Trends Cogn. Sci.* **15**, 200–209 (2011).
2. Shipp, S. Structure and function of the cerebral cortex. *Curr. Biol.* **17**, R443–R449 (2007).
3. Rajmohan, V. & Mohandas, E. The limbic system. *Indian J. Psychiatry* **49**, 132–139 (2007).
4. Leiner, H. C., Leiner, A. L. & Dow, R. S. Cognitive and language functions of the human cerebellum. *Trends Neurosci.* **16**, 444–447 (1993).
5. Benam, K. H. *et al.* Engineered In Vitro Disease Models. *Annu. Rev. Pathol. Mech. Dis.* **10**, 195–262 (2015).
6. Kopell, N. & Ermentrout, B. Chemical and electrical synapses perform complementary roles in the synchronization of interneuronal networks. *Proc. Natl. Acad. Sci.* **101**, 15482–15487 (2004).
7. Zhou, Q. *et al.* Neuroinflammatory astrocytes generated from cord blood-derived human induced pluripotent stem cells. *J. Neuroinflammation* **16**, 164 (2019).
8. Nave, K.-A. & Werner, H. B. Myelination of the nervous system: mechanisms and functions. *Annu Rev Cell Dev Biol* **30**, 503–533 (2014).
9. Tejera, D. & Heneka, M. T. Microglia in Neurodegenerative Disorders. in *Microglia* 57–67 (Springer, 2019).
10. Sweeney, M. D., Ayyadurai, S. & Zlokovic, B. V. Pericytes of the neurovascular unit: key functions and signaling pathways. *Nat. Neurosci.* **19**, 771–783 (2016).
11. Zhao, Z., Nelson, A. R., Betsholtz, C. & Zlokovic, B. V. Establishment and dysfunction of the blood-brain barrier. *Cell* **163**, 1064–1078 (2015).
12. Pogoda, K. & Janmey, P. A. Glial tissue mechanics and mechanosensing by glial cells. *Front. Cell. Neurosci.* **12**, 25 (2018).
13. Rauch, U. Extracellular matrix components associated with remodeling processes in brain. *Cell. Mol. Life Sci.* **61**, 2031–2045 (2004).

14. Shin, Y., Kamm, R. D., Osaki, T., Campisi, M. & Sivathanu, V. In Vitro Microfluidic Models for Neurodegenerative Disorders. *Adv. Healthc. Mater.* **7**, 1700489 (2017).
15. Engler, A. J., Sen, S., Sweeney, H. L. & Discher, D. E. Matrix Elasticity Directs Stem Cell Lineage Specification. *Cell* **126**, 677–689 (2006).
16. Wu, S., Xu, R., Duan, B. & Jiang, P. Three-dimensional hyaluronic acid hydrogel-based models for in vitro human iPSC-derived NPC culture and differentiation. *J. Mater. Chem. B* **5**, 3870–3878 (2017).
17. Budday, S. *et al.* Mechanical properties of gray and white matter brain tissue by indentation. *J. Mech. Behav. Biomed. Mater.* **46**, 318–330 (2015).
18. Russo, C., Senese, R. & Muto, M. Neurodegenerative Diseases in Geriatric Patients BT - Imaging in Geriatrics. in (eds. Guglielmi, G. & Maas, M.) 11–35 (Springer International Publishing, 2023). doi:10.1007/978-3-031-14877-4_2.
19. Kovacs, G. G. Molecular pathology of neurodegenerative diseases: principles and practice. *J. Clin. Pathol.* jclinpath-2019-205952 (2019) doi:10.1136/jclinpath-2019-205952.
20. Garwood, C. J. *et al.* astrocytes in Alzheimer’s disease and other age-associated dementias: a supporting player with a central role. *Neuropathol. Appl. Neurobiol.* **43**, 281–298 (2017).
21. González-Reyes, R. E., Nava-Mesa, M. O., Vargas-Sánchez, K., Ariza-Salamanca, D. & Mora-Muñoz, L. Involvement of astrocytes in Alzheimer’s disease from a neuroinflammatory and oxidative stress perspective. *Front. Mol. Neurosci.* **10**, 427 (2017).
22. Lees, A. J., Hardy, J. & Revesz, T. Parkinson’s disease. *Lancet (British Ed.)* **373**, 2055–2066 (2009).
23. Blauwendraat, C., Nalls, M. A. & Singleton, A. B. The genetic architecture of Parkinson’s disease. *Lancet Neurol.* **19**, 170–178 (2020).
24. Reiner, A. *et al.* Differential loss of striatal projection neurons in Huntington disease. *Proc. Natl. Acad. Sci.* **85**, 5733–5737 (1988).
25. An, P. & Sun, X. Huntington’s Disease : Current Status and Prospects. *J. Cell Signal.* **4**,

- 1–7 (2019).
26. Franklin, R. J. M., Edgar, J. M. & Smith, K. J. Neuroprotection and repair in multiple sclerosis. *Nat. Rev. Neurol.* **8**, 624–634 (2012).
 27. Chun, S. J., Rasband, M. N., Sidman, R. L., Habib, A. A. & Vartanian, T. Integrin-linked kinase is required for laminin-2–induced oligodendrocyte cell spreading and CNS myelination. *J. Cell Biol.* **163**, 397–408 (2003).
 28. Van Horsen, J., Dijkstra, C. D. & De Vries, H. E. The extracellular matrix in multiple sclerosis pathology. *J. Neurochem.* **103**, 1293–1301 (2007).
 29. Shi, Y. *et al.* ApoE4 markedly exacerbates tau-mediated neurodegeneration in a mouse model of tauopathy. *Nature* **549**, 523–527 (2017).
 30. Badhe, R. V., Chejara, D. R., Kumar, P., Choonara, Y. E. & Pillay, V. Neurodegenerative Disease Conditions and Genomic Treatment for Better Health. in *Genomics-Driven Healthcare* 281–310 (Springer, 2018).
 31. Ruiz-Garcia, R. The growing evidence of neurodegenerative diseases risk factors. *Rev. Mex. Neurocienc.* **24**, 1–2 (2023).
 32. Patterson, C. World Alzheimer Report 2018—The state of the art of dementia research: New frontiers. *Alzheimer's Dis. Int. London, UK* (2018).
 33. Cimler, R., Maresova, P., Kuhnova, J. & Kuca, K. Predictions of Alzheimer's disease treatment and care costs in European countries. *PLoS One* **14**, e0210958 (2019).
 34. Möller, H.-J. & Graeber, M. B. The case described by Alois Alzheimer in 1911. *Eur. Arch. Psychiatry Clin. Neurosci.* **248**, 111–122 (1998).
 35. Ahadian, S. *et al.* Organ-On-A-Chip Platforms: A Convergence of Advanced Materials, Cells, and Microscale Technologies. *Adv. Healthc. Mater.* **7**, 1700506 (2017).
 36. Sparrow, J., Hughes, S. M. & Segalat, L. Other model organisms for sarcomeric muscle diseases. *Sarcomere Skelet. Muscle Dis.* 192–206 (2008).
 37. Ericsson, A. C., Crim, M. J. & Franklin, C. L. A brief history of animal modeling. *Mo. Med.* **110**, 201 (2013).
 38. Lorrio, S. *et al.* Novel multitarget ligand ITH33/IQM9. 21 provides neuroprotection in in vitro and in vivo models related to brain ischemia. *Neuropharmacology* **67**, 403–411

- (2013).
39. Huszthy, P. C. *et al.* In vivo models of primary brain tumors: pitfalls and perspectives. *Neuro. Oncol.* **14**, 979–993 (2012).
 40. Daphu, I. *et al.* In vivo animal models for studying brain metastasis: value and limitations. *Clin. Exp. Metastasis* **30**, 695–710 (2013).
 41. und Halbach, O. von B. Modeling neurodegenerative diseases in vivo review. *Neurodegener. Dis.* **2**, 313–320 (2005).
 42. Zhuang, P., Chua, C. K., Chew, S. Y., An, J. & Sun, A. X. 3D neural tissue models: From spheroids to bioprinting. *Biomaterials* **154**, 113–133 (2017).
 43. Breslin, S. & O’Driscoll, L. Three-dimensional cell culture: The missing link in drug discovery. *Drug Discov. Today* **18**, 240–249 (2013).
 44. Tarricone, G., Carmagnola, I. & Chiono, V. Tissue-Engineered Models of the Human Brain: State-of-the-Art Analysis and Challenges. *J. Funct. Biomater.* **13**, 146 (2022).
 45. Harrison, R. G., Greenman, M. J., Mall, F. P. & Jackson, C. M. Observations of the living developing nerve fiber. *Anat. Rec.* **1**, 116–128 (1907).
 46. Centeno, E. G. Z., Cimarosti, H. & Bithell, A. 2D versus 3D human induced pluripotent stem cell-derived cultures for neurodegenerative disease modelling. *Mol. Neurodegener.* **13**, 1–16 (2018).
 47. Wu, S. M. & Hochedlinger, K. Harnessing the potential of induced pluripotent stem cells for regenerative medicine. *Nat. Cell Biol.* **13**, 497–505 (2011).
 48. Gupta, N. *et al.* Microfluidics-based 3D cell culture models: Utility in novel drug discovery and delivery research. *Bioeng. Transl. Med.* **1**, 63–81 (2016).
 49. Duval, K. *et al.* Modeling Physiological Events in 2D vs. 3D Cell Culture. *Physiology* **32**, 266–277 (2017).
 50. Sun, T. *et al.* Development of a 3D cell culture system for investigating cell interactions with electrospun fibers. *Biotechnol. Bioeng.* **97**, 1318–1328 (2007).
 51. Kunze, A., Giugliano, M., Valero, A. & Renaud, P. Micropatterning neural cell cultures in 3D with a multi-layered scaffold. *Biomaterials* **32**, 2088–2098 (2011).

52. Nguyen-Vu, T. D. B. *et al.* Vertically aligned carbon nanofiber architecture as a multifunctional 3-D neural electrical interface. *IEEE Trans. Biomed. Eng.* **54**, 1121–1128 (2007).
53. Soares, C. P. *et al.* 2D and 3D-Organized Cardiac Cells Shows Differences in Cellular Morphology, Adhesion Junctions, Presence of Myofibrils and Protein Expression. *PLoS One* **7**, e38147 (2012).
54. Baharvand, H., Hashemi, S. M., Kazemi Ashtiani, S. & Farrokhi, A. Differentiation of human embryonic stem cells into hepatocytes in 2D and 3D culture systems in vitro. *Int. J. Dev. Biol.* **50**, 645–652 (2006).
55. Liu, H., Lin, J. & Roy, K. Effect of 3D scaffold and dynamic culture condition on the global gene expression profile of mouse embryonic stem cells. *Biomaterials* **27**, 5978–5989 (2006).
56. Jeong, H.-J. *et al.* Engineering Human Brain Organoids: From Basic Research to Tissue Regeneration. *Tissue Eng. Regen. Med.* (2020).
57. Laschke, M. W. & Menger, M. D. Life is 3D: Boosting Spheroid Function for Tissue Engineering. *Trends Biotechnol.* **35**, 133–144 (2017).
58. Dingle, Y.-T. L. *et al.* Three-dimensional neural spheroid culture: an in vitro model for cortical studies. *Tissue Eng. Part C Methods* **21**, 1274–1283 (2015).
59. Sloan, S. A., Andersen, J., Paşca, A. M., Birey, F. & Paşca, S. P. Generation and assembly of human brain region-specific three-dimensional cultures. *Nat. Protoc.* **13**, 2062–2085 (2018).
60. Leite, P. E. C. *et al.* Suitability of 3D human brain spheroid models to distinguish toxic effects of gold and poly-lactic acid nanoparticles to assess biocompatibility for brain drug delivery. *Part. Fibre Toxicol.* **16**, 22 (2019).
61. Lee, H. K. *et al.* Three dimensional human neuro-spheroid model of Alzheimer’s disease based on differentiated induced pluripotent stem cells. *PLoS One* **11**, 1–23 (2016).
62. Xiao, W. *et al.* Alginate Hydrogel Modified with a Ligand Interacting with $\alpha 3\beta 1$ Integrin Receptor Promotes the Differentiation of 3D Neural Spheroids toward Oligodendrocytes in Vitro. *ACS Appl. Mater. Interfaces* **11**, 5821–5833 (2019).

63. Tang-Schomer, M. D., Wu, W. B., Kaplan, D. L. & Bookland, M. J. In vitro 3D regeneration-like growth of human patient brain tissue. *J. Tissue Eng. Regen. Med.* **12**, 1247–1260 (2018).
64. Jorfi, M., D’Avanzo, C., Tanzi, R. E., Kim, D. Y. & Irimia, D. Human neurospheroid arrays for in vitro studies of Alzheimer’s disease. *Sci. Rep.* **8**, 2450 (2018).
65. Brawner, A. T., Xu, R., Liu, D. & Jiang, P. Generating CNS organoids from human induced pluripotent stem cells for modelling neurological disorders. *Int. J. Physiol. Pathophysiol. Pharmacol.* **9**, 101–111 (2017).
66. Hofer, M. & Lutolf, M. P. Engineering organoids. *Nat. Rev. Mater.* **6**, 402–420 (2021).
67. Arlotta, P. Organoids required! A new path to understanding human brain development and disease. *Nat. Methods* **15**, 27 (2018).
68. Lancaster, M. A. *et al.* Cerebral organoids model human brain development and microcephaly. *Nature* **501**, 373 (2013).
69. Lancaster, M. A. *et al.* Guided self-organization and cortical plate formation in human brain organoids. *Nat. Biotechnol.* **35**, 659–666 (2017).
70. Quadrato, G. *et al.* Cell diversity and network dynamics in photosensitive human brain organoids. *Nature* **545**, 48 (2017).
71. Zhou, T. *et al.* High-content screening in hPSC-neural progenitors identifies drug candidates that inhibit Zika virus infection in fetal-like organoids and adult brain. *Cell Stem Cell* **21**, 274–283 (2017).
72. Raja, W. K. *et al.* Self-organizing 3D human neural tissue derived from induced pluripotent stem cells recapitulate Alzheimer’s disease phenotypes. *PLoS One* **11**, e0161969 (2016).
73. Wulansari, N. *et al.* Neurodevelopmental defects and neurodegenerative phenotypes in human brain organoids carrying Parkinson’s disease-linked DNAJC6 mutations. *Sci. Adv.* **7**, eabb1540 (2021).
74. Kelava, I. & Lancaster, M. A. Dishing out mini-brains: Current progress and future prospects in brain organoid research. *Dev. Biol.* **420**, 199–209 (2016).
75. Eglen, R. M. & Reisine, T. Human iPS Cell-Derived Patient Tissues and 3D Cell Culture

Part 2: Spheroids, Organoids, and Disease Modeling. *SLAS Technol. Transl. Life Sci. Innov.* **24**, 18–27 (2019).

76. Gopalakrishnan, J. The Emergence of Stem Cell-Based Brain Organoids: Trends and Challenges. *BioEssays* **41**, 1900011 (2019).
77. Qian, X. *et al.* Brain-region-specific organoids using mini-bioreactors for modeling ZIKV exposure. *Cell* **165**, 1238–1254 (2016).
78. Pham, M. T. *et al.* Generation of human vascularized brain organoids. *Neuroreport* **29**, 588–593 (2018).
79. Lancaster, M. A. & Knoblich, J. A. Generation of cerebral organoids from human pluripotent stem cells. *Nat. Protoc.* **9**, 2329–2340 (2014).
80. Breuls, R. G. M., Jiya, T. U. & Smit, T. H. Scaffold stiffness influences cell behavior: opportunities for skeletal tissue engineering. *Open Orthop. J.* **2**, 103 (2008).
81. Choi, S. H. *et al.* A three-dimensional human neural cell culture model of Alzheimer’s disease. *Nature* **515**, 274 (2014).
82. Sun, J. *et al.* Biomaterials and Advanced Biofabrication Techniques in hiPSCs Based Neuromyopathic Disease Modeling. *Front. Bioeng. Biotechnol.* **7**, (2019).
83. Mofazzal Jahromi, M. A. *et al.* Microfluidic Brain-on-a-Chip: Perspectives for Mimicking Neural System Disorders. *Mol. Neurobiol.* (2019) doi:10.1007/s12035-019-01653-2.
84. Esch, E. W., Bahinski, A. & Huh, D. Organs-on-chips at the frontiers of drug discovery. *Nat. Rev. Drug Discov.* **14**, 248–260 (2015).
85. Roach, P., Fricker, R. A., Evans, M. G., Kamudzandu, M. & Köse-Dunn, M. J. A micro-fabricated in vitro complex neuronal circuit platform. *Biomed. Phys. Eng. Express* (2019).
86. Mackerron, C., Robertson, G., Zagnoni, M. & Bushell, T. J. A Microfluidic Platform for the Characterisation of CNS Active Compounds. doi:10.1038/s41598-017-15950-0.
87. Oddo, A. *et al.* Advances in Microfluidic Blood–Brain Barrier (BBB) Models. *Trends Biotechnol.* (2019) doi:10.1016/J.TIBTECH.2019.04.006.
88. Stacey, G. Primary Cell Cultures and Immortal Cell Lines. in *Encyclopedia of Life*

- Sciences* (John Wiley & Sons, Ltd, 2006). doi:10.1038/npg.els.0003960.
89. Potjewyd, G., Moxon, S., Wang, T., Domingos, M. & Hooper, N. M. Tissue Engineering 3D Neurovascular Units: A Biomaterials and Bioprinting Perspective. *Trends Biotechnol.* **36**, 457–472 (2018).
 90. Rahman, N. A. *et al.* Immortalized endothelial cell lines for in vitro blood–brain barrier models: A systematic review. *Brain Res.* **1642**, 532–545 (2016).
 91. Bordoni, M. *et al.* From Neuronal Differentiation of iPSCs to 3D Neuro-Organoids: Modelling and Therapy of Neurodegenerative Diseases. *Int. J. Mol. Sci.* **19**, 3972 (2018).
 92. Zimmermann, J. A. & Schaffer, D. V. Engineering Biomaterials to Control the Neural Differentiation of Stem Cells. *Brain Res. Bull.* (2019).
 93. Takahashi, K. *et al.* Induction of pluripotent stem cells from adult human fibroblasts by defined factors. *Cell* **131**, 861–872 (2007).
 94. Vadodaria, K. C., Amatya, D. N., Marchetto, M. C. & Gage, F. H. Modeling psychiatric disorders using patient stem cell-derived neurons: a way forward. *Genome Med.* **10**, 6–8 (2018).
 95. Poon, A. *et al.* Modeling neurodegenerative diseases with patient-derived induced pluripotent cells: Possibilities and challenges. *N. Biotechnol.* **39**, 190–198 (2017).
 96. Mahumane, G. D., Kumar, P., du Toit, L. C., Choonara, Y. E. & Pillay, V. 3D scaffolds for brain tissue regeneration: architectural challenges. *Biomater. Sci.* **6**, 2812–2837 (2018).
 97. Koffler, J. *et al.* Biomimetic 3D-printed scaffolds for spinal cord injury repair. *Nat. Med.* **25**, 263–269 (2019).
 98. Jensen, G., Morrill, C. & Huang, Y. 3D tissue engineering, an emerging technique for pharmaceutical research. *Acta Pharm. Sin. B* **8**, 756–766 (2018).
 99. Ali, S., Wall, I. B., Mason, C., Pelling, A. E. & Veraitch, F. S. The effect of Young’s modulus on the neuronal differentiation of mouse embryonic stem cells. *Acta Biomater.* **25**, 253–267 (2015).
 100. Knowlton, S., Anand, S., Shah, T. & Tasoglu, S. Bioprinting for Neural Tissue Engineering. *Trends Neurosci.* **41**, 31–46 (2018).

101. Zhang, D. *et al.* A 3D Alzheimer's disease culture model and the induction of P21-activated kinase mediated sensing in iPSC derived neurons. *Biomaterials* **35**, 1420–1428 (2013).
102. Adil, M. M. *et al.* hPSC-derived striatal cells generated using a scalable 3D hydrogel promote recovery in a Huntington disease mouse model. *Stem Cell Reports* **10**, 1481–1491 (2018).
103. Xu, X. Y. *et al.* The behaviour of neural stem cells on polyhydroxyalkanoate nanofiber scaffolds. *Biomaterials* **31**, 3967–3975 (2010).
104. Silva, G. A. *et al.* Selective differentiation of neural progenitor cells by high-epitope density nanofibers. *Science (80-.)*. **303**, 1352–1355 (2004).
105. Zhang, Q. *et al.* Preparation of uniaxial multichannel silk fibroin scaffolds for guiding primary neurons. *Acta Biomater.* **8**, 2628–2638 (2012).
106. Hanson Shepherd, J. N. *et al.* 3D Microperiodic Hydrogel Scaffolds for Robust Neuronal Cultures. *Adv. Funct. Mater.* **21**, 47–54 (2011).
107. Yang, F., Xu, C. Y., Kotaki, M., Wang, S. & Ramakrishna, S. Characterization of neural stem cells on electrospun poly(L-lactic acid) nanofibrous scaffold. *J. Biomater. Sci. Polym. Ed.* **15**, 1483–1497 (2004).
108. Papadimitriou, L., Manganas, P., Ranella, A. & Stratakis, E. Biofabrication for neural tissue engineering applications. *Mater. Today Bio* **6**, 100043 (2020).
109. Fantini, V. *et al.* Bioink Composition and Printing Parameters for 3D Modeling Neural Tissue. *Cells* **8**, 830 (2019).
110. Potter, W., Kalil, R. E. & Kao, W. J. Biomimetic material systems for neural progenitor cell-based therapy. *Front Biosci* **13**, 21 (2008).
111. Benny, P. & Raghunath, M. Making microenvironments: A look into incorporating macromolecular crowding into in vitro experiments, to generate biomimetic microenvironments which are capable of directing cell function for tissue engineering applications. *J. Tissue Eng.* **8**, 2041731417730467 (2017).
112. Stabenfeldt, S. E., García, A. J. & LaPlaca, M. C. Thermoreversible laminin-functionalized hydrogel for neural tissue engineering. *J. Biomed. Mater. Res. Part A An*

- Off. J. Soc. Biomater. Japanese Soc. Biomater. Aust. Soc. Biomater. Korean Soc. Biomater.* **77**, 718–725 (2006).
113. Khaing, Z. Z. & Seidlits, S. K. Hyaluronic acid and neural stem cells: implications for biomaterial design. *J. Mater. Chem. B* **3**, 7850–7866 (2015).
 114. Lozano, R. *et al.* 3D printing of layered brain-like structures using peptide modified gellan gum substrates. *Biomaterials* **67**, 264–273 (2015).
 115. Crompton, K. E. *et al.* Polylysine-functionalised thermoresponsive chitosan hydrogel for neural tissue engineering. *Biomaterials* **28**, 441–449 (2007).
 116. Haile, Y. *et al.* The effect of modified polysialic acid based hydrogels on the adhesion and viability of primary neurons and glial cells. *Biomaterials* **29**, 1880–1891 (2008).
 117. Wen, Y.-Q. *et al.* Substrate stiffness affects neural network activity in an extracellular matrix proteins dependent manner. *Colloids Surfaces B Biointerfaces* **170**, 729–735 (2018).
 118. Saha, K. *et al.* Substrate Modulus Directs Neural Stem Cell Behavior. *Biophys. J.* **95**, 4426–4438 (2008).
 119. Her, G. J. *et al.* Control of three-dimensional substrate stiffness to manipulate mesenchymal stem cell fate toward neuronal or glial lineages. *Acta Biomater.* **9**, 5170–5180 (2013).
 120. Cadena, M. *et al.* 3D Bioprinting of Neural Tissues. *Adv. Healthc. Mater.* **10**, 2001600 (2021).
 121. Lerner, T. N., Ye, L. & Deisseroth, K. Communication in Neural Circuits: Tools, Opportunities, and Challenges. *Cell* **164**, 1136–1150 (2016).
 122. Lai, Y., Cheng, K. & Kisaalita, W. Three dimensional neuronal cell cultures more accurately model voltage gated calcium channel functionality in freshly dissected nerve tissue. (2012).
 123. Garrudo, F. F. F. *et al.* Polyaniline-polycaprolactone blended nanofibers for neural cell culture. *Eur. Polym. J.* **117**, 28–37 (2019).
 124. Garrudo, F. F. F. *et al.* Polyaniline-polycaprolactone fibers for neural applications: Electroconductivity enhanced by pseudo-doping. *Mater. Sci. Eng. C* **120**, 111680

- (2021).
125. Hwang, J.-Y. *et al.* Biofunctionalized carbon nanotubes in neural regeneration: a mini-review. *Nanoscale* **5**, 487–497 (2013).
 126. Steel, E. M., Azar, J.-Y. & Sundararaghavan, H. G. Electrospun hyaluronic acid-carbon nanotube nanofibers for neural engineering. *Materialia* **9**, 100581 (2020).
 127. Jurga, M. *et al.* The performance of laminin-containing cryogel scaffolds in neural tissue regeneration. *Biomaterials* **32**, 3423–3434 (2011).
 128. Zhao, Q., Sun, J., Lin, Y. & Zhou, Q. Study of the properties of hydrolyzed polyacrylamide hydrogels with various pore structures and rapid pH-sensitivities. *React. Funct. Polym.* **70**, 602–609 (2010).
 129. Huang, G. Y. *et al.* Microfluidic hydrogels for tissue engineering. *Biofabrication* **3**, 12001 (2011).
 130. Wang, L. *et al.* Biomechanical studies on biomaterial degradation and co-cultured cells: mechanisms {}, potential applications {}, challenges and prospects. *J. Mater. Chem. B* **7**, 7439–7459 (2019).
 131. Heljak, M. K., Swieszkowski, W. & Kurzydowski, K. J. Modeling of the degradation kinetics of biodegradable scaffolds: The effects of the environmental conditions. *J. Appl. Polym. Sci.* **131**, (2014).
 132. Madl, C. M. *et al.* Maintenance of neural progenitor cell stemness in 3D hydrogels requires matrix remodelling. (2017) doi:10.1038/NMAT5020.
 133. Madl, C. M. *et al.* Matrix Remodeling Enhances the Differentiation Capacity of Neural Progenitor Cells in 3D Hydrogels. (2019) doi:10.1002/adv.201801716.
 134. Kajtez, J., Nilsson, F., Fiorenzano, A., Parmar, M. & Emnéus, J. 3D biomaterial models of human brain disease. *Neurochem. Int.* **147**, 105043 (2021).
 135. Hull, S. M., Brunel, L. G. & Heilshorn, S. C. 3D bioprinting of cell-laden hydrogels for improved biological functionality. *Adv. Mater.* **34**, 2103691 (2022).
 136. Jose, G., Shalumon, K. T. & Chen, J.-P. Natural polymers based hydrogels for cell culture applications. *Curr. Med. Chem.* **27**, 2734–2776 (2020).
 137. Poorna, M. R., Jayakumar, R., Chen, J.-P. & Mony, U. Hydrogels: A potential platform

- for induced pluripotent stem cell culture and differentiation. *Colloids Surfaces B Biointerfaces* **207**, 111991 (2021).
138. Neves, S. C., Moroni, L., Barrias, C. C. & Granja, P. L. Leveling Up Hydrogels: Hybrid Systems in Tissue Engineering. *Trends Biotechnol.* 1–24 (2019) doi:10.1016/j.tibtech.2019.09.004.
 139. Baiguera, S. *et al.* Electrospun gelatin scaffolds incorporating rat decellularized brain extracellular matrix for neural tissue engineering. *Biomaterials* **35**, 1205–1214 (2014).
 140. Mosahebi, A., Simon, M., Wiberg, M. & Terenghi, G. A novel use of alginate hydrogel as Schwann cell matrix. *Tissue Eng.* **7**, 525–534 (2001).
 141. Sundararaghavan, H. G., Monteiro, G. A., Firestein, B. L. & Shreiber, D. I. Neurite growth in 3D collagen gels with gradients of mechanical properties. *Biotechnol. Bioeng.* **102**, 632–643 (2009).
 142. Cho, H. J., Verbridge, S. S., Davalos, R. V. & Lee, Y. W. Development of an In Vitro 3D Brain Tissue Model Mimicking In Vivo-Like Pro-inflammatory and Pro-oxidative Responses. *Ann. Biomed. Eng.* **46**, 877–887 (2018).
 143. Liang, Y., Walczak, P. & Bulte, J. W. M. The survival of engrafted neural stem cells within hyaluronic acid hydrogels. *Biomaterials* **34**, 5521–5529 (2013).
 144. Hopkins, A. M. *et al.* Silk hydrogels as soft substrates for neural tissue engineering. *Adv. Funct. Mater.* **23**, 5140–5149 (2013).
 145. Pértile, R., Moreira, S., Andrade, F., Domingues, L. & Gama, M. Bacterial cellulose modified using recombinant proteins to improve neuronal and mesenchymal cell adhesion. *Biotechnol. Prog.* **28**, 526–532 (2012).
 146. Tsou, Y.-H., Khoneisser, J., Huang, P.-C. & Xu, X. Hydrogel as a bioactive material to regulate stem cell fate. *Bioact. Mater.* **1**, 39–55 (2016).
 147. Jorfi, M., D’Avanzo, C., Kim, D. Y. & Irimia, D. Three-Dimensional Models of the Human Brain Development and Diseases. *Adv. Healthc. Mater.* **7**, 1700723 (2018).
 148. Kuo, Y.-C. & Wang, C.-C. Guided differentiation of induced pluripotent stem cells into neuronal lineage in alginate–chitosan–gelatin hydrogels with surface neuron growth factor. *Colloids Surfaces B Biointerfaces* **104**, 194–199 (2013).

149. Rauch, U. Extracellular matrix components associated with remodeling processes in brain. *Cell. Mol. Life Sci.* **61**, 2031–2045 (2004).
150. Huang, K.-F., Hsu, W.-C., Chiu, W.-T. & Wang, J.-Y. Functional improvement and neurogenesis after collagen-GAG matrix implantation into surgical brain trauma. *Biomaterials* **33**, 2067–2075 (2012).
151. Cairns, D. M. *et al.* A 3D human brain-like tissue model of herpes-induced Alzheimer's disease. *Sci. Adv.* **6**, eaay8828 (2020).
152. Führmann, T., Hillen, L. M., Montzka, K., Wöltje, M. & Brook, G. A. Cell–Cell interactions of human neural progenitor-derived astrocytes within a microstructured 3D-scaffold. *Biomaterials* **31**, 7705–7715 (2010).
153. Zhou, X. *et al.* Three-dimensional-bioprinted dopamine-based matrix for promoting neural regeneration. *ACS Appl. Mater. Interfaces* **10**, 8993–9001 (2018).
154. Moxon, S. R. *et al.* Blended alginate/collagen hydrogels promote neurogenesis and neuronal maturation. *Mater. Sci. Eng. C* **104**, 109904 (2019).
155. Seidlits, S. K. *et al.* Peptide-modified, hyaluronic acid-based hydrogels as a 3D culture platform for neural stem/progenitor cell engineering. *J. Biomed. Mater. Res. Part A* **107**, 704–718 (2019).
156. Tang-Schomer, M. D. *et al.* Bioengineered functional brain-like cortical tissue. *Proc. Natl. Acad. Sci.* **111**, 13811–13816 (2014).
157. Lynn, A. K., Yannas, I. V & Bonfield, W. Antigenicity and immunogenicity of collagen. *J. Biomed. Mater. Res. Part B Appl. Biomater. An Off. J. Soc. Biomater. Japanese Soc. Biomater. Aust. Soc. Biomater. Korean Soc. Biomater.* **71**, 343–354 (2004).
158. Xiao, S. *et al.* Gelatin Methacrylate (GelMA)-Based Hydrogels for Cell Transplantation: an Effective Strategy for Tissue Engineering. *Stem Cell Rev. Reports* 1–16.
159. Yue, K. *et al.* Synthesis, properties, and biomedical applications of gelatin methacryloyl (GelMA) hydrogels. *Biomaterials* **73**, 254–271 (2015).
160. Bigi, A., Cojazzi, G., Panzavolta, S., Rubini, K. & Roveri, N. Mechanical and thermal properties of gelatin films at different degrees of glutaraldehyde crosslinking. *Biomaterials* **22**, 763–768 (2001).

161. Draye, J.-P. *et al.* In vitro release characteristics of bioactive molecules from dextran dialdehyde cross-linked gelatin hydrogel films. *Biomaterials* **19**, 99–107 (1998).
162. Kim, H., Knowles, J. C. & Kim, H. Hydroxyapatite and gelatin composite foams processed via novel freeze-drying and crosslinking for use as temporary hard tissue scaffolds. *J. Biomed. Mater. Res. Part A An Off. J. Soc. Biomater. Japanese Soc. Biomater. Aust. Soc. Biomater. Korean Soc. Biomater.* **72**, 136–145 (2005).
163. Yue, K. *et al.* Structural analysis of photocrosslinkable methacryloyl-modified protein derivatives. *Biomaterials* **139**, 163–171 (2017).
164. Łabowska, M. B. *et al.* A Review on the Adaption of Alginate-Gelatin Hydrogels for 3D Cultures and Bioprinting. *Materials (Basel)*. **14**, 858 (2021).
165. Neves, M. I., Moroni, L. & Barrias, C. C. Modulating Alginate Hydrogels for Improved Biological Performance as Cellular 3D Microenvironments. *Front. Bioeng. Biotechnol.* **8**, 665 (2020).
166. Chen, Q. *et al.* An interpenetrating alginate/gelatin network for three-dimensional (3D) cell cultures and organ bioprinting. *Molecules* **25**, 756 (2020).
167. Sachdev, A. *et al.* A Review on Techniques and Biomaterials Used in 3D Bioprinting. *Cureus* **14**, (2022).
168. Ning, L. *et al.* Bioprinting Schwann cell-laden scaffolds from low-viscosity hydrogel compositions. *J. Mater. Chem. B* **7**, 4538–4551 (2019).
169. Ding, Y.-W. *et al.* Recent advances in hyaluronic acid-based hydrogels for 3D bioprinting in tissue engineering applications. *Smart Mater. Med.* **4**, 59–68 (2023).
170. Ouyang, L., Highley, C. B., Rodell, C. B., Sun, W. & Burdick, J. A. 3D Printing of Shear-Thinning Hyaluronic Acid Hydrogels with Secondary Cross-Linking. *ACS Biomater. Sci. Eng.* **2**, 1743–1751 (2016).
171. Noh, I., Kim, N., Tran, H. N., Lee, J. & Lee, C. 3D printable hyaluronic acid-based hydrogel for its potential application as a bioink in tissue engineering. *Biomater. Res.* **23**, 3 (2019).
172. Hong, S. *et al.* Hyaluronic acid catechol: a biopolymer exhibiting a pH-dependent adhesive or cohesive property for human neural stem cell engineering. *Adv. Funct.*

- Mater.* **23**, 1774–1780 (2013).
173. Zhang, Z.-N. *et al.* Layered hydrogels accelerate iPSC-derived neuronal maturation and reveal migration defects caused by MeCP2 dysfunction. *Proc. Natl. Acad. Sci.* **113**, 3185–3190 (2016).
 174. Kaiser, A., Kale, A., Novozhilova, E. & Olivius, P. The effects of Matrigel® on the survival and differentiation of a human neural progenitor dissociated sphere culture. *Anat. Rec.* (2019).
 175. Miguel, L. *et al.* Detection of all adult Tau isoforms in a 3D culture model of iPSC-derived neurons. *Stem Cell Res.* **40**, 101541 (2019).
 176. Abbott, R. D., Kimmerling, E. P., Cairns, D. M. & Kaplan, D. L. Silk as a Biomaterial to Support Long-Term Three-Dimensional Tissue Cultures. *ACS Appl. Mater. Interfaces* **8**, 21861–21868 (2016).
 177. Namba, R. M., Cole, A. A., Bjugstad, K. B. & Mahoney, M. J. Development of porous PEG hydrogels that enable efficient, uniform cell-seeding and permit early neural process extension. *Acta Biomater.* **5**, 1884–1897 (2009).
 178. Plant, G. W., Harvey, A. R. & Chirila, T. V. Axonal growth within poly (2-hydroxyethyl methacrylate) sponges infiltrated with Schwann cells and implanted into the lesioned rat optic tract. *Brain Res.* **671**, 119–130 (1995).
 179. Ashammakhi, N. *et al.* Bioinks and bioprinting technologies to make heterogeneous and biomimetic tissue constructs. *Mater. Today Bio* **1**, (2019).
 180. Crowe, J. A. *et al.* Development of two-photon polymerised scaffolds for optical interrogation and neurite guidance of human iPSC-derived cortical neuronal networks. *Lab Chip* (2020).
 181. Woodruff, M. A. & Hutmacher, D. W. The return of a forgotten polymer—Polycaprolactone in the 21st century. *Prog. Polym. Sci.* **35**, 1217–1256 (2010).
 182. Suzuki, K. *et al.* Electrospun nanofiber sheets incorporating methylcobalamin promote nerve regeneration and functional recovery in a rat sciatic nerve crush injury model. *Acta Biomater.* **53**, 250–259 (2017).
 183. Cerrone, F. *et al.* Polyhydroxyphenylvalerate/polycaprolactone nanofibers improve the

- life-span and mechanoresponse of human iPSC-derived cortical neuronal cells. *Mater. Sci. Eng. C* **111**, 110832 (2020).
184. Zhang, S. Designer self-assembling peptide nanofiber scaffolds for study of 3-D cell biology and beyond. *Adv. Cancer Res.* **99**, 335–362 (2008).
 185. Gelain, F., Bottai, D., Vescovi, A. & Zhang, S. Designer self-assembling peptide nanofiber scaffolds for adult mouse neural stem cell 3-dimensional cultures. *PLoS One* **1**, e119 (2006).
 186. Cunha, C., Panseri, S., Villa, O., Silva, D. & Gelain, F. 3D culture of adult mouse neural stem cells within functionalized self-assembling peptide scaffolds. *Int. J. Nanomedicine* **6**, 943–955 (2011).
 187. Aurand, E. R., Wagner, J. L., Shandas, R. & Bjugstad, K. B. Hydrogel formulation determines cell fate of fetal and adult neural progenitor cells. *Stem Cell Res.* **12**, 11–23 (2014).
 188. Cantley, W. L. *et al.* Functional and Sustainable 3D Human Neural Network Models from Pluripotent Stem Cells. *ACS Biomater. Sci. Eng.* **4**, 4278–4288 (2018).
 189. Karvinen, J. *et al.* Soft hydrazone crosslinked hyaluronan- and alginate-based hydrogels as 3D supportive matrices for human pluripotent stem cell-derived neuronal cells. *React. Funct. Polym.* **124**, 29–39 (2018).
 190. Gilbert, T. W., Sellaro, T. L. & Badylak, S. F. Decellularization of tissues and organs. *Biomaterials* **27**, 3675–3683 (2006).
 191. Kabirian, F. & Mozafari, M. Decellularized ECM-derived Bioinks: Prospects for the future. *Methods* (2019) doi:10.1016/J.YMETH.2019.04.019.
 192. DeQuach, J. A., Yuan, S. H., Goldstein, L. S. B. & Christman, K. L. Decellularized porcine brain matrix for cell culture and tissue engineering scaffolds. *Tissue Eng. Part A* **17**, 2583–2592 (2011).
 193. Sood, D. *et al.* Functional maturation of human neural stem cells in a 3D bioengineered brain model enriched with fetal brain-derived matrix. *Sci. Rep.* **9**, 17874 (2019).
 194. Santschi, M., Vernengo, A., Eglin, D., D’Este, M. & Wuertz-Kozak, K. Decellularized matrix as a building block in bioprinting and electrospinning. *Curr. Opin. Biomed. Eng.*

- (2019) doi:10.1016/j.cobme.2019.05.003.
195. Murphy, S. V. 3D bioprinting of tissues and organs: Nature Biotechnology. *Nat. Biotechnol.* **32**, 773 (2014).
 196. Ding, S. *et al.* Bioprinting of Stem Cells: Interplay of Bioprinting Process, Bioinks, and Stem Cell Properties. *ACS Biomater. Sci. Eng.* **4**, 3108–3124 (2018).
 197. Heidarian, P., Kouzani, A., Kaynak, A., Paulino, M. & Nasri-Nasrabadi, B. Dynamic Hydrogels and Polymers as Inks for 3D Printing. *ACS Biomater. Sci. Eng.* acsbiomaterials.9b00047 (2019) doi:10.1021/acsbiomaterials.9b00047.
 198. Naghieh, S., Sarker, M., Sharma, N. K., Barhoumi, Z. & Chen, X. Printability of 3D Printed Hydrogel Scaffolds: Influence of Hydrogel Composition and Printing Parameters. *Appl. Sci.* (2019) doi:10.3390/app10010292.
 199. Chang, R., Nam, J. & Sun, W. Effects of dispensing pressure and nozzle diameter on cell survival from solid freeform fabrication–based direct cell writing. *Tissue Eng. Part A* **14**, 41–48 (2008).
 200. Malda, J. *et al.* 25th anniversary article: engineering hydrogels for biofabrication. *Adv. Mater.* **25**, 5011–5028 (2013).
 201. Xu, C., Dai, G. & Hong, Y. Recent advances in high-strength and elastic hydrogels for 3D printing in biomedical applications. *Acta Biomater.* (2019) doi:10.1016/J.ACTBIO.2019.05.032.
 202. Nahmias, Y. & Odde, D. J. Micropatterning of living cells by laser-guided direct writing: application to fabrication of hepatic–endothelial sinusoid-like structures. *Nat. Protoc.* **1**, 2288 (2006).
 203. Schiele, N. R. *et al.* Laser-based direct-write techniques for cell printing. *Biofabrication* **2**, 32001 (2010).
 204. Ma, J., Wang, Y. & Liu, J. Bioprinting of 3D tissues/organs combined with microfluidics. *RSC Adv.* **8**, 21712–21727 (2018).
 205. Thomas, M. & Willerth, S. M. 3-D Bioprinting of Neural Tissue for Applications in Cell Therapy and Drug Screening. *Front. Bioeng. Biotechnol.* **5**, 1–11 (2017).
 206. Zhang, B. *et al.* 3D Bioprinting: A Novel Avenue for Manufacturing Tissues and

- Organs. *Engineering* (2019) doi:10.1016/J.ENG.2019.03.009.
207. O'Brien, C. M., Holmes, B., Faucett, S. & Zhang, L. G. Three-dimensional printing of nanomaterial scaffolds for complex tissue regeneration. *Tissue Eng. Part B Rev.* **21**, 103–114 (2014).
 208. Gudapati, H., Dey, M. & Ozbolat, I. A comprehensive review on droplet-based bioprinting: Past, present and future. *Biomaterials* **102**, 20–42 (2016).
 209. Sarker, M. D., Naghieh, S., Sharma, N. K., Ning, L. & Chen, X. Bioprinting of Vascularized Tissue Scaffolds: Influence of Biopolymer, Cells, Growth Factors, and Gene Delivery. *J. Healthc. Eng.* **2019**, (2019).
 210. Ouyang, L., Yao, R., Zhao, Y. & Sun, W. Effect of bioink properties on printability and cell viability for 3D bioplotting of embryonic stem cells. *Biofabrication* **8**, 35020 (2016).
 211. Joung, D. *et al.* 3D Printed Stem-Cell Derived Neural Progenitors Generate Spinal Cord Scaffolds. *Adv. Funct. Mater.* **28**, 1–10 (2018).
 212. de la Vega, L. *et al.* 3D Bioprinting Human Induced Pluripotent Stem Cell-Derived Neural Tissues Using a Novel Lab-on-a-Printer Technology. *Appl. Sci.* **8**, 2414 (2018).
 213. Gu, Q., Tomaskovic-Crook, E., Wallace, G. G. & Crook, J. M. 3D Bioprinting Human Induced Pluripotent Stem Cell Constructs for In Situ Cell Proliferation and Successive Multilineage Differentiation. *Adv. Healthc. Mater.* **6**, 1700175 (2017).
 214. Hospodiuk, M., Dey, M., Sosnoski, D. & Ozbolat, I. T. The bioink: a comprehensive review on bioprintable materials. *Biotechnol. Adv.* **35**, 217–239 (2017).
 215. Oliveira, E. P. *et al.* *Advances in bioinks and in vivo imaging of biomaterials for CNS applications.* *Acta Biomaterialia* (Acta Materialia Inc., 2019). doi:10.1016/j.actbio.2019.05.006.
 216. Charwat, V. *et al.* Potential and limitations of microscopy and Raman spectroscopy for live-cell analysis of 3D cell cultures. *J. Biotechnol.* **205**, 70–81 (2015).
 217. Carragher, N. *et al.* Concerns, challenges and promises of high-content analysis of 3D cellular models. *Nat. Rev. Drug Discov.* **17**, 606 (2018).
 218. Odawara, A., Gotoh, M. & Suzuki, I. A three-dimensional neuronal culture technique that controls the direction of neurite elongation and the position of soma to mimic the

- layered structure of the brain. *RSC Adv.* **3**, 23620–23630 (2013).
219. Temple, J., Velliou, E., Shehata, M. & Lévy, R. Current strategies with implementation of three-dimensional cell culture: the challenge of quantification. *Interface Focus* **12**, 20220019 (2022).
 220. Marino, A. *et al.* A 3D real-scale, biomimetic, and biohybrid model of the blood-brain barrier fabricated through two-photon lithography. *Small* **14**, 1702959 (2018).
 221. Yang, Z. & Xiong, H.-R. Culture conditions and types of growth media for mammalian cells. *Biomed. Tissue Cult.* **1**, 3–18 (2012).
 222. Joseph, X., Akhil, V., Arathi, A. & Mohanan, P. V. Comprehensive development in organ-on-a-chip technology. *J. Pharm. Sci.* **111**, 18–31 (2022).
 223. Bhatia, S. N. & Ingber, D. E. Microfluidic organs-on-chips. *Nat. Biotechnol.* **32**, 760–772 (2014).
 224. Wang, Z. *et al.* A High-Resolution Minimicroscope System for Wireless Real-Time Monitoring. *IEEE Trans. Biomed. Eng.* **65**, 1524–1531 (2018).
 225. Moutaux, E., Charlot, B., Genoux, A., Saudou, F. & Cazorla, M. An integrated microfluidic/microelectrode array for the study of activity-dependent intracellular dynamics in neuronal networks. *Lab Chip* **18**, 3425–3435 (2018).
 226. Bhagat, A. A. S. *et al.* Microfluidics for cell separation. *Med. Biol. Eng. Comput.* **48**, 999–1014 (2010).
 227. Zhang, Q. & Austin, R. H. Applications of microfluidics in stem cell biology. *Bionanoscience* **2**, 277–286 (2012).
 228. Achyuta, A. K. H. *et al.* A modular approach to create a neurovascular unit-on-a-chip. *Lab Chip* **13**, 542–553 (2013).
 229. Coquinco, A. *et al.* A microfluidic based in vitro model of synaptic competition. *Mol. Cell. Neurosci.* **60**, 43–52 (2014).
 230. Taylor, A. M. *et al.* A microfluidic culture platform for CNS axonal injury, regeneration and transport. *Nat. Methods* **2**, 599–605 (2005).
 231. Virlogeux, A. *et al.* Reconstituting Corticostriatal Network on-a-Chip Reveals the Contribution of the Presynaptic Compartment to Huntington’s Disease. *Cell Rep.* **22**,

- 110–122 (2018).
232. Li, W. *et al.* Investigation of the Subcellular Neurotoxicity of Amyloid- β Using a Device Integrating Microfluidic Perfusion and Chemotactic Guidance. *Adv. Healthc. Mater.* **6**, 1600895 (2017).
 233. Sala-Jarque, J. *et al.* Neuromuscular Activity Induces Paracrine Signaling and Triggers Axonal Regrowth after Injury in Microfluidic Lab-On-Chip Devices. *Cells* **9**, 302 (2020).
 234. Mahto, S. K., Song, H. & Rhee, S. W. Functional synapse formation between compartmentalized cortical neurons cultured inside microfluidic devices. *BioChip J.* **5**, 289–298 (2011).
 235. Pan, L., Alagapan, S., Franca, E., Brewer, G. J. & Wheeler, B. C. Propagation of action potential activity in a predefined microtunnel neural network. *J. Neural Eng.* **8**, 46031 (2011).
 236. Peyrin, J. M. *et al.* Axon diodes for the reconstruction of oriented neuronal networks in microfluidic chambers. *Lab Chip* **11**, 3663–3673 (2011).
 237. Gladkov, A. *et al.* Design of Cultured Neuron Networks in vitro with Predefined Connectivity Using Asymmetric Microfluidic Channels. *Sci. Rep.* **7**, 15625 (2017).
 238. Forró, C. *et al.* Modular microstructure design to build neuronal networks of defined functional connectivity. *Biosens. Bioelectron.* **122**, 75–87 (2018).
 239. Liu, H., Lin, J. & Roy, K. Effect of 3D scaffold and dynamic culture condition on the global gene expression profile of mouse embryonic stem cells. *Biomaterials* **27**, 5978–5989 (2006).
 240. Hakanen, J., Ruiz-Reig, N. & Tissir, F. Linking cell polarity to cortical development and malformations. *Front. Cell. Neurosci.* **13**, 244 (2019).
 241. Kothapalli, C. R. *et al.* A high-throughput microfluidic assay to study neurite response to growth factor gradients. *Lab Chip* **11**, 497–507 (2011).
 242. Sloan, T. F. W., Qasaimeh, M. A., Juncker, D., Yam, P. T. & Charron, F. Integration of shallow gradients of Shh and Netrin-1 guides commissural axons. *PLoS Biol.* **13**, e1002119 (2015).

243. Ramamurthy, P. *et al.* Concomitant differentiation of a population of mouse embryonic stem cells into neuron-like cells and schwann cell-like cells in a slow-flow microfluidic device. *Dev. Dyn.* **246**, 7–27 (2017).
244. Demers, C. J. *et al.* Development-on-chip: in vitro neural tube patterning with a microfluidic device. *Development* **143**, 1884–1892 (2016).
245. Uzel, S. G. M. *et al.* Simultaneous or Sequential Orthogonal Gradient Formation in a 3D Cell Culture Microfluidic Platform. *Small* **12**, 612–622 (2016).
246. Chow, B. W. & Gu, C. The Molecular Constituents of the Blood–Brain Barrier. *Trends Neurosci.* **38**, 598–608 (2015).
247. Campisi, M. *et al.* 3D self-organized microvascular model of the human blood-brain barrier with endothelial cells, pericytes and astrocytes. *Biomaterials* **180**, 117–129 (2018).
248. Adriani, G., Ma, D., Pavesi, A., Kamm, R. D. & Goh, E. L. K. A 3D neurovascular microfluidic model consisting of neurons, astrocytes and cerebral endothelial cells as a blood-brain barrier. *Lab Chip* **17**, 448–459 (2017).
249. Bang, S. *et al.* A low permeability microfluidic blood-brain barrier platform with direct contact between perfusable vascular network and astrocytes. *Sci. Rep.* **7**, 8083 (2017).
250. Deosarkar, S. P. *et al.* A novel dynamic neonatal blood-brain barrier on a chip. *PLoS One* **10**, 1–21 (2015).
251. Chung, B. *et al.* Evaluation of Cell-Penetrating Peptides Using Microfluidic In Vitro 3D Brain Endothelial Barrier. *Macromol. Biosci.* 1900425 (2020).
252. Sances, S. *et al.* Human iPSC-derived endothelial cells and microengineered organ-chip enhance neuronal development. *Stem cell reports* **10**, 1222–1236 (2018).
253. Vatine, G. D. *et al.* Human iPSC-Derived Blood-Brain Barrier Chips Enable Disease Modeling and Personalized Medicine Applications. *Cell Stem Cell* **24**, 995–1005 (2019).
254. Cullen, D. K. & LaPlaca, M. C. Neuronal Response to High Rate Shear Deformation Depends on Heterogeneity of the Local Strain Field. *J. Neurotrauma* **23**, 1304–1319 (2006).
255. Osaki, T., Sivathanu, V. & Kamm, R. D. Engineered 3D vascular and neuronal networks

- in a microfluidic platform. *Sci. Rep.* **8**, 1–13 (2018).
256. Wang, Y., Wang, L., Zhu, Y. & Qin, J. Human brain organoid-on-a-chip to model prenatal nicotine exposure. *Lab Chip* **18**, 851–860 (2018).
257. Klim, J. R. *et al.* ALS-implicated protein TDP-43 sustains levels of STMN2, a mediator of motor neuron growth and repair. *Nat. Neurosci.* **22**, (2019).
258. Kamande, J. W., Nagendran, T., Harris, J. & Taylor, A. M. Multi-compartment Microfluidic Device Geometry and Covalently Bound Poly-D-Lysine Influence Neuronal Maturation. **7**, 1–9 (2019).
259. Park, J. *et al.* A 3D human triculture system modeling neurodegeneration and neuroinflammation in Alzheimer’s disease. *Nat. Neurosci.* **21**, 941–951 (2018).
260. Osaki, T., Uzel, S. G. M. & Kamm, R. D. Microphysiological 3D model of amyotrophic lateral sclerosis (ALS) from human iPS-derived muscle cells and optogenetic motor neurons. *Sci. Adv.* **4**, eaat5847 (2018).
261. Lee, S. W. L. *et al.* Modeling Nanocarrier Transport across a 3D In Vitro Human Blood–Brain–Barrier Microvasculature. *Adv. Healthc. Mater.* **9**, 1901486 (2020).
262. Liu, H. *et al.* Advances in Hydrogels in Organoids and Organs-on-a-Chip. *Adv. Mater.* **31**, 1–28 (2019).
263. Park, J. *et al.* Three-dimensional brain-on-a-chip with an interstitial level of flow and its application as an in vitro model of Alzheimer’s disease. *Lab Chip* **15**, 141–150 (2015).
264. Habibey, R., Rojo Arias, J. E., Striebel, J. & Busskamp, V. Microfluidics for Neuronal cell and circuit engineering. *Chem. Rev.* **122**, 14842–14880 (2022).
265. Halldorsson, S., Lucumi, E., Gómez-Sjöberg, R. & Fleming, R. M. T. Advantages and challenges of microfluidic cell culture in polydimethylsiloxane devices. *Biosens. Bioelectron.* **63**, 218–231 (2015).
266. Habibey, R. *et al.* A multielectrode array microchannel platform reveals both transient and slow changes in axonal conduction velocity. *Sci. Rep.* **7**, 8558 (2017).
267. Shin, H. *et al.* 3D high-density microelectrode array with optical stimulation and drug delivery for investigating neural circuit dynamics. *Nat. Commun.* **12**, 1–18 (2021).
268. Visser, J. *et al.* Reinforcement of hydrogels using three-dimensionally printed

- microfibrils. *Nat. Commun.* **6**, 6933 (2015).
269. Kloxin, A. M., Benton, J. A. & Anseth, K. S. In situ elasticity modulation with dynamic substrates to direct cell phenotype. *Biomaterials* **31**, 1–8 (2010).
270. Snyder, E. Y. *et al.* Multipotent neural cell lines can engraft and participate in development of mouse cerebellum. *Cell* **68**, 33–51 (1992).
271. Nishimura, K. *et al.* Single-cell transcriptomics reveals correct developmental dynamics and high-quality midbrain cell types by improved hESC differentiation. *Stem Cell Reports* **18**, 337–353 (2023).
272. Orlandi, J. G. *et al.* NETCAL: an interactive platform for large-scale, NETWORK and population dynamics analysis of calcium imaging recordings. *Neuroscience* (2017) doi:doi.org/10.5281/zenodo.1119026.
273. Palma-Tortosa, S. *et al.* Activity in grafted human iPSC cell-derived cortical neurons integrated in stroke-injured rat brain regulates motor behavior. *Proc. Natl. Acad. Sci.* **117**, 9094–9100 (2020).
274. Comella-Bolla, A. *et al.* Human Pluripotent Stem Cell-Derived Neurons Are Functionally Mature In Vitro and Integrate into the Mouse Striatum Following Transplantation. *Mol. Neurobiol.* **57**, 2766–2798 (2020).
275. Lundqvist, J., EL Andaloussi-Lilja, J., Svensson, C., Gustafsson Dorfh, H. & Forsby, A. Optimisation of culture conditions for differentiation of C17.2 neural stem cells to be used for in vitro toxicity tests. *Toxicol. Vitro.* **27**, 1565–1569 (2013).
276. Kaindl, J. & Winner, B. Disease Modeling of Neuropsychiatric Brain Disorders Using Human Stem Cell-Based Neural Models. (2019).
277. Gupta, P. *et al.* Microfluidic platforms for single neuron analysis. *Mater. Today Bio* 100222 (2022).
278. Ranjan, V. D., Qiu, L., Tan, E. K., Zeng, L. & Zhang, Y. Modelling Alzheimer’s disease: Insights from in vivo to in vitro three-dimensional culture platforms. *J. Tissue Eng. Regen. Med.* **12**, 1944–1958 (2018).
279. Brunetti, V. *et al.* Neurons sense nanoscale roughness with nanometer sensitivity. *Proc. Natl. Acad. Sci.* **107**, 6264–6269 (2010).

280. Rastogi, P. & Kandasubramanian, B. Review of alginate-based hydrogel bioprinting for application in tissue engineering. *Biofabrication* **11**, 042001 (2019).
281. Sherman, L. S. *et al.* Hyaluronate-based extracellular matrix: Keeping glia in their place. *Glia* **38**, 93–102 (2002).
282. Annabi, N. *et al.* Controlling the Porosity and Microarchitecture of Hydrogels for Tissue Engineering. *Tissue Eng. Part B Rev.* **16**, 371–383 (2010).
283. García-Lizarribar, A. *et al.* Composite Biomaterials as Long-Lasting Scaffolds for 3D Bioprinting of Highly Aligned Muscle Tissue. *Macromol. Biosci.* **18**, 1800167 (2018).
284. Wen, Y.-Q. *et al.* Substrate stiffness affects neural network activity in an extracellular matrix proteins dependent manner. *Colloids Surfaces B Biointerfaces* **170**, 729–735 (2018).
285. Kharkar, P. M., Kiick, K. L. & Kloxin, A. M. Designing degradable hydrogels for orthogonal control of cell microenvironments. *Chem. Soc. Rev.* **42**, 7335–7372 (2013).
286. Madl, C. M. *et al.* Maintenance of neural progenitor cell stemness in 3D hydrogels requires matrix remodelling. *Nat. Mater.* **16**, 1233–1242 (2017).
287. Noshadi, I. *et al.* In vitro and in vivo analysis of visible light crosslinkable gelatin methacryloyl (GelMA) hydrogels. *Biomater. Sci.* **5**, 2093–2105 (2017).
288. Krishnamoorthy, S., Zhang, Z. & Xu, C. Biofabrication of three-dimensional cellular structures based on gelatin methacrylate–alginate interpenetrating network hydrogel. *J. Biomater. Appl.* **33**, 1105–1117 (2019).
289. Santana, B. P. *et al.* Comparing different methods to fix and to dehydrate cells on alginate hydrogel scaffolds using scanning electron microscopy. *Microsc. Res. Tech.* **78**, 553–561 (2015).
290. Kim, M.-C., Silberberg, Y. R., Abeyaratne, R., Kamm, R. D. & Asada, H. H. Computational modeling of three-dimensional ECM-rigidity sensing to guide directed cell migration. *Proc. Natl. Acad. Sci.* **115**, E390–E399 (2018).
291. Bechara, S., Wadman, L. & Popat, K. C. Electroconductive polymeric nanowire templates facilitates in vitro C17.2 neural stem cell line adhesion, proliferation and differentiation. *Acta Biomater.* **7**, 2892–2901 (2011).

292. Wang, B., Jedlicka, S. & Cheng, X. Maintenance and Neuronal Cell Differentiation of Neural Stem Cells C17.2 Correlated to Medium Availability Sets Design Criteria in Microfluidic Systems. *PLoS One* **9**, e109815 (2014).
293. Attoff, K., Kertika, D., Lundqvist, J., Oredsson, S. & Forsby, A. Acrylamide affects proliferation and differentiation of the neural progenitor cell line C17.2 and the neuroblastoma cell line SH-SY5Y. *Toxicol. Vitro*. **35**, 100–111 (2016).
294. McAdams, H. H. & Arkin, A. Stochastic mechanisms in gene expression. *Proc. Natl. Acad. Sci.* **94**, 814–819 (1997).
295. Tao, Y., Zheng, X. & Sun, Y. Effect of feedback regulation on stochastic gene expression. *J. Theor. Biol.* **247**, 827–836 (2007).
296. Nair, K. *et al.* Characterization of cell viability during bioprinting processes. *Biotechnol. J.* **4**, 1168–1177 (2009).
297. Lee, Y. B. *et al.* Bio-printing of collagen and VEGF-releasing fibrin gel scaffolds for neural stem cell culture. *Exp. Neurol.* **223**, 645–652 (2010).
298. Chiappalone, M., Bove, M., Vato, A., Tedesco, M. & Martinoia, S. Dissociated cortical networks show spontaneously correlated activity patterns during in vitro development. *Brain Res.* **1093**, 41–53 (2006).
299. Biffi, E. Microfluidic and compartmentalized platforms for neurobiological research. *Microfluid. Compart. Platforms Neurobiol. Res.* **103**, 1–248 (2015).
300. Noble, E. E., Billington, C. J., Kotz, C. M. & Wang, C. The lighter side of BDNF. *Am. J. Physiol. Integr. Comp. Physiol.* **300**, R1053–R1069 (2011).
301. Kearns, C. M. & Gash, D. M. GDNF protects nigral dopamine neurons against 6-hydroxydopamine in vivo. *Brain Res.* **672**, 104–111 (1995).
302. Moore, S. *et al.* APP metabolism regulates tau proteostasis in human cerebral cortex neurons. *Cell Rep.* **11**, 689–696 (2015).
303. Baysal, K., Aroguz, A. Z., Adiguzel, Z. & Baysal, B. M. Chitosan/alginate crosslinked hydrogels: Preparation, characterization and application for cell growth purposes. *Int. J. Biol. Macromol.* **59**, 342–348 (2013).
304. Li, Z. *et al.* Tuning Alginate-Gelatin Bioink Properties by Varying Solvent and Their

- Impact on Stem Cell Behavior. *Sci. Rep.* **8**, 8020 (2018).
305. Suárez, L. E., Markello, R. D., Betzel, R. F. & Misic, B. Linking structure and function in macroscale brain networks. *Trends Cogn. Sci.* **24**, 302–315 (2020).
306. Testa, C. M. & Jankovic, J. Huntington disease: A quarter century of progress since the gene discovery. *J. Neurol. Sci.* **396**, 52–68 (2019).

1. Bassett, D. S. & Gazzaniga, M. S. Understanding complexity in the human brain. *Trends Cogn. Sci.* **15**, 200–209 (2011).
2. Shipp, S. Structure and function of the cerebral cortex. *Curr. Biol.* **17**, R443–R449 (2007).
3. Rajmohan, V. & Mohandas, E. The limbic system. *Indian J. Psychiatry* **49**, 132–139 (2007).
4. Leiner, H. C., Leiner, A. L. & Dow, R. S. Cognitive and language functions of the human cerebellum. *Trends Neurosci.* **16**, 444–447 (1993).
5. Benam, K. H. *et al.* Engineered In Vitro Disease Models. *Annu. Rev. Pathol. Mech. Dis.* **10**, 195–262 (2015).
6. Kopell, N. & Ermentrout, B. Chemical and electrical synapses perform complementary roles in the synchronization of interneuronal networks. *Proc. Natl. Acad. Sci.* **101**, 15482–15487 (2004).
7. Zhou, Q. *et al.* Neuroinflammatory astrocytes generated from cord blood-derived human induced pluripotent stem cells. *J. Neuroinflammation* **16**, 164 (2019).
8. Nave, K.-A. & Werner, H. B. Myelination of the nervous system: mechanisms and functions. *Annu Rev Cell Dev Biol* **30**, 503–533 (2014).
9. Tejera, D. & Heneka, M. T. Microglia in Neurodegenerative Disorders. in *Microglia* 57–67 (Springer, 2019).
10. Sweeney, M. D., Ayyadurai, S. & Zlokovic, B. V. Pericytes of the neurovascular unit: key functions and signaling pathways. *Nat. Neurosci.* **19**, 771–783 (2016).
11. Zhao, Z., Nelson, A. R., Betsholtz, C. & Zlokovic, B. V. Establishment and dysfunction of the blood-brain barrier. *Cell* **163**, 1064–1078 (2015).
12. Pogoda, K. & Janmey, P. A. Glial tissue mechanics and mechanosensing by glial cells. *Front. Cell. Neurosci.* **12**, 25 (2018).
13. Rauch, U. Extracellular matrix components associated with remodeling processes in brain. *Cell. Mol. Life Sci.* **61**, 2031–2045 (2004).
14. Shin, Y., Kamm, R. D., Osaki, T., Campisi, M. & Sivathanu, V. In Vitro Microfluidic Models for Neurodegenerative Disorders. *Adv. Healthc. Mater.* **7**, 1700489 (2017).

15. Engler, A. J., Sen, S., Sweeney, H. L. & Discher, D. E. Matrix Elasticity Directs Stem Cell Lineage Specification. *Cell* **126**, 677–689 (2006).
16. Wu, S., Xu, R., Duan, B. & Jiang, P. Three-dimensional hyaluronic acid hydrogel-based models for in vitro human iPSC-derived NPC culture and differentiation. *J. Mater. Chem. B* **5**, 3870–3878 (2017).
17. Budday, S. *et al.* Mechanical properties of gray and white matter brain tissue by indentation. *J. Mech. Behav. Biomed. Mater.* **46**, 318–330 (2015).
18. Russo, C., Senese, R. & Muto, M. Neurodegenerative Diseases in Geriatric Patients BT - Imaging in Geriatrics. in (eds. Guglielmi, G. & Maas, M.) 11–35 (Springer International Publishing, 2023). doi:10.1007/978-3-031-14877-4_2.
19. Kovacs, G. G. Molecular pathology of neurodegenerative diseases: principles and practice. *J. Clin. Pathol.* jclinpath-2019-205952 (2019) doi:10.1136/jclinpath-2019-205952.
20. Garwood, C. J. *et al.* astrocytes in Alzheimer’s disease and other age-associated dementias: a supporting player with a central role. *Neuropathol. Appl. Neurobiol.* **43**, 281–298 (2017).
21. González-Reyes, R. E., Nava-Mesa, M. O., Vargas-Sánchez, K., Ariza-Salamanca, D. & Mora-Muñoz, L. Involvement of astrocytes in Alzheimer’s disease from a neuroinflammatory and oxidative stress perspective. *Front. Mol. Neurosci.* **10**, 427 (2017).
22. Lees, A. J., Hardy, J. & Revesz, T. Parkinson’s disease. *Lancet (British Ed.)* **373**, 2055–2066 (2009).
23. Blauwendraat, C., Nalls, M. A. & Singleton, A. B. The genetic architecture of Parkinson’s disease. *Lancet Neurol.* **19**, 170–178 (2020).
24. Reiner, A. *et al.* Differential loss of striatal projection neurons in Huntington disease. *Proc. Natl. Acad. Sci.* **85**, 5733–5737 (1988).
25. An, P. & Sun, X. Huntington’s Disease : Current Status and Prospects. *J. Cell Signal.* **4**, 1–7 (2019).
26. Franklin, R. J. M., Edgar, J. M. & Smith, K. J. Neuroprotection and repair in multiple

- sclerosis. *Nat. Rev. Neurol.* **8**, 624–634 (2012).
27. Chun, S. J., Rasband, M. N., Sidman, R. L., Habib, A. A. & Vartanian, T. Integrin-linked kinase is required for laminin-2–induced oligodendrocyte cell spreading and CNS myelination. *J. Cell Biol.* **163**, 397–408 (2003).
 28. Van Horsen, J., Dijkstra, C. D. & De Vries, H. E. The extracellular matrix in multiple sclerosis pathology. *J. Neurochem.* **103**, 1293–1301 (2007).
 29. Shi, Y. *et al.* ApoE4 markedly exacerbates tau-mediated neurodegeneration in a mouse model of tauopathy. *Nature* **549**, 523–527 (2017).
 30. Badhe, R. V., Chejara, D. R., Kumar, P., Choonara, Y. E. & Pillay, V. Neurodegenerative Disease Conditions and Genomic Treatment for Better Health. in *Genomics-Driven Healthcare* 281–310 (Springer, 2018).
 31. Ruiz-Garcia, R. The growing evidence of neurodegenerative diseases risk factors. *Rev. Mex. Neurocienc.* **24**, 1–2 (2023).
 32. Patterson, C. World Alzheimer Report 2018—The state of the art of dementia research: New frontiers. *Alzheimer's Dis. Int. London, UK* (2018).
 33. Cimler, R., Maresova, P., Kuhnova, J. & Kuca, K. Predictions of Alzheimer's disease treatment and care costs in European countries. *PLoS One* **14**, e0210958 (2019).
 34. Möller, H.-J. & Graeber, M. B. The case described by Alois Alzheimer in 1911. *Eur. Arch. Psychiatry Clin. Neurosci.* **248**, 111–122 (1998).
 35. Ahadian, S. *et al.* Organ-On-A-Chip Platforms: A Convergence of Advanced Materials, Cells, and Microscale Technologies. *Adv. Healthc. Mater.* **7**, 1700506 (2017).
 36. Sparrow, J., Hughes, S. M. & Segalat, L. Other model organisms for sarcomeric muscle diseases. *Sarcomere Skelet. Muscle Dis.* 192–206 (2008).
 37. Ericsson, A. C., Crim, M. J. & Franklin, C. L. A brief history of animal modeling. *Mo. Med.* **110**, 201 (2013).
 38. Lorrio, S. *et al.* Novel multitarget ligand ITH33/IQM9. 21 provides neuroprotection in in vitro and in vivo models related to brain ischemia. *Neuropharmacology* **67**, 403–411 (2013).
 39. Huszthy, P. C. *et al.* In vivo models of primary brain tumors: pitfalls and perspectives.

- Neuro. Oncol.* **14**, 979–993 (2012).
40. Daphu, I. *et al.* In vivo animal models for studying brain metastasis: value and limitations. *Clin. Exp. Metastasis* **30**, 695–710 (2013).
 41. und Halbach, O. von B. Modeling neurodegenerative diseases in vivo review. *Neurodegener. Dis.* **2**, 313–320 (2005).
 42. Zhuang, P., Chua, C. K., Chew, S. Y., An, J. & Sun, A. X. 3D neural tissue models: From spheroids to bioprinting. *Biomaterials* **154**, 113–133 (2017).
 43. Breslin, S. & O’Driscoll, L. Three-dimensional cell culture: The missing link in drug discovery. *Drug Discov. Today* **18**, 240–249 (2013).
 44. Tarricone, G., Carmagnola, I. & Chiono, V. Tissue-Engineered Models of the Human Brain: State-of-the-Art Analysis and Challenges. *J. Funct. Biomater.* **13**, 146 (2022).
 45. Harrison, R. G., Greenman, M. J., Mall, F. P. & Jackson, C. M. Observations of the living developing nerve fiber. *Anat. Rec.* **1**, 116–128 (1907).
 46. Centeno, E. G. Z., Cimarosti, H. & Bithell, A. 2D versus 3D human induced pluripotent stem cell-derived cultures for neurodegenerative disease modelling. *Mol. Neurodegener.* **13**, 1–16 (2018).
 47. Wu, S. M. & Hochedlinger, K. Harnessing the potential of induced pluripotent stem cells for regenerative medicine. *Nat. Cell Biol.* **13**, 497–505 (2011).
 48. Gupta, N. *et al.* Microfluidics-based 3D cell culture models: Utility in novel drug discovery and delivery research. *Bioeng. Transl. Med.* **1**, 63–81 (2016).
 49. Duval, K. *et al.* Modeling Physiological Events in 2D vs. 3D Cell Culture. *Physiology* **32**, 266–277 (2017).
 50. Sun, T. *et al.* Development of a 3D cell culture system for investigating cell interactions with electrospun fibers. *Biotechnol. Bioeng.* **97**, 1318–1328 (2007).
 51. Kunze, A., Giugliano, M., Valero, A. & Renaud, P. Micropatterning neural cell cultures in 3D with a multi-layered scaffold. *Biomaterials* **32**, 2088–2098 (2011).
 52. Nguyen-Vu, T. D. B. *et al.* Vertically aligned carbon nanofiber architecture as a multifunctional 3-D neural electrical interface. *IEEE Trans. Biomed. Eng.* **54**, 1121–1128 (2007).

53. Soares, C. P. *et al.* 2D and 3D-Organized Cardiac Cells Shows Differences in Cellular Morphology, Adhesion Junctions, Presence of Myofibrils and Protein Expression. *PLoS One* **7**, e38147 (2012).
54. Baharvand, H., Hashemi, S. M., Kazemi Ashtiani, S. & Farrokhi, A. Differentiation of human embryonic stem cells into hepatocytes in 2D and 3D culture systems in vitro. *Int. J. Dev. Biol.* **50**, 645–652 (2006).
55. Liu, H., Lin, J. & Roy, K. Effect of 3D scaffold and dynamic culture condition on the global gene expression profile of mouse embryonic stem cells. *Biomaterials* **27**, 5978–5989 (2006).
56. Jeong, H.-J. *et al.* Engineering Human Brain Organoids: From Basic Research to Tissue Regeneration. *Tissue Eng. Regen. Med.* (2020).
57. Laschke, M. W. & Menger, M. D. Life is 3D: Boosting Spheroid Function for Tissue Engineering. *Trends Biotechnol.* **35**, 133–144 (2017).
58. Dingle, Y.-T. L. *et al.* Three-dimensional neural spheroid culture: an in vitro model for cortical studies. *Tissue Eng. Part C Methods* **21**, 1274–1283 (2015).
59. Sloan, S. A., Andersen, J., Paşca, A. M., Birey, F. & Paşca, S. P. Generation and assembly of human brain region-specific three-dimensional cultures. *Nat. Protoc.* **13**, 2062–2085 (2018).
60. Leite, P. E. C. *et al.* Suitability of 3D human brain spheroid models to distinguish toxic effects of gold and poly-lactic acid nanoparticles to assess biocompatibility for brain drug delivery. *Part. Fibre Toxicol.* **16**, 22 (2019).
61. Lee, H. K. *et al.* Three dimensional human neuro-spheroid model of Alzheimer’s disease based on differentiated induced pluripotent stem cells. *PLoS One* **11**, 1–23 (2016).
62. Xiao, W. *et al.* Alginate Hydrogel Modified with a Ligand Interacting with $\alpha 3\beta 1$ Integrin Receptor Promotes the Differentiation of 3D Neural Spheroids toward Oligodendrocytes in Vitro. *ACS Appl. Mater. Interfaces* **11**, 5821–5833 (2019).
63. Tang-Schomer, M. D., Wu, W. B., Kaplan, D. L. & Bookland, M. J. In vitro 3D regeneration-like growth of human patient brain tissue. *J. Tissue Eng. Regen. Med.* **12**, 1247–1260 (2018).

64. Jorfi, M., D'Avanzo, C., Tanzi, R. E., Kim, D. Y. & Irimia, D. Human neurospheroid arrays for in vitro studies of Alzheimer's disease. *Sci. Rep.* **8**, 2450 (2018).
65. Brawner, A. T., Xu, R., Liu, D. & Jiang, P. Generating CNS organoids from human induced pluripotent stem cells for modelling neurological disorders. *Int. J. Physiol. Pathophysiol. Pharmacol.* **9**, 101–111 (2017).
66. Hofer, M. & Lutolf, M. P. Engineering organoids. *Nat. Rev. Mater.* **6**, 402–420 (2021).
67. Arlotta, P. Organoids required! A new path to understanding human brain development and disease. *Nat. Methods* **15**, 27 (2018).
68. Lancaster, M. A. *et al.* Cerebral organoids model human brain development and microcephaly. *Nature* **501**, 373 (2013).
69. Lancaster, M. A. *et al.* Guided self-organization and cortical plate formation in human brain organoids. *Nat. Biotechnol.* **35**, 659–666 (2017).
70. Quadrato, G. *et al.* Cell diversity and network dynamics in photosensitive human brain organoids. *Nature* **545**, 48 (2017).
71. Zhou, T. *et al.* High-content screening in hPSC-neural progenitors identifies drug candidates that inhibit Zika virus infection in fetal-like organoids and adult brain. *Cell Stem Cell* **21**, 274–283 (2017).
72. Raja, W. K. *et al.* Self-organizing 3D human neural tissue derived from induced pluripotent stem cells recapitulate Alzheimer's disease phenotypes. *PLoS One* **11**, e0161969 (2016).
73. Wulansari, N. *et al.* Neurodevelopmental defects and neurodegenerative phenotypes in human brain organoids carrying Parkinson's disease-linked DNAJC6 mutations. *Sci. Adv.* **7**, eabb1540 (2021).
74. Kelava, I. & Lancaster, M. A. Dishing out mini-brains: Current progress and future prospects in brain organoid research. *Dev. Biol.* **420**, 199–209 (2016).
75. Eglen, R. M. & Reisine, T. Human iPS Cell-Derived Patient Tissues and 3D Cell Culture Part 2: Spheroids, Organoids, and Disease Modeling. *SLAS Technol. Transl. Life Sci. Innov.* **24**, 18–27 (2019).
76. Gopalakrishnan, J. The Emergence of Stem Cell-Based Brain Organoids: Trends and

- Challenges. *BioEssays* **41**, 1900011 (2019).
77. Qian, X. *et al.* Brain-region-specific organoids using mini-bioreactors for modeling ZIKV exposure. *Cell* **165**, 1238–1254 (2016).
 78. Pham, M. T. *et al.* Generation of human vascularized brain organoids. *Neuroreport* **29**, 588–593 (2018).
 79. Lancaster, M. A. & Knoblich, J. A. Generation of cerebral organoids from human pluripotent stem cells. *Nat. Protoc.* **9**, 2329–2340 (2014).
 80. Breuls, R. G. M., Jiya, T. U. & Smit, T. H. Scaffold stiffness influences cell behavior: opportunities for skeletal tissue engineering. *Open Orthop. J.* **2**, 103 (2008).
 81. Choi, S. H. *et al.* A three-dimensional human neural cell culture model of Alzheimer's disease. *Nature* **515**, 274 (2014).
 82. Sun, J. *et al.* Biomaterials and Advanced Biofabrication Techniques in hiPSCs Based Neuromyopathic Disease Modeling. *Front. Bioeng. Biotechnol.* **7**, (2019).
 83. Mofazzal Jahromi, M. A. *et al.* Microfluidic Brain-on-a-Chip: Perspectives for Mimicking Neural System Disorders. *Mol. Neurobiol.* (2019) doi:10.1007/s12035-019-01653-2.
 84. Esch, E. W., Bahinski, A. & Huh, D. Organs-on-chips at the frontiers of drug discovery. *Nat. Rev. Drug Discov.* **14**, 248–260 (2015).
 85. Roach, P., Fricker, R. A., Evans, M. G., Kamudzandu, M. & Köse-Dunn, M. J. A micro-fabricated in vitro complex neuronal circuit platform. *Biomed. Phys. Eng. Express* (2019).
 86. Mackerron, C., Robertson, G., Zagnoni, M. & Bushell, T. J. A Microfluidic Platform for the Characterisation of CNS Active Compounds. doi:10.1038/s41598-017-15950-0.
 87. Oddo, A. *et al.* Advances in Microfluidic Blood–Brain Barrier (BBB) Models. *Trends Biotechnol.* (2019) doi:10.1016/J.TIBTECH.2019.04.006.
 88. Stacey, G. Primary Cell Cultures and Immortal Cell Lines. in *Encyclopedia of Life Sciences* (John Wiley & Sons, Ltd, 2006). doi:10.1038/npg.els.0003960.
 89. Potjewyd, G., Moxon, S., Wang, T., Domingos, M. & Hooper, N. M. Tissue Engineering 3D Neurovascular Units: A Biomaterials and Bioprinting Perspective. *Trends*

- Biotechnol.* **36**, 457–472 (2018).
90. Rahman, N. A. *et al.* Immortalized endothelial cell lines for in vitro blood–brain barrier models: A systematic review. *Brain Res.* **1642**, 532–545 (2016).
 91. Bordoni, M. *et al.* From Neuronal Differentiation of iPSCs to 3D Neuro-Organoids: Modelling and Therapy of Neurodegenerative Diseases. *Int. J. Mol. Sci.* **19**, 3972 (2018).
 92. Zimmermann, J. A. & Schaffer, D. V. Engineering Biomaterials to Control the Neural Differentiation of Stem Cells. *Brain Res. Bull.* (2019).
 93. Takahashi, K. *et al.* Induction of pluripotent stem cells from adult human fibroblasts by defined factors. *Cell* **131**, 861–872 (2007).
 94. Vadodaria, K. C., Amatya, D. N., Marchetto, M. C. & Gage, F. H. Modeling psychiatric disorders using patient stem cell-derived neurons: a way forward. *Genome Med.* **10**, 6–8 (2018).
 95. Poon, A. *et al.* Modeling neurodegenerative diseases with patient-derived induced pluripotent cells: Possibilities and challenges. *N. Biotechnol.* **39**, 190–198 (2017).
 96. Mahumane, G. D., Kumar, P., du Toit, L. C., Choonara, Y. E. & Pillay, V. 3D scaffolds for brain tissue regeneration: architectural challenges. *Biomater. Sci.* **6**, 2812–2837 (2018).
 97. Koffler, J. *et al.* Biomimetic 3D-printed scaffolds for spinal cord injury repair. *Nat. Med.* **25**, 263–269 (2019).
 98. Jensen, G., Morrill, C. & Huang, Y. 3D tissue engineering, an emerging technique for pharmaceutical research. *Acta Pharm. Sin. B* **8**, 756–766 (2018).
 99. Ali, S., Wall, I. B., Mason, C., Pelling, A. E. & Veraitch, F. S. The effect of Young’s modulus on the neuronal differentiation of mouse embryonic stem cells. *Acta Biomater.* **25**, 253–267 (2015).
 100. Knowlton, S., Anand, S., Shah, T. & Tasoglu, S. Bioprinting for Neural Tissue Engineering. *Trends Neurosci.* **41**, 31–46 (2018).
 101. Zhang, D. *et al.* A 3D Alzheimer’s disease culture model and the induction of P21-activated kinase mediated sensing in iPSC derived neurons. *Biomaterials* **35**, 1420–1428 (2013).

102. Adil, M. M. *et al.* hPSC-derived striatal cells generated using a scalable 3D hydrogel promote recovery in a Huntington disease mouse model. *Stem Cell Reports* **10**, 1481–1491 (2018).
103. Xu, X. Y. *et al.* The behaviour of neural stem cells on polyhydroxyalkanoate nanofiber scaffolds. *Biomaterials* **31**, 3967–3975 (2010).
104. Silva, G. A. *et al.* Selective differentiation of neural progenitor cells by high-epitope density nanofibers. *Science (80-.)*. **303**, 1352–1355 (2004).
105. Zhang, Q. *et al.* Preparation of uniaxial multichannel silk fibroin scaffolds for guiding primary neurons. *Acta Biomater.* **8**, 2628–2638 (2012).
106. Hanson Shepherd, J. N. *et al.* 3D Microperiodic Hydrogel Scaffolds for Robust Neuronal Cultures. *Adv. Funct. Mater.* **21**, 47–54 (2011).
107. Yang, F., Xu, C. Y., Kotaki, M., Wang, S. & Ramakrishna, S. Characterization of neural stem cells on electrospun poly(L-lactic acid) nanofibrous scaffold. *J. Biomater. Sci. Polym. Ed.* **15**, 1483–1497 (2004).
108. Papadimitriou, L., Manganas, P., Ranella, A. & Stratakis, E. Biofabrication for neural tissue engineering applications. *Mater. Today Bio* **6**, 100043 (2020).
109. Fantini, V. *et al.* Bioink Composition and Printing Parameters for 3D Modeling Neural Tissue. *Cells* **8**, 830 (2019).
110. Potter, W., Kalil, R. E. & Kao, W. J. Biomimetic material systems for neural progenitor cell-based therapy. *Front Biosci* **13**, 21 (2008).
111. Benny, P. & Raghunath, M. Making microenvironments: A look into incorporating macromolecular crowding into in vitro experiments, to generate biomimetic microenvironments which are capable of directing cell function for tissue engineering applications. *J. Tissue Eng.* **8**, 2041731417730467 (2017).
112. Stabenfeldt, S. E., García, A. J. & LaPlaca, M. C. Thermoreversible laminin-functionalized hydrogel for neural tissue engineering. *J. Biomed. Mater. Res. Part A An Off. J. Soc. Biomater. Japanese Soc. Biomater. Aust. Soc. Biomater. Korean Soc. Biomater.* **77**, 718–725 (2006).
113. Khaing, Z. Z. & Seidlits, S. K. Hyaluronic acid and neural stem cells: implications for

- biomaterial design. *J. Mater. Chem. B* **3**, 7850–7866 (2015).
114. Lozano, R. *et al.* 3D printing of layered brain-like structures using peptide modified gellan gum substrates. *Biomaterials* **67**, 264–273 (2015).
 115. Crompton, K. E. *et al.* Polylysine-functionalised thermoresponsive chitosan hydrogel for neural tissue engineering. *Biomaterials* **28**, 441–449 (2007).
 116. Haile, Y. *et al.* The effect of modified polysialic acid based hydrogels on the adhesion and viability of primary neurons and glial cells. *Biomaterials* **29**, 1880–1891 (2008).
 117. Wen, Y.-Q. *et al.* Substrate stiffness affects neural network activity in an extracellular matrix proteins dependent manner. *Colloids Surfaces B Biointerfaces* **170**, 729–735 (2018).
 118. Saha, K. *et al.* Substrate Modulus Directs Neural Stem Cell Behavior. *Biophys. J.* **95**, 4426–4438 (2008).
 119. Her, G. J. *et al.* Control of three-dimensional substrate stiffness to manipulate mesenchymal stem cell fate toward neuronal or glial lineages. *Acta Biomater.* **9**, 5170–5180 (2013).
 120. Cadena, M. *et al.* 3D Bioprinting of Neural Tissues. *Adv. Healthc. Mater.* **10**, 2001600 (2021).
 121. Lerner, T. N., Ye, L. & Deisseroth, K. Communication in Neural Circuits: Tools, Opportunities, and Challenges. *Cell* **164**, 1136–1150 (2016).
 122. Lai, Y., Cheng, K. & Kisaalita, W. Three dimensional neuronal cell cultures more accurately model voltage gated calcium channel functionality in freshly dissected nerve tissue. (2012).
 123. Garrudo, F. F. F. *et al.* Polyaniline-polycaprolactone blended nanofibers for neural cell culture. *Eur. Polym. J.* **117**, 28–37 (2019).
 124. Garrudo, F. F. F. *et al.* Polyaniline-polycaprolactone fibers for neural applications: Electroconductivity enhanced by pseudo-doping. *Mater. Sci. Eng. C* **120**, 111680 (2021).
 125. Hwang, J.-Y. *et al.* Biofunctionalized carbon nanotubes in neural regeneration: a mini-review. *Nanoscale* **5**, 487–497 (2013).

126. Steel, E. M., Azar, J.-Y. & Sundararaghavan, H. G. Electrospun hyaluronic acid-carbon nanotube nanofibers for neural engineering. *Materialia* **9**, 100581 (2020).
127. Jurga, M. *et al.* The performance of laminin-containing cryogel scaffolds in neural tissue regeneration. *Biomaterials* **32**, 3423–3434 (2011).
128. Zhao, Q., Sun, J., Lin, Y. & Zhou, Q. Study of the properties of hydrolyzed polyacrylamide hydrogels with various pore structures and rapid pH-sensitivities. *React. Funct. Polym.* **70**, 602–609 (2010).
129. Huang, G. Y. *et al.* Microfluidic hydrogels for tissue engineering. *Biofabrication* **3**, 12001 (2011).
130. Wang, L. *et al.* Biomechanical studies on biomaterial degradation and co-cultured cells: mechanisms {,} potential applications {,} challenges and prospects. *J. Mater. Chem. B* **7**, 7439–7459 (2019).
131. Heljak, M. K., Swieszkowski, W. & Kurzydowski, K. J. Modeling of the degradation kinetics of biodegradable scaffolds: The effects of the environmental conditions. *J. Appl. Polym. Sci.* **131**, (2014).
132. Madl, C. M. *et al.* Maintenance of neural progenitor cell stemness in 3D hydrogels requires matrix remodelling. (2017) doi:10.1038/NMAT5020.
133. Madl, C. M. *et al.* Matrix Remodeling Enhances the Differentiation Capacity of Neural Progenitor Cells in 3D Hydrogels. (2019) doi:10.1002/adv.201801716.
134. Kajtez, J., Nilsson, F., Fiorenzano, A., Parmar, M. & Emnéus, J. 3D biomaterial models of human brain disease. *Neurochem. Int.* **147**, 105043 (2021).
135. Hull, S. M., Brunel, L. G. & Heilshorn, S. C. 3D bioprinting of cell-laden hydrogels for improved biological functionality. *Adv. Mater.* **34**, 2103691 (2022).
136. Jose, G., Shalumon, K. T. & Chen, J.-P. Natural polymers based hydrogels for cell culture applications. *Curr. Med. Chem.* **27**, 2734–2776 (2020).
137. Poorna, M. R., Jayakumar, R., Chen, J.-P. & Mony, U. Hydrogels: A potential platform for induced pluripotent stem cell culture and differentiation. *Colloids Surfaces B Biointerfaces* **207**, 111991 (2021).
138. Neves, S. C., Moroni, L., Barrias, C. C. & Granja, P. L. Leveling Up Hydrogels: Hybrid

- Systems in Tissue Engineering. *Trends Biotechnol.* 1–24 (2019)
doi:10.1016/j.tibtech.2019.09.004.
139. Baiguera, S. *et al.* Electrospun gelatin scaffolds incorporating rat decellularized brain extracellular matrix for neural tissue engineering. *Biomaterials* **35**, 1205–1214 (2014).
 140. Mosahebi, A., Simon, M., Wiberg, M. & Terenghi, G. A novel use of alginate hydrogel as Schwann cell matrix. *Tissue Eng.* **7**, 525–534 (2001).
 141. Sundararaghavan, H. G., Monteiro, G. A., Firestein, B. L. & Shreiber, D. I. Neurite growth in 3D collagen gels with gradients of mechanical properties. *Biotechnol. Bioeng.* **102**, 632–643 (2009).
 142. Cho, H. J., Verbridge, S. S., Davalos, R. V. & Lee, Y. W. Development of an In Vitro 3D Brain Tissue Model Mimicking In Vivo-Like Pro-inflammatory and Pro-oxidative Responses. *Ann. Biomed. Eng.* **46**, 877–887 (2018).
 143. Liang, Y., Walczak, P. & Bulte, J. W. M. The survival of engrafted neural stem cells within hyaluronic acid hydrogels. *Biomaterials* **34**, 5521–5529 (2013).
 144. Hopkins, A. M. *et al.* Silk hydrogels as soft substrates for neural tissue engineering. *Adv. Funct. Mater.* **23**, 5140–5149 (2013).
 145. Pértile, R., Moreira, S., Andrade, F., Domingues, L. & Gama, M. Bacterial cellulose modified using recombinant proteins to improve neuronal and mesenchymal cell adhesion. *Biotechnol. Prog.* **28**, 526–532 (2012).
 146. Tsou, Y.-H., Khoneisser, J., Huang, P.-C. & Xu, X. Hydrogel as a bioactive material to regulate stem cell fate. *Bioact. Mater.* **1**, 39–55 (2016).
 147. Jorfi, M., D’Avanzo, C., Kim, D. Y. & Irimia, D. Three-Dimensional Models of the Human Brain Development and Diseases. *Adv. Healthc. Mater.* **7**, 1700723 (2018).
 148. Kuo, Y.-C. & Wang, C.-C. Guided differentiation of induced pluripotent stem cells into neuronal lineage in alginate–chitosan–gelatin hydrogels with surface neuron growth factor. *Colloids Surfaces B Biointerfaces* **104**, 194–199 (2013).
 149. Rauch, U. Extracellular matrix components associated with remodeling processes in brain. *Cell. Mol. Life Sci.* **61**, 2031–2045 (2004).
 150. Huang, K.-F., Hsu, W.-C., Chiu, W.-T. & Wang, J.-Y. Functional improvement and

- neurogenesis after collagen-GAG matrix implantation into surgical brain trauma. *Biomaterials* **33**, 2067–2075 (2012).
151. Cairns, D. M. *et al.* A 3D human brain-like tissue model of herpes-induced Alzheimer's disease. *Sci. Adv.* **6**, eaay8828 (2020).
 152. Führmann, T., Hillen, L. M., Montzka, K., Wöltje, M. & Brook, G. A. Cell–Cell interactions of human neural progenitor-derived astrocytes within a microstructured 3D-scaffold. *Biomaterials* **31**, 7705–7715 (2010).
 153. Zhou, X. *et al.* Three-dimensional-bioprinted dopamine-based matrix for promoting neural regeneration. *ACS Appl. Mater. Interfaces* **10**, 8993–9001 (2018).
 154. Moxon, S. R. *et al.* Blended alginate/collagen hydrogels promote neurogenesis and neuronal maturation. *Mater. Sci. Eng. C* **104**, 109904 (2019).
 155. Seidlits, S. K. *et al.* Peptide-modified, hyaluronic acid-based hydrogels as a 3D culture platform for neural stem/progenitor cell engineering. *J. Biomed. Mater. Res. Part A* **107**, 704–718 (2019).
 156. Tang-Schomer, M. D. *et al.* Bioengineered functional brain-like cortical tissue. *Proc. Natl. Acad. Sci.* **111**, 13811–13816 (2014).
 157. Lynn, A. K., Yannas, I. V & Bonfield, W. Antigenicity and immunogenicity of collagen. *J. Biomed. Mater. Res. Part B Appl. Biomater. An Off. J. Soc. Biomater. Japanese Soc. Biomater. Aust. Soc. Biomater. Korean Soc. Biomater.* **71**, 343–354 (2004).
 158. Xiao, S. *et al.* Gelatin Methacrylate (GelMA)-Based Hydrogels for Cell Transplantation: an Effective Strategy for Tissue Engineering. *Stem Cell Rev. Reports* 1–16.
 159. Yue, K. *et al.* Synthesis, properties, and biomedical applications of gelatin methacryloyl (GelMA) hydrogels. *Biomaterials* **73**, 254–271 (2015).
 160. Bigi, A., Cojazzi, G., Panzavolta, S., Rubini, K. & Roveri, N. Mechanical and thermal properties of gelatin films at different degrees of glutaraldehyde crosslinking. *Biomaterials* **22**, 763–768 (2001).
 161. Draye, J.-P. *et al.* In vitro release characteristics of bioactive molecules from dextran dialdehyde cross-linked gelatin hydrogel films. *Biomaterials* **19**, 99–107 (1998).
 162. Kim, H., Knowles, J. C. & Kim, H. Hydroxyapatite and gelatin composite foams

- processed via novel freeze-drying and crosslinking for use as temporary hard tissue scaffolds. *J. Biomed. Mater. Res. Part A An Off. J. Soc. Biomater. Japanese Soc. Biomater. Aust. Soc. Biomater. Korean Soc. Biomater.* **72**, 136–145 (2005).
163. Yue, K. *et al.* Structural analysis of photocrosslinkable methacryloyl-modified protein derivatives. *Biomaterials* **139**, 163–171 (2017).
 164. Łabowska, M. B. *et al.* A Review on the Adaption of Alginate-Gelatin Hydrogels for 3D Cultures and Bioprinting. *Materials (Basel)*. **14**, 858 (2021).
 165. Neves, M. I., Moroni, L. & Barrias, C. C. Modulating Alginate Hydrogels for Improved Biological Performance as Cellular 3D Microenvironments. *Front. Bioeng. Biotechnol.* **8**, 665 (2020).
 166. Chen, Q. *et al.* An interpenetrating alginate/gelatin network for three-dimensional (3D) cell cultures and organ bioprinting. *Molecules* **25**, 756 (2020).
 167. Sachdev, A. *et al.* A Review on Techniques and Biomaterials Used in 3D Bioprinting. *Cureus* **14**, (2022).
 168. Ning, L. *et al.* Bioprinting Schwann cell-laden scaffolds from low-viscosity hydrogel compositions. *J. Mater. Chem. B* **7**, 4538–4551 (2019).
 169. Ding, Y.-W. *et al.* Recent advances in hyaluronic acid-based hydrogels for 3D bioprinting in tissue engineering applications. *Smart Mater. Med.* **4**, 59–68 (2023).
 170. Ouyang, L., Highley, C. B., Rodell, C. B., Sun, W. & Burdick, J. A. 3D Printing of Shear-Thinning Hyaluronic Acid Hydrogels with Secondary Cross-Linking. *ACS Biomater. Sci. Eng.* **2**, 1743–1751 (2016).
 171. Noh, I., Kim, N., Tran, H. N., Lee, J. & Lee, C. 3D printable hyaluronic acid-based hydrogel for its potential application as a bioink in tissue engineering. *Biomater. Res.* **23**, 3 (2019).
 172. Hong, S. *et al.* Hyaluronic acid catechol: a biopolymer exhibiting a pH-dependent adhesive or cohesive property for human neural stem cell engineering. *Adv. Funct. Mater.* **23**, 1774–1780 (2013).
 173. Zhang, Z.-N. *et al.* Layered hydrogels accelerate iPSC-derived neuronal maturation and reveal migration defects caused by MeCP2 dysfunction. *Proc. Natl. Acad. Sci.* **113**,

- 3185–3190 (2016).
174. Kaiser, A., Kale, A., Novozhilova, E. & Olivius, P. The effects of Matrigel® on the survival and differentiation of a human neural progenitor dissociated sphere culture. *Anat. Rec.* (2019).
 175. Miguel, L. *et al.* Detection of all adult Tau isoforms in a 3D culture model of iPSC-derived neurons. *Stem Cell Res.* **40**, 101541 (2019).
 176. Abbott, R. D., Kimmerling, E. P., Cairns, D. M. & Kaplan, D. L. Silk as a Biomaterial to Support Long-Term Three-Dimensional Tissue Cultures. *ACS Appl. Mater. Interfaces* **8**, 21861–21868 (2016).
 177. Namba, R. M., Cole, A. A., Bjugstad, K. B. & Mahoney, M. J. Development of porous PEG hydrogels that enable efficient, uniform cell-seeding and permit early neural process extension. *Acta Biomater.* **5**, 1884–1897 (2009).
 178. Plant, G. W., Harvey, A. R. & Chirila, T. V. Axonal growth within poly (2-hydroxyethyl methacrylate) sponges infiltrated with Schwann cells and implanted into the lesioned rat optic tract. *Brain Res.* **671**, 119–130 (1995).
 179. Ashammakhi, N. *et al.* Bioinks and bioprinting technologies to make heterogeneous and biomimetic tissue constructs. *Mater. Today Bio* **1**, (2019).
 180. Crowe, J. A. *et al.* Development of two-photon polymerised scaffolds for optical interrogation and neurite guidance of human iPSC-derived cortical neuronal networks. *Lab Chip* (2020).
 181. Woodruff, M. A. & Hutmacher, D. W. The return of a forgotten polymer—Polycaprolactone in the 21st century. *Prog. Polym. Sci.* **35**, 1217–1256 (2010).
 182. Suzuki, K. *et al.* Electrospun nanofiber sheets incorporating methylcobalamin promote nerve regeneration and functional recovery in a rat sciatic nerve crush injury model. *Acta Biomater.* **53**, 250–259 (2017).
 183. Cerrone, F. *et al.* Polyhydroxyphenylvalerate/polycaprolactone nanofibers improve the life-span and mechanoresponse of human IPSC-derived cortical neuronal cells. *Mater. Sci. Eng. C* **111**, 110832 (2020).
 184. Zhang, S. Designer self-assembling peptide nanofiber scaffolds for study of 3-D cell

- biology and beyond. *Adv. Cancer Res.* **99**, 335–362 (2008).
185. Gelain, F., Bottai, D., Vescovi, A. & Zhang, S. Designer self-assembling peptide nanofiber scaffolds for adult mouse neural stem cell 3-dimensional cultures. *PLoS One* **1**, e119 (2006).
 186. Cunha, C., Panseri, S., Villa, O., Silva, D. & Gelain, F. 3D culture of adult mouse neural stem cells within functionalized self-assembling peptide scaffolds. *Int. J. Nanomedicine* **6**, 943–955 (2011).
 187. Aurand, E. R., Wagner, J. L., Shandas, R. & Bjugstad, K. B. Hydrogel formulation determines cell fate of fetal and adult neural progenitor cells. *Stem Cell Res.* **12**, 11–23 (2014).
 188. Cantley, W. L. *et al.* Functional and Sustainable 3D Human Neural Network Models from Pluripotent Stem Cells. *ACS Biomater. Sci. Eng.* **4**, 4278–4288 (2018).
 189. Karvinen, J. *et al.* Soft hydrazone crosslinked hyaluronan- and alginate-based hydrogels as 3D supportive matrices for human pluripotent stem cell-derived neuronal cells. *React. Funct. Polym.* **124**, 29–39 (2018).
 190. Gilbert, T. W., Sellaro, T. L. & Badylak, S. F. Decellularization of tissues and organs. *Biomaterials* **27**, 3675–3683 (2006).
 191. Kabirian, F. & Mozafari, M. Decellularized ECM-derived Bioinks: Prospects for the future. *Methods* (2019) doi:10.1016/J.YMETH.2019.04.019.
 192. DeQuach, J. A., Yuan, S. H., Goldstein, L. S. B. & Christman, K. L. Decellularized porcine brain matrix for cell culture and tissue engineering scaffolds. *Tissue Eng. Part A* **17**, 2583–2592 (2011).
 193. Sood, D. *et al.* Functional maturation of human neural stem cells in a 3D bioengineered brain model enriched with fetal brain-derived matrix. *Sci. Rep.* **9**, 17874 (2019).
 194. Santschi, M., Vernengo, A., Eglin, D., D’Este, M. & Wuertz-Kozak, K. Decellularized matrix as a building block in bioprinting and electrospinning. *Curr. Opin. Biomed. Eng.* (2019) doi:10.1016/j.cobme.2019.05.003.
 195. Murphy, S. V. 3D bioprinting of tissues and organs: Nature Biotechnology. *Nat. Biotechnol.* **32**, 773 (2014).

196. Ding, S. *et al.* Bioprinting of Stem Cells: Interplay of Bioprinting Process, Bioinks, and Stem Cell Properties. *ACS Biomater. Sci. Eng.* **4**, 3108–3124 (2018).
197. Heidarian, P., Kouzani, A., Kaynak, A., Paulino, M. & Nasri-Nasrabadi, B. Dynamic Hydrogels and Polymers as Inks for 3D Printing. *ACS Biomater. Sci. Eng.* acsbiomaterials.9b00047 (2019) doi:10.1021/acsbiomaterials.9b00047.
198. Naghieh, S., Sarker, M., Sharma, N. K., Barhoumi, Z. & Chen, X. Printability of 3D Printed Hydrogel Scaffolds: Influence of Hydrogel Composition and Printing Parameters. *Appl. Sci.* (2019) doi:10.3390/app10010292.
199. Chang, R., Nam, J. & Sun, W. Effects of dispensing pressure and nozzle diameter on cell survival from solid freeform fabrication–based direct cell writing. *Tissue Eng. Part A* **14**, 41–48 (2008).
200. Malda, J. *et al.* 25th anniversary article: engineering hydrogels for biofabrication. *Adv. Mater.* **25**, 5011–5028 (2013).
201. Xu, C., Dai, G. & Hong, Y. Recent advances in high-strength and elastic hydrogels for 3D printing in biomedical applications. *Acta Biomater.* (2019) doi:10.1016/J.ACTBIO.2019.05.032.
202. Nahmias, Y. & Odde, D. J. Micropatterning of living cells by laser-guided direct writing: application to fabrication of hepatic–endothelial sinusoid-like structures. *Nat. Protoc.* **1**, 2288 (2006).
203. Schiele, N. R. *et al.* Laser-based direct-write techniques for cell printing. *Biofabrication* **2**, 32001 (2010).
204. Ma, J., Wang, Y. & Liu, J. Bioprinting of 3D tissues/organs combined with microfluidics. *RSC Adv.* **8**, 21712–21727 (2018).
205. Thomas, M. & Willerth, S. M. 3-D Bioprinting of Neural Tissue for Applications in Cell Therapy and Drug Screening. *Front. Bioeng. Biotechnol.* **5**, 1–11 (2017).
206. Zhang, B. *et al.* 3D Bioprinting: A Novel Avenue for Manufacturing Tissues and Organs. *Engineering* (2019) doi:10.1016/J.ENG.2019.03.009.
207. O’Brien, C. M., Holmes, B., Faucett, S. & Zhang, L. G. Three-dimensional printing of nanomaterial scaffolds for complex tissue regeneration. *Tissue Eng. Part B Rev.* **21**,

- 103–114 (2014).
208. Gudapati, H., Dey, M. & Ozbolat, I. A comprehensive review on droplet-based bioprinting: Past, present and future. *Biomaterials* **102**, 20–42 (2016).
 209. Sarker, M. D., Naghieh, S., Sharma, N. K., Ning, L. & Chen, X. Bioprinting of Vascularized Tissue Scaffolds: Influence of Biopolymer, Cells, Growth Factors, and Gene Delivery. *J. Healthc. Eng.* **2019**, (2019).
 210. Ouyang, L., Yao, R., Zhao, Y. & Sun, W. Effect of bioink properties on printability and cell viability for 3D bioplotting of embryonic stem cells. *Biofabrication* **8**, 35020 (2016).
 211. Joung, D. *et al.* 3D Printed Stem-Cell Derived Neural Progenitors Generate Spinal Cord Scaffolds. *Adv. Funct. Mater.* **28**, 1–10 (2018).
 212. de la Vega, L. *et al.* 3D Bioprinting Human Induced Pluripotent Stem Cell-Derived Neural Tissues Using a Novel Lab-on-a-Printer Technology. *Appl. Sci.* **8**, 2414 (2018).
 213. Gu, Q., Tomaskovic-Crook, E., Wallace, G. G. & Crook, J. M. 3D Bioprinting Human Induced Pluripotent Stem Cell Constructs for In Situ Cell Proliferation and Successive Multilineage Differentiation. *Adv. Healthc. Mater.* **6**, 1700175 (2017).
 214. Hospodiuk, M., Dey, M., Sosnoski, D. & Ozbolat, I. T. The bioink: a comprehensive review on bioprintable materials. *Biotechnol. Adv.* **35**, 217–239 (2017).
 215. Oliveira, E. P. *et al.* *Advances in bioinks and in vivo imaging of biomaterials for CNS applications.* *Acta Biomaterialia* (Acta Materialia Inc., 2019). doi:10.1016/j.actbio.2019.05.006.
 216. Charwat, V. *et al.* Potential and limitations of microscopy and Raman spectroscopy for live-cell analysis of 3D cell cultures. *J. Biotechnol.* **205**, 70–81 (2015).
 217. Carragher, N. *et al.* Concerns, challenges and promises of high-content analysis of 3D cellular models. *Nat. Rev. Drug Discov.* **17**, 606 (2018).
 218. Odawara, A., Gotoh, M. & Suzuki, I. A three-dimensional neuronal culture technique that controls the direction of neurite elongation and the position of soma to mimic the layered structure of the brain. *RSC Adv.* **3**, 23620–23630 (2013).
 219. Temple, J., Velliou, E., Shehata, M. & Lévy, R. Current strategies with implementation of three-dimensional cell culture: the challenge of quantification. *Interface Focus* **12**,

- 20220019 (2022).
220. Marino, A. *et al.* A 3D real-scale, biomimetic, and biohybrid model of the blood-brain barrier fabricated through two-photon lithography. *Small* **14**, 1702959 (2018).
 221. Yang, Z. & Xiong, H.-R. Culture conditions and types of growth media for mammalian cells. *Biomed. Tissue Cult.* **1**, 3–18 (2012).
 222. Joseph, X., Akhil, V., Arathi, A. & Mohanan, P. V. Comprehensive development in organ-on-a-chip technology. *J. Pharm. Sci.* **111**, 18–31 (2022).
 223. Bhatia, S. N. & Ingber, D. E. Microfluidic organs-on-chips. *Nat. Biotechnol.* **32**, 760–772 (2014).
 224. Wang, Z. *et al.* A High-Resolution Minimicroscope System for Wireless Real-Time Monitoring. *IEEE Trans. Biomed. Eng.* **65**, 1524–1531 (2018).
 225. Moutaux, E., Charlot, B., Genoux, A., Saudou, F. & Cazorla, M. An integrated microfluidic/microelectrode array for the study of activity-dependent intracellular dynamics in neuronal networks. *Lab Chip* **18**, 3425–3435 (2018).
 226. Bhagat, A. A. S. *et al.* Microfluidics for cell separation. *Med. Biol. Eng. Comput.* **48**, 999–1014 (2010).
 227. Zhang, Q. & Austin, R. H. Applications of microfluidics in stem cell biology. *Bionanoscience* **2**, 277–286 (2012).
 228. Achyuta, A. K. H. *et al.* A modular approach to create a neurovascular unit-on-a-chip. *Lab Chip* **13**, 542–553 (2013).
 229. Coquinco, A. *et al.* A microfluidic based in vitro model of synaptic competition. *Mol. Cell. Neurosci.* **60**, 43–52 (2014).
 230. Taylor, A. M. *et al.* A microfluidic culture platform for CNS axonal injury, regeneration and transport. *Nat. Methods* **2**, 599–605 (2005).
 231. Virlogeux, A. *et al.* Reconstituting Corticostriatal Network on-a-Chip Reveals the Contribution of the Presynaptic Compartment to Huntington’s Disease. *Cell Rep.* **22**, 110–122 (2018).
 232. Li, W. *et al.* Investigation of the Subcellular Neurotoxicity of Amyloid- β Using a Device Integrating Microfluidic Perfusion and Chemotactic Guidance. *Adv. Healthc. Mater.* **6**,

- 1600895 (2017).
233. Sala-Jarque, J. *et al.* Neuromuscular Activity Induces Paracrine Signaling and Triggers Axonal Regrowth after Injury in Microfluidic Lab-On-Chip Devices. *Cells* **9**, 302 (2020).
 234. Mahto, S. K., Song, H. & Rhee, S. W. Functional synapse formation between compartmentalized cortical neurons cultured inside microfluidic devices. *BioChip J.* **5**, 289–298 (2011).
 235. Pan, L., Alagapan, S., Franca, E., Brewer, G. J. & Wheeler, B. C. Propagation of action potential activity in a predefined microtunnel neural network. *J. Neural Eng.* **8**, 46031 (2011).
 236. Peyrin, J. M. *et al.* Axon diodes for the reconstruction of oriented neuronal networks in microfluidic chambers. *Lab Chip* **11**, 3663–3673 (2011).
 237. Gladkov, A. *et al.* Design of Cultured Neuron Networks in vitro with Predefined Connectivity Using Asymmetric Microfluidic Channels. *Sci. Rep.* **7**, 15625 (2017).
 238. Forró, C. *et al.* Modular microstructure design to build neuronal networks of defined functional connectivity. *Biosens. Bioelectron.* **122**, 75–87 (2018).
 239. Liu, H., Lin, J. & Roy, K. Effect of 3D scaffold and dynamic culture condition on the global gene expression profile of mouse embryonic stem cells. *Biomaterials* **27**, 5978–5989 (2006).
 240. Hakanen, J., Ruiz-Reig, N. & Tissir, F. Linking cell polarity to cortical development and malformations. *Front. Cell. Neurosci.* **13**, 244 (2019).
 241. Kothapalli, C. R. *et al.* A high-throughput microfluidic assay to study neurite response to growth factor gradients. *Lab Chip* **11**, 497–507 (2011).
 242. Sloan, T. F. W., Qasaimeh, M. A., Juncker, D., Yam, P. T. & Charron, F. Integration of shallow gradients of Shh and Netrin-1 guides commissural axons. *PLoS Biol.* **13**, e1002119 (2015).
 243. Ramamurthy, P. *et al.* Concomitant differentiation of a population of mouse embryonic stem cells into neuron-like cells and schwann cell-like cells in a slow-flow microfluidic device. *Dev. Dyn.* **246**, 7–27 (2017).

244. Demers, C. J. *et al.* Development-on-chip: in vitro neural tube patterning with a microfluidic device. *Development* **143**, 1884–1892 (2016).
245. Uzel, S. G. M. *et al.* Simultaneous or Sequential Orthogonal Gradient Formation in a 3D Cell Culture Microfluidic Platform. *Small* **12**, 612–622 (2016).
246. Chow, B. W. & Gu, C. The Molecular Constituents of the Blood–Brain Barrier. *Trends Neurosci.* **38**, 598–608 (2015).
247. Campisi, M. *et al.* 3D self-organized microvascular model of the human blood-brain barrier with endothelial cells, pericytes and astrocytes. *Biomaterials* **180**, 117–129 (2018).
248. Adriani, G., Ma, D., Pavesi, A., Kamm, R. D. & Goh, E. L. K. A 3D neurovascular microfluidic model consisting of neurons, astrocytes and cerebral endothelial cells as a blood-brain barrier. *Lab Chip* **17**, 448–459 (2017).
249. Bang, S. *et al.* A low permeability microfluidic blood-brain barrier platform with direct contact between perfusable vascular network and astrocytes. *Sci. Rep.* **7**, 8083 (2017).
250. Deosarkar, S. P. *et al.* A novel dynamic neonatal blood-brain barrier on a chip. *PLoS One* **10**, 1–21 (2015).
251. Chung, B. *et al.* Evaluation of Cell-Penetrating Peptides Using Microfluidic In Vitro 3D Brain Endothelial Barrier. *Macromol. Biosci.* 1900425 (2020).
252. Sances, S. *et al.* Human iPSC-derived endothelial cells and microengineered organ-chip enhance neuronal development. *Stem cell reports* **10**, 1222–1236 (2018).
253. Vatine, G. D. *et al.* Human iPSC-Derived Blood-Brain Barrier Chips Enable Disease Modeling and Personalized Medicine Applications. *Cell Stem Cell* **24**, 995–1005 (2019).
254. Cullen, D. K. & LaPlaca, M. C. Neuronal Response to High Rate Shear Deformation Depends on Heterogeneity of the Local Strain Field. *J. Neurotrauma* **23**, 1304–1319 (2006).
255. Osaki, T., Sivathanu, V. & Kamm, R. D. Engineered 3D vascular and neuronal networks in a microfluidic platform. *Sci. Rep.* **8**, 1–13 (2018).
256. Wang, Y., Wang, L., Zhu, Y. & Qin, J. Human brain organoid-on-a-chip to model prenatal nicotine exposure. *Lab Chip* **18**, 851–860 (2018).

257. Klim, J. R. *et al.* ALS-implicated protein TDP-43 sustains levels of STMN2, a mediator of motor neuron growth and repair. *Nat. Neurosci.* **22**, (2019).
258. Kamande, J. W., Nagendran, T., Harris, J. & Taylor, A. M. Multi-compartment Microfluidic Device Geometry and Covalently Bound Poly-D-Lysine Influence Neuronal Maturation. **7**, 1–9 (2019).
259. Park, J. *et al.* A 3D human triculture system modeling neurodegeneration and neuroinflammation in Alzheimer’s disease. *Nat. Neurosci.* **21**, 941–951 (2018).
260. Osaki, T., Uzel, S. G. M. & Kamm, R. D. Microphysiological 3D model of amyotrophic lateral sclerosis (ALS) from human iPS-derived muscle cells and optogenetic motor neurons. *Sci. Adv.* **4**, eaat5847 (2018).
261. Lee, S. W. L. *et al.* Modeling Nanocarrier Transport across a 3D In Vitro Human Blood–Brain–Barrier Microvasculature. *Adv. Healthc. Mater.* **9**, 1901486 (2020).
262. Liu, H. *et al.* Advances in Hydrogels in Organoids and Organs-on-a-Chip. *Adv. Mater.* **31**, 1–28 (2019).
263. Park, J. *et al.* Three-dimensional brain-on-a-chip with an interstitial level of flow and its application as an in vitro model of Alzheimer’s disease. *Lab Chip* **15**, 141–150 (2015).
264. Habibey, R., Rojo Arias, J. E., Striebel, J. & Busskamp, V. Microfluidics for Neuronal cell and circuit engineering. *Chem. Rev.* **122**, 14842–14880 (2022).
265. Halldorsson, S., Lucumi, E., Gómez-Sjöberg, R. & Fleming, R. M. T. Advantages and challenges of microfluidic cell culture in polydimethylsiloxane devices. *Biosens. Bioelectron.* **63**, 218–231 (2015).
266. Habibey, R. *et al.* A multielectrode array microchannel platform reveals both transient and slow changes in axonal conduction velocity. *Sci. Rep.* **7**, 8558 (2017).
267. Shin, H. *et al.* 3D high-density microelectrode array with optical stimulation and drug delivery for investigating neural circuit dynamics. *Nat. Commun.* **12**, 1–18 (2021).
268. Visser, J. *et al.* Reinforcement of hydrogels using three-dimensionally printed microfibrils. *Nat. Commun.* **6**, 6933 (2015).
269. Kloxin, A. M., Benton, J. A. & Anseth, K. S. In situ elasticity modulation with dynamic substrates to direct cell phenotype. *Biomaterials* **31**, 1–8 (2010).

270. Snyder, E. Y. *et al.* Multipotent neural cell lines can engraft and participate in development of mouse cerebellum. *Cell* **68**, 33–51 (1992).
271. Orlandi, J. G. *et al.* NETCAL: an interactive platform for large-scale, NETWORK and population dynamics analysis of calcium imaging recordings. *Neuroscience* (2017) doi:doi.org/10.5281/zenodo.1119026.
272. Palma-Tortosa, S. *et al.* Activity in grafted human iPS cell-derived cortical neurons integrated in stroke-injured rat brain regulates motor behavior. *Proc. Natl. Acad. Sci.* **117**, 9094–9100 (2020).
273. Comella-Bolla, A. *et al.* Human Pluripotent Stem Cell-Derived Neurons Are Functionally Mature In Vitro and Integrate into the Mouse Striatum Following Transplantation. *Mol. Neurobiol.* **57**, 2766–2798 (2020).
274. Lundqvist, J., EL Andaloussi-Lilja, J., Svensson, C., Gustafsson Dorfh, H. & Forsby, A. Optimisation of culture conditions for differentiation of C17.2 neural stem cells to be used for in vitro toxicity tests. *Toxicol. Vitro.* **27**, 1565–1569 (2013).
275. Kaindl, J. & Winner, B. Disease Modeling of Neuropsychiatric Brain Disorders Using Human Stem Cell-Based Neural Models. (2019).
276. Gupta, P. *et al.* Microfluidic platforms for single neuron analysis. *Mater. Today Bio* 100222 (2022).
277. Ranjan, V. D., Qiu, L., Tan, E. K., Zeng, L. & Zhang, Y. Modelling Alzheimer’s disease: Insights from in vivo to in vitro three-dimensional culture platforms. *J. Tissue Eng. Regen. Med.* **12**, 1944–1958 (2018).
278. Brunetti, V. *et al.* Neurons sense nanoscale roughness with nanometer sensitivity. *Proc. Natl. Acad. Sci.* **107**, 6264–6269 (2010).
279. Rastogi, P. & Kandasubramanian, B. Review of alginate-based hydrogel bioprinting for application in tissue engineering. *Biofabrication* **11**, 042001 (2019).
280. Sherman, L. S. *et al.* Hyaluronate-based extracellular matrix: Keeping glia in their place. *Glia* **38**, 93–102 (2002).
281. Annabi, N. *et al.* Controlling the Porosity and Microarchitecture of Hydrogels for Tissue Engineering. *Tissue Eng. Part B Rev.* **16**, 371–383 (2010).

282. García-Lizarriar, A. *et al.* Composite Biomaterials as Long-Lasting Scaffolds for 3D Bioprinting of Highly Aligned Muscle Tissue. *Macromol. Biosci.* **18**, 1800167 (2018).
283. Wen, Y.-Q. *et al.* Substrate stiffness affects neural network activity in an extracellular matrix proteins dependent manner. *Colloids Surfaces B Biointerfaces* **170**, 729–735 (2018).
284. Kharkar, P. M., Kiick, K. L. & Kloxin, A. M. Designing degradable hydrogels for orthogonal control of cell microenvironments. *Chem. Soc. Rev.* **42**, 7335–7372 (2013).
285. Madl, C. M. *et al.* Maintenance of neural progenitor cell stemness in 3D hydrogels requires matrix remodelling. *Nat. Mater.* **16**, 1233–1242 (2017).
286. Noshadi, I. *et al.* In vitro and in vivo analysis of visible light crosslinkable gelatin methacryloyl (GelMA) hydrogels. *Biomater. Sci.* **5**, 2093–2105 (2017).
287. Krishnamoorthy, S., Zhang, Z. & Xu, C. Biofabrication of three-dimensional cellular structures based on gelatin methacrylate–alginate interpenetrating network hydrogel. *J. Biomater. Appl.* **33**, 1105–1117 (2019).
288. Santana, B. P. *et al.* Comparing different methods to fix and to dehydrate cells on alginate hydrogel scaffolds using scanning electron microscopy. *Microsc. Res. Tech.* **78**, 553–561 (2015).
289. Kim, M.-C., Silberberg, Y. R., Abeyaratne, R., Kamm, R. D. & Asada, H. H. Computational modeling of three-dimensional ECM-rigidity sensing to guide directed cell migration. *Proc. Natl. Acad. Sci.* **115**, E390–E399 (2018).
290. Bechara, S., Wadman, L. & Popat, K. C. Electroconductive polymeric nanowire templates facilitates in vitro C17.2 neural stem cell line adhesion, proliferation and differentiation. *Acta Biomater.* **7**, 2892–2901 (2011).
291. Wang, B., Jedlicka, S. & Cheng, X. Maintenance and Neuronal Cell Differentiation of Neural Stem Cells C17.2 Correlated to Medium Availability Sets Design Criteria in Microfluidic Systems. *PLoS One* **9**, e109815 (2014).
292. Attoff, K., Kertika, D., Lundqvist, J., Oredsson, S. & Forsby, A. Acrylamide affects proliferation and differentiation of the neural progenitor cell line C17.2 and the neuroblastoma cell line SH-SY5Y. *Toxicol. Vitro.* **35**, 100–111 (2016).

293. McAdams, H. H. & Arkin, A. Stochastic mechanisms in gene expression. *Proc. Natl. Acad. Sci.* **94**, 814–819 (1997).
294. Tao, Y., Zheng, X. & Sun, Y. Effect of feedback regulation on stochastic gene expression. *J. Theor. Biol.* **247**, 827–836 (2007).
295. Nair, K. *et al.* Characterization of cell viability during bioprinting processes. *Biotechnol. J.* **4**, 1168–1177 (2009).
296. Lee, Y. B. *et al.* Bio-printing of collagen and VEGF-releasing fibrin gel scaffolds for neural stem cell culture. *Exp. Neurol.* **223**, 645–652 (2010).
297. Chiappalone, M., Bove, M., Vato, A., Tedesco, M. & Martinoia, S. Dissociated cortical networks show spontaneously correlated activity patterns during in vitro development. *Brain Res.* **1093**, 41–53 (2006).
298. Biffi, E. Microfluidic and compartmentalized platforms for neurobiological research. *Microfluid. Compart. Platforms Neurobiol. Res.* **103**, 1–248 (2015).
299. Noble, E. E., Billington, C. J., Kotz, C. M. & Wang, C. The lighter side of BDNF. *Am. J. Physiol. Integr. Comp. Physiol.* **300**, R1053–R1069 (2011).
300. Kearns, C. M. & Gash, D. M. GDNF protects nigral dopamine neurons against 6-hydroxydopamine in vivo. *Brain Res.* **672**, 104–111 (1995).
301. Moore, S. *et al.* APP metabolism regulates tau proteostasis in human cerebral cortex neurons. *Cell Rep.* **11**, 689–696 (2015).
302. Baysal, K., Aroguz, A. Z., Adiguzel, Z. & Baysal, B. M. Chitosan/alginate crosslinked hydrogels: Preparation, characterization and application for cell growth purposes. *Int. J. Biol. Macromol.* **59**, 342–348 (2013).
303. Li, Z. *et al.* Tuning Alginate-Gelatin Bioink Properties by Varying Solvent and Their Impact on Stem Cell Behavior. *Sci. Rep.* **8**, 8020 (2018).
304. Suárez, L. E., Markello, R. D., Betzel, R. F. & Misic, B. Linking structure and function in macroscale brain networks. *Trends Cogn. Sci.* **24**, 302–315 (2020).
305. Testa, C. M. & Jankovic, J. Huntington disease: A quarter century of progress since the gene discovery. *J. Neurol. Sci.* **396**, 52–68 (2019).

Appendix 1 - ^1H -NMR spectra of AlgMA and GelMA

This Annex provides supportive information to the results presented in PART 1 of the Result section of this thesis. It consists of the nuclear magnetic resonance (^1H -NMR) spectra performed to confirm the methacrylation of the gelatin and alginate. This analysis was performed in collaboration with Anna Vilche from Nanobioengineering group at IBEC.

Methodology

^1H -NMR analysis was performed to evaluate the effectiveness of methacrylation methacrylated alginate (AlgMA) and methacrylated gelatin (GelMA) and compared with alginate and gelatin samples. To perform the analysis, 20 mg of each polymer was dissolved in 0.8 ml of deuterium oxide (D_2O) (VWR Chemicals). As an internal NMR reference, 0.002% of D_2O solution of Trimethylsilylpropanoic acid was previously prepared. Samples were dissolved at 65-70 °C at constant stirring for 1 h. Later, 0.8 ml of each solution was transferred into temperature-resistant Class A NMR tubes. GelMA samples were kept and tested at 37 °C to avoid gelation while AlgMA samples were kept at room temperature and tested at 70 °C. Samples were tested using a 500 MHz Bruker Avance Neo unit and the data was processed using MestReNova software. For the analysis of the ^1H -NMR spectra, PRESAT technology was used to eliminate the solvent (D_2O) peak since it was positioned in the interest region.

Results

When comparing the alginate (Figure 1A) and AlgMA (Figure 1B) spectra we could see two peaks present only in AlgMA spectrum at 5.17 and 6.11 ppm, corresponding to the methacrylic groups, confirming the methacrylation. As for the GelMA sample (Figure 1D), its spectrum revealed two new peaks at 5.43 and 5.66 ppm in addition to the modification of the peak at 2 ppm which are attributed to the methacrylic groups, validating the methacrylation protocol.

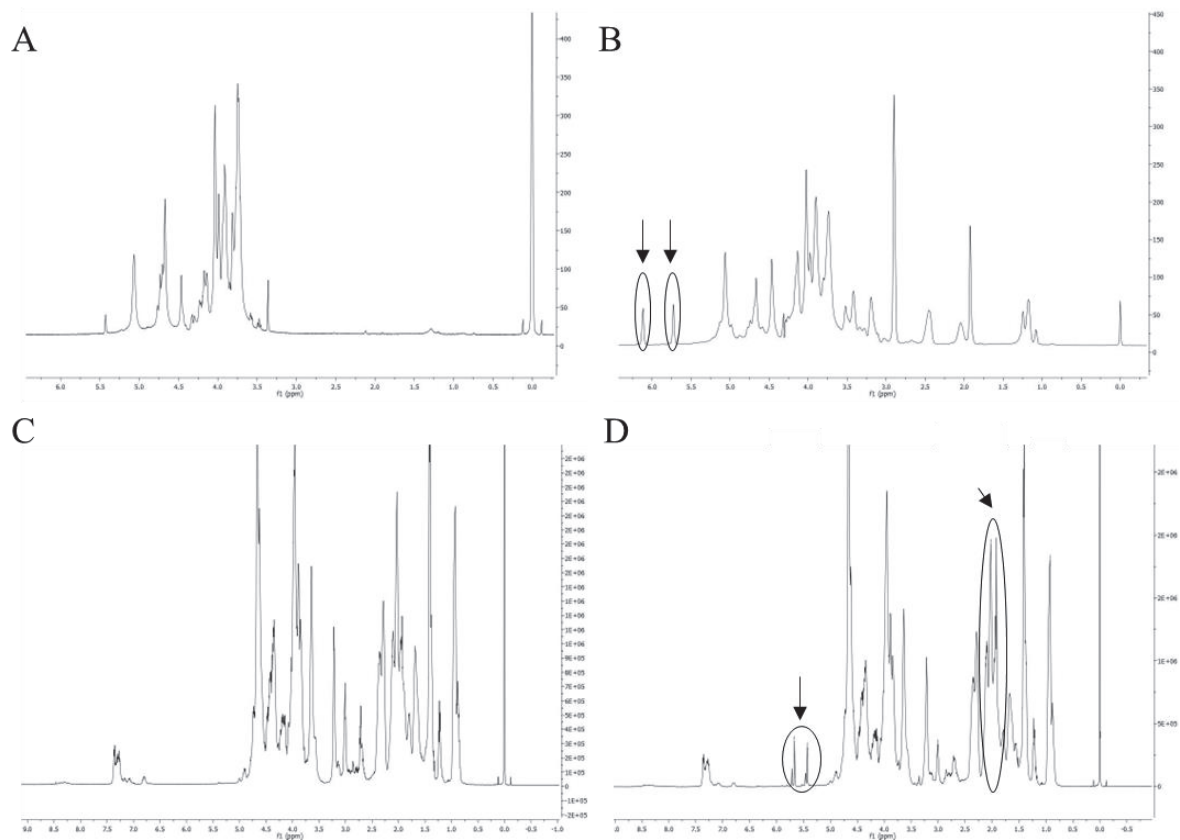


Figure 53 $^1\text{H-NMR}$ analysis of polymer precursor samples. (A) $^1\text{H-NMR}$ spectrum of alginate; (B) $^1\text{H-NMR}$ spectrum of AlgMA; (C) table with the corresponding peaks in the AlgMA spectrum. (C) $^1\text{H-NMR}$ spectrum of gelatin; (D) $^1\text{H-NMR}$ spectrum of GelMA.

Appendix 2 – GelMA + AlgMA + HA crosslinked at 395 nm

This appendix section provides a pilot study using the developed biomaterial in PART I but crosslinked with a different UV light source. In collaboration with Biomaterials for Regenerative Therapies group from IBEC, we studied the culture of C17.2 cells in the 3D microfluidic device with GelMA + AlgMA + HA assessing the viability and differentiation of the cells. In parallel, we characterized the physical properties of the hydrogel.

Introduction

The fabrication of hydrogels for cell culture can be achieved through several methodologies. In the case of composite materials, one of the common techniques to link them is by chemically modifying the materials with methacrylate groups and crosslinking them with UV light when combined with a photocrosslinker. In this thesis, the photocrosslinker we used was LAP. This reagent allows a stronger crosslinking with UV light in the length of 365nm. However, the crosslink can happen at lower wavelengths like 395nm¹. The exposure of the cell to UV light can be harmful and so viability studies are important for UV-crosslinked materials. However, lower wavelengths such as 395 nm are known to be less harmful to the cells².

In this proof-of-concept study, we wanted to assess if by changing the UV-light source, the GelMA + AlgMA + HA biomaterial would provide similar or better results than the ones performed with the UV lamp 365 nm and presented in the Result section of this thesis.

Methodology

The microfluidic devices used in these studies were the same described in the Methods section 7.1.1 3D Microfluidic device – 3D device. The hydrogel was prepared as described in section 2. Composite hydrogel preparation. In case of the physical assays, the samples were prepared as described in 3. Physical characterization, using the 395 nm lamp (395-400nm LED lamp, Sevenjuly, Amazon) instead of the 365 nm UV lamp from the 3D bioprinter (3DDiscovery BioSafety, RegenHU). Samples were exposed at 10.5 cm of distance from the lamp, for 40 seconds, and with a 2 cm PDMS layer between the sample and the lamp to simulate the PDMS present in the microfluid device.

The inclusion of the hydrogel and cells in the microfluidic device was performed as described in 8. Inclusion of the cells in the 3D microfluidic device using the 395 nm lamp instead. The biological assays, LIVE/DEAD and Immunolabelling were performed as described in 8.3.1 and 8.3.2 in Methods section.

Results

For the physical characterization of the GelMA + AlgMA + HA formulation, we performed a degradation assay and a compression modulus assay (Figure 1). The degradation rate of the two hydrogels did not have any significant differences (Figure 1A) as well as the compression modulus values (Figure 1B).

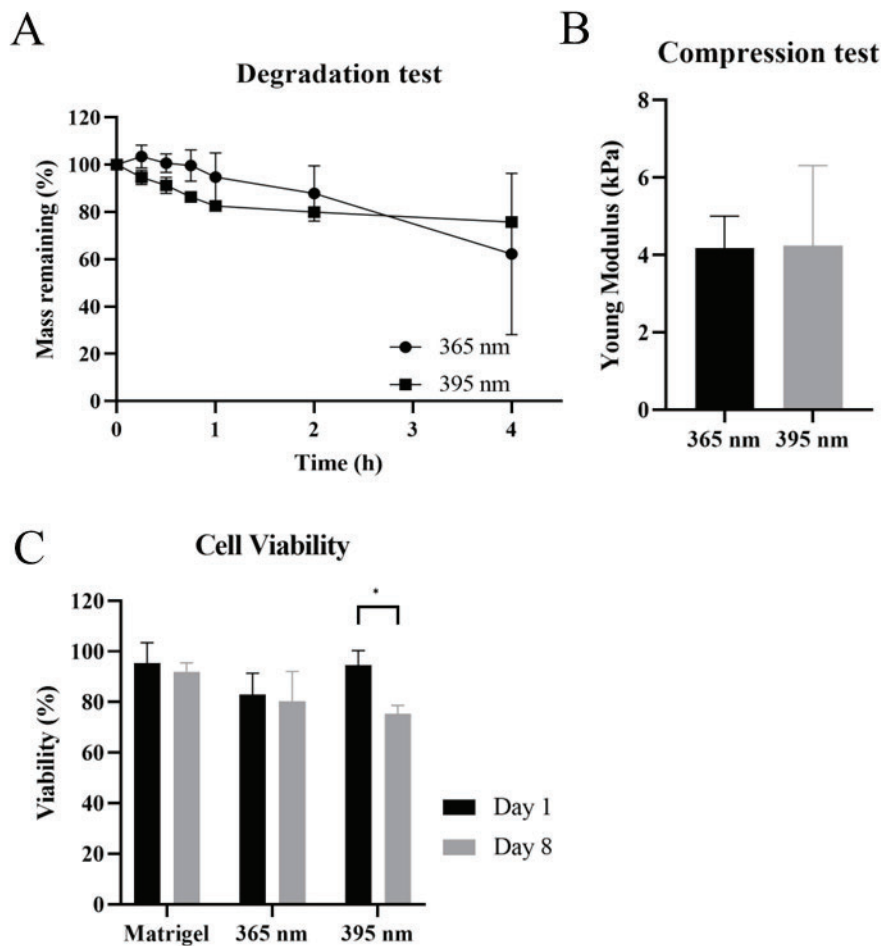


Figure 1 Physical characterization and viability assays using GelMA + AlgMA + HA samples crosslinked with 365 nm or 395 nm UV lamp. (A) degradation assay; (B) compression modulus evaluation; (C) quantification of the viability rate on days 1 and 8 of C17.2 cells culture Matrigel and in GelMA + AlgMA + HA hydrogel crosslinked with 365 nm or 395 nm UV lamp. Data are presented as mean \pm standard deviation.

We assessed the viability of C17.2 cells for up to 8 days in culture inside the 3D device and compared it with Matrigel (Figure 1C). Results showed no significant differences on day 1 between formulations, which can indicate that the use of a different UV light source was not more beneficial for the cells as we would have predicted. However, there was a significant decrease in viability from day 1 to day 8 on the formulation crosslinked with 395 nm, indicating that the formulation with 365 nm had more promising viability rates.

After, we evaluated the differentiation of C17.2 cells in the 3D device and compare the cell and the hydrogel behavior up until day 15 (Figure 2). In both hydrogels we could see nestin expression on the first timepoint and an increase in the expression of β -III tubulin over the 15 days (Figure 2). These results indicate that cells were able to start their differentiation process independently of the crosslinking UV lamp.

The cell morphology is also distinguished between the two conditions. On the first time point, both conditions have round cells, consistent with the other experiments in the other models. By day 8, cells started to show small projections. However, in the samples crosslinked with a 395 nm UV lamp, the staining of the cells seems to have reached farther inside the channel and allowed better visualization of the cell morphology. On day 15, the cells were placed differently. On the samples fabricated with a 395nm UV lamp, the cells are mostly placed on the border of the remaining biomaterial, but on the right side of the pillars. In the case of the samples fabricated with the 365nm lamp, the cells and the biomaterial have moved to pass the pillars and into part of the lateral channel, while keeping connected. The morphology is not easily identified since the cells seem clustered. The staining of the cells is also weaker towards the center of the middle channel.

We could also observe that from day 8 the hydrogel started to retract into the center when the crosslink was performed with a 395 nm UV lamp. With the 365 nm UV lamp, that behavior was only observed by day 21 of the culture (Figure 18 of Result section). On day 15, this behavior is even more noticeable on the samples crosslinked with the 395 nm UV lamp. This could be an indicator that the sample degraded faster with the 395 nm UV lamp due to a weaker crosslink.

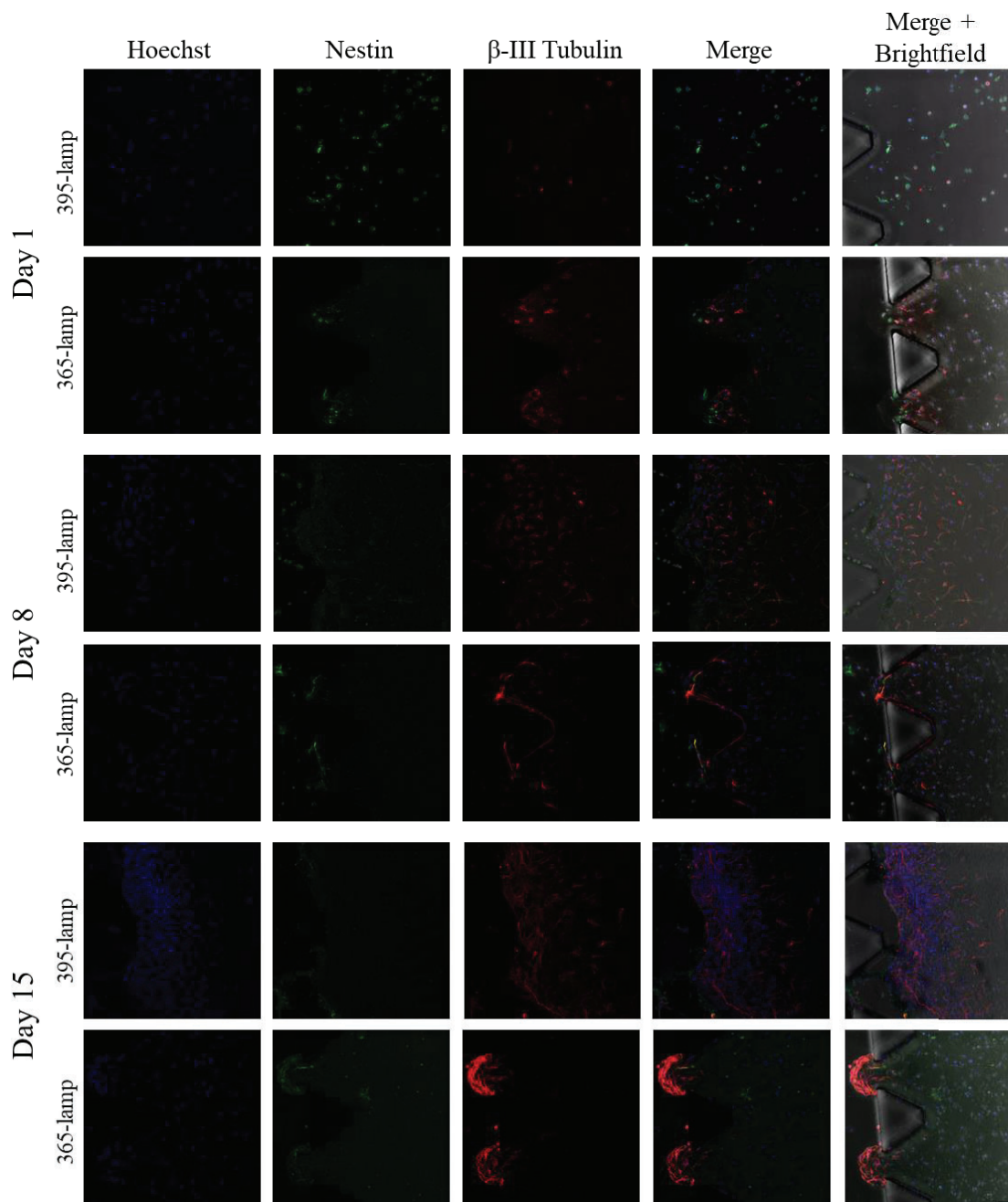


Figure 2 Representative confocal images of the differentiation of C17.2 cells in the 3D microfluidic device crosslinked with two different UV light sources (365 nm vs 395 nm) on days 1, 8 and 15 of culture. Progenitor marker nestin is stained in green, neuron marker β -III tubulin is stained in red and nuclei in blue. Scale bar 100 μ m.

Conclusions and Future Perspectives

The crosslinking of hydrogels with lower wavelengths have been described as less harmful for the cells. In this study we evaluated the physical properties of GelMA + AlgMA + HA hydrogel crosslinked with a 395 nm lamp and compared with the results obtains with 365 nm lamp used throughout the thesis. The results from both hydrogels were similar in all the physical

characterization, proving that the parameters of the hydrogel production were adequate for a comparison between the two materials in the biological assays. C17.2 cells were embedded in both hydrogels and cultured in a 3D microfluidic device, where their viability and differentiation were assessed. The viability of the cells was not improved using a lower wavelength lamp, decreasing significantly by day 8 on that sample. The differentiation of the cells was visible in both materials, but the hydrogel crosslinked with 395 nm started to shrink earlier than the hydrogel crosslinked with 365 nm, proving to be less suitable for long-term culture. Further assays would be recommended to further characterize the culture using this UV source and confirm if the material is suitable for only short-term assays.

Bibliography

1. Erkoc, P. et al. Photocurable pentaerythritol triacrylate/lithium phenyl-2,4,6-trimethylbenzoylphosphinate-based ink for extrusion-based 3D printing of magneto-responsive materials. *J. Appl. Polym. Sci.* 137, 49043 (2020).
2. Fairbanks, B. D., Schwartz, M. P., Bowman, C. N. & Anseth, K. S. Photoinitiated polymerization of PEG-diacrylate with lithium phenyl-2, 4, 6-trimethylbenzoylphosphinate: polymerization rate and cytocompatibility. *Biomaterials* 30, 6702–6707 (2009).